Final Scientific Report

Award Number: DE-FG36-08GO18191
Federal Agency and Organization: DOE EERE – Geothermal Technologies Program

Recipient Organization: Hi-Q Geophysical Inc.
DUNS Number: 826996170
Recipient Address: 106 Fairview Avenue, Ponca City, OK 74601

Project Title: Seismic Fracture Characterization Methodologies for Enhanced Geothermal Systems.
Project Period: March 4, 2009 – January 31, 2016

Principal Investigator: John H. Queen
President
queenjh@cableone.net
(580) 765-9846

Report Submitted by: John H. Queen

Project Partners:
Cost Sharing:
Hi-Q Geophysical Inc.
Stephen G. Muir, Consulting Geologist and Geophysicist
Ormat Nevada Inc.

Non-Cost Sharing:
Lawrence Berkeley National Laboratory

DOE Project Team: DOE Contracting Officer – Laura Merrick
DOE Project Officer – William Vandermeer
Project Monitor – none

Executive Summary

The overall objective of this work was the development of surface and borehole seismic methodologies using both compressional and shear waves for characterizing faults and fractures in Enhanced Geothermal Systems. We used both surface seismic and vertical seismic profile (VSP) methods. We adapted these methods to the unique conditions encountered in Enhanced Geothermal Systems (EGS) creation. These conditions include geological environments with volcanic cover, highly altered rocks, severe structure, extreme near surface velocity contrasts and lack of distinct velocity contrasts at depth. One of the objectives was the development of methods for identifying more appropriate seismic acquisition parameters for overcoming problems associated with these geological factors. Because temperatures up to 300º C are often encountered in these systems, another objective was the testing of VSP borehole tools capable of operating at depths in excess of 1,000 m and at temperatures in excess of 200º C. A final objective was the development of new processing and interpretation techniques based on scattering and time-frequency analysis, as well as the application of modern seismic migration imaging algorithms to seismic data acquired over geothermal areas.

The use of surface seismic reflection data at Brady's Hot Springs was found useful in building a geological model, but only when combined with other extensive geological and geophysical data. The use of fine source and geophone spacing was critical in producing useful images. The surface seismic reflection data gave no information about the internal structure (extent, thickness and filling) of faults and fractures, and modeling suggests that they are unlikely to do so. Time-frequency analysis was applied to these data, but was not found to be significantly useful in their interpretation.

Modeling does indicate that VSP and other seismic methods with sensors located at depth in wells will be the most effective seismic tools for getting information on the internal structure of faults and fractures in support of fluid flow pathway management and EGS treatment. Scattered events similar to those expected from faults and fractures are seen in the VSP reported here. Unfortunately, the source offset and well depth coverage do not allow for detailed analysis of these events. This limited coverage also precluded the use of advanced migration and imaging algorithms. More extensive acquisition is needed to support fault and fracture characterization in the geothermal reservoir at Brady's Hot Springs.

The VSP was effective in generating interval velocity estimates over the depths covered by the array. Upgoing reflection events are also visible in the VSP results at locations corresponding to reflection events in the surface seismic. Overall, the high temperature rated fiber optic sensors used in the VSP produced useful results.

Modeling has been found useful in the interpretation of both surface reflection seismic and VSP data. It has helped identify possible near surface scattering in the surface seismic data. It has highlighted potential scattering events from deeper faults in the VSP data. Inclusion of more detailed fault and fracture specific stiffness parameters are needed to fully interpret fault and fracture scattered events for flow properties (Pyrak-Nolte and Morris, 2000, Zhu and Snieder, 2002).

Shear wave methods were applied in both the surface seismic reflection and VSP work. They were not found to be effective in the Brady's Hot Springs area. This was due to the extreme attenuation of shear waves in the near surface at Brady's. This does not imply that they will be ineffective in general. In geothermal areas where good shear waves can be recorded, modeling suggests they should be very useful for characterizing faults and fractures.

Table of Contents

Executive Summary....2
Accomplishments Compared to Goals and Objectives....6
Project Activities....7
Phase I....7
Task 1: Data Collection and Evaluation....7
Proposed Objectives....7
Accomplishments....7
Data Collection....7
Geological Setting of Brady's Hot Springs Area....9
Preliminary 2009 Geological Model....13
Task 2: Model Building....21
Proposed Objectives....21
Accomplishments....22
2D Modeling....22
Finite Difference Modeling....23
Kirchhoff Modeling....28
3D Modeling....37
Simple Fault Model....38
Simple fault with ellipsoidal heterogeneities....43
Brady's Hot Springs Geophysical Model....46
Simple 3D Seismic Fracture Model....53
Geophysical Modeling Summary....58
Task 3: Seismic Simulation and Survey Design....59
Proposed Objectives....59
Accomplishments....59
Seismic Simulations....59
Survey Design....62
Simulation and Survey Design Summary....63
Phase II....64
Task 4: Surface Orientation Tests....64
Proposed Objectives....64
Accomplishments....64
Permitting....64
Data Acquisition....65
Data Processing....70
Processing Choices....71
Time to Depth Conversion....73
Comparison with Near Offset VSP....76
Preparation for Interpretation....76
Gravity Data....77
Task 5: Near Offset VSP....79

Proposed Objectives....79
Accomplishments....79
Permitting....79
VSP Data Acquisition....79
VSP data processing....80
Rotation Analysis....81
Median Filtering and Mode Separation....84
Corridor Stacks....87
Interval Velocities....87
Task 6: Final Modeling and Acquisition Design....89
Proposed Objectives....89
Accomplishments....90
Permitting....90
Surface Seismic Interpretation....91
Geophysical Model Building and Seismic Simulation....93
Simplified Geophysical Model Results....95
Complex Geophysical Model Results....96
Acquisition Design....97
Multi Offset VSP Design....97
High Areal Coverage Surface Seismic Design....99
Phase III....101
Task 7: Multi Offset VSP....101
Proposed Objectives....101
Accomplishments....101
VSP Data Acquisition....102
VSP Processing....104
VSP Results....104
Task 8: High Areal Coverage Surface Seismic....109
Proposed Objectives....109
Accomplishments....109
Data Acquisition....109
Data Processing....115
Line 9 Results....117
Line 10 Results....121
Line 8 Results....124
Line 6 Results....126
Line 1 Results....128
Line 5 Results....131
Line 7 Results....133
Task 9: Final Interpretation....135
Proposed Objectives....135
Accomplishments....135
Surface Reflection Seismic....135
Dip Lines....138
Strike Lines....144

Shot Gathers....149
Multi Offset VSP....150
Task 10: Technology Transfer....151
Proposed Objectives....151
Accomplishments....151
Task 11: Project Management and Reporting....151
Accomplishments....151
Products Developed Under The Award....152
Publications....152
Web Sites....152
Collaborations....152
Technologies/Techniques....152
Inventions....152
Other Products....152
Computer Modeling....152
References....154

Accomplishments Compared to Goals and Objectives

The overall objective of the proposed work was the development of surface and borehole seismic methodologies using both compressional and shear waves for characterizing fractures in Enhanced Geothermal Systems. We proposed development of both surface seismic and vertical seismic profile (VSP) methods, adapting them to the unique conditions encountered in Enhanced Geothermal Systems (EGS) creation. These conditions include geological environments with volcanic cover, highly altered rocks, severe structure, and lack of distinct velocity contrasts. One of the objectives of our proposed work was the development of methods for identifying more appropriate seismic acquisition parameters for overcoming problems associated with these geological factors. Because temperatures up to 300º C are often encountered in these systems, another objective was the testing of VSP borehole tools capable of operating at depths in excess of 1,000 m and at temperatures in excess of 200º C. A final objective was the development of new processing and interpretation techniques based on scattering and time-frequency analysis, as well as the application of modern seismic migration imaging algorithms to seismic data acquired over geothermal areas.

One of the major accomplishments coming out of this work was the demonstration of the effectiveness of finely spaced point source – point receiver surface seismic acquisition methods at Brady's Hot Springs. In geothermal areas like Brady's, with complex closely spaced faults and large near surface velocity contrasts, these finely spaced acquisition arrays allowed for the application of very long filters for removing the highly scattered noise generated by such geological features.

Shear wave methods were also investigated at Brady's Hot Springs. Three component geophones were used in some surface seismic acquisition. Mode converted shear wave processing was then applied to those data. Shear wave sources were also used in multicomponent VSP acquisition. Unfortunately, the near surface at Brady's Hot Springs was seen to severely attenuate shear waves. Very little shear energy was recovered in the surface seismic data. Almost no source generated shear waves were seen in the VSP measurements in spite of the use of shear sources. However seismic modeling did suggest that shear wave techniques can be useful in fracture and fault characterization and should not be abandoned in general.

Another accomplishment was the acquisition of a full 9-component multiple source offset VSP at Brady's Hot Springs using a newly developed fiber optic sensor string rated at 200º C. A 9-component VSP uses two horizontal and one vertical source recording seismic arrivals at depth in a well on 3-component downhole sensors. This new VSP tool was found to produce reliable data. Events were seen in these VSP data that seismic modeling suggests can be interpreted as fault scattered events. However, due to the limited number of source offsets, modern seismic migration imaging algorithms such as reverse time migration and inversion could not be applied to fully qualify and analyze these events.

Time-frequency analysis was applied to the surface seismic data. While these results were interesting, they were not found to be useful in the final interpretation of these data for faults and fractures.

Details of these accomplishments are discussed below.

Project Activities

The proposed work plan was broken up into three major phases. Ormat Technologies Inc., a major geothermal operator, agreed to be a major participant in this work. They provided access to and data from their Brady's Hot Springs geothermal area. The first phase started with collection and assessment of existing data provided by Ormat. This was followed by a major modeling effort leading to design of an acquisition plan. In the second phase, extensive field testing of the model based acquisition plan took place. Surface seismic orientation tests were run as well as a near offset VSP. Gravity data was also acquired along surveyed surface locations. These data were then processed and modeled to validate and modify the initial models and acquisition plan. The final phase of the program was the acquisition, processing, and interpretation of extensive VSP and surface reflection surveys with large areal coverage. In collaboration with James Faulds and co-workers at University of Nevada, Reno, an interpretation of these data was integrated with their geological data to produce a geological model of the Brady's Hot Springs geothermal area.

Lawrence Berkeley National Laboratory, a Federally Funded Research and Development Center, has unique capabilities in designing and deploying down hole seismic tools in geothermal areas. They also have extensive experience in the acquisition, processing, and interpretation of VSP data. With these unique capabilities in mind, they were separately contracted by DOE for their assistance with several of the tasks described below.

Phase I

Task 1: Data Collection and Evaluation

Proposed Objectives

The proposed objective of this task was the collection and evaluation of existing geological and geophysical data from the area around Brady's Hot Springs. These studies will result in the formulation of a geological model of the Brady's Hot Springs area.

Accomplishments

Data Collection

We collected and reviewed an extensive bibliography of journal articles and presentations on Brady's Hot Springs and Desert Peak geothermal areas. In collaboration with Steve Muir, contacted Ezra Zemach and Peter Drakos of ORMAT and Gene Suemnicht of EGS Inc., and developed a list of data requested as part of ORMAT's in kind contribution to the project. Received Brady's geology, surface alteration and well location map from ORMAT, as well as Faulds and Garside (2003) surface and cross section geological map. Received and reviewed report on Desert Peak surface seismic work.

Personnel from Hi-Q Geophysical Inc., Stephen G. Muir, Consulting Geologist and Geophysicist, and ORMAT met in ORMAT's offices in Reno, NV. A significant amount of geological material, including proprietary reports, well logs, and geophysical data from the Brady's Hot Springs geothermal field were reviewed and discussed. During this meeting, ORMAT transferred a large amount of data in electronic format to Hi-Q Geophysical Inc.

These data included location and well track data, drilling reports, horizon data, injection testing results, and temperature and pressure logs for the 88-11, BCH-3 and 15-12 wells. Extensive geological data were also transferred, including structure and alteration maps and cross sections, proprietary faulting maps and cross sections, and thermal anomaly maps. A large data base of temperature and pressure logs for many of the wells in the Brady's field were also transferred. Geophysical data including gravity maps, resistivity maps, and INSAR results were transferred.

Numerous proprietary ORMAT internal reports were also transferred. These included a preliminary geological conceptual model for Brady's Hot Springs geothermal system prepared by a subcontractor. The Desert Peak West and Brady's South exploration plan was also distributed. In addition, a report was included that gave results for the Brady's 15-12 well and a report discussing concepts for new drilling targets

These preliminary maps and geological cross sections were based on temperature gradient maps, geological maps from various sources, surface thermal anomaly maps, interpretation of downhole geophysical induction wireline log correlations, and thermal cross sections interpreted from temperature logs. One of the significant conclusions of this report was the presence of a series of northeast-trending normal faults that form a trend at least four miles long that are cut by northwest trending high-angle normal and reverse faults.

The area around ORMAT Brady's Hot Springs geothermal plant was visited. This included a review of the geological core storage facility located at the field. Geological core from both Brady's Hot Springs and Desert Peak exploratory wells were examined and discussed with ORMAT personnel. The core reviewed demonstrated the nature of complex vertical and horizontal lithological variations throughout the field, as well as the presence of complex and extensive open and mineralized fractures. ORMAT personnel are currently conducting a detailed analysis of these core samples and results of those studies will be transferred to Hi-Q Geophysical Inc. once they are completed.

After visiting the core storage facility, ORMAT personnel led a walking tour of the field area. Extensive surface rock alteration and other manifestations of geothermal activity were observed, as well as surface expression of the extensive faulting in the area. Potential vehicle access for future geophysical surveys was discussed and it was concluded that no major problems were anticipated for geophysical surveys planned for later stages of the project.

Following the field visit, personnel from Hi-Q Geophysical Inc. and Stephen G. Muir, Consulting Geologist and Geophysicist, visited the Nevada Bureau of Mines and Geology library where a number of maps and reports related to the project were purchased. A meeting was also held with Prof. James Faulds at the University of Nevada, Reno. Prof. Faulds was extremely helpful, discussing his extensive work mapping the lithology and faulting throughout the Brady's Hot Springs area. At the end of this meeting, Prof. Faulds transferred an electronic copy of his latest mapping results to Hi-Q Geophysical Inc.

Over the next few months, multiple trips were made to Reno by Stephen G. Muir in order to review and obtain additional geological data from the Nevada Bureau of Mines and Geology and the Nevada Bureau of Minerals. Numerous logs from exploratory wells not previously provided by ORMAT were obtained. These data included mud logs, downhole geophysical induction logs and temperature surveys. Ground and Kelly bushing elevations for the various wells were also obtained. Hot water production and injection data were also acquired from Nevada Bureau of Minerals for wells at Brady's

Hot Springs.

Meetings and follow-up data transfer were conducted with Mr. Larry Garside, Nevada Bureau of Mines and Geology regarding historical development of the Brady's Hot Springs geothermal field and other fields in northwestern Nevada. Discussions with Mr. Gary Opplinger of Magma Energy regarding his previous gravity work at Brady's Hot Springs were held. Based on these conversations additional data was requested from Nevada Bureau of Mines and Geology.

Following these meetings, personnel from the organization of Stephen G. Muir, Consulting Geologist and Geophysicist and Hi-Q Geophysical Inc. undertook the task of evaluating this extensive collection of data. Based on these data and other public sources, a preliminary geological model of the Brady's Hot Springs area was formulated.

Geological Setting of Brady's Hot Springs Area

Figure 1.1 Below shows the location of the Brady's Hot Springs Known Geothermal Resource Area (KGRA). It is located approximately 80 km (50 miles) northeast of Reno, NV.

Index map of Nevada showing 1 by 2 degree quadrangles.

Figure 1.1: Location Map For Brady's Hot Springs KGRA.

Figures 1.2 and 1.3 show the geological setting for the Great Basin and the area surrounding Brady's Hot Springs obtained from public sources. They present the geological structural framework of the northwestern Nevada area.

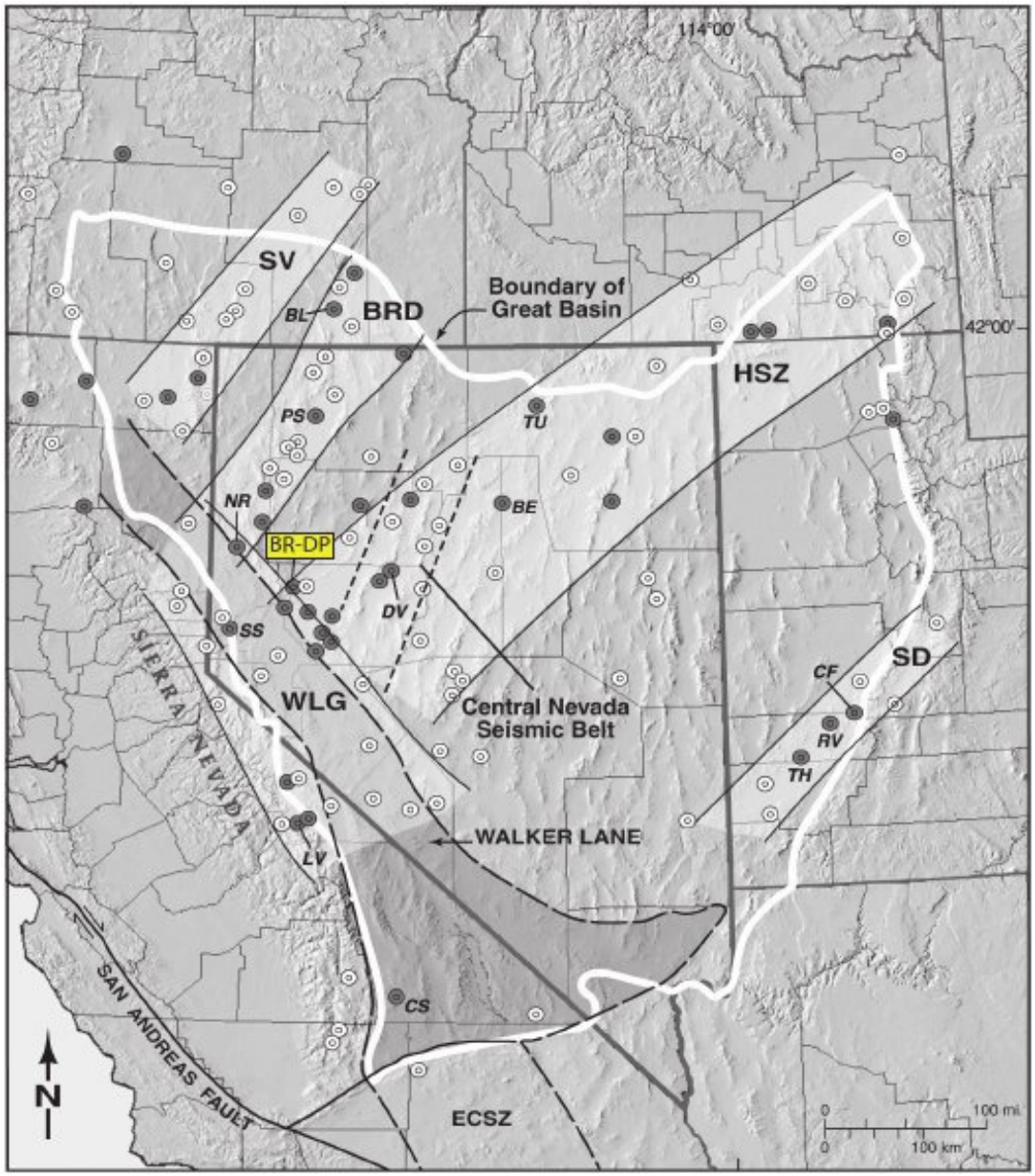

Figure 1.2: Geothermal belts in the Great Basin (modified from Faulds et. al., 2006). Geothermal fields cluster in the Sevier Desert (SD), Humboldt structural zone (HSZ), Black Rock Desert (BRD), Surprise Valley (SV), and Walker Lane (WLG) belts. The northwestern Great Basin contains the greatest concentration of fields. White circles are geothermal systems with maximum temperatures of 100 – 160º C; gray circles have maximum temperatures > 160º C. ECSZ, eastern California shear zone. The boundary of the Great Basin is indicated by a closed white polygon. Short dashed lines bound the central Nevada seismic belt. Abbreviations for individual geothermal fields: BL, Borax Lake Hot Springs; BE, Beowave; BR-DP, Brady's and Desert Peak; CF, Cove Fort; CS, Coso; DV, Dixie Valley; LV, Long Valley–Mammoth; NR, Needle Rocks; PS, Pinto Hot Springs; RV, Roosevelt; SS, Steamboat; TH, Thermo Hot Springs; TU, Tuscarora.

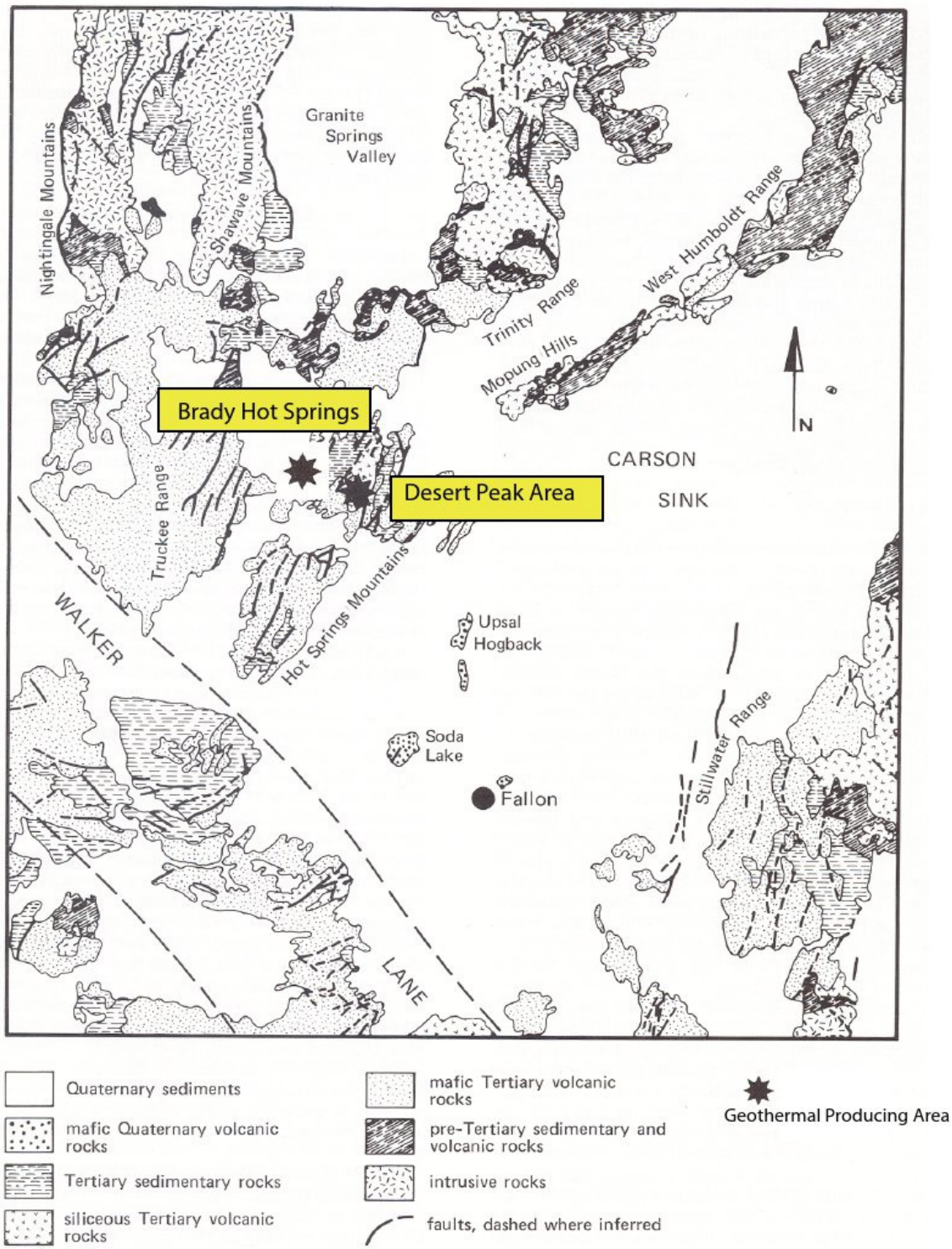

Figure 1.3: Regional surface geology in the area surrounding Brady's Hot Springs geothermal area.

Figure 1.4 is a surface geological map of the Brady's Hot Springs area based on data provided by ORMAT in 2009. It depicts the surface geology as understood at that time. Geothermal well locations

and hydrothermal alteration of surface rocks are shown. Also included are locations of surface manifestations of the Brady's Hot Springs geothermal system including: fumeroles; mud-pots, sinter deposits and calcareous tufa deposits. Understanding of the geology around the Brady's Hot Springs area has changed since that time.

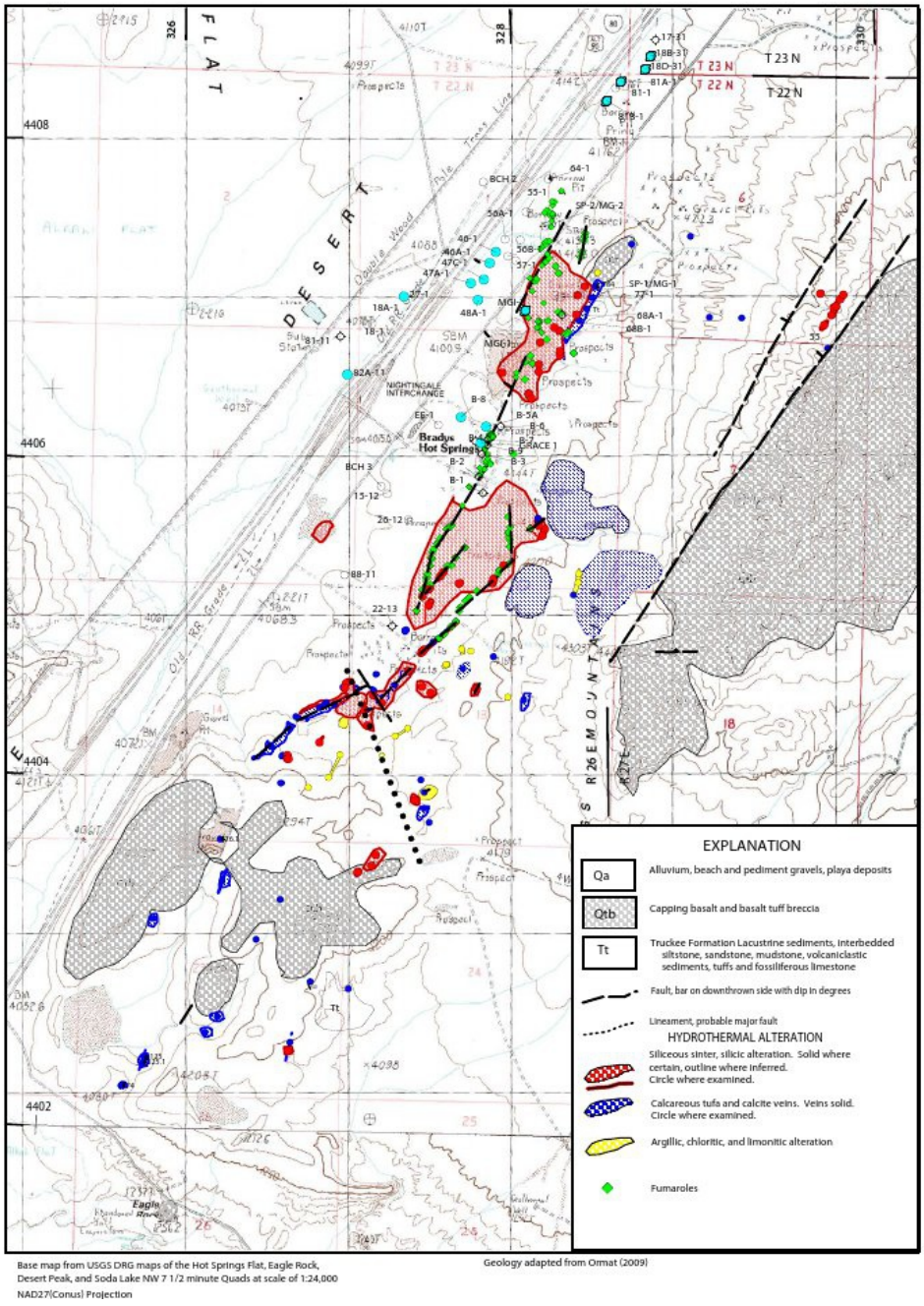

Figure 1.4: Surface geological map of the Brady's Hot Springs area depicting the surface geology as understood in 2009. This view of the geology around the Brady's Hot Springs area has changed since that time.

Preliminary 2009 Geological Model

Utilizing the data provided in 2009, a preliminary geological model of the Brady's Hot Springs area was developed. This included newer ideas on the faulting in the area. A series of 7 geological cross sections were produced.

Figure 1.5 shows the locations of these cross sections. This figure also depicts the locations of hot water producing wells that show the reported production volumes obtained from Nevada Division of Minerals. Locations of the surface thermal anomalies are shown as well. It also shows revised surface fault locations.

These geological features were based on data provided by ORMAT in 2009. The map identifies individual identified fault strands of the northeast-trending fault system. Offset along the northeast-trending faults is down-to-the-west or normal sense of displacement. The fault geometry from this map is based on interpretation of subsurface geophysical and mud logs from the geothermal exploratory wells. Normal sense of displacement of up to 500 to 1000 feet is inferred to be present along these faults. Also shown is a series of northwest-trending normal faults. This fault pattern is similar to that shown on Figure 1.3 and is inferred to have a strike direction roughly 60 degrees to the Walker Lane. The location of the Brady's Hot Springs geothermal system is roughly at the intersection of the Walker Lane and the Humboldt Structural Zone (Figure 1.2).

Faults depicted on Figure 1.5 have been named as follows: 27-1 Fault, Middle Fault, and Brady’s Fault. All of these faults are inferred to have been older than the northwest-trending cross-fault zone. The northwest-trending faults have been identified as follows: USFI Cross-Fault, BPP-Cross-Fault and an unnamed third fault.

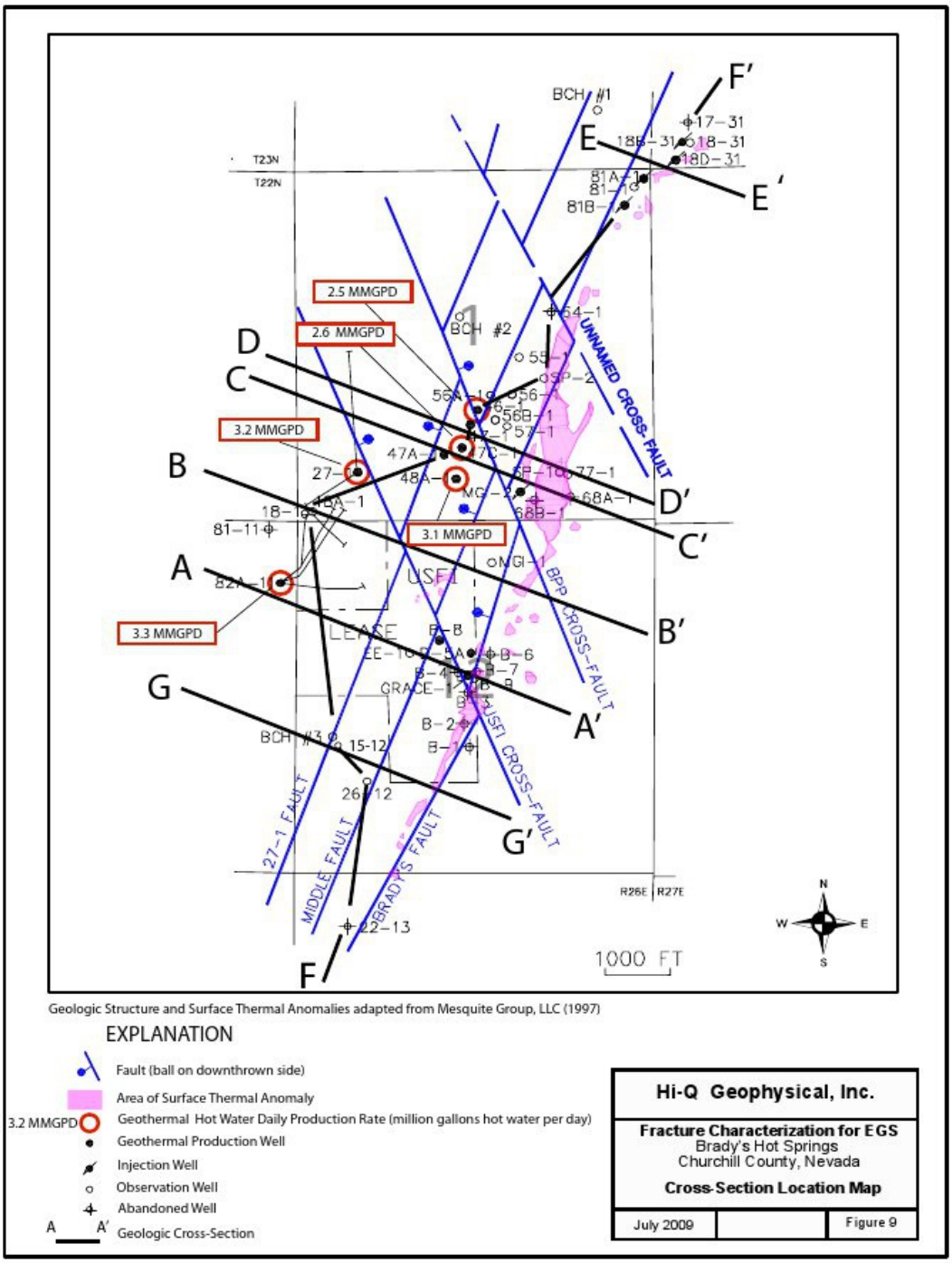

Figure 1.5: Locations of cross sections for the preliminary Brady's Hot Springs geological model based on 2009 data. Also shown are well locations, water production rates, areas of surface thermal anomalies, and fault locations.

Figures 1.6 through 1.12 show geological cross sections through the Brady's Hot Spring geothermal field based on data available in 2009. These sections were prepared from the subsurface data obtained

from ORMAT and from additional data collected from Nevada Bureau of Mines and Geology, and from Nevada Division of Minerals. Geological units for these cross-sections include: Undifferentiated Truckee and Desert Peak Formations; Chloropagus Formation; Tertiary Rhyolite and pre-Tertiary basement complex. Quaternary alluvium has not been identified on the cross-sections. These geological units are based previous subsurface descriptions made by ORMAT, Faulds and Garside (2003) and by Benoit et al., (1982).

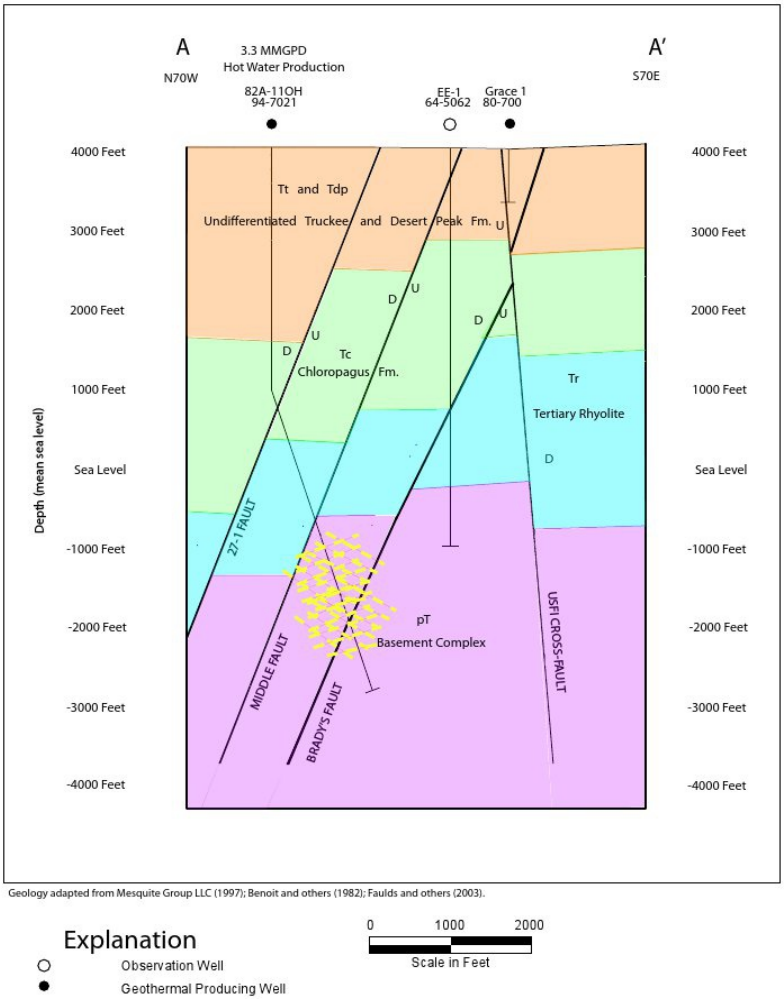

Geology adapted from Mesquite Group LLC (1997); Benoit and others (1982); Faulds and others (2003).

Explanation
Observation Well
Geothermal Producing Well

0 1000 2000
Scale in Feet

Figure 1.6: Geological cross section A – A' based on 2009 preliminary geological model. Location is shown in Figure 1.5. Geology adopted from Benoit et al., (1982), and Faulds and Garside (2003).

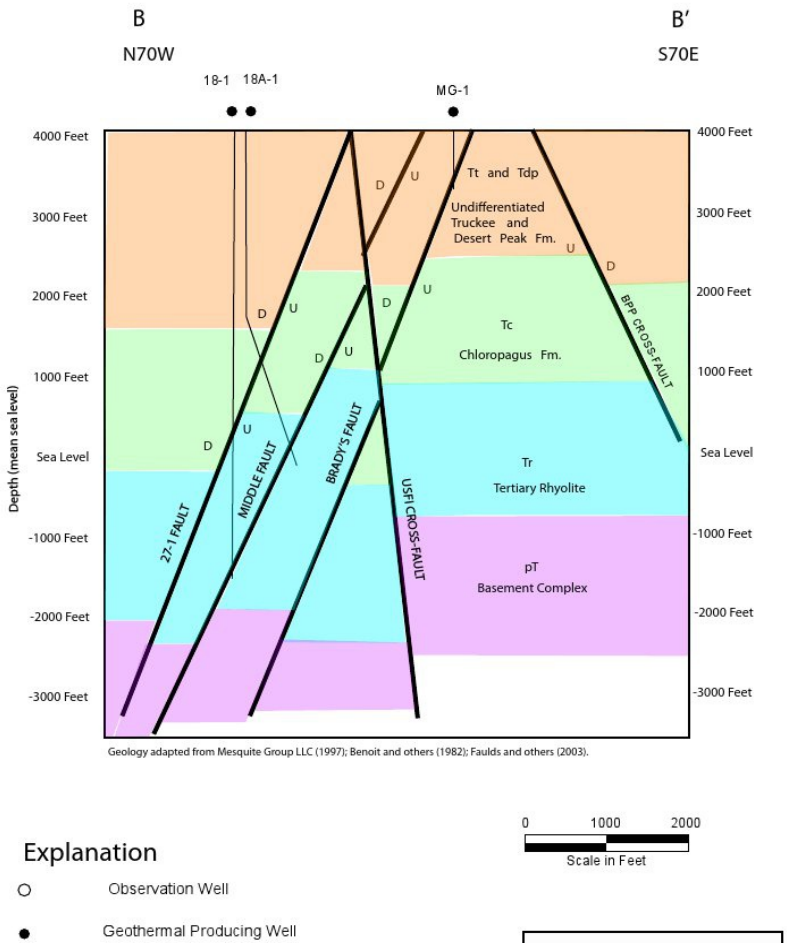

Figure 1.7: Geological cross section B – B' based on 2009 preliminary geological model. Location is shown in Figure 1.5. Geology adopted from Benoit et al., (1982), and Faulds and Garside (2003).

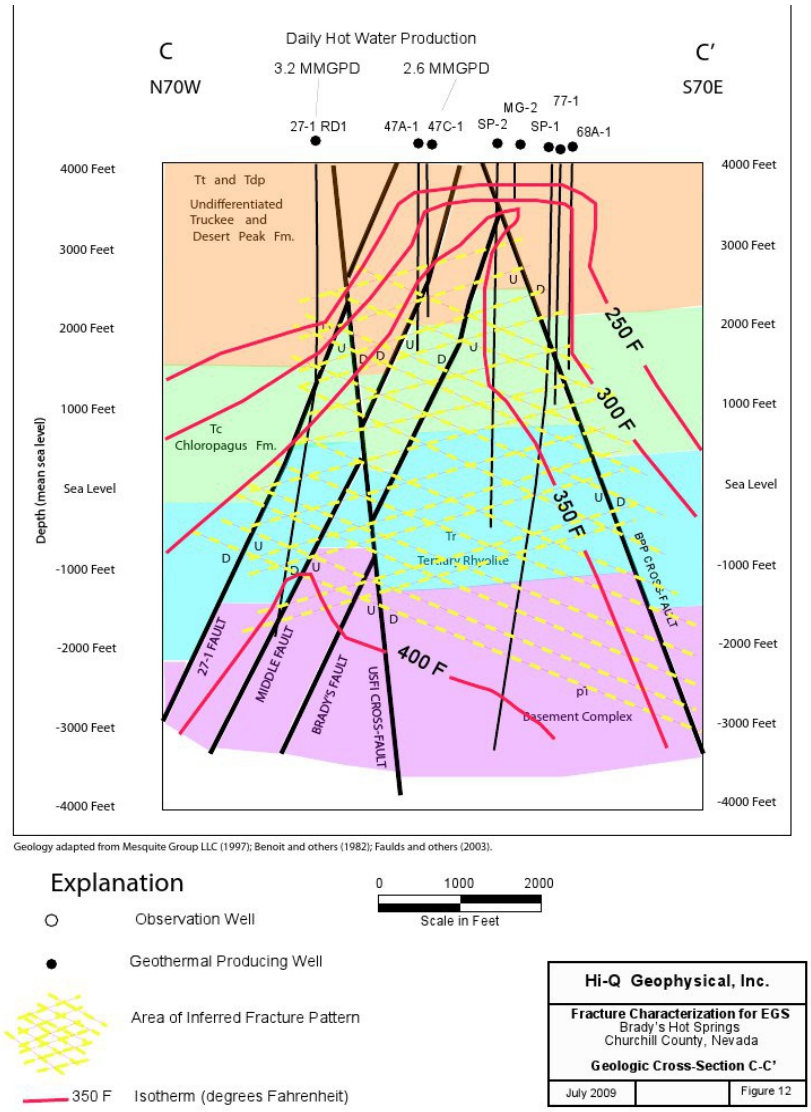

Figure 1.8: Geological cross section C – C' based on 2009 preliminary geological model. Location is shown in Figure 1.5. Isotherms are shown as red lines. Yellow stippled areas show regions of inferred fractures. Geology adopted from Benoit et al., (1982), and Faulds and Garside (2003).

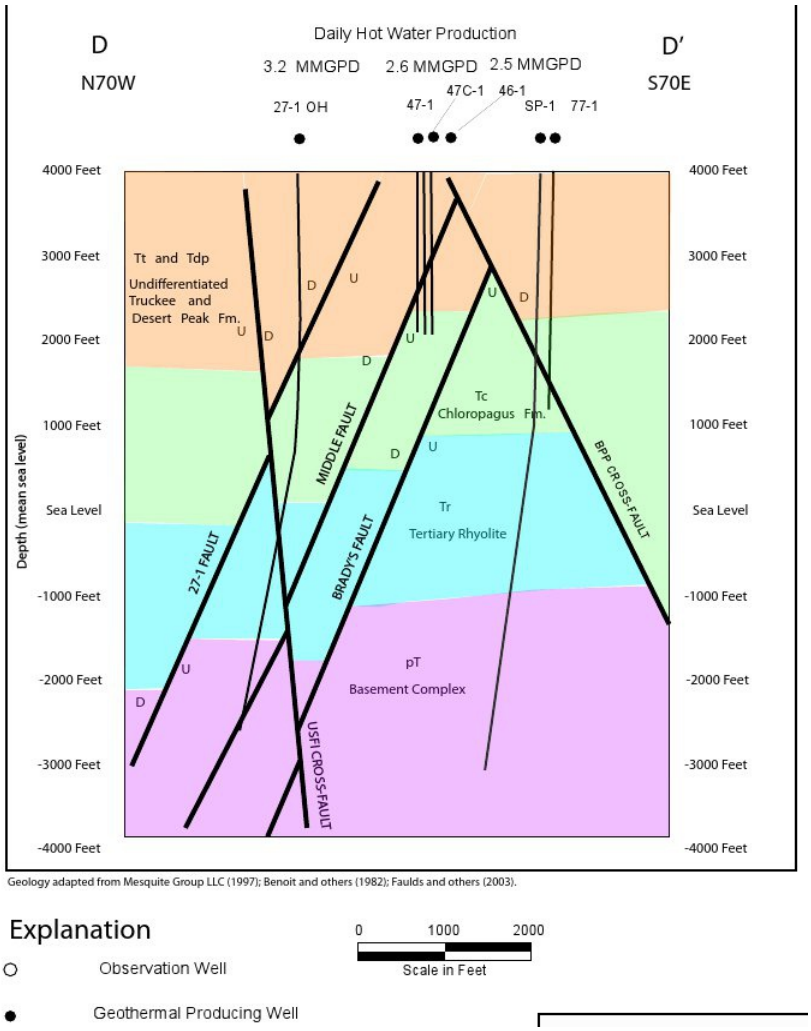

Geology adapted from Mesquite Group LLC (1997); Benoit and others (1982); Faulds and others (2003).

Figure 1.9: Geological cross section D – D' based on 2009 preliminary geological model. Location is shown in Figure 1.5. Geology adopted from Benoit et al., (1982), and Faulds and Garside (2003).

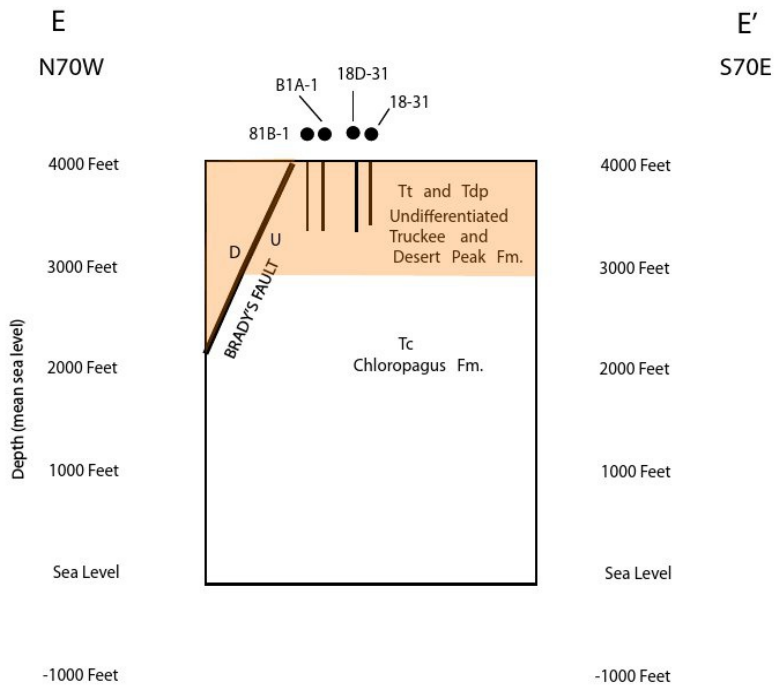

Figure 1.10: Geological cross section E – E' based on 2009 preliminary geological model. Location is shown in Figure 1.5. Geology adopted from Benoit et al., (1982), and Faulds and Garside (2003).

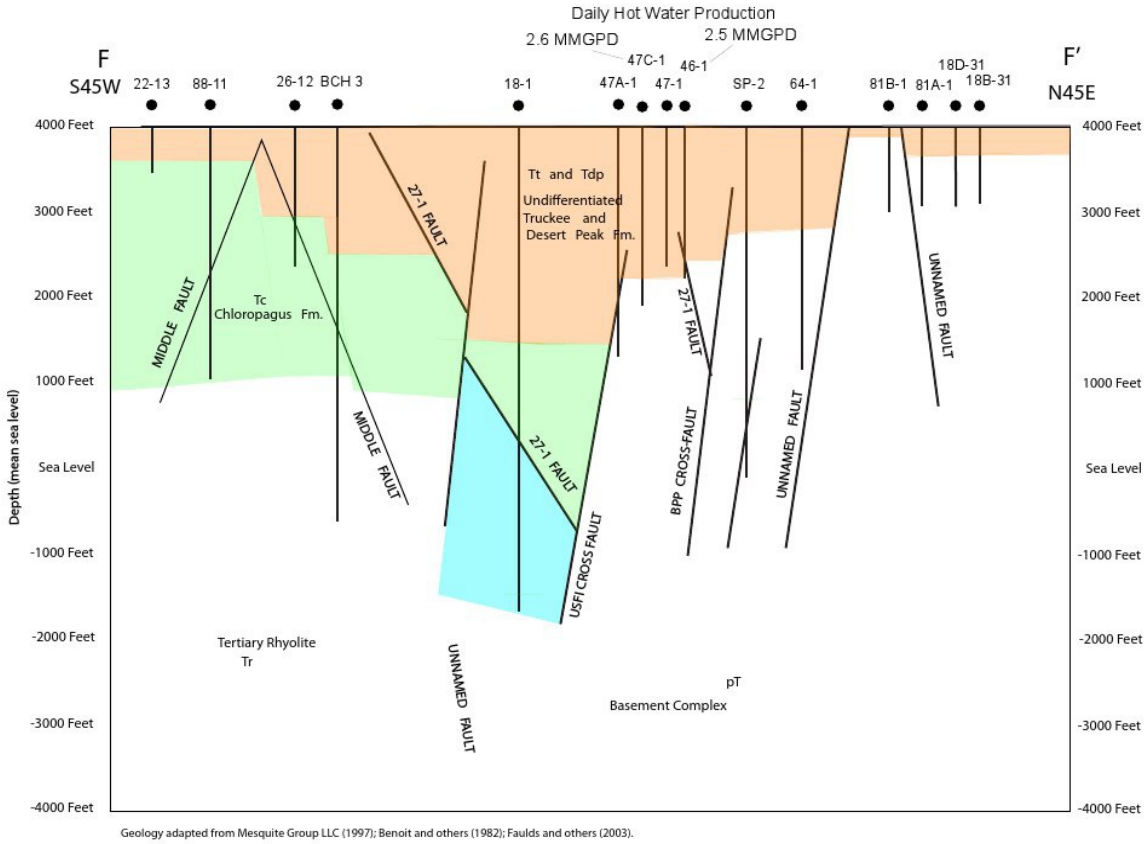

Figure 1.11: Geological cross section F – F' based on 2009 preliminary geological model. Location is shown in Figure 1.5. Geology adopted from Benoit et al., (1982), and Faulds and Garside (2003).

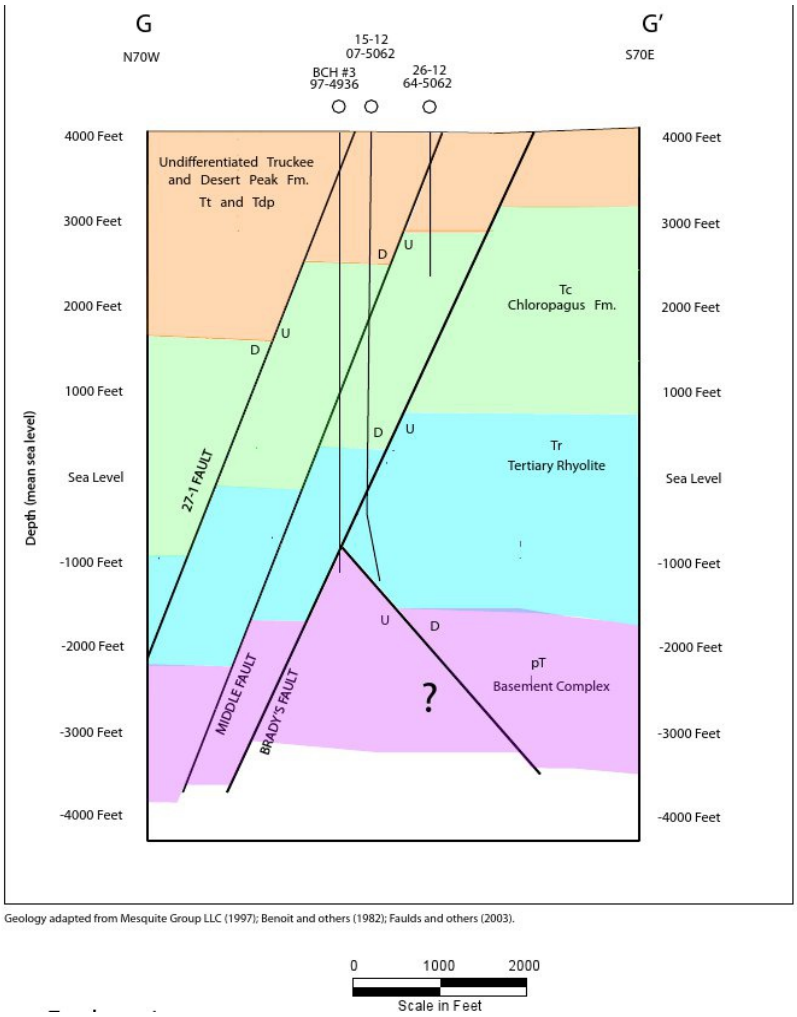

Geology adapted from Mesquite Group LLC (1997); Benoit and others (1982); Faulds and others (2003).

Figure 1.12: Geological cross section G – G' based on 2009 preliminary geological model. Location is shown in Figure 1.5. Geology adopted from Benoit et al., (1982), and Faulds and Garside (2003).

Task 2: Model Building.

Proposed Objectives

The proposed objective for this task was the building of a 3D geophysical velocity and density model based on the geological model. Density, compressional and shear velocity estimates will be based on identified lithologies from task1 factoring in any velocity and density information available from the Brady's Hot Springs area as well as nearby areas. A major geophysical acquisition program is currently underway at the Desert Peak EGS area operated by Ormat Technologies Inc. Desert Peak is adjacent to Brady's Hot Springs, and data generated by the Desert Peak project may be incorporated into the Brady's Hot Springs models. Rock physics principles will be applied in cases where no direct data are available.

Accomplishments

2D Modeling

Using the preliminary geological description discussed above, an initial 2D geophysical velocity and density model was constructed.

Very few if any sonic logs were available at this time from the Brady's Hot Springs wells. To assign velocities and densities to the various lithological units found in the Brady's geological description, velocities and densities from the nearby Desert Peak wells were used.

An extensive data base of sonic logs exists for the Desert Peak geothermal wells. As part of the Desert Peak studies, a detailed velocity model was generated from these logs. With approval from ORMAT, digital copies of sonic logs and velocity models were transferred from personnel at Lawrence Berkeley National Laboratory to Hi-Q Geophysical Inc.

Cross section A-A' (Figure 1.6) from the geological description of Brady's Hot Springs discussed above was combined with knowledge of velocities and densities for each lithology derived from the Desert Peak sonic logs to generate a preliminary 2D seismic velocity and density model. Compressional seismic velocities for this model are shown in Figure 2.1.

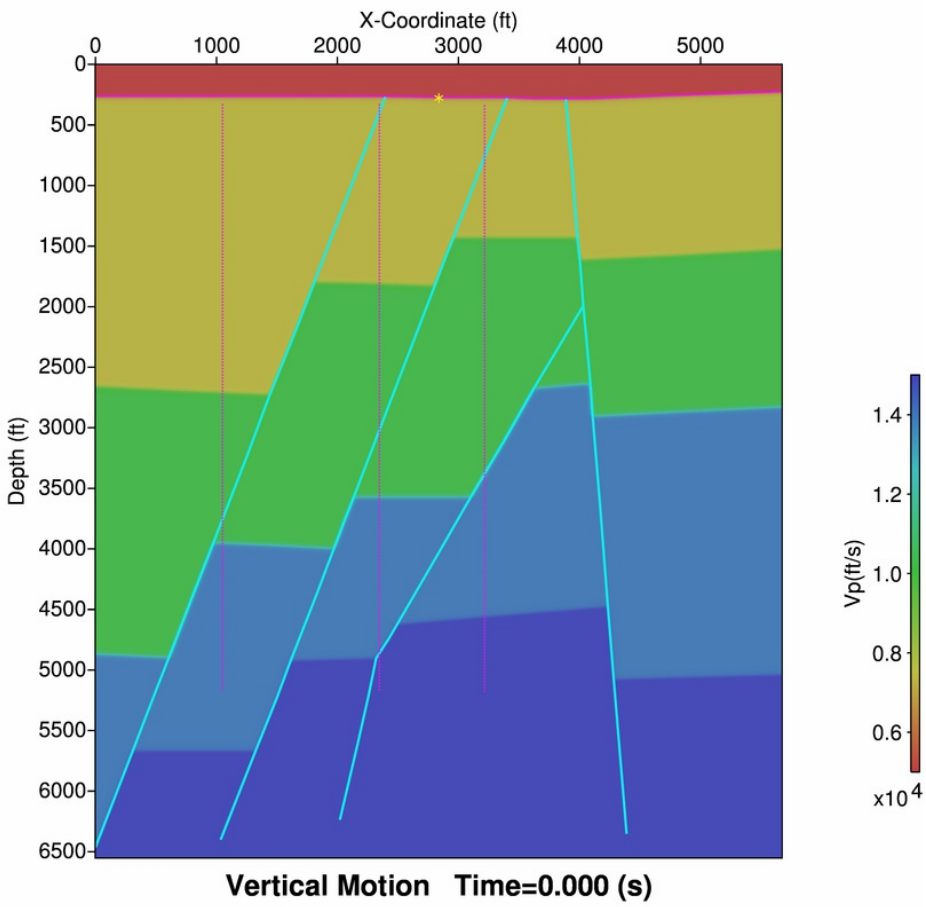

Figure 2.1: 2D Geophysical model along cross section A – A' (Figure 1.6). Colors represent compressional velocities following color bar on right of figure. The location of the simulated source is shown by the yellow asterisk near the center-top of the model. A simulated surface array of geophones is shown by the horizontal magenta line, and the locations of 3 simulated VSP wells is shown by the vertical magenta lines.

Finite Difference Modeling

A number of seismic simulations were run for this model using a staggered grid finite difference method (Levander, 1983; Juhlin, 1995). The primary objective of these first simulations was to determine stable grid spacing, time step and smoothing parameters for this method given the velocities expected for the Brady's Hot Springs geothermal area.

Surface reflection and VSP geometries were simulated. The location of the simulated source is shown by the yellow asterisk near the top center of the model in Figure 2.1. The simulated surface array of geophones is shown by the horizontal magenta line, and the locations of 3 simulated VSP wells is shown by the vertical magenta lines.

An aspect of the staggered grid finite difference method is that if grid spacing is too coarse or time steps too large for a given velocity model, numerical dispersion is introduced into the results. On the

other hand, the amount of memory and run time required to complete a given simulation increases dramatically as grid spacing is reduced. Run time also increases as time step size is reduced. In order to stably run as large a model as possible in a reasonable time, optimal grid spacing and time step size must be determined.

Numerical velocity and density grids must also be smoothed. For dipping interfaces, the “stair case” introduced by using a rectangular grid can lead to diffractions in the simulated wave fields if appropriate smoothing is not used. This is particularly a problem when high velocity contrasts are present such as those anticipated in the Brady's Hot Springs area.

Using the Courant stability condition (Courant et al., 1967) as a starting point, a number of grid spacing and time step sizes were used to simulate the seismic response of the model shown in Figure 2.1. It was finally decided that a grid spacing of 0.5 m and a time step size of 0.00005 s were sufficiently small to give dispersion free results, while still large enough to allow the completion of the simulation in reasonable time. A smoothing radius of 8 m was found to sufficiently remove grid related diffractions.

Figure 2.2 shows a snapshot of the seismic wave field simulated over the model of the A – A' cross section at a time of 0.25 s after the onset of the seismic source using the above mentioned grid spacing, time step size, and smoothing radius. The simulated source is a vertical source located at the position of the yellow asterisk near the top center of the figure. The wave field shown in black to gray represents the amplitude of the vertical velocity. Again, the magenta lines show the locations of simulated geophone positions used to generate the synthetic seismograms for this model.

At 0.25 s, the down going P-wave field has just impinged on the top of the Chloropagus formation. The severe effects of the faulting can be seen even at these early times. Both the down going transmitted wave fields and the up going reflected wave fields are severely distorted by the structure of the faults. However, the wave fields are seen to propagate without significant grid dispersion, indicating a satisfactory choice for grid spacing and time step size. No diffractions are apparent in wave fields propagating along uniform boundaries, which shows that adequate smoothing has been applied.

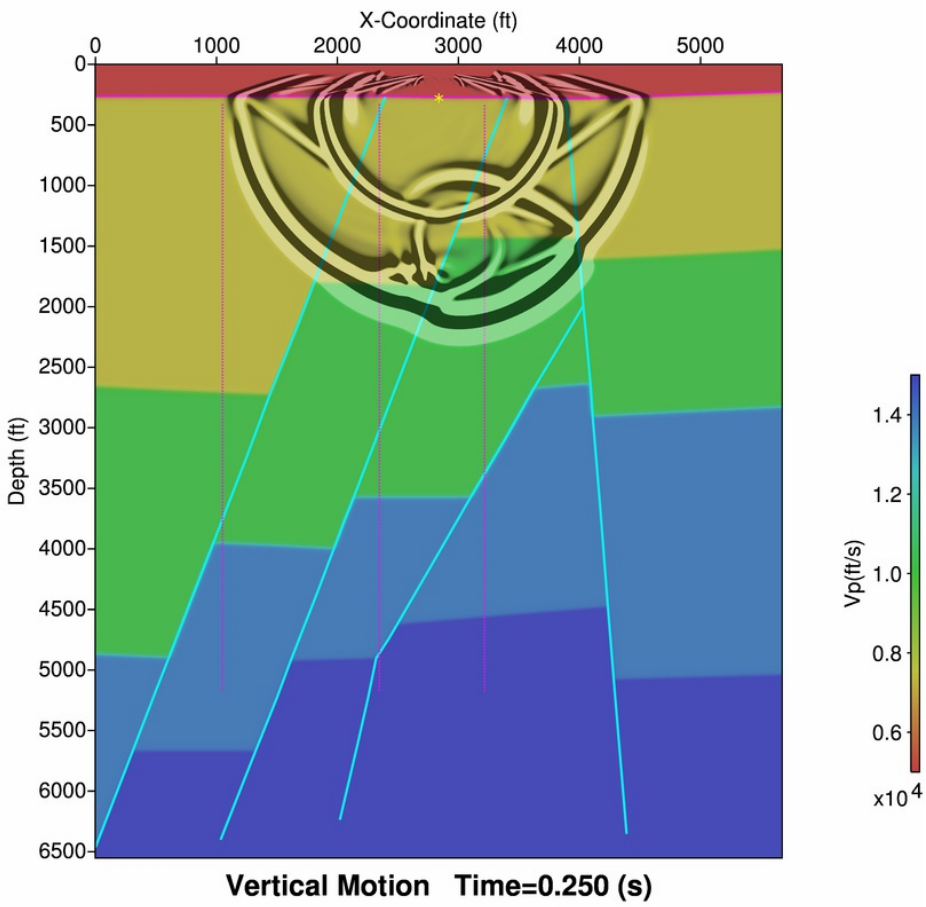

Figure 2.2: Simulated snapshot of the seismic wave field at 0.25 s as the down going wave crosses a major fault. The wave field is seen to be severely disrupted by the fault structure. No grid dispersion or diffractions are visible indicating a satisfactory choice for grid spacing and time step.

Figure 2.3 shows a similar snapshot for a time of 0.50 s. The wave fields have been severely disrupted by the faulting and associated velocity contrasts. This underscores one of the problems in acquiring and processing seismic data in areas such as Brady's Hot Springs. The extreme structure related to faulting highly disrupts the wave fields, emphasizing the need for choosing appropriate offset and flag spacing parameters in order to properly image the wave fields, many of which are propagating nearly horizontally. The goal in Task 3 is to use these seismic models to determine appropriate seismic acquisition parameters.

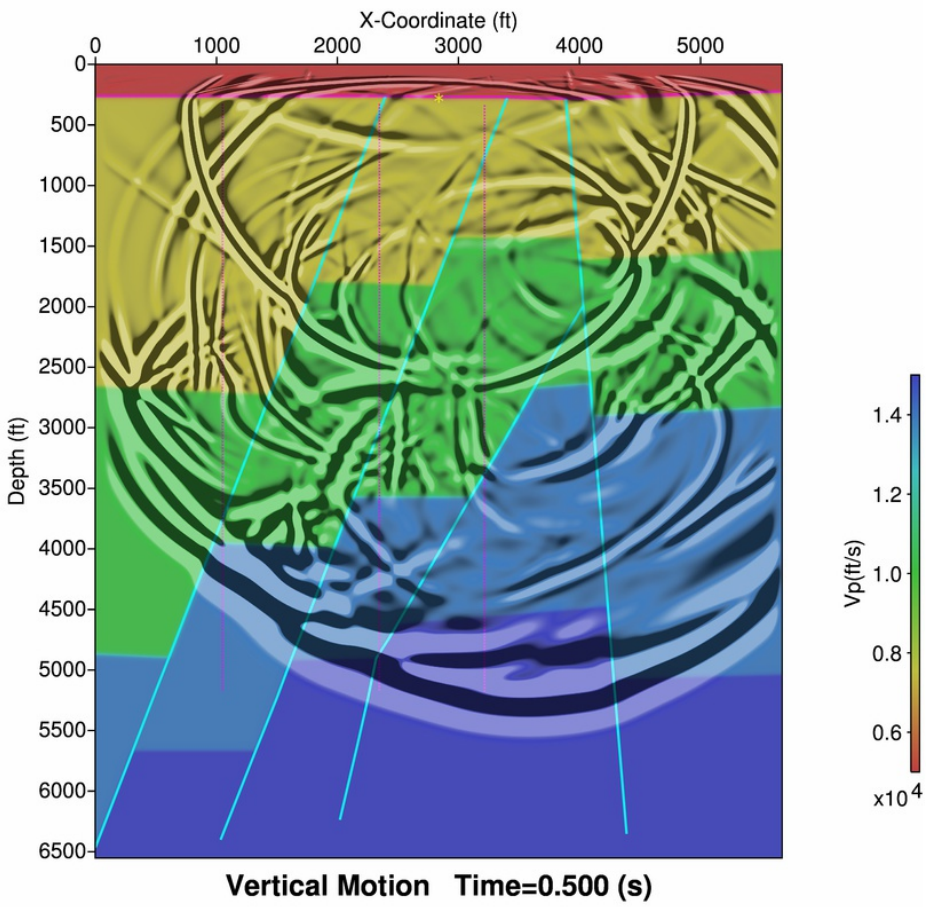

Figure 2.3: Simulated snapshot of the seismic wave field at 0.50 s. Scattering from the offset beds associated with faulting has severely disrupted the wave field.

Figure 2.4 shows the simulated surface vertical component seismograms obtained using the staggered grid finite difference method for the model of Figure 2.1. Figure 2.5 shows similar seismograms for the simulated VSP well in the center. Consistent with the disrupted response shown in the snapshots, these synthetic seismograms show a very complex response, even though the simulated lithology has been simplified.

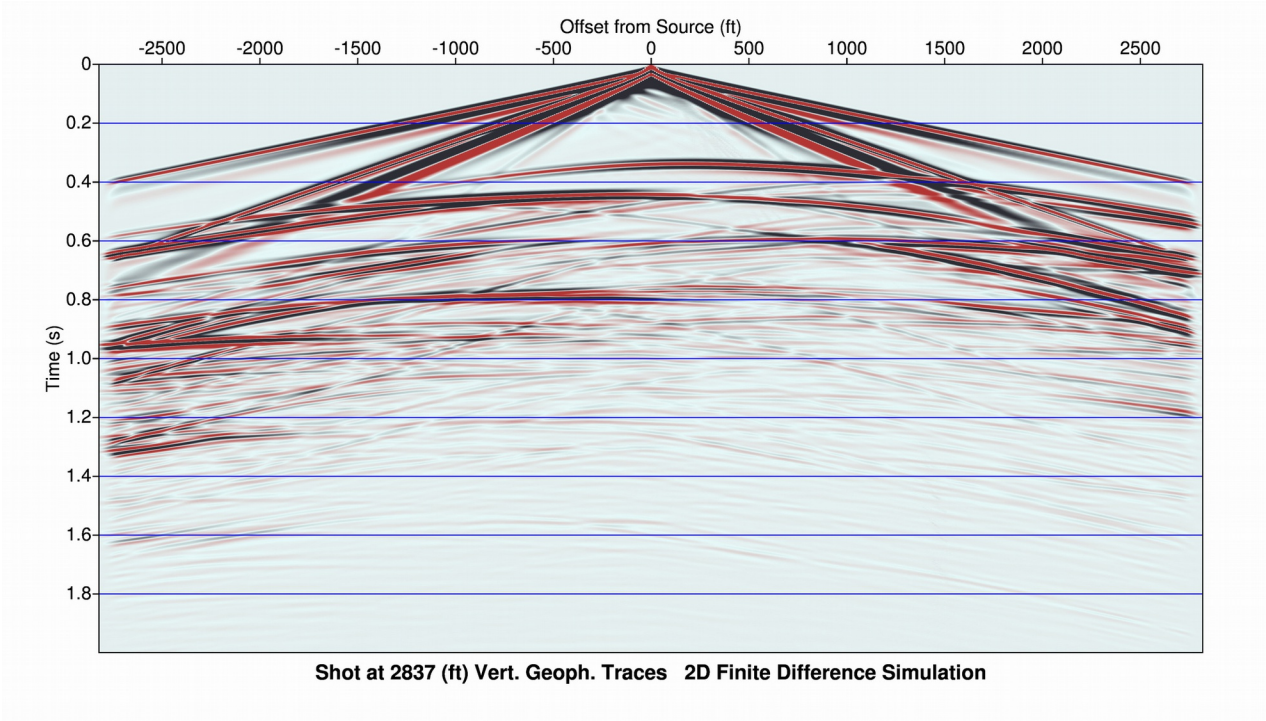

Figure 2.4: Simulated surface reflection shot gather from the model shown in Figure 2.1.

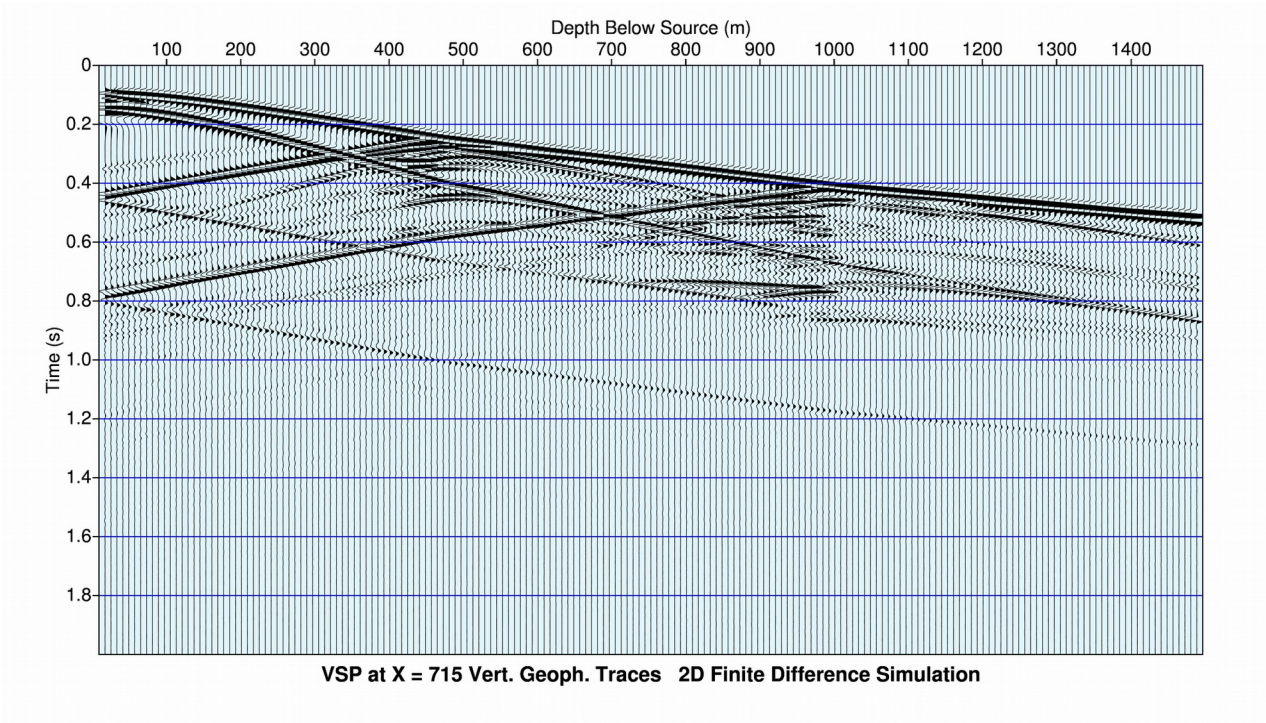

Figure 2.5: Simulated vertical seismic traces from the center VSP shown in Figure 2.1. Energy scattered from the faults shows up as lines of events with near horizontal slope.

An interesting aspect of these simulations is the near horizontal propagation of events scattered from the fault interfaces. Related to this horizontal propagation, very little of the energy scattered from the faults actually reaches the surface array. This horizontally propagating energy does strike the VSP arrays, resulting in many of the events showing near horizontal slope in Figure 2.5. The near horizontal slope of these events distinguishes them from events propagating up and down, which have a slope characteristic of the shear and compressional velocity.

Recording energy directly scattered from the faults is important. Modeling reported by Gritto and Majer (2003) suggests that such events can be interpreted in terms of specific stiffness of the faults and fractures. Specific stiffness is in turn related to the flow properties of the fault (e. g., Pyrak-Nolte and Morris, 2000, Zhu and Snieder, 2002).

Aside from the problems associated with severe structure related to faulting, an additional problem encountered in areas such as Brady's Hot Springs is the presence of highly altered near surface zones. To begin investigating the effects of such zones and the need to include them in the seismic model, the model of cross section A-A' (Figure 2.1) was slightly modified. As a preliminary step in simulating the effects of highly variable near surface alteration, a very low velocity horizontal layer was placed in the top of the seismic model.

Kirchhoff Modeling

For the modeling discussed above, the staggered grid finite difference method was used. An alternative modeling method is the Kirchhoff modeling approach. The Kirchhoff method is much faster than the staggered grid finite difference method, but includes more approximations. One limitation is the need for highly smoothed velocity models. A highly smoothed version of the model shown in Figure 2.1 was modified to include a near surface alteration zone. Using a Seismic Un*x (SU) (Cohen and Stockwell, 2007) Kirchhoff modeling program based on the work of Bleistein (1986), this model was used to simulate a single offset Common Depth Point (CDP, also called Common Mid Point or CMP) seismic section. A smoothing radius of 64 m was found to be adequate for the Kirchhoff method using these velocities. Discrete reflectors were included in this model using reflection coefficients based on the velocity contrasts shown in Figure 2.1.

Results of this simulation are shown in Figure 2.6. The location of many of the faults is apparent due to the bed offsets. There is not evidence of strong fault plane reflections. Such scattered events are really needed to characterize details of the internal fault structure such as specific stiffness. It is hoped that such properties could be further interpreted in terms of the flow properties of the fault (e. g., Pyrak-Nolte and Morris, 2000, Zhu and Snieder, 2002).

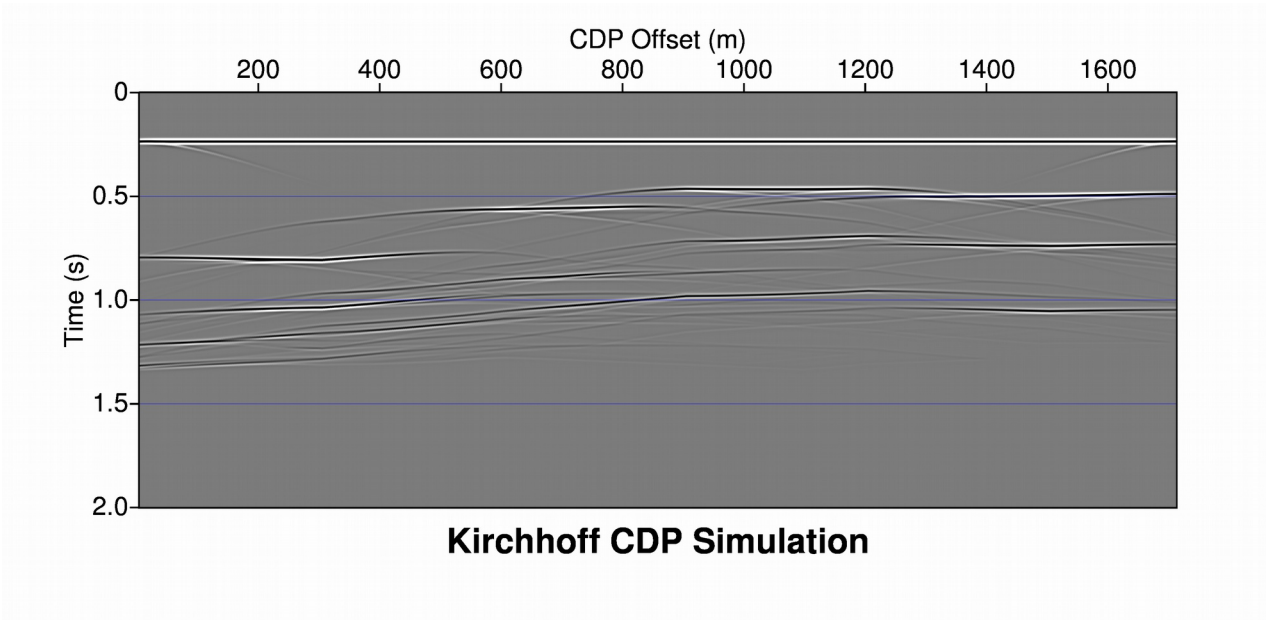

Figure 2.6: Simulated surface seismic reflection section for the model of Figure 2.1 after inclusion of a surface alteration layer. The Kirchhoff method was used. Fault locations are visible due to offset beds, but there is no evidence of strong fault plane reflections.

The next step was to simulate a complete Common Depth Point (CDP) survey over the model of Figure 2.1 after inclusion of a near surface altered zone using the staggered grid finite difference method. Figure 2.7 shows the velocity structure of this model after inclusion of the low velocity near surface alteration zone.

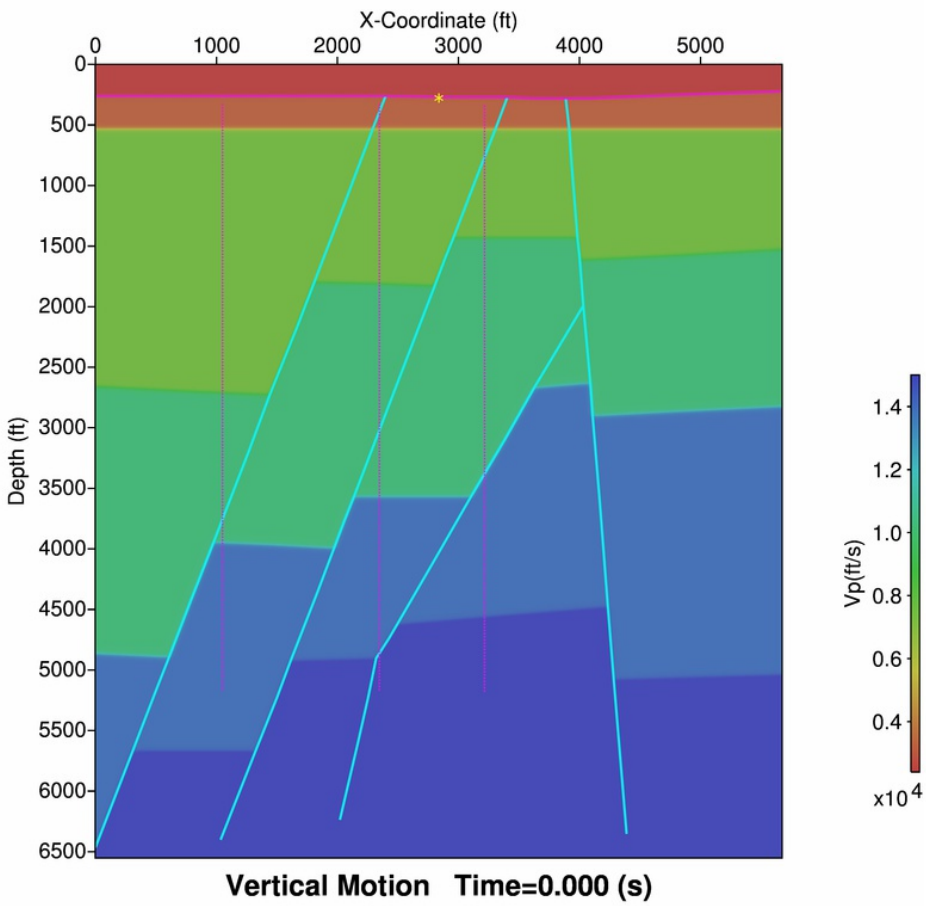

Figure 2.7: 2D Geophysical model along cross section A – A' (Figure 1.6) after inclusion of a low velocity near surface layer to simulate an alteration zone. This is a modification of the model shown in Figure 2.1.

Simulation of a 2D CDP seismic survey requires a large number of model runs, each with a different source location. In this case, 275 different source locations were simulated, with a nominal source spacing of 6 m (19.69 ft). For each source location, synthetic seismic traces for 542 surface geophones were simulated (horizontal magenta line in Figure 2.7). Surface geophones extended from 53 m (173.88 ft) to 1676 m (5498.69 ft) across the model with 3 m (9.84 ft) spacings. Synthetic traces for 3 distinct Vertical Seismic Profile (VSP) arrays were also generated for each source location (vertical magenta lines in Figure 2.7). These VSP arrays were located at: (left) 320 m (1049.87 ft); (center) 715 m (2345.80 ft); and (right) 980 m (3215.22 ft) horizontal offsets, each with a geophone depth spacing of 8 m (26.25 ft).

For each source location, the source wavelet was a 40 Hz Ricker wavelet. In order to accommodate the very low velocity simulated air layer above the surface, a grid spacing of 0.5 m was used. There were 3461 grid nodes in the X-direction, and 4201 grid nodes in the Z-direction. Time step size was 0.00005 s. A total of time of 1.75 s, or 35001 time steps was simulated.

Figures 2.8 – 2.10 show snapshots of the seismic wave field simulated over the model of the A-A' cross

section at a time of 0.45 s after the onset of the seismic source for sources located at 75.5 m, 840.5 m and 1650.5 m respectively. The simulated source is a vertical source located at the position of the yellow asterisk near the top of the figure. The wave field shown in black to gray represents the amplitude of the vertical velocity. The magenta lines show the locations of simulated geophone positions used to generate the synthetic seismograms for this model. The surface array and three VSP arrays are shown.

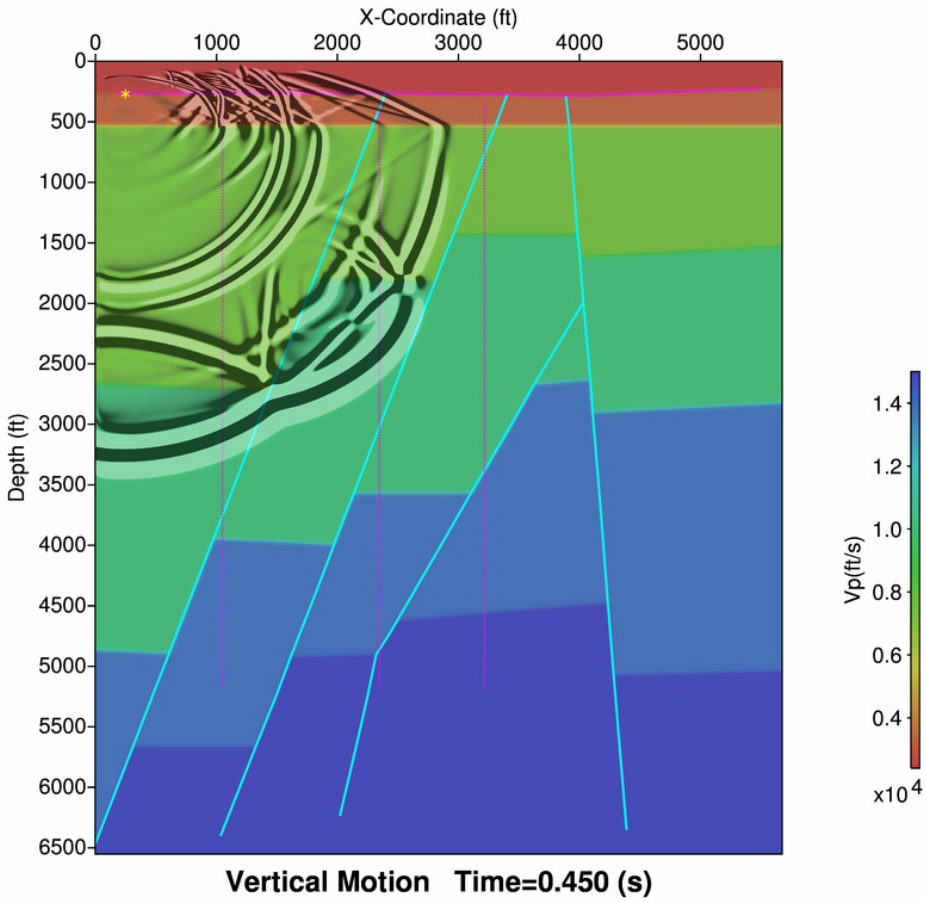

Figure 2.8: Snapshot of the vertical component of the wave field at 0.45 s for a source located at 75.5 m (247.7 ft) near the left side of the model. The simulated source is a vertical source located at the position of the yellow asterisk near the top of the figure. The magenta lines show the locations of simulated geophones.

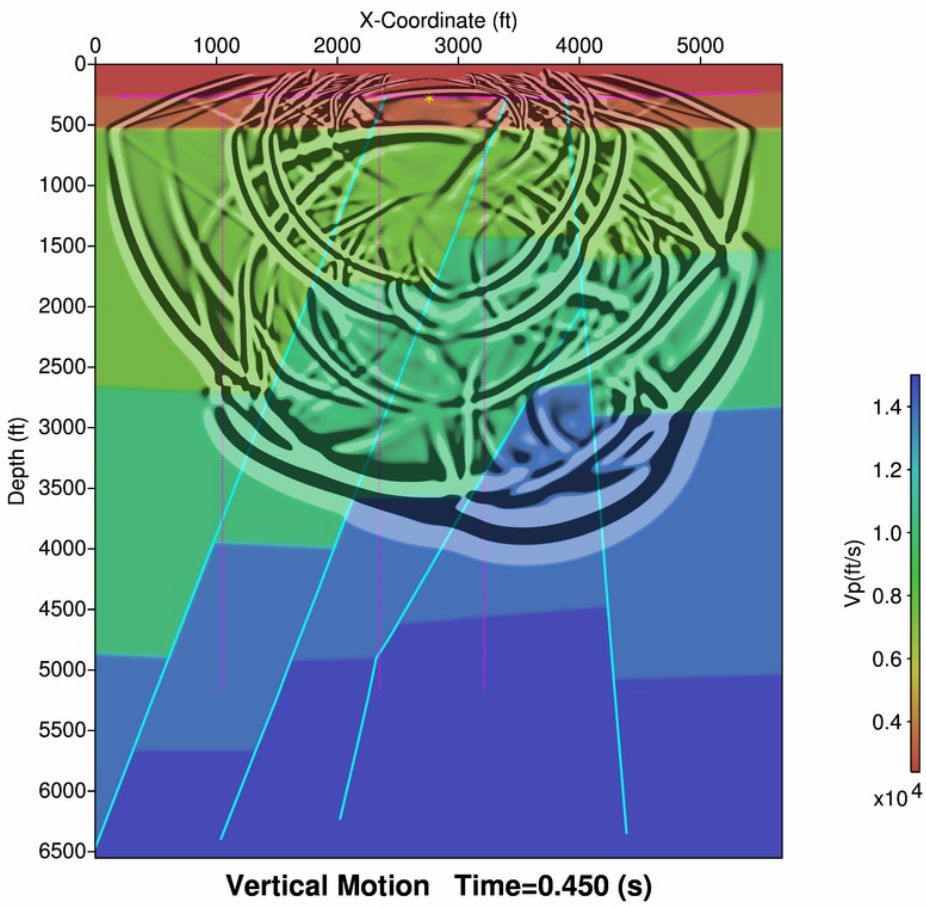

Figure 2.9: Snapshot of the vertical component of the wave field at 0.45 s for a source located at 840.5 m (2757.55 ft) near the center of the model. The simulated source is a vertical source located at the position of the yellow asterisk near the top of the figure. The magenta lines show the locations of simulated geophones.

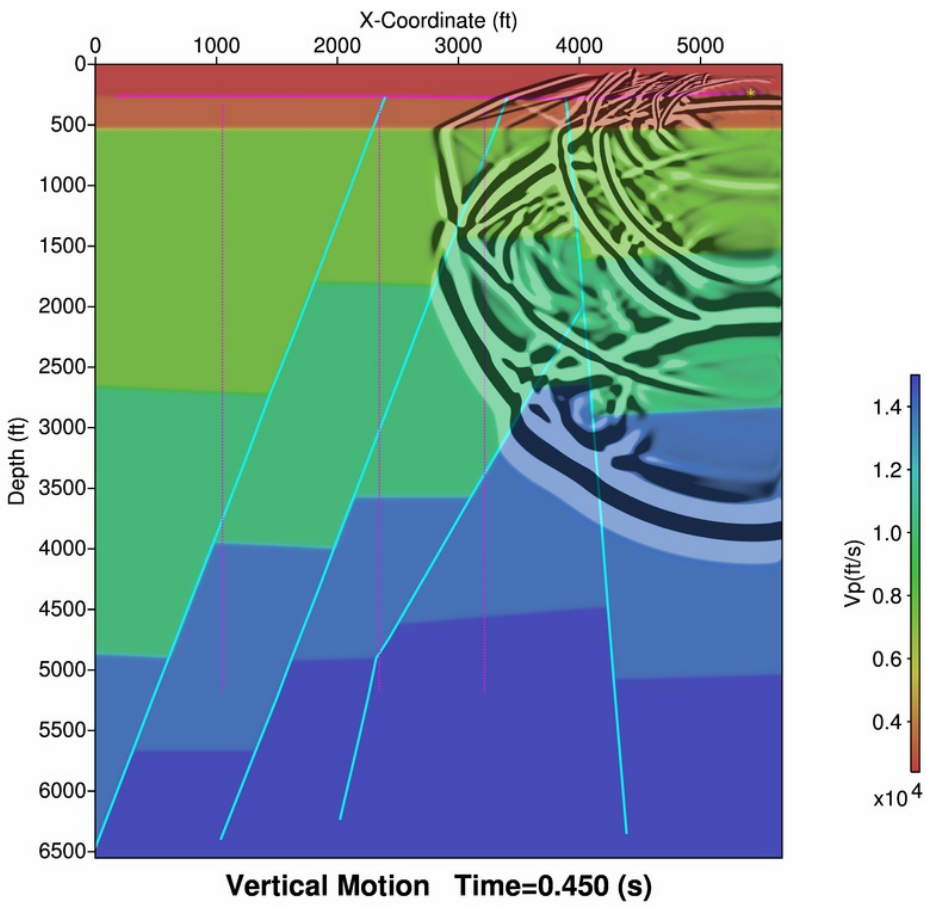

Figure 2.10: Snapshot of the vertical component of the wave field at 0.45 s for a source located at 1650.5 m (5415.03 ft) near the right side of the model. The simulated source is a vertical source located at the position of the yellow asterisk near the top of the figure. The magenta lines show the locations of simulated geophones.

Synthetic common source gathers (field files) are shown for each of these source locations in Figures 2.11 – 2.13. For comparison, actual field data source gathers from the nearby Desert Peak 2D surface seismic survey are shown in Figures 2.14 – 2.16 plotted at the same scales and with similar offsets as the synthetic traces. Geophone spacing for the field data is approximately 8 times the spacing in the synthetics, leading to significantly lower coherency of the events.

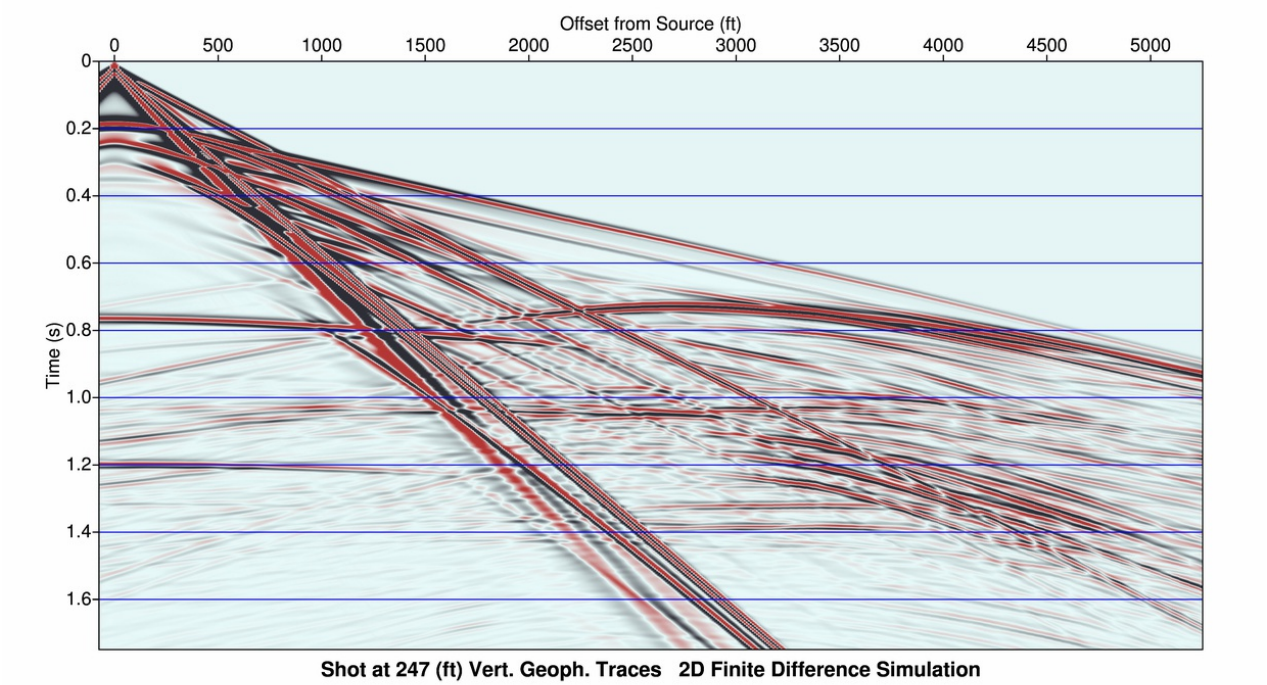

Figure 2.11: Synthetic common source gather (field file) for a source located at 75.5 m (247.7 ft) near left of model. Vertical geophone traces are shown. Geophone spacing is 3 m (9.84 ft).

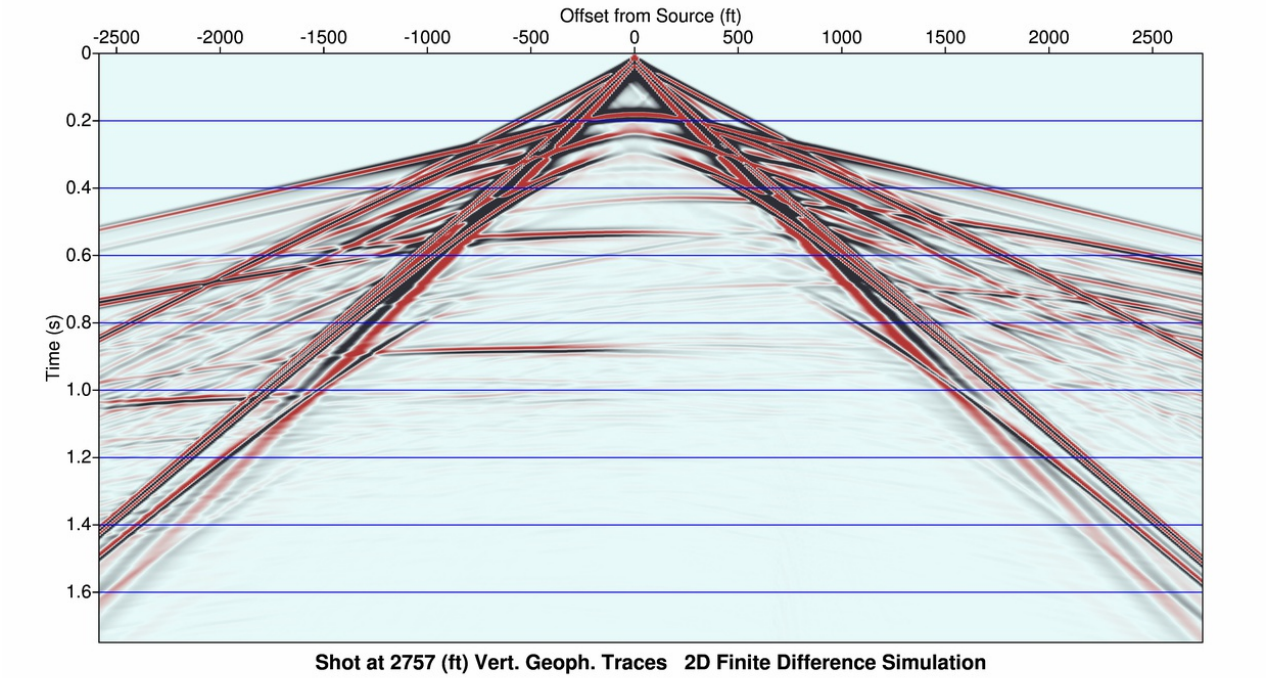

Figure 2.12: Synthetic common source gather (field file) for a source located at 840.5 m (2757.5 ft) near center of model. Vertical geophone traces are shown. Geophone spacing is 3 m (9.84 ft).

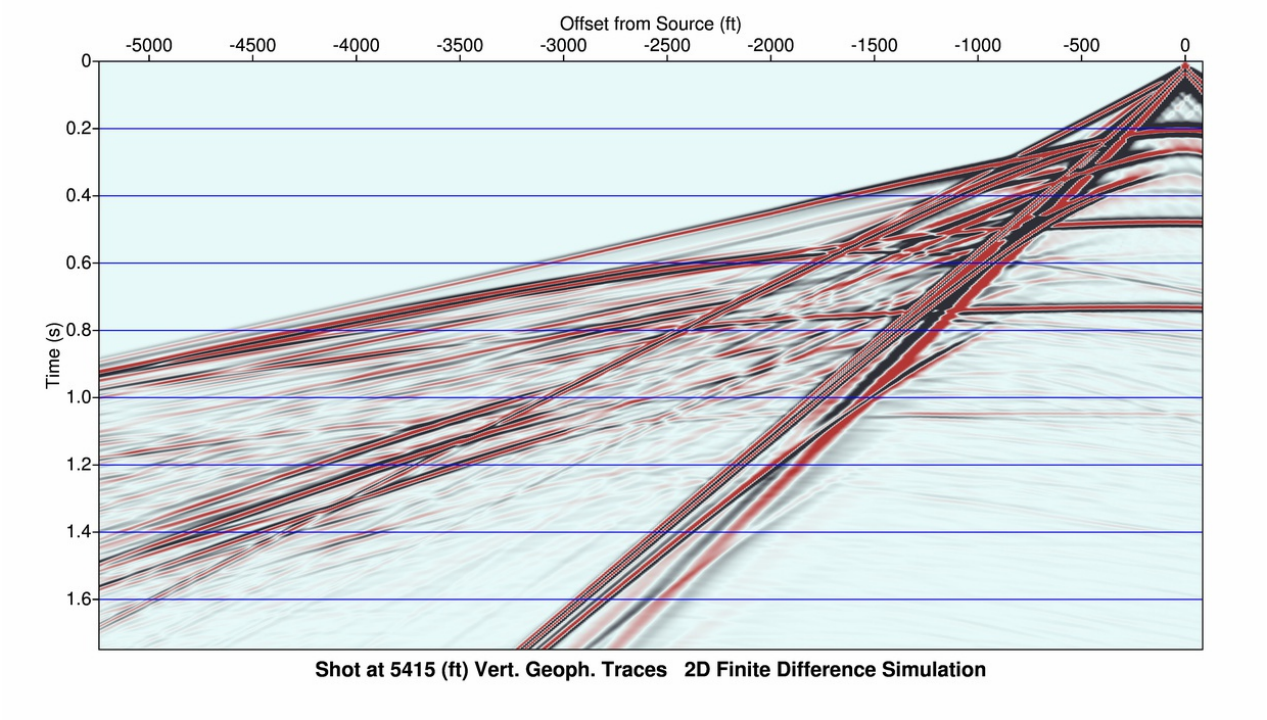

Figure 2.13: Synthetic common source gather (field file) for a source located at 1650.5 m (5415.0 ft) near right of model. Vertical geophone traces are shown. Geophone spacing is 3 m (9.84 ft).

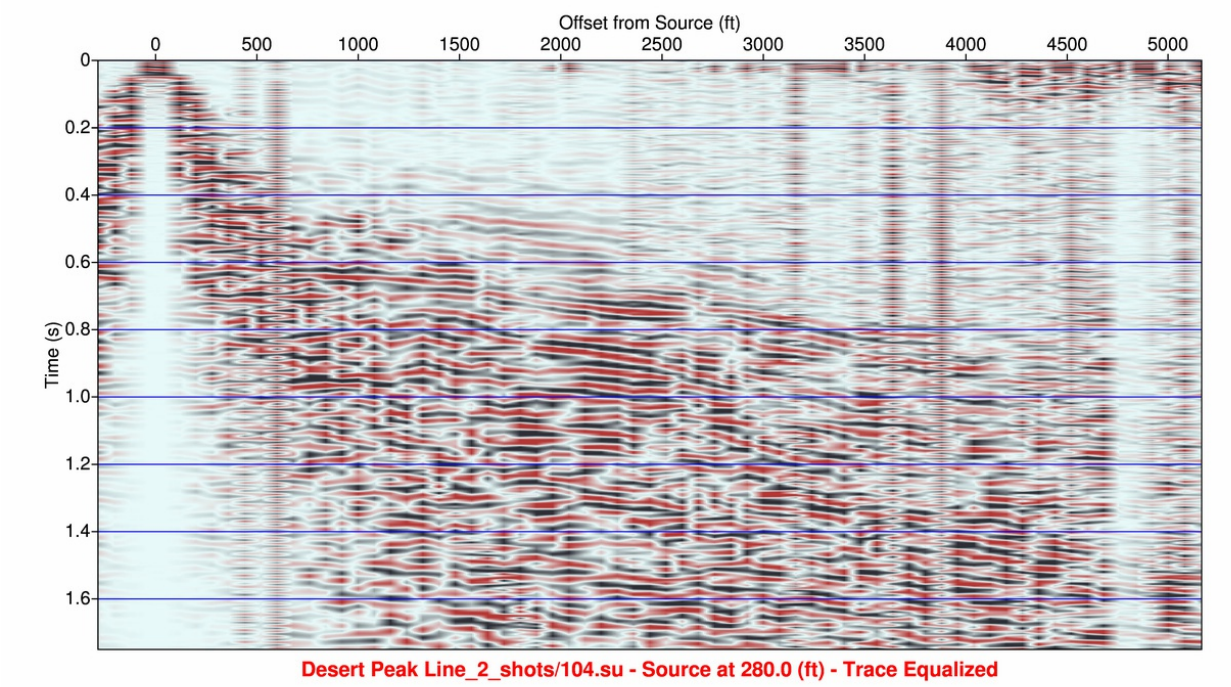

Figure 2.14: Field data from the Desert Peak seismic survey. Common source gather (field file) for a source located 85.3 m (280.0 ft.) from the end of the line. Geophone spacing is 24.4 m (80 ft.).

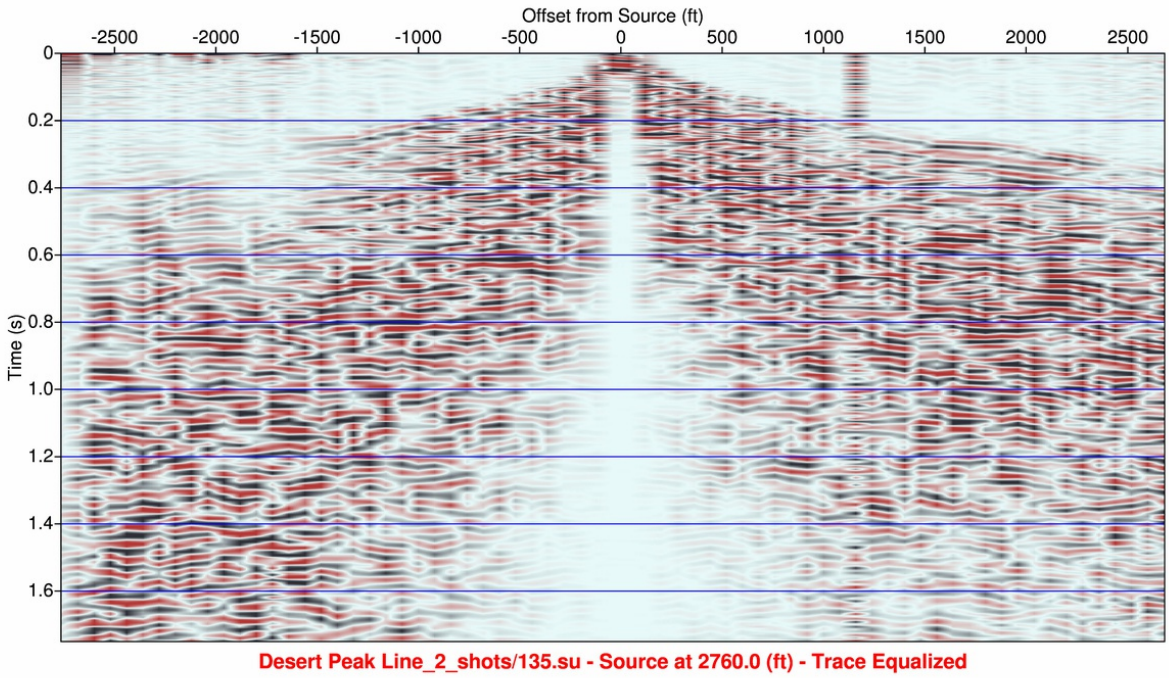

Figure 2.15: Field data from the Desert Peak seismic survey. Common source gather (field file) for a source located 841.2 m (2760.0 ft.) from the end of the line. Geophone spacing is 24.4 m (80 ft.).

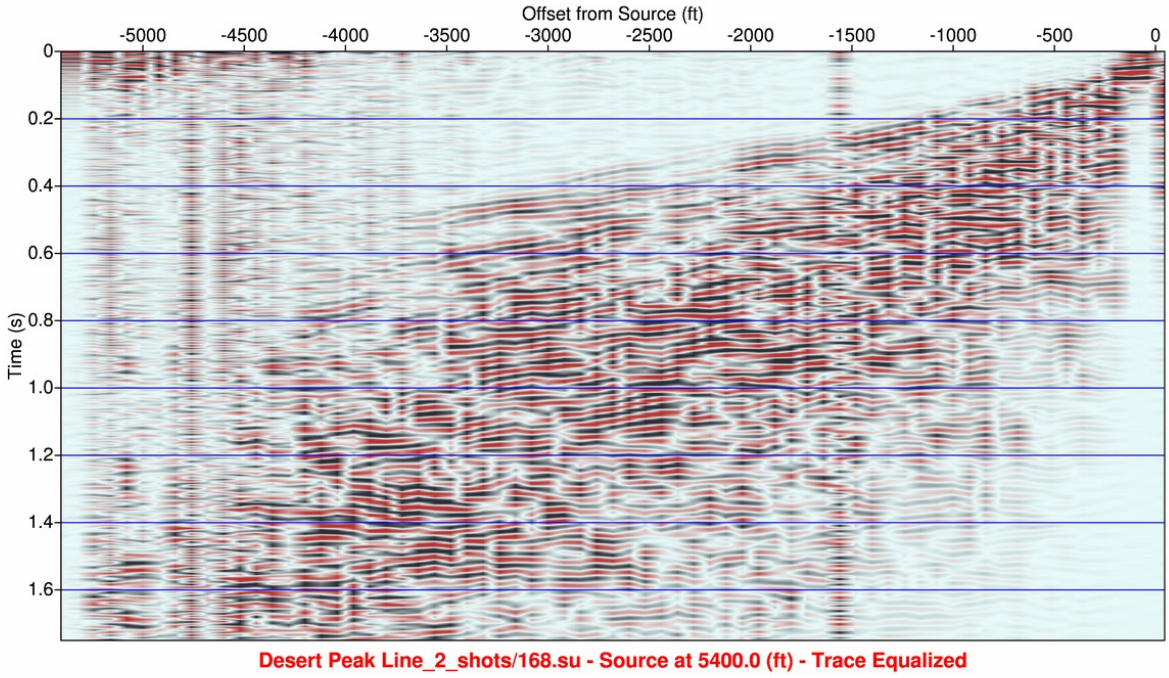

Figure 2.16: Field data from the Desert Peak seismic survey. Common source gather (field file) for a source located 1645.9 m (5400.0 ft.) from the end of the line. Geophone spacing is 24.4 m (80 ft.).

Inspection of these Figures shows that a number of the salient features visible in the actual field data have been captured in the model results. The prominent noise cone associated with the air wave, ground roll, and refractions is perhaps the dominant characteristic visible in both the synthetics and field data. Overcoming the influence of this noise cone will be one of the major objectives of the parameter design tasks. Complex reflection events associated with the severe structure are visible below the noise cone in the field data and the synthetics. These reflections have different character since the synthetics are based on the Brady's Hot Springs structure as opposed to the Desert Peak geology. Visibility of these reflection is an encouraging result, particularly for the field data, as the presence of such events is often the overriding factor in producing coherent interpretable seismic images.

Figure 2.17 shows a Common Depth Point (CDP) or common midpoint (CMP) gather obtained from near the middle of the synthetic survey after sorting all the source gathers. This form of the data is required to produce stacked and migrated images.

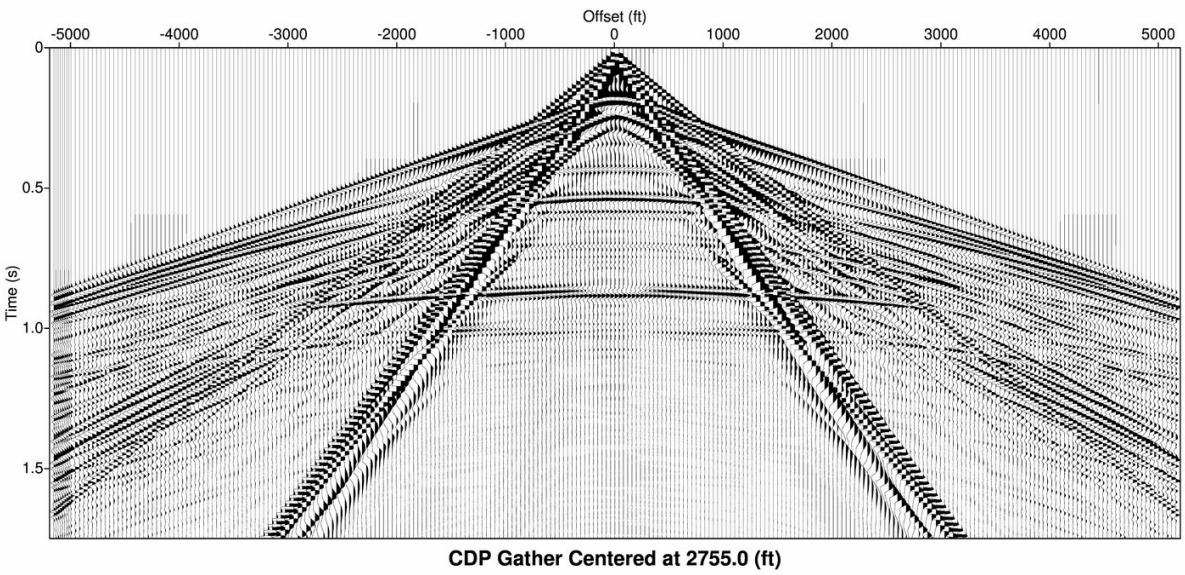

Figure 2.17: Synthetic vertical geophone Common Depth Point (CDP) or common midpoint gather centered at 839.7 m (2755 ft.) near the center of the model.

3D Modeling

2D modeling can be very useful in the design of acquisition and processing parameters. However, the extreme structure of the Brady's Hot Springs area suggests that 3D modeling will be beneficial in capturing many of the potential pitfalls in acquiring and processing surface reflection and Vertical Seismic Profile (VSP) seismic data in this area.

To this end, a number of 3D seismic velocity and density models were constructed. These include a simple fault in a layered medium, a simple fault in a layered medium with ellipsoidal near surface heterogeneities, and a preliminary model of the Brady's Hot Springs area based on the 2009 geological

description discussed under Task 1.

Due to the large amount of memory needed to model the extremely fine grids required to simulate an air layer in 3D, such a layer is not included in any of these models.

Simple Fault Model

Figure 2.18 shows the compressional velocities for the simple fault in a layered medium model. This is a 3D model made up of three horizontal layers offset by a normal fault. The fault curves both laterally and with depth. This model is useful for examining the types of seismic events generated by such faults including reflections and mode converted waves. It is also useful in identifying the source and geophone locations which best capture seismic events scattered from the fault surface.

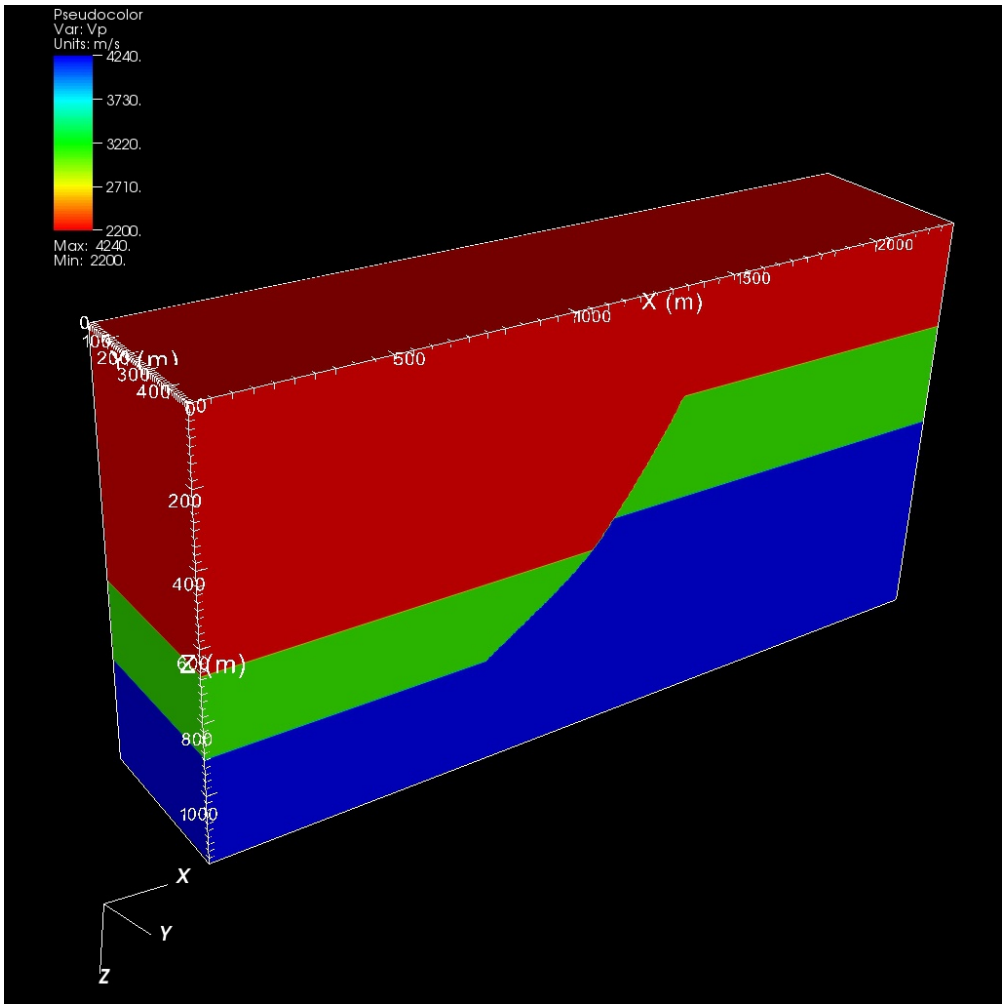

Figure 2.18: Compressional velocities for a 3D model of a simple curved fault in a medium with 3 horizontal layers.

Figure 2.19 displays the iso-surfaces for the simple fault model. This Figure shows the relatively simple geometry of the fault surface and offset beds in 3D.

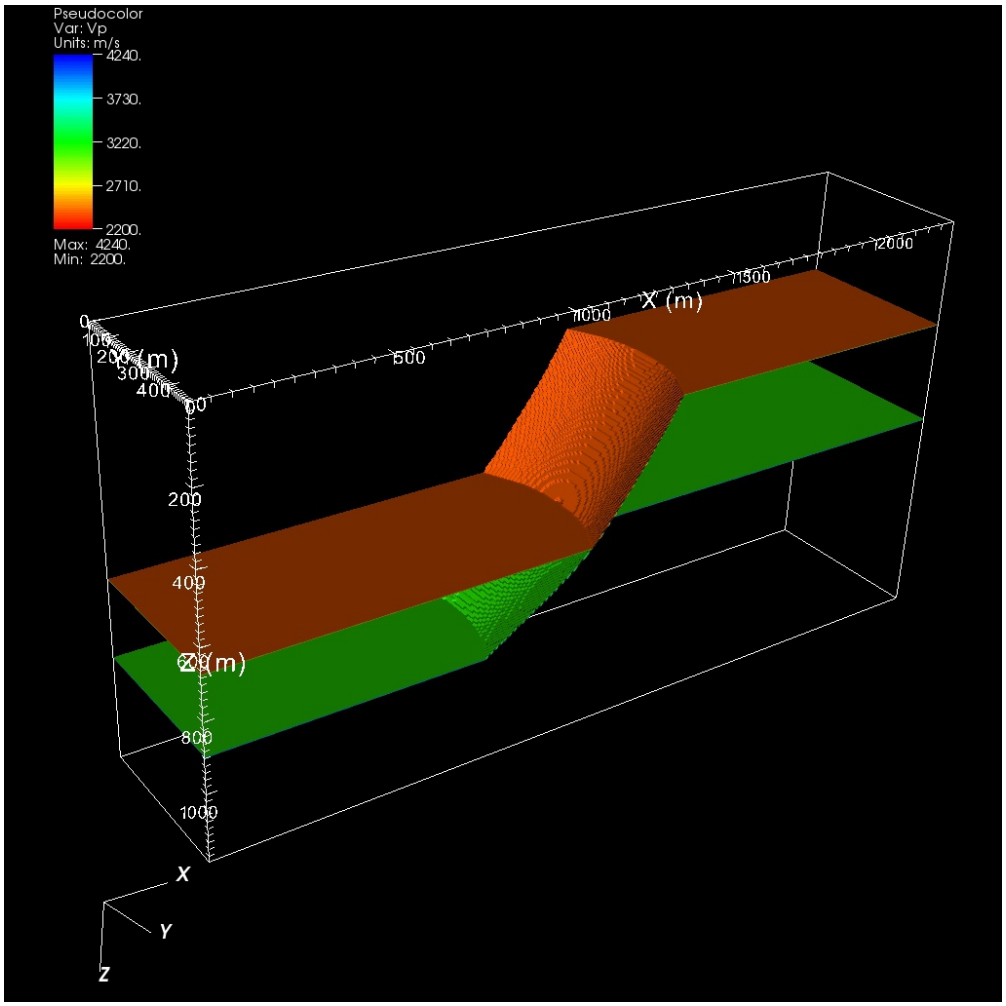

Figure 2.19: Iso-surface display for the 3D simple fault model.

A 3D surface seismic reflection survey and three VSP's were simulated with this model using a staggered grid finite difference modeling program. For this simulation, a vertical point velocity source was placed at X=1100.0 m, Y=200.0 m and Z=75.0 m below the top of the model in the model coordinate frame. The source wavelet was a 35 Hz Ricker wavelet.

The 3 simulated VSP's were for wells located (in model coordinates) at: X=800.0 m, Y=250.0 m; X=1200.0 m, Y=250 m; and X=1600.0 m, Y=250 m. Simulated VSP geophones were multicomponent geophones placed at depths ranging from 102.5 m to 1137.5 m in 5 m increments.

The simulated 3D surface array consisted of 3 lines of multicomponent geophones running in the X-direction. These lines were placed at Y coordinates of 125.0 m, 250.0 m, and 375.0 m. For each line, geophone X-coordinates ranged from 62.5 m to 2237.5 m in 5 m increments.

Grid parameters were a 2.5 m grid spacing, with 921 grid nodes in the X direction, 201 grid nodes in the Y direction, and 481 nodes in Depth (Z). A time step size of 0.0001 s was used. A total time of 2 s, or 20001 time steps, was simulated.

Figure 2.20 shows a vertical X-Z plane slice through the compressional velocity model. It is overlain by the vertical motion (Vz) wave field snapshot at 0.50 s. This slice passes through the source position. The source Y coordinate is 200 m. In the Figure, the source is located at an X-coordinate of 1100 m.

Figure 2.21 shows a horizontal X-Y plane slice through the compressional velocity model, overlain by a wave field snapshot of the vertical motion at 0.50 s. The slice is a horizontal cut through the model at a depth of 450 m.

Figure 2.22 shows a similar horizontal X-Y plane slice through the shear velocity model, overlain by a wave field snapshot of the horizontal X motion at 0.50 s. The slice is a horizontal cut through the model at a depth of 450 m.

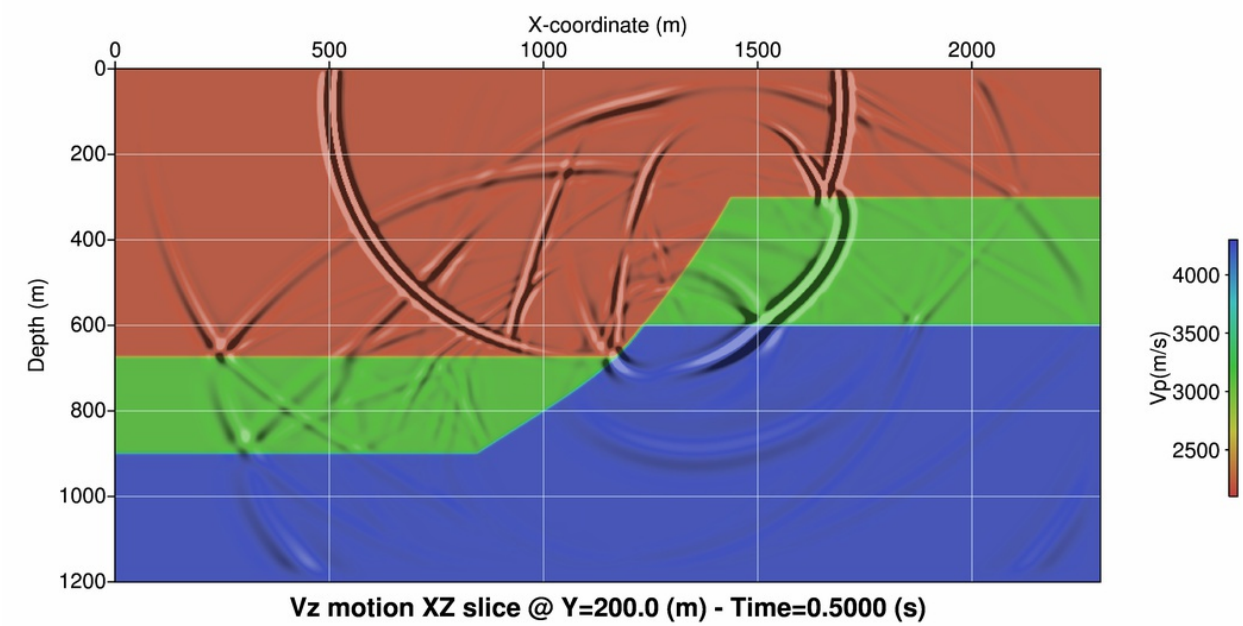

Figure 2.20: Vertical slice X-Z plane slice through the simple fault model. This slice contains the source point, and shows a snapshot of the vertical Z component of the wave field at 0.50 s. Colors represent compressional wave velocities.

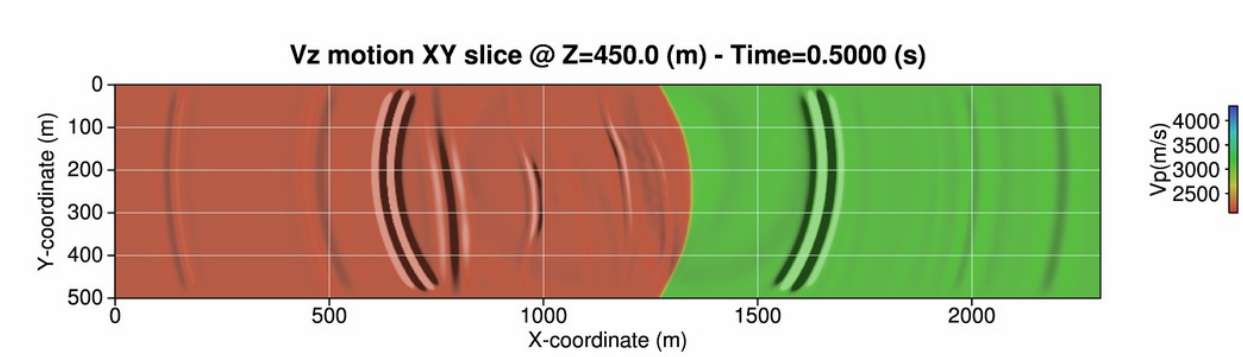

Figure 2.21: Horizontal X-Y plane slice through the simple fault model at a depth of 450.0 m showing a snapshot of the vertical Z component of the wave field at 0.50 s. Colors represent compressional wave velocities.

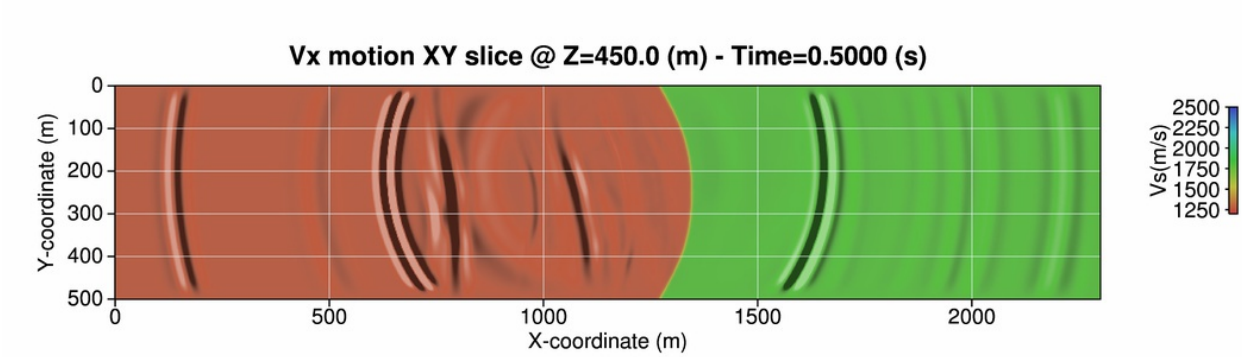

Figure 2.22: Horizontal X-Y plane slice through the simple fault model at a depth of 450.0 m showing a snapshot of the horizontal X component of the wave field at 0.50 s. Colors represent shear wave velocities.

Figure 2.20 (the vertical particle motion) shows two strong horizontally propagating events moving to the left that have been scattered off the offset beds of the fault. The first event is seen at an X coordinate of approximately 1000 m. The second event is at an X offset of approximately 1200 m. These same two events can be seen at the same X locations in Figure 2.21, which also shows the vertical motion.

In contrast, Figure 2.22, which displays the horizontal particle motion, barely shows these same two events. A third event with very strong horizontal motion is visible in Figure 2.22 at an offset of approximately 1100 m.

For waves propagating horizontally along the X-direction, compressional waves will predominately have X particle velocity (Vx) directed longitudinally along the propagation direction. Mode converted shear waves will predominately have Z particle velocity (Vz). This leads to the interpretation of the events at 1000 m and 1200 m in Figures 2.20 and 2.21 being mode converted shear waves. The event at 1100 m in Figure 2.22 is interpreted as a scattered compressional wave. Examination of the velocity at which these events propagate across the model (not shown here) further supports this interpretation.

Figure 2.23 shows the Vx horizontal component simulated traces for the VSP well at X=800 m. The strong horizontally polarized compressional wave seen at an X coordinate of 1100 m in the snapshot of Figure 2.22 is quite visible. It crosses this VSP array at a time of approximately 0.65 s between depths of 400 m and 600 m.

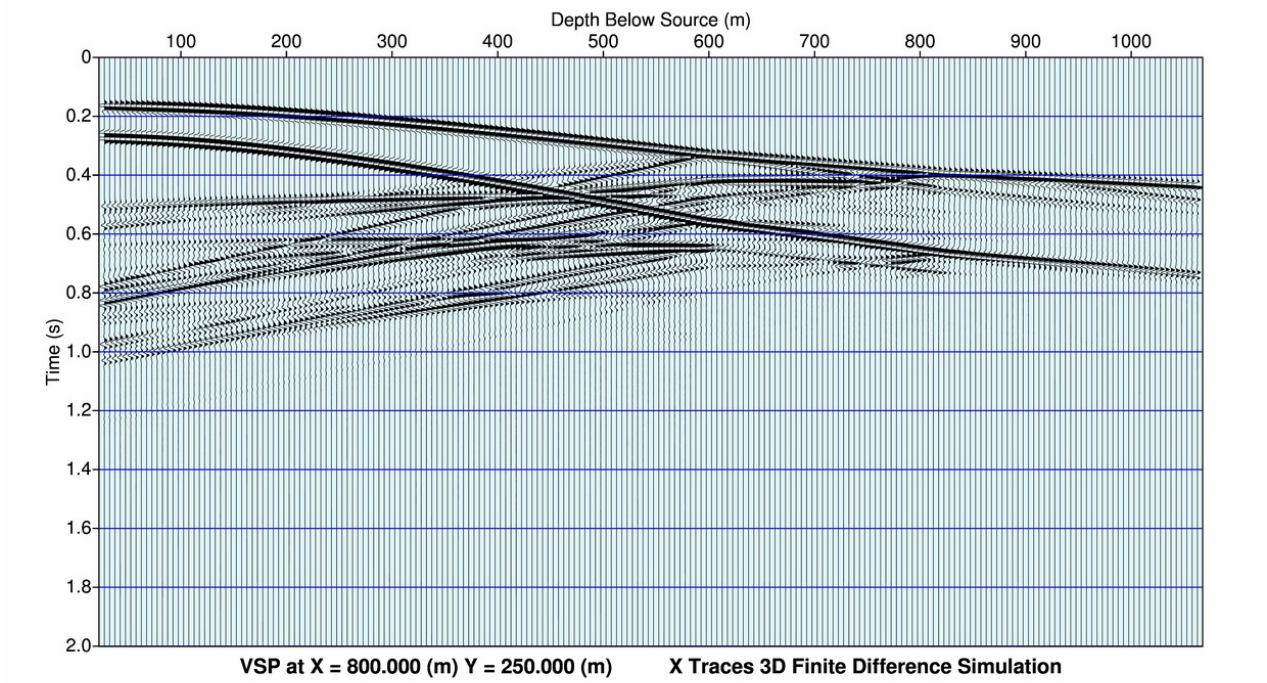

Figure 2.23: Synthetic VSP traces from the 3D simple fault model. Simulated horizontal X geophone traces are shown for a VSP at X = 800 m, Y = 250 m. The nearly horizontal event arriving at 0.65 s between depths of 400 m and 600 m corresponds to the horizontally propagating compressional wave seen at X coordinate 1100 m in Figure 2.22.

This underscores the value of multicomponent recording, particularly for VSP geometries. For such geometries, compressional waves are often of higher amplitude on the horizontal geophones, particularly for horizontally propagating events.

Another observation from this simple fault model is that the horizontally propagating fault scattered events never really reach the surface array of geophones. This implies that they will not be recorded by surface seismic methods.

Figure 2.24 shows the simulated Vz shot gather traces generated over the simple fault model. This figure shows the traces for the line at Y=250 m. The reflected wave fields are seen to be disrupted by the offset beds, including diffractions from the bed terminations. However, there is little evidence for direct fault scattered events.

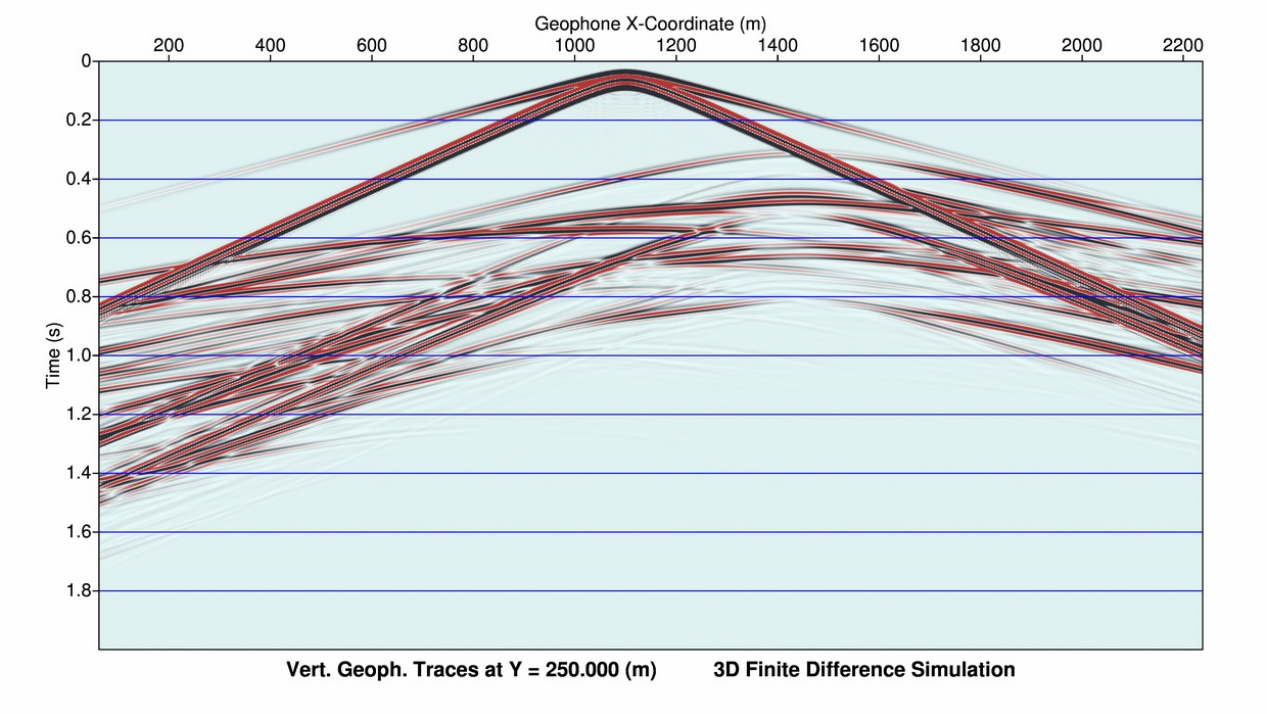

Figure 2.24: Synthetic surface seismic shot gather traces from the simulated 3D survey over the simple fault model. Simulated vertical geophone traces are shown for a line at Y = 250 m.

This highlights one of the major problems in recording surface seismic data over highly faulted areas. Reflections from the tops of the offset beds will be recorded on the surface array, and if properly imaged, faults can be inferred from the offset of the beds. Unfortunately, very little energy from the fault plane reflections reaches the surface, and then only at long offsets where ground roll events can severely mask them. Very little can be inferred about the nature of the fault interfaces, such as associated fracturing, with surface data. These observations suggest that VSP acquisition geometries, which are capable of recording these horizontally propagating events, will be much more effective in inferring fault plane properties in highly faulted areas such as those encountered in geothermal field development.

As mentioned in the 2D modeling discussion, recording energy directly scattered from the faults is important. Modeling reported by Gritto and Majer (2003) suggests that such events can be interpreted in terms of specific stiffness of the faults and fractures. It has been suggested that specific stiffness is in turn related to the flow properties of the fault (e. g., Pyrak-Nolte and Morris, 2000, Zhu and Snieder, 2002). Further, the ability to analyze both compressional and shear events strengthens such interpretations.

Simple fault with ellipsoidal heterogeneities

The next 3D model extended the simple fault model by adding a number of ellipsoidal near surface heterogeneities with varying velocities. In many geothermal areas, near surface heterogeneities associated with alteration and highly variable surface lithology are considered to be one of the major

stumbling blocks for seismic methods. This model was constructed in order to investigate the effects of such heterogeneities, and identify possible remedies for overcoming these effects.

Figure 2.25 shows the compressional velocities for this model with the top layer stripped off. This figure shows the distribution of the near surface ellipsoidal heterogeneities, as well as the 3D structure of the fault and offset beds. For this model, the size of the model was increased in the Y-direction compared to the simple fault model previously discussed.

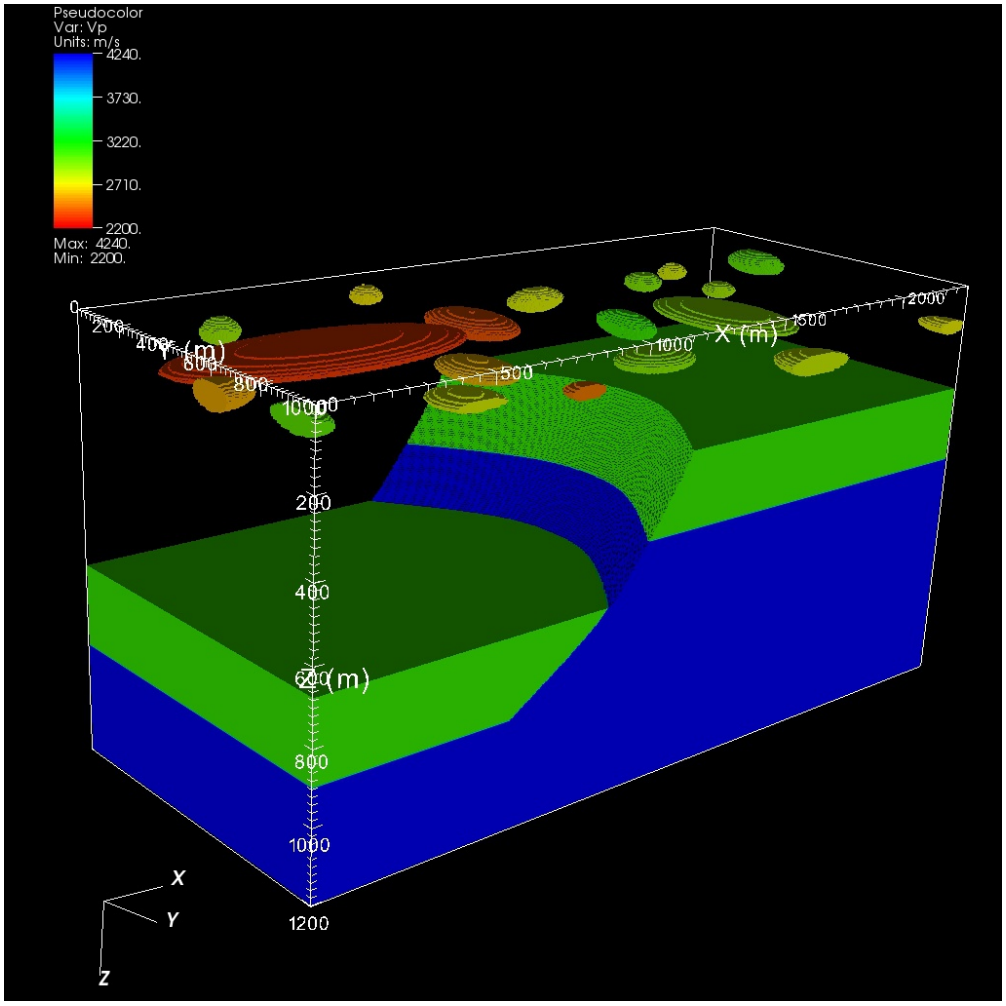

Figure 2.25: 3D compressional velocity display of the simple fault model with ellipsoidal heterogeneities with the top layer stripped off to show the velocity distribution of the ellipsoidal alteration zones.

Similar to the simple fault model, a 3D surface seismic reflection survey and three VSP's were simulated with this model using a staggered grid finite difference modeling program. For this simulation, a vertical point velocity source was placed at X=1100.0 m, Y=400.0 m and Z=50.0 m below the top of the model in the model coordinate frame. The source wavelet was a 35 Hz Ricker

wavelet.

The 3 simulated VSP's were for wells located (in model coordinates) at: X=800.0 m, Y=500.0 m; X=1200.0 m, Y=50 m; and X=1600.0 m, Y=500 m. Simulated VSP geophones were multicomponent geophones placed at depths ranging from 60.0 m to 1135.0 m in 5 m increments.

The simulated 3D surface array consisted of 7 lines of multicomponent geophones running in the X-direction. These lines were placed at Y coordinates of 125.0 m, 250.0 m, 375.0 m, 500.0 m, 625.0 m, 750.0 m, and 875.0 m. For each line, geophone X-coordinates ranged from 62.5 m to 2237.5 m in 2.5 m increments.

Grid parameters were a 2.5 m grid spacing, with 921 grid nodes in the X direction, 401 grid nodes in the Y direction, and 481 nodes in Depth (Z). A time step size of 0.0001 s was used. A total time of 2 s, or 20001 time steps, was simulated.

Figure 2.26 shows the simulated Vz shot gather traces generated over the simple fault model with ellipsoidal heterogeneities. This figure shows the traces for the line at Y=375 m.

Comparison of Figure 2.26 with Figure 2.24 shows remarkable differences between the simulated surface seismic traces for the simple fault model and the model with ellipsoidal heterogeneities. The near surface heterogeneities have generated significant back scattered energy in the surface traces. This energy is seen to have very low apparent velocities (high slopes for the events). Without the use of finely spaced geophones, these events could be easily spatially aliased. This would lead to poor results when trying to filter out these near surface events with spatial filters.

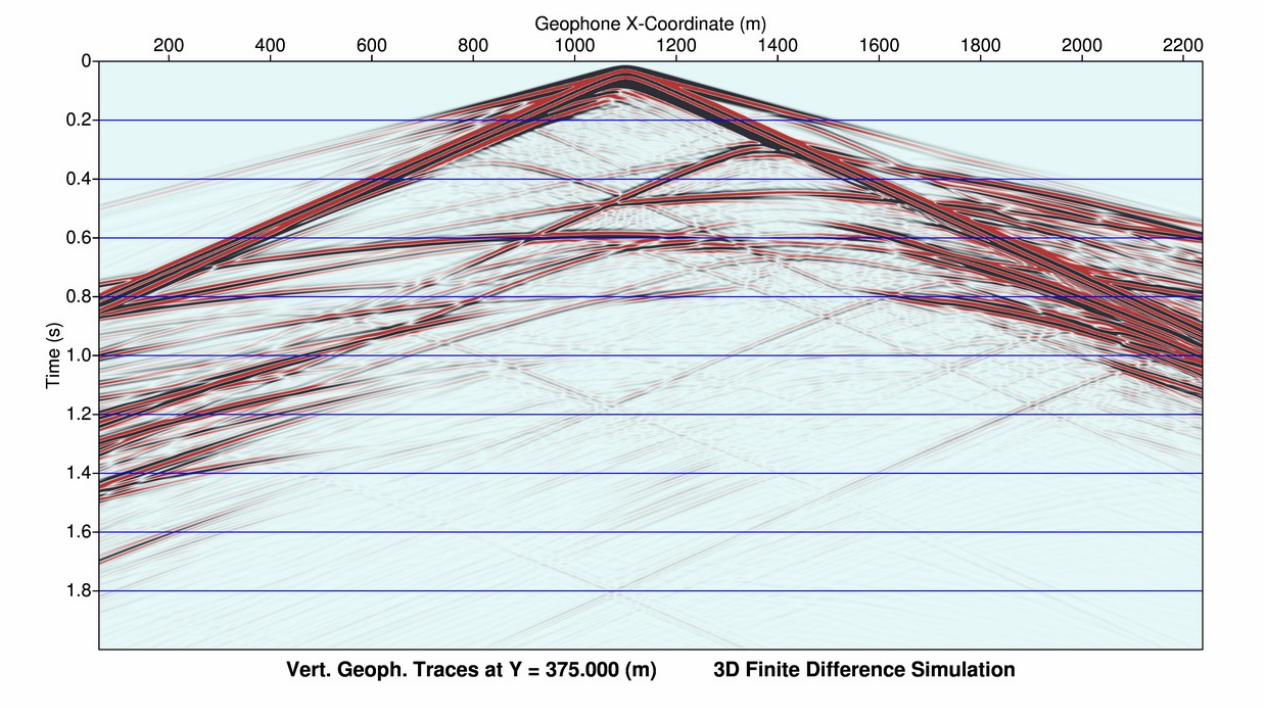

Figure 2.26: Synthetic surface seismic shot gather traces from the simulated 3D survey over the simple fault model with ellipsoidal heterogeneities. Simulated vertical geophone traces are shown for a line at Y = 375 m.

Brady's Hot Springs Geophysical Model

As discussed under Task 1, the geological description of the Brady's Hots Springs study area is dominated by a series of northeast trending fault strands cross cut by a series of northwest trending faults (see Figure 1.5). Three major northeast trending fault strands were identified, and have been named the 27-1 Fault, the Middle Fault, and the Brady's Fault by ORMAT. Similarly, three northwest trending cross faults have been identified as the USFI Cross-Fault, the BPP Cross-Fault, and the Unnamed Cross Fault. This complex fault pattern leads to a series of structural blocks. Within each structural block, geological units have been broken up into four simplified members. Ordered from surface to depth, they are Undifferentiated Truckee and Desert Peak Formation, Chloropagus Formation, Tertiary Rhyolite, and pre-Tertiary basement complex.

For reasons related to the way the modeling software partitions the various grid nodes across different compute nodes in the computing cluster, it is desirable to chose the X-dimension as the longest horizontal dimension. For this reason, in the Brady's Hot Springs geophysical model, the X-dimension corresponds to Northing, and the Y-dimension to Easting.

Within each structural block, the four geological units were specified as sub horizontal beds, with formation tops estimated from the geological cross sections (see Figures 1.6 – 1.12). These, in turn, were estimated from well logs penetrating each structural block. In cases where no wells penetrated a particular unit in a given structural block, tops were estimated from geological trends. Velocities for each unit were specified based on velocity logs from the nearby Desert Peak area. Densities were

chosen based on these Desert Peak area well logs as well as results on core and cuttings (provided by ORMAT) conducted as part of this work.

A total of 48 individual core and lithological samples were obtained for laboratory analysis of bulk density (specific gravity). A series of laboratory standard tests to determine the bulk densities of the samples were conducted.

Faults are assumed to be near vertical. North east trending fault strands were given dips between 75 and 80 degrees to the north west. With the exception of the unnamed cross fault, the cross cutting faults were given similar dips to the north east. In all cases, fault dips were chosen to be consistent with extension or normal faulting. The unnamed cross fault was given a slight dip to the south west based on formation tops in adjacent structural blocks. Some minor inconsistencies in formation tops still needed to be adjusted to honor this structural style, particularly in structural blocks with no well control.

Figure 2.27 shows the compressional velocities for the 2009 Brady's Hot Springs geophysical model. Figure 2.28 displays the iso-surfaces for the top Chloropagus, top Tertiary Rhyolite, and top basement complex. This figure captures the structure of the faulting in the geophysical model.

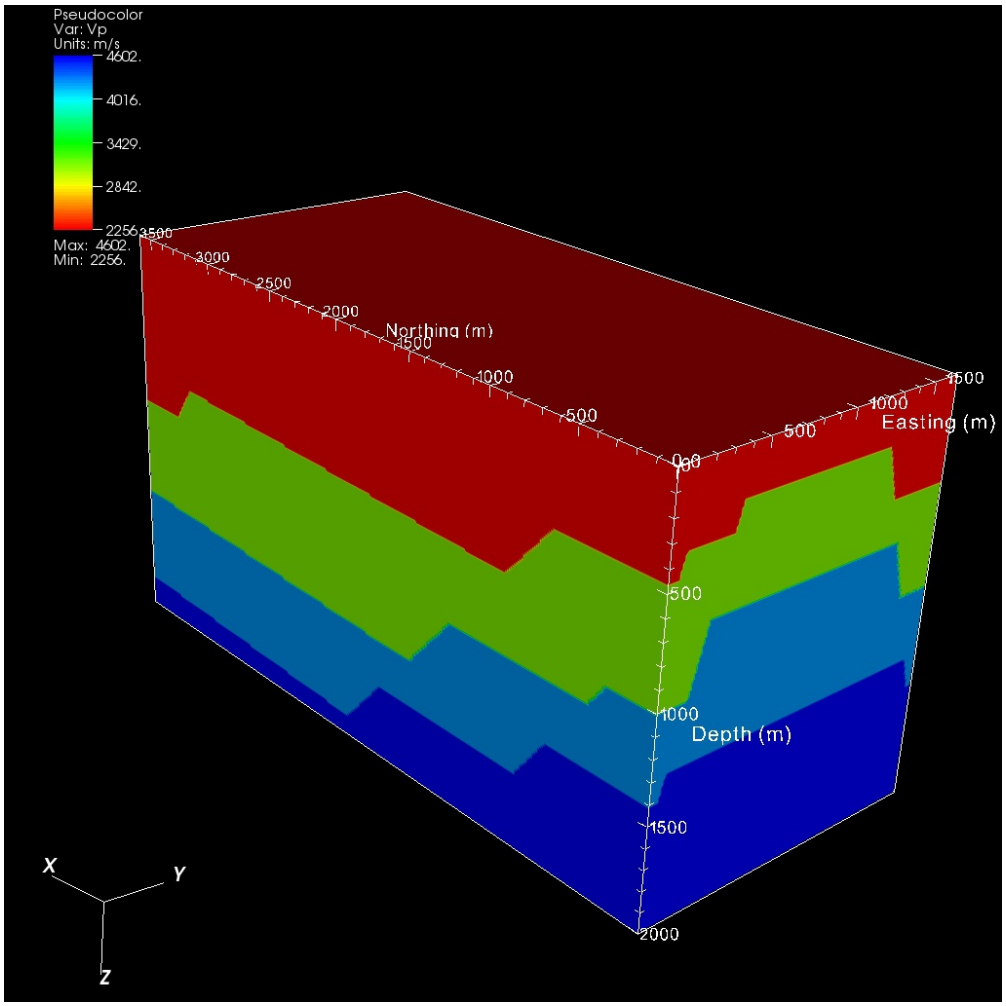

Figure 2.27: Compressional velocities for the 3D Brady's Hot Springs geophysical model.

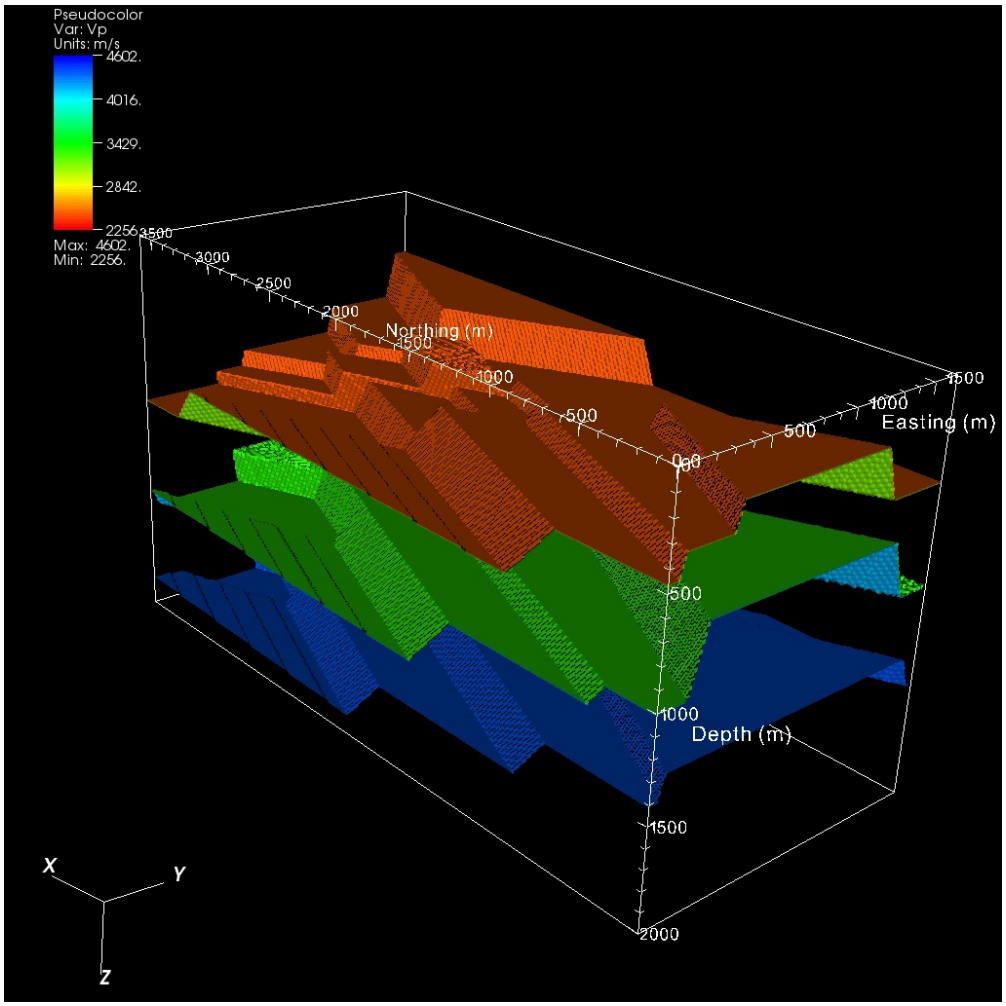

Figure 2.28: Iso-surface display for the 3D Brady's Hot Springs geophysical model showing the structure of the faulting.

Figure 2.29 shows the compressional velocities for the Brady's Hot Springs geophysical model with a cut along the approximate location of Cross Section A-A' (Figure 1.6). It can be seen that it compares well to Figure 2.1, the 2D geophysical model along this cross section. There are some slight differences due to the adjustment of formation tops for geological consistency in the overall 3D model.

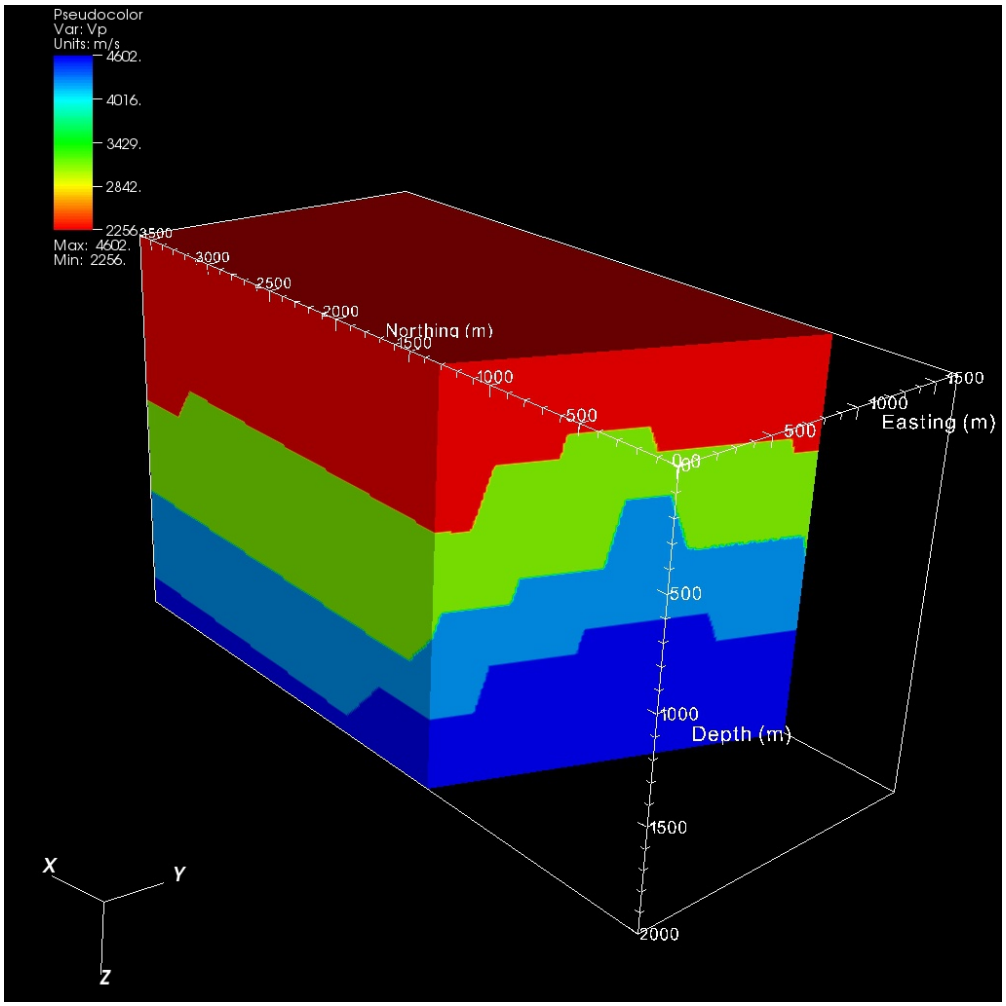

Figure 2.29: Compressional velocities for the Brady's Hot Springs geophysical model with a cut along the approximate location of Cross Section A-A' (Figure 1.6).

The maximum grid size that can be used in finite difference modeling with the 3D Brady's Hot Springs geophysical model and still avoid grid dispersion effects is 2.5 m. For this grid spacing, the computing cluster available to us at this time did not have enough memory to load the entire model. A subset of this model extending 2000 m in the X (Northing) direction, 750 m in the Y (Easting) direction, and 2000 m in depth was used to run some preliminary seismic simulations.

The primary purpose of the initial seismic simulation with this model was to investigate the potential response of a near offset VSP experiment in the Brady's 15-12 well. The 15-12 is anticipated to be the well made available for VSP acquisition during the actual field acquisition tasks of the project.

The simulated VSP well was at 607.5 m Northing, 205.0 m Easting in the model coordinate system. Multicomponent geophone depths ranging from 102.5 m to 1940.0 m in 2.5 m increments were simulated. In addition, a 3D surface array was simulated. This consisted of 25 North-South lines spaced from 75 m Easting to 675 m Easting in the model coordinates with 25 m spacing between lines. The multicomponent geophone spacing in each line extended from 75 m Northing to 1925 m Northing in the model coordinate frame with 10 m increments.

For this simulation, a vertical source was placed at: 645 m Northing, 110 m Easting at a depth of 90 m from the top of the model in the model coordinates. The source wavelet was a 35 Hz Ricker wavelet.

Grid parameters were a 2.5 m grid spacing, with 801 grid nodes in the Northing (X) direction, 301 grid nodes in the Easting (Y) direction, and 801 nodes in Depth (Z). A time step size of 0.0001 s was used. A total time of 2 s, or 20001 time steps, was simulated.

Figure 2.30 shows a vertical X-Z plane slice through the model. X coordinates correspond to Northing and Y coordinates to Easting. It is overlain by the vertical motion (Vz) wave field snapshot at 0.50 s. This slice is a North-South slice through the source position. The source Y coordinate (Easting) is 110 m. In the Figure, the source is located at an X-coordinate (Northing) of 645 m.

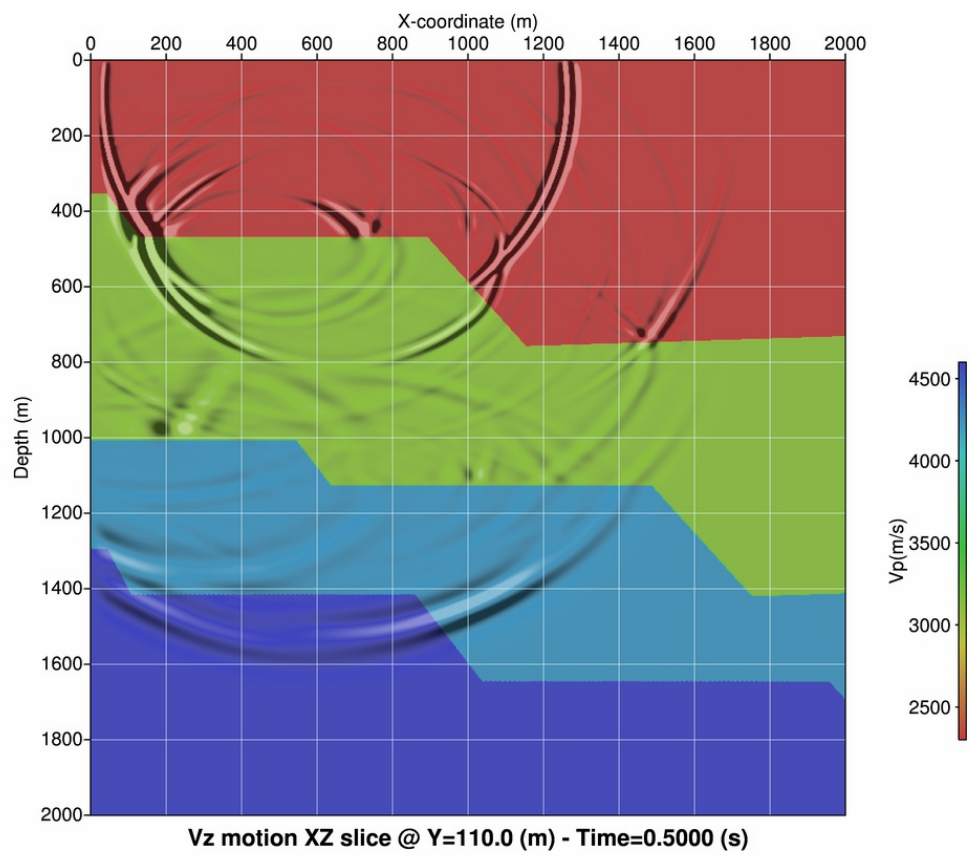

Figure 2.30: Vertical X-Z plane slice through the Brady's Hot Springs model. The X coordinate corresponds to Northing, and Y coordinate to Easting. This slice contains the source point, and shows a snapshot of the vertical component (Vz) of the wave field at 0.50 s. The simulated VSP well is at a model X coordinate (Northing) of 607.5 m.

Figure 2.31 shows a vertical Y-Z plane slice through the model, also overlain by the vertical motion (Vz) wave field snapshot at 0.50 s. This slice is an East-West slice at (Northing) X=645 m, and also contains the source. The source is located at the Y coordinate (Easting) of 110 m. The simulated VSP

well is at a model Y coordinate (Easting) of 205 m. A near horizontally propagating fault scattered event is seen to just be crossing the VSP well Y coordinate between depths of ~800 m and 1000 m at this time.

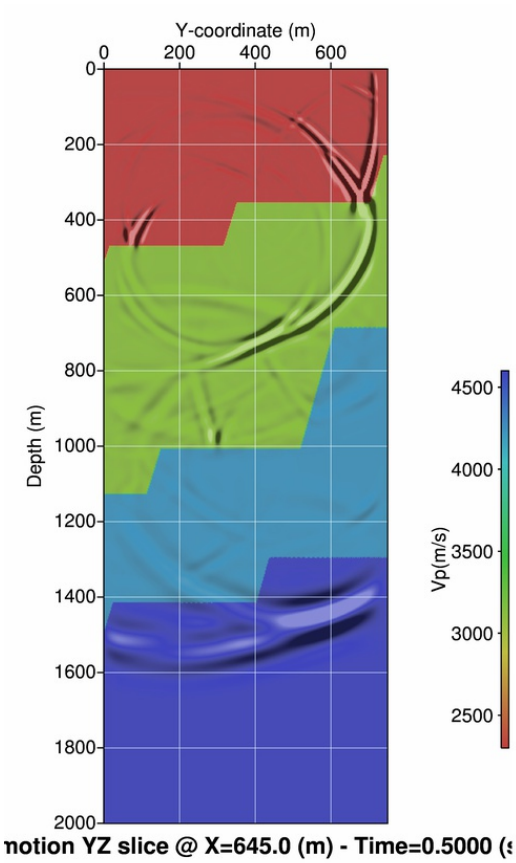

Figure 2.31: Vertical Y-Z plane slice through the Brady's Hot Springs geophysical model. This slice contains the source point, and shows a snapshot of the vertical component (Vz) of the wave field at 0.50 s. The X coordinate corresponds to Northing and the Y coordinate to Easting. The simulated VSP well is at a model Y coordinate (Easting) of 205 m. A fault scattered event is seen to just be crossing the VSP well Y coordinate between depths of ~800 m and 1000 m at this time.

Figure 2.32 shows the vertical component (Vz) simulated traces for the VSP well. The fault scattered event seen in Figure 2.31 is seen as a series of complex near horizontal events. These events occur around 0.5 s and in the vicinity of 800 m depth.

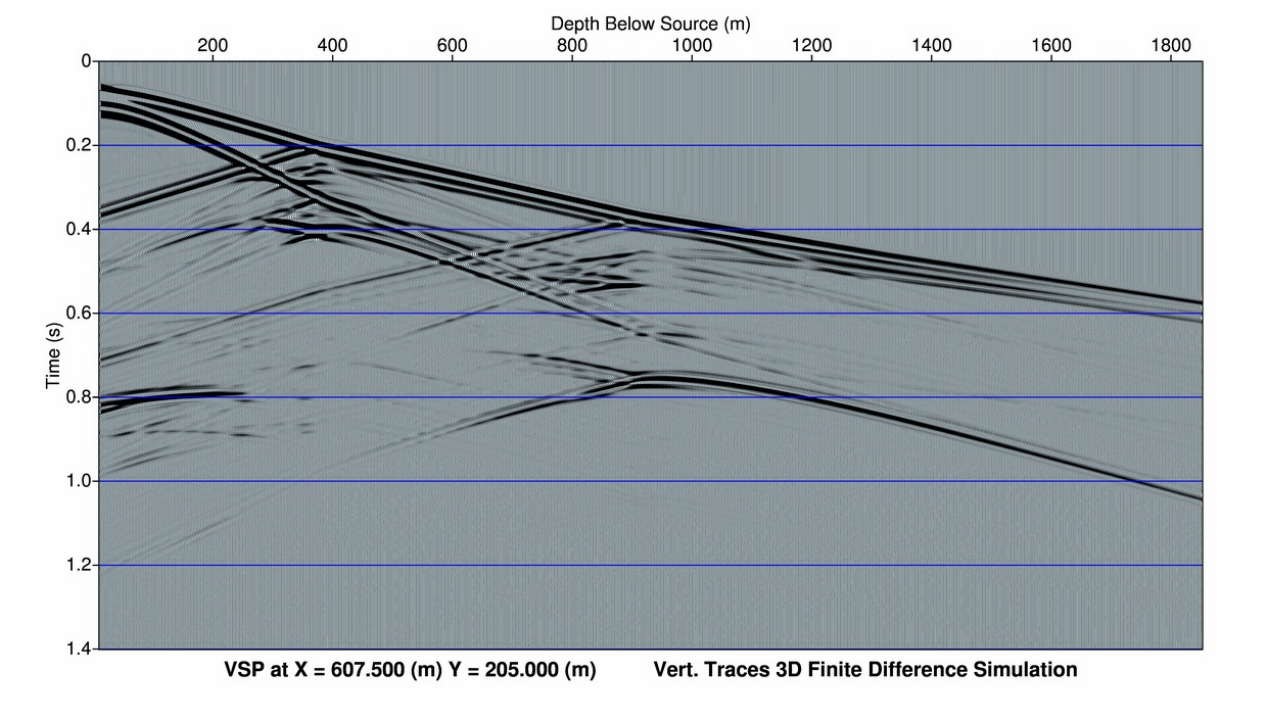

Figure 2.32: Synthetic VSP traces from the 3D Brady's Hot Springs geophysical model. Simulated Vertical geophone traces are shown for a VSP at (Northing) X = 607.5 m, (Easting) Y = 205.0 m in model coordinates, simulating a VSP in the 15-12 well. The fault scattered event seen in Figure 2.31 is seen around 0.5 s and in the vicinity of 800 m depth.

Simple 3D Seismic Fracture Model

A simple 3D seismic model including the effects of fractures was also formulated during this reporting period. Fractures were modeled using the effective medium formulation of Hudson (1980, 1981) which assumes sub seismic fractures.

The primary purpose in constructing this model was to verify the ability to accurately model sub seismic fractures using 3D staggered grid finite difference modeling algorithms. The primary effect of sub seismic fractures is to impart a velocity anisotropy to the rocks (Hudson 1980, 1981). Associated with this seismic anisotropy is the variation of compressional and shear velocities with azimuth, and the associated phenomenon of shear wave splitting, also called shear wave birefringence or double refraction (see Queen and Rizer, 1990 and references therein).

A two layer 3D model was constructed in which the top layer was isotropic (no fractures) and the bottom layer was anisotropic, with elastic constants characteristic of fracture planes striking 63 degrees from the X axis. Seismic sources were placed at a depth of 140 m near the center of the X-Y plane of the model. Simulations were run for all 3 components of applied source motion (X, Y, and Z) and all 3 components of receiver motion, resulting in what is commonly referred to as nine component data. Five different VSP well locations were simulated, as well as a 3D surface array.

Figure 2.33 shows an X-Z plane Vx motion snapshot generated by an X-motion source overlain on the model at a simulation time of 0.6 s. At this time, the direct shear wave has penetrated to a depth of

approximately 1500 m. Two distinct events can be seen in the direct down going shear wave, characteristic of the shear wave splitting generated by the fracture related anisotropy in the lower layer.

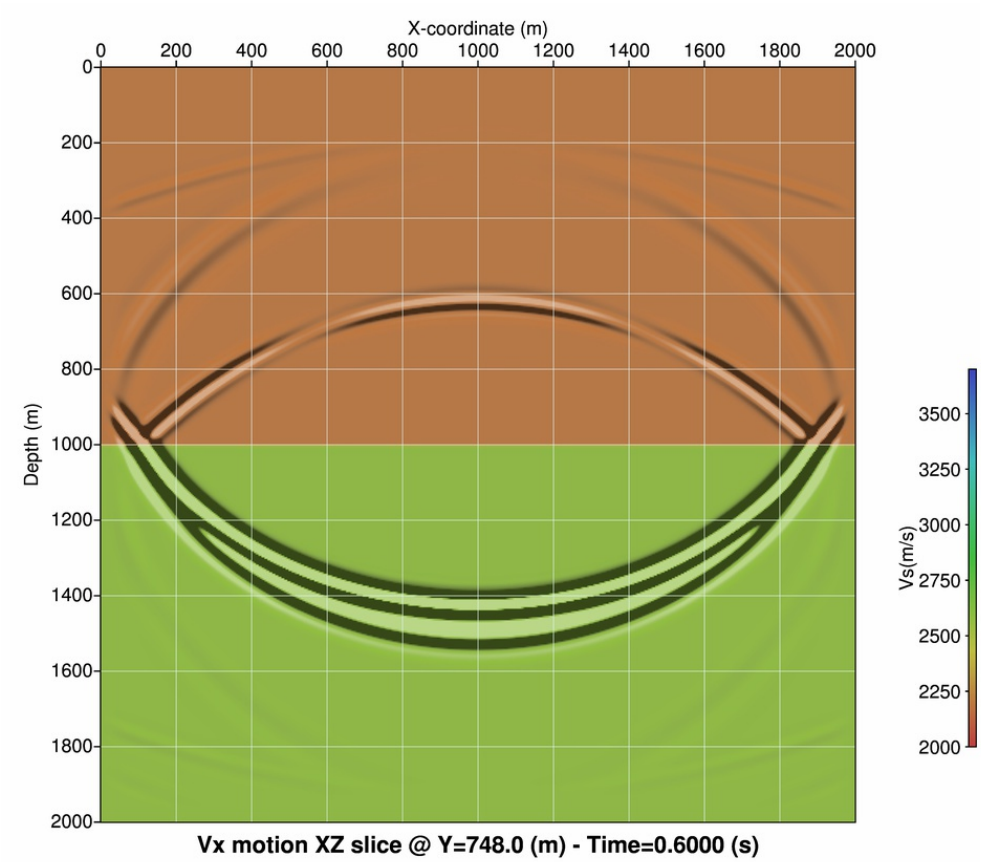

Figure 2.33: X-Z plane Vx motion snapshot generated by an X-motion source overlain on the model at a simulation time of 0.6 s.

Figure 2.34 shows the nine component (3 X 3) seismogram display for one of the simulated VSP's. For the particular case shown in the Figure, the 3-component source is offset 100 m along the X-axis from the VSP well. The presence of significant cross line or off diagonal energy in the horizontal components (source X, receiver Y and source Y, receiver X) is commonly regarded as a strong indicator of fracture anisotropy in 9-component VSP's. Such energy is clearly visible in the Figure once the down going shear wave encounters the second layer at a depth of 1000 m. The shear wave splitting associated with the fracture anisotropy can also be seen in the horizontal diagonal components (source X, receiver X and source Y, receiver Y), where the down going shear wave has split into two distinct events by the time it reaches a depth of approximately 1500 m at 0.6 s.

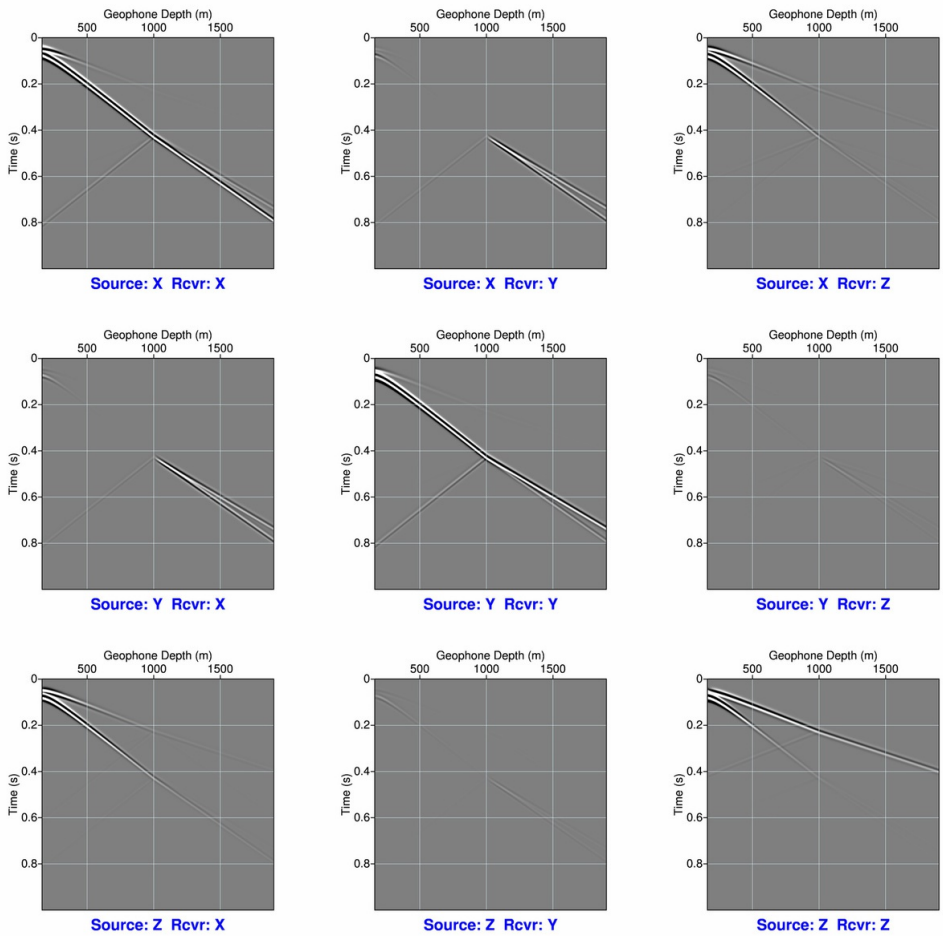

Figure 2.34: Nine component (3 X 3) seismogram display for a VSP with a 3 component source offset 100 m from the VSP well.

The widely accepted method of coordinate frame rotation about the vertical axis (Alford, 1986) was used to analyze these synthetic data. In this method, for each depth, the coordinate frame of the 2 X 2 (4C) sub matrix of horizontal components is rotated through various azimuths using a computer based coordinate frame rotation algorithm. The angle which minimizes or extinguishes the off diagonal energy of the 4C matrix is taken to be the polarization or fracture plane direction. Once rotated to the polarization direction, each diagonal component should contain one of the split shear waves, with the other split shear wave showing up on the other diagonal component. A cross correlation method is then used to estimate the travel time splitting between these two separated shear waves. This method is equivalent to the use of crossed Nicols filters in a polarizing microscope applied in optical mineralogy to find the polarization direction of anisotropic crystals. The filters are rotated until extinction is observed. The extinction angle is then taken as the crystalline orientation.

Figure 2.35 shows the 4C matrix of Figure 2.34. Figure 2.36 shows the same traces after rotation to the minimizing coordinate frame. As can be seen, the energy in the off diagonal components of the down going shear wave has been extinguished. For depths below 1000 m, the two split shear waves which are seen to interfere strongly on the unrotated synthetics (Figure 2.35) have been cleanly separated into

pure modes on the minimized synthetics (Figure 2.36), with a clear travel time difference developing with depth.

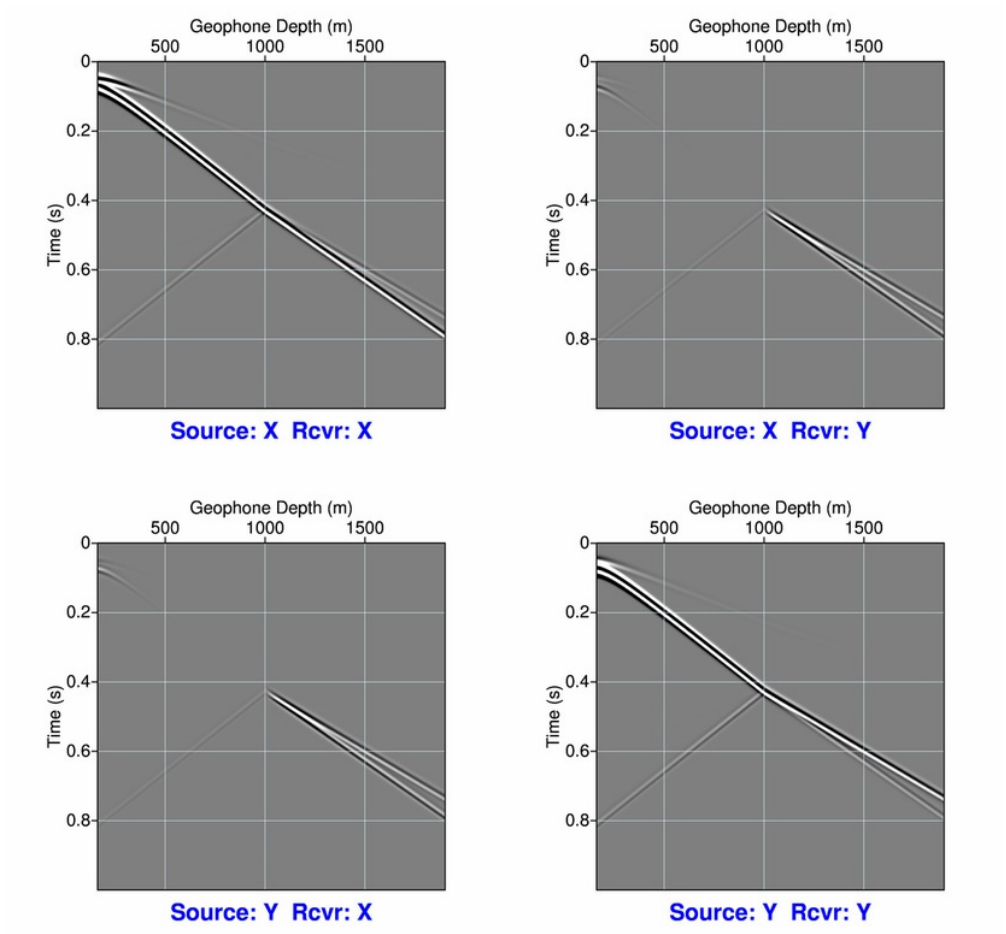

Figure 2.35: 4C sub matrix of Figure 2.34. Traces are shown before the application of minimizing horizontal coordinate rotation. The presence of the off diagonal energy (source X, receiver Y and source Y, receiver X) indicates the presence of fracture related anisotropy not aligned with the acquisition coordinate frame. The diagonal components (source X, receiver X and source Y, receiver Y) contain mixed fast and shear modes.

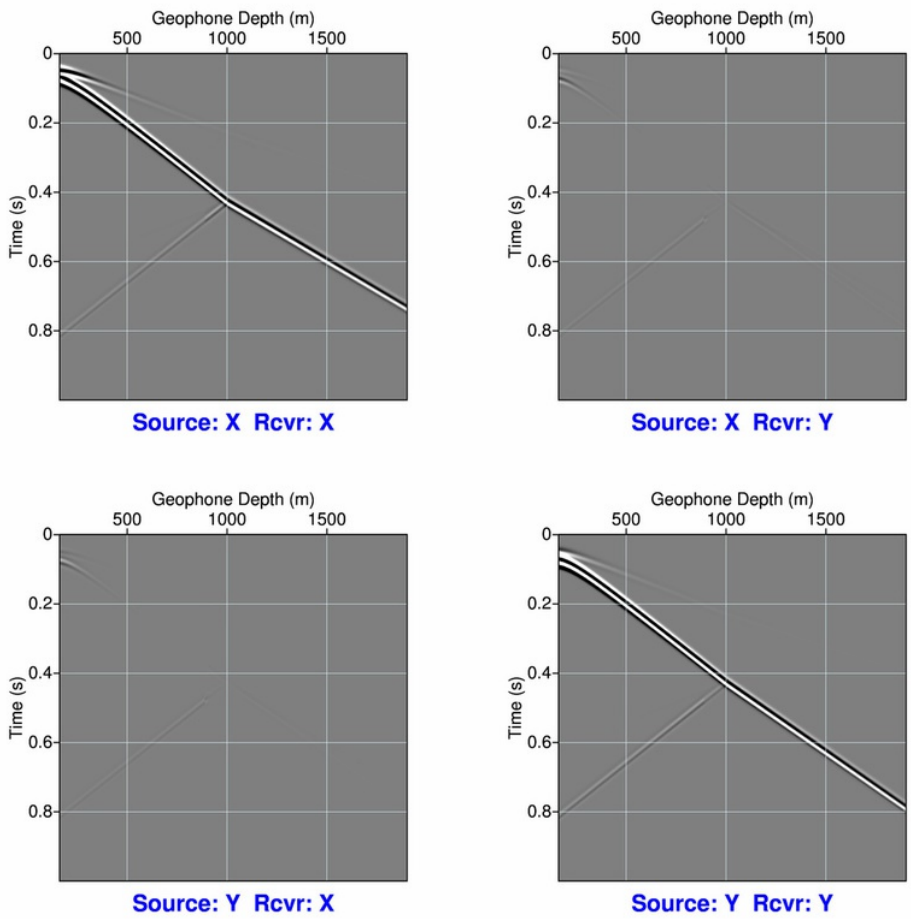

Figure 2.36: 4C sub matrix of simulated VSP traces after rotation to minimizing coordinate frame. The off diagonal components of the down going shear wave has been extinguished. For depths below 1000 m, the two split shear waves which are seen to interfere strongly on the unrotated synthetics (Figure 2.35) have been cleanly separated into pure modes.

Details of these results are shown in Figure 2.37. This figure shows the minimizing polarization angles with depth, and the estimated travel time splitting with depth. For the very shallowest depths above 200 m, the simulated traces are in the near field region of the source. At these depths, compressional and shear waves interfere, corrupting the travel time splitting estimates. For depths above 1000 m in the unfractured layer, the travel time splitting is seen to be near zero. Since there is no off diagonal energy in the 4C traces for any coordinate frame azimuth at these depths, polarization angles are unstable, and usually follow the source receiver azimuth (0 degrees in this case). For depths in the fractured layer below 1000 m, the polarization angles are seen to quickly stabilize at a value of 63 degrees, which is the fracture azimuth. The travel time splitting is seen to increase linearly with depth, indicating a uniform fracture density for depths below 1000 m. The slope of this increasing travel time splitting is proportional to the fracture density.

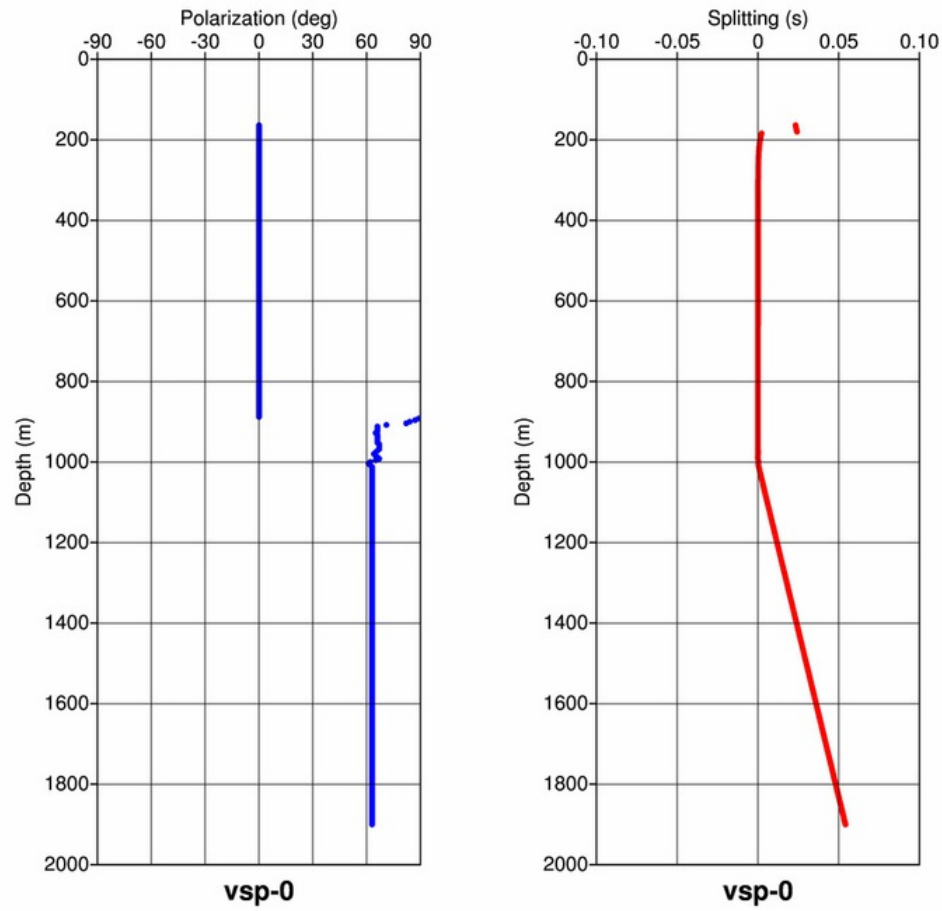

Figure 2.37: Minimizing polarization angles with depth, and the estimated travel time splitting with depth.

The recovery of the correct fracture direction and travel time splitting with depth verify the fracture modeling capabilities of the staggered grid finite difference algorithm for sub seismic vertical fractures. This also demonstrates the method of coordinate frame rotation for recovering fracture information from multicomponent VSP.

Geophysical Modeling Summary

2D and 3D geophysical models in support of acquisition design were developed. The 2D geophysical model results should be useful in selecting station spacing and investigating approaches for limiting the effects of noise related to ground roll and air wave. Comparison of the 2D geophysical model results with actual field data from the nearby Desert Peak geothermal area shows that we are capturing many of the features seen in the field data.

The 3D geophysical modeling of the simple fault has shown the importance of using multicomponent VSP arrays to record fault plane reflections. The 3D geophysical model incorporating near surface heterogeneities suggests that using wide areal coverage surface and VSP arrays will greatly improve the chance of success in acquiring and processing seismic data in geothermal areas which are typically

plagued by this problem. Finally, the Brady's Hot Springs 3D model indicates that even with the intricate seismic response shown in such a complexly faulted area, valuable results can still be obtained with the correct choice of source locations, station spacings, and line orientations.

Task 3: Seismic Simulation and Survey Design

Proposed Objectives

The proposed objective of this task was the running of a number of seismic simulations using both publicly available ray trace modeling codes and proprietary fully elastic 2D and 3D staggered grid finite difference programs already developed in house by Hi-Q Geophysical. These simulations will be run on a computer cluster provided by Hi-Q Geophysical. These simulations will be used to design the planned surface multicomponent seismic orientation and the near offset VSP tests. An acquisition plan for these tests will be generated, as well as a preliminary design for the full areal coverage surface and VSP surveys. This task will overlap with Task 2, with some iteration between the formulation of model parameters and actual running of the models.

Accomplishments

Seismic Simulations

Using the preliminary geological description discussed under Task 1, a series of geophysical velocity and density models characteristic of the Brady's Hot Springs area have been created. Many of these geophysical models were discussed under Task 2. In addition, three newer geophysical models were created. These included an isotropic fully 3D model of the Brady's Hot Springs area, a 3D model with the x-axis oriented along the major fault strike direction, and an anisotropic 3D model including fracture zones along the Brady's fault.

Figure 3.1 shows these three models with the top layer (undifferentiated Truckee and Desert Peak) stripped off to show the fault structure. The model on the left is the full 3D model with the x-axis oriented North and y-axis oriented East. The middle model is the 3D model rotated so that the x-axis is aligned with the major fault direction, and the model on the right shows the layers with transparency so the location of two elliptical zones of vertical fractures along the Brady's fault are visible.

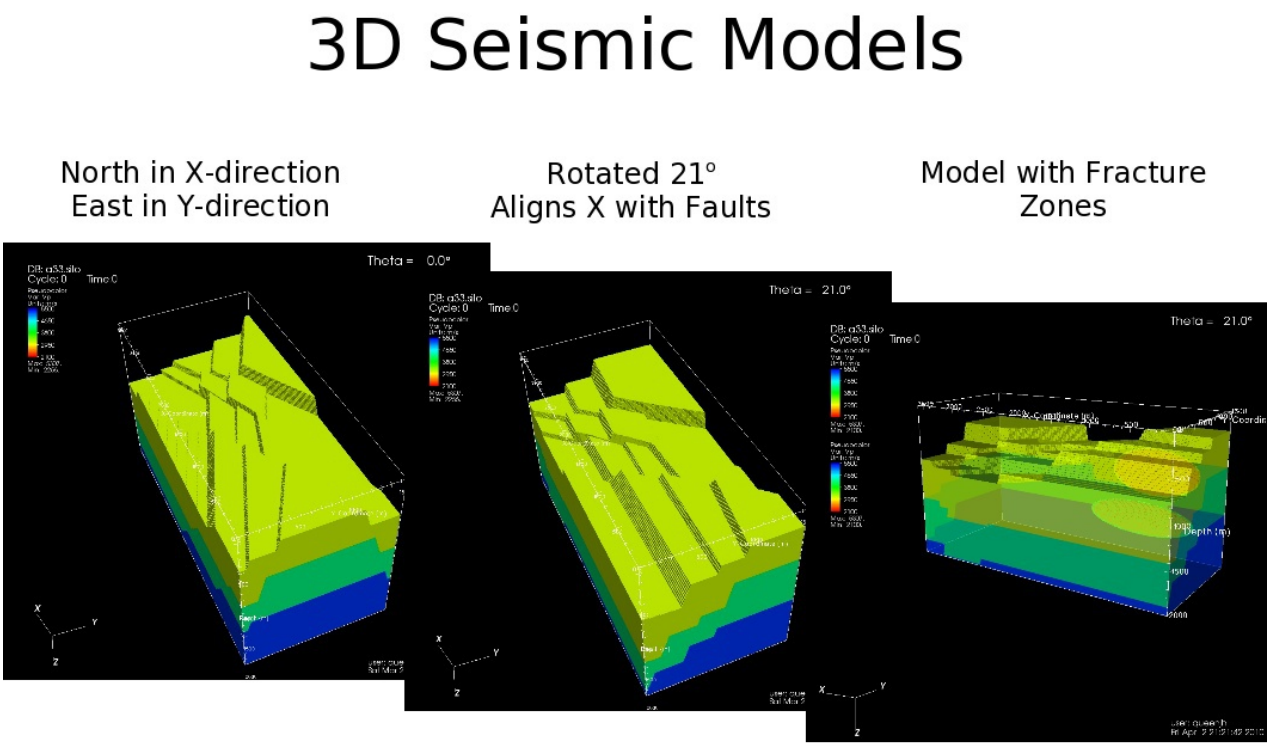

Figure 3.1: Three different 3D seismic velocity models of Brady's Hot Springs.

Following construction of these seismic models, a number of seismic simulations were run. Many of these simulations were discussed under Task 2. Figure 3.2 shows simulation results for the center (no fractures) and right (with fractures) models shown in Fig. 3.1. A VSP in the 15-12 well at Brady's (the well primarily being considered for EGS treatment) and a swath 3D surface geophone array were simulated.

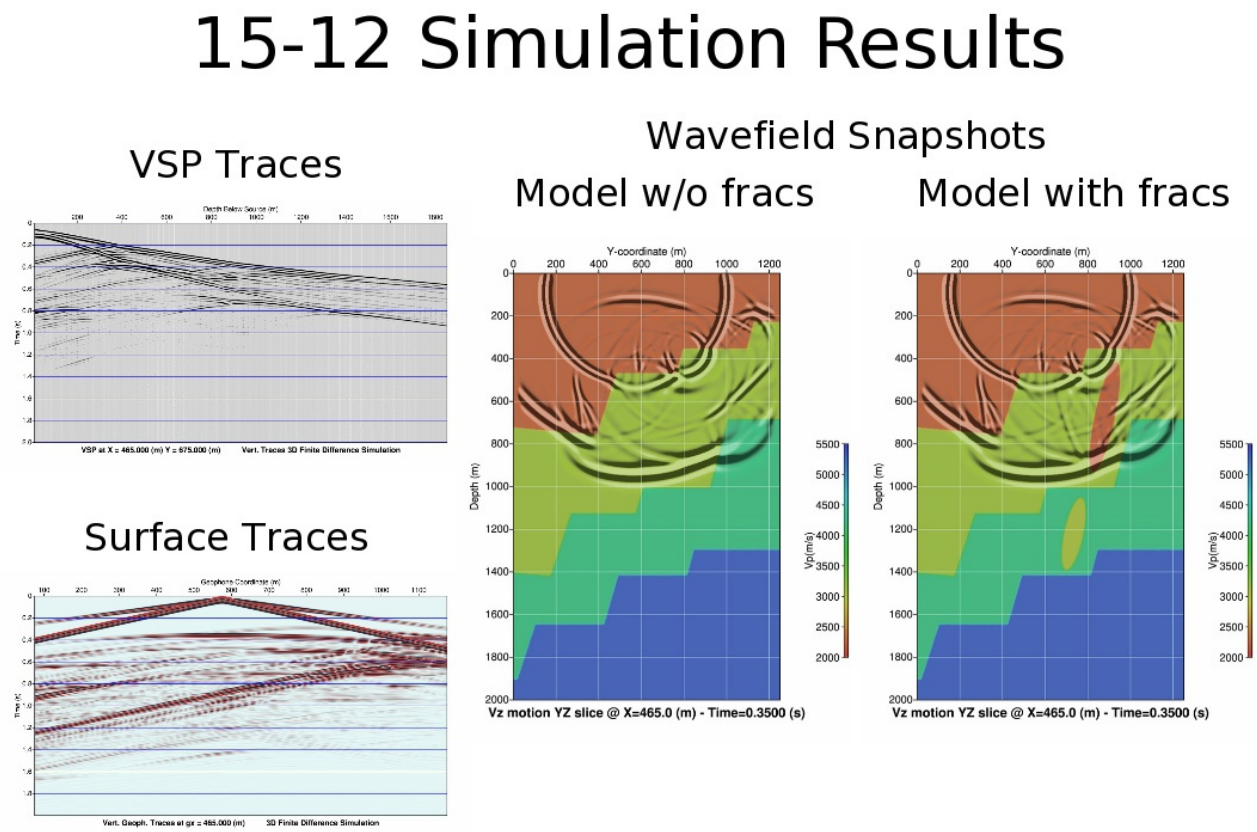

Figure 3.2: Seismic simulation results for two models shown in Fig. 3.1: Without fractures (Fig. 3.1 center model); With fractures (Fig. 3.1 right model).

These simulations led to a number of key learnings. Among the more significant are: VSP is more suitable for recording energy scattered from fractures and faults due to the dominant horizontal propagation of these events; surface seismic will do a much better job delineating overall structure by imaging bed offsets due to faulting with greater areal coverage; very fine geophone spacings will be needed to allow filtering of near surface scattered events and to image the short wavelength fault block structure expected at Brady's; multicomponent geophones are important for recording horizontally propagating compressional waves in VSP and for recording shear waves in both surface and VSP geometries. Finally, a large amount of out of plane energy is expected from the complex fault structures, and orientation of sources and geophones with respect to fault directions is important for minimizing this energy. Wide areal coverage acquisition and imaging will help mitigate these effects.

With these learnings in mind, an acquisition plan for a near offset VSP, a seismic noise

test, a surface orientation test, and a micro gravity survey has been designed.

Survey Design

Figure 3.3 summarizes the data acquisition plan.

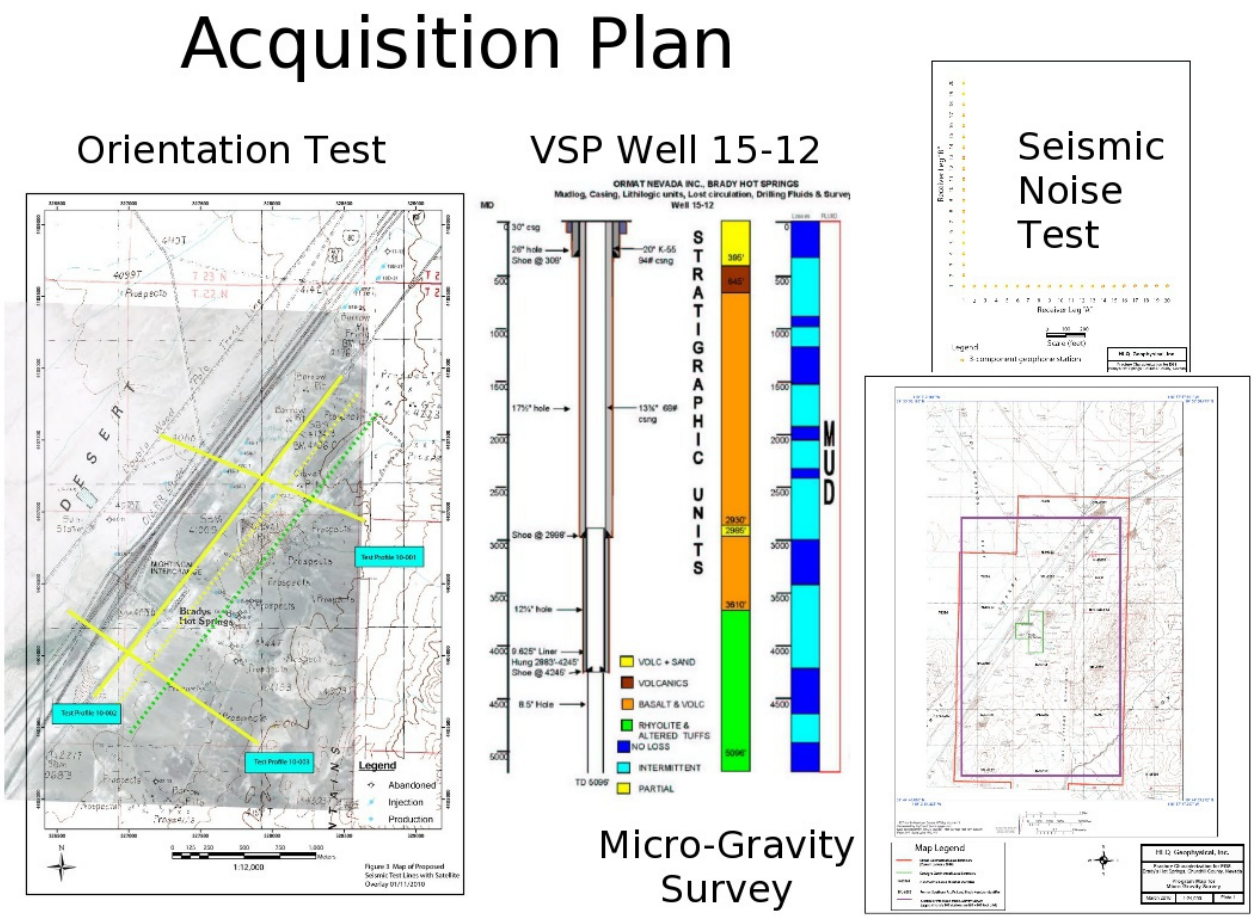

Figure 3.3: Seismic orientation test layout (left), the VSP well plan (center), the seismic noise test layout (top right), and the micro gravity survey (magenta rectangle, bottom right).

In this plan, field work will begin with a micro gravity survey. Coverage of this survey is outlined in the magenta rectangle on the bottom right of Fig. 3. Approximately 800 gravity stations will be acquired on a 660 X 600 foot grid.

Commensurate with the micro gravity work, a seismic noise test will be acquired to asses the level of cultural seismic noise associated with freeway traffic from I-80 as well as operations from several plants in the area. Natural seismic noise related to the active fumaroles along the Brady's fault will also be monitored. The layout of this noise monitoring array is shown at the top right of Fig. 3.3. The array will be an L shaped array, with 20 multicomponent geophones along each leg, spaced at 50 foot intervals. Controlled seismic sources will also be applied at several stations along the array to

determine the relative levels of source and noise amplitudes.

Based on aerial photograph review and site inspection a series of three possible seismic test lines were selected for the seismic orientation test. The layout of these lines is shown on the left of Fig. 3.3. Details for each test line is provided in Table 1 below.

Table 1. Orientation Test Parameters

Line	Length	Orientation	Rationale for Location
10-001	1 mile	NW-SE	Line is located in identified hydrothermal system area with significant geologic control. Approximately parallel with Geologic Section C-C'.
10-002	1.5 mile	NE-SW	Line is proposed as source line along old US40 embankment with offset parallel receiver line about 1400 feet south. Subsurface CMP line will extend through well 15-12 location and also through main production area in Section 1. Line is approximately parallel with Geologic Section F-F'.
10-003	1 mile	NW-SE	Line is located in area away from identified geothermal production and through wells BCH3, 15-12 and 26-12. Section is located to take advantage of limited subsurface control from wells.

In this plan, source and geophone spacings will be highly oversampled at 10 foot over certain sections of the lines. Nominal spacing will be 20 foot. Bolt LSS3B Land Airguns will be used for sourcing. Vertical geophones will be the primary surface seismic sensors, though three component geophones will be deployed on a limited section of one of the lines. Point source and point receivers will be used. Sample rate will be 0.5 ms with 3 s record time. Line and station locations may shift slightly to accommodate permit restrictions.

Near offset VSP acquisition will take place in the 15-12 well. Completion details of this well are shown in the center of Fig. 3.3. As originally planned, the downhole receiver will consist of a single level high temperature multicomponent geophone sonde. Depth spacing will be 10 foot, and depths from bottom of casing (3000') to near surface will be covered. A single source location approximately 300 foot NW of the well is planned. Sourcing will be accomplished with a single vibroseis source capable of generating all three components of source motion leading to a full nine component near offset VSP.

Simulation and Survey Design Summary

Task 2 and 3 objectives were met. While we originally envisioned using ray tracing in the seismic modeling, we replaced this approach with Kirchhoff modeling as described under Task 2. An acquisition plan for the future surface orientation tests (Task 4) and near offset VSP (Task 5) was formulated utilizing the results from Tasks 1 – 3.. This plan was modified in subsequent work to adapt to the changing conditions of actual field work, including permitting restrictions and equipment

availability.

Phase II

Task 4: Surface Orientation Tests

Proposed Objectives

The proposed objectives for this task was the acquisition of a series of surface seismic orientation test lines in the Brady's Hot Springs area. Lines will be acquired with highly oversampled source and geophone spacings as determined by the modeling effort from Budget Period I Task 3. Acquisition will be performed by Stephen G. Muir, consulting geologist and geophysicist, using in house equipment. Sourcing will be accomplished using both Bolt Technologies land air guns and explosives. Standard as well as multicomponent geophones will be used. In addition, micro gravity data will be acquired at each surveyed location. Both the seismic and micro gravity data will be processed and interpreted. Results will then be compared to the model predictions, applying suitable modifications to the model parameters.

Accomplishments

Permitting

Permitting issues were a stumbling block in completing Task 4. Significant delays were encountered due to the permitting process with the Bureau of Land Management (BLM).

An approved Notice of Intent for the micro-gravity component of the Surface Orientation Tests has was received from the BLM.

Personnel from Stephen G. Muir, Consulting Geologist and Geophysicist traveled to the Brady's Hot Springs KGRA to conduct permitting related activities from June 4 to 9, 2010. They reviewed seismic test line locations in the field. All lines were found to be satisfactory for equipment access. Individual receiver and source station flags were placed on the ground with specific station numbers. Over 2,000 points were laid out. Figure 4.1 shows the planned layout of the surface seismic orientation lines.

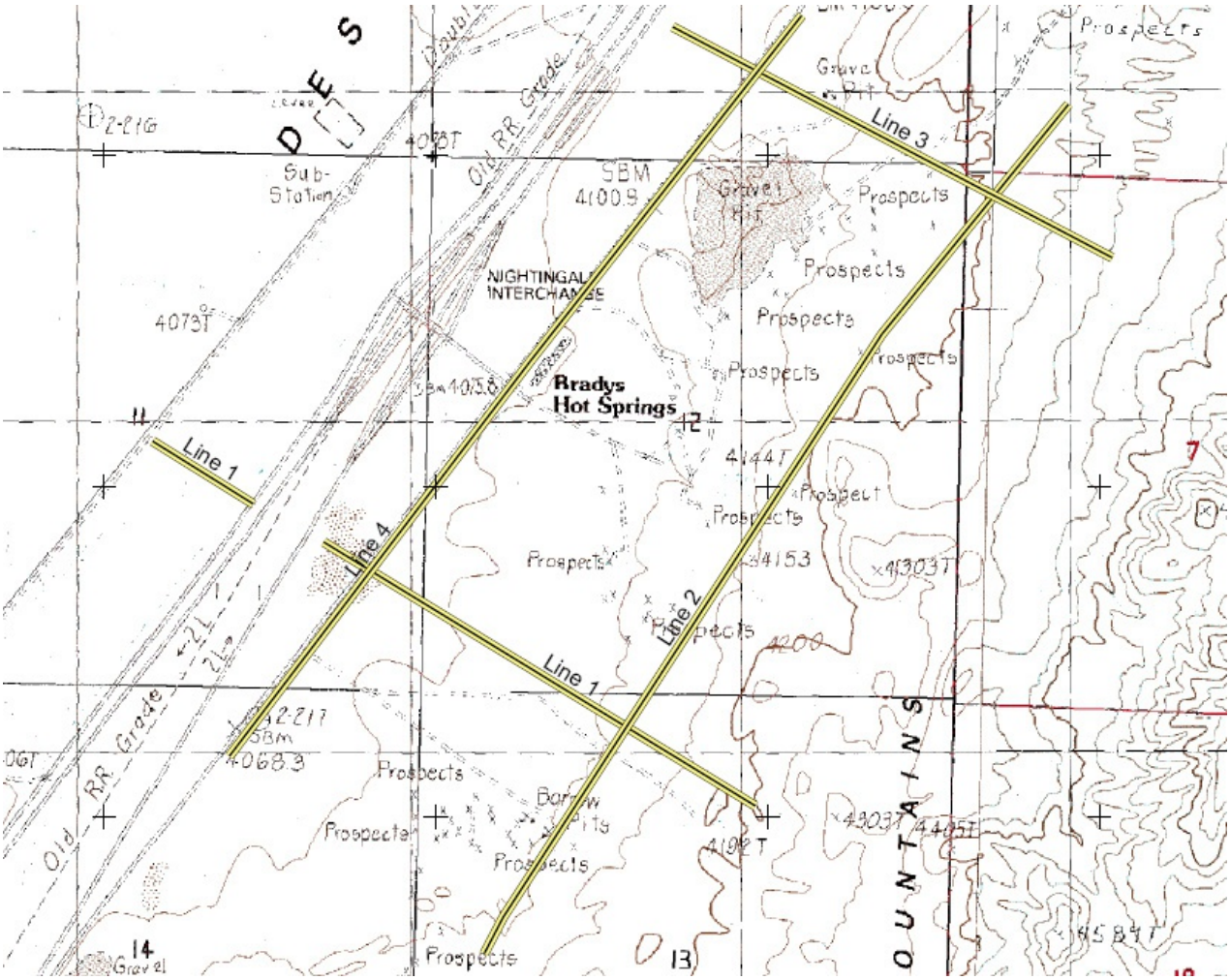

Figure 4.1: Map of proposed seismic lines for surface seismic orientation tests.

Following layout of the stations, personnel from Native-X, Inc., Archaeological Services were contracted by Stephen G. Muir, Consulting Geologist and Geophysicist, to identify potential archaeological and historical cultural issues. Line 1 (western most northwest-southeast line) was moved approximately 300 feet to offset identified archaeological issues. A minor source point offset was required on the western portion of the southern northeast-southwest line (Line 4). Line 3 required source point offsets due to historical culture. Native-X then forwarded their report on this work to the BLM Winnemucca office in support of the previously filed Notice of Intent for the surface seismic work. No issues were identified as source points will avoid identified problems. Native-X has also indicated that no on-site archaeological monitoring will be required for the seismic effort. Our Notice of Intent (NOI) to conduct geophysical operations in the Brady's Hot Springs Area was approved by BLM on August 12, 2010, and our NEPA determination was issued shortly after that.

Data Acquisition

Three distinct surface reflection lines as well as data from a multicomponent noise monitoring array were acquired at the Brady's Hot Springs Area. All data were acquired with geophone spacings of 20 f,

approximately five times finer than standard oil industry spacing. This spacing, limited by the desire for far offsets and the number of recording channels available, was a departure from the hoped for 10 f spacing outlined in Task 3. Line 1 was collected using 3-Component geophones.

Figure 4.1 shows a map of the approximate line locations. Line 1 strikes NW-SE, and passes within a few hundred feet of the Ormat 15-12 well. Line 1 was acquired using 3-Component geophones. It is approximately perpendicular to, and crosses the Brady's Fault. Line 3 also strikes NW-SE, and passes through the most productive part of the field. It was acquired using conventional vertical component geophones. Line 4 strikes NE-SW, approximately parallel to the Brady's Fault. It runs along old U.S. Highway 40. As with Line 3, it was acquired using conventional vertical geophones. Line 2 was not acquired. Note that the line numbering differs from that shown in Table 1.

Based on in field processing of the data, a number of observations can be made based on simple displays of shot gathers. In many areas, reflections are apparent in the shot gathers extending to offsets beyond 6000' and times down to 2 s. Figure 4.2 shows an example of such a shot gather.

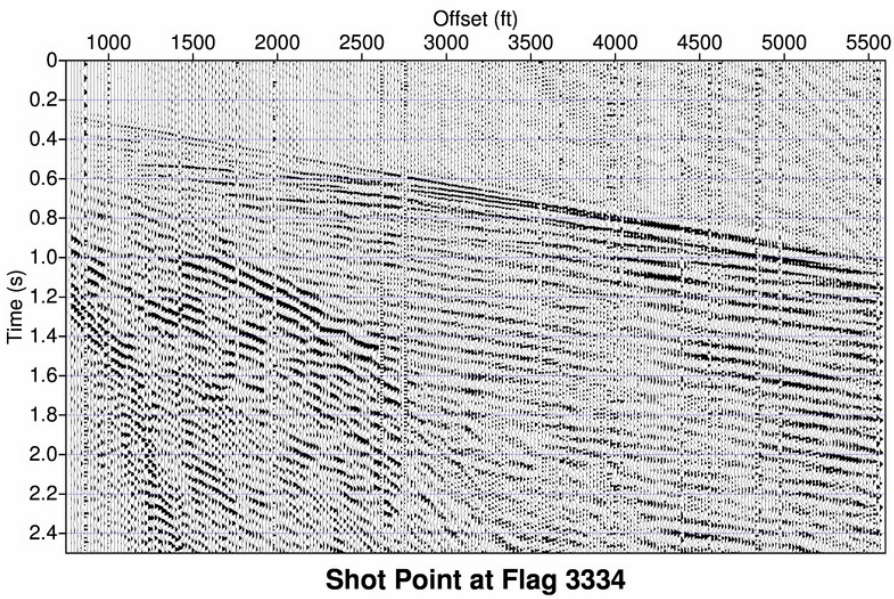

Figure 4.2: Vertical component shot gather from source located at flag 3334 along Line 3. Reflections are visible out to the farthest offsets (~6000') and originating at times as late as 2 s.

Reflector discontinuities interpreted as offset beds related to faulting are visible in many shot gathers. Figure 4.3 shows an example of such reflector discontinuities.

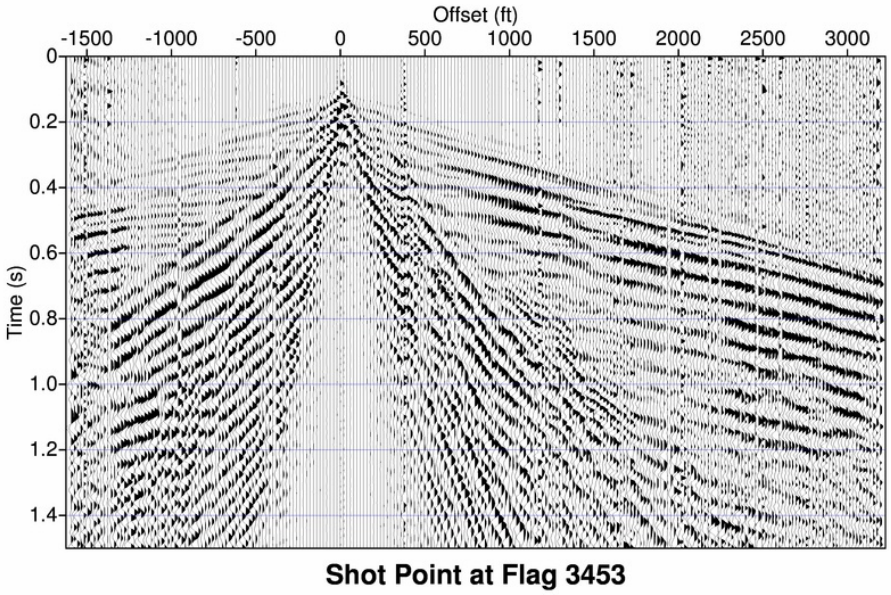

Figure 4.3: Shot gather from flag 3453 along Line 3. Note the discontinuities in the reflectors at an offset of approximately 1300'.

Very low apparent velocity events were seen in certain shot gathers. This was particularly true for shot gathers acquired over the Brady's Fault zone. For such low velocity events, the 20 ft. geophone spacings used represent the maximum spacing that can be used at the frequencies seen in the data and still avoid spatial aliasing. This demonstrates one of the values in using such fine spacings. Figure 4.4 shows an example of such events.

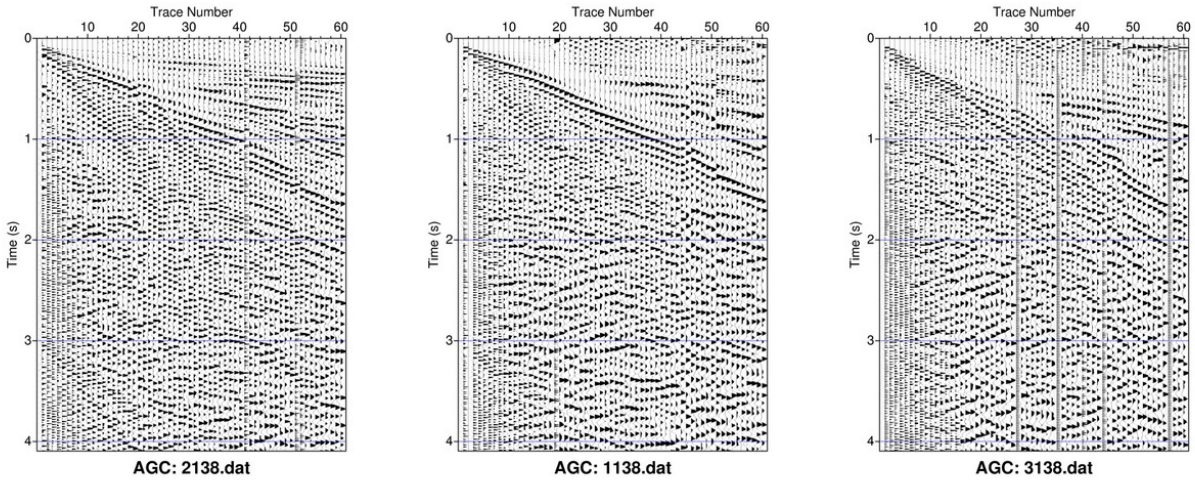

Figure 4.4: Multicomponent shot gather from Line 1 with the source located near the Brady's Fault zone. These traces have had automatic gain control (AGC) applied. Vertical component data are shown on the left, in-line in the center, and cross-line on the right. Note the very slow apparent velocities of the events visible on Trace Numbers 1 – 20 at 0 – 2 s, particularly on the vertical component data. These events are nearly spatially aliased.

It has been suggested in the literature (e.g., Hanssen et al., 2003) that one advantage in acquiring multicomponent data is that the mode converted shear waves (P – S) seen on the in-line components may better image through volcanics. In some of the multicomponent shot gathers acquired along Line 1, reflection events appear to be much clearer on the in-line component than on the vertical component. This supports the idea that mode converted processing may be effective in imaging through volcanics. Figure 4.5 shows an example.

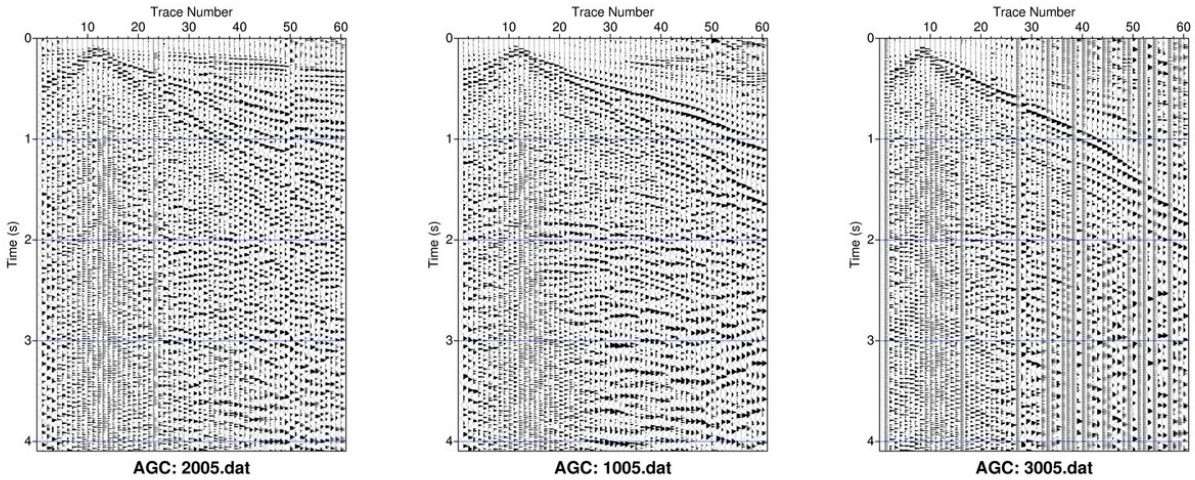

Figure 4.5: Multicomponent shot gather acquired over Line 1. Vertical component data are shown on the left, in-line in the center, and cross-line on the right. Note the reflection events visible on the in-line component (center) at approximately 2 s and later. These events are not apparent on the vertical component data (left).

Data quality was highly variable. In most areas, high quality reflections are visible. In other areas with highly altered surface morphology, no events were visible in shot gathers. Noise related to traffic on Interstate 80 was also a problem. It was found that waiting for periods with little traffic before recording helped limit some of this noise.

In other areas in which complex surface faulting has been mapped, shot gathers show many complex scattered diffraction arcs. Data from these locations will probably require sophisticated migration processing to satisfactorily image these faults.

Figure 4.6 demonstrates many of these effects. This shows a shot gather acquired at flag 3260 along Line 3. Prof. Jim Faulds of the University of Nevada at Reno has mapped surface faulting cutting across this line at approximately the location of the -600' offset of the figure. A series of diffraction arcs are visible in the figure at this offset. The severe noise seen at offsets beyond +500' is where the line crosses Interstate 80, and is caused by heavy traffic on the highway.

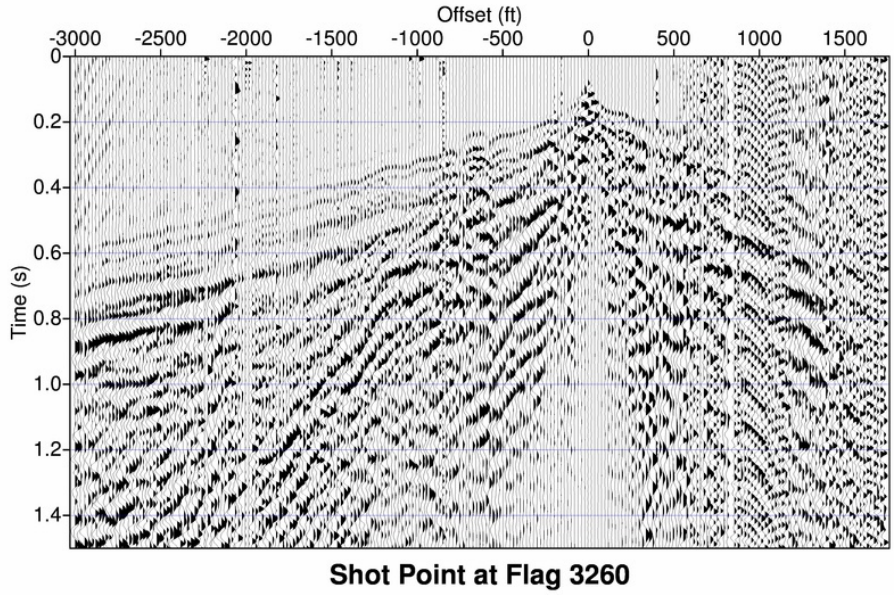

Figure 4.6: Shot gather from flag 3260 along Line 3. Surface Faulting has been mapped at the position of the -600 ft. offset, where numerous diffraction arcs are visible.

Data Processing

Following acquisition, these data were passed on to Western Geco for advanced processing and imaging. Personnel from Western Geco under contract to Stephen G. Muir, Consulting Geologist and Geophysicist collaborating with Hi-Q Geophysical Inc. personnel completed the processing of the vertical component data (P-wave), and delivered a number of processing results.

As described above, three distinct 2D surface reflection lines were acquired. For each of these three lines, processed results fell into the major categories of Final CDP Stack, Post Stack Migration, and Pre Stack Migration. For each of these categories, various noise and filtering processes were applied, including Western Geco's Random Noise Attenuation (RNA) and time varying filters (tvf).

Figure 4.7 shows a map of image points or Common Depth Points (CDP), also called Common Mid Points (CMP) produced by the pre-stack time migration processing stream overlain on a preliminary surface geology map produced by James Faulds at Nevada Bureau of Mines and Geology. Mapped faults are shown as green lines, while “hidden” faults are shown in dark red. Understanding of the geology at the Brady's Hot Springs area has developed significantly since this map was made.

Image points are labeled at every 50th point. Image points in the 2000 series correspond to Line 1, points in the 6000 series to Line 3, and points in the 8000 series to Line 4. Line 1 was acquired using 3-Component geophones. It is approximately perpendicular to, and crosses the Brady's Fault. Line 3 also strikes NW-SE, and passes through the most productive part of the field. It was acquired using conventional vertical component geophones. Line 4 strikes NE-SW, approximately parallel to the Brady's Fault. It runs along old U.S. Highway 40. As with Line 3, it was acquired using conventional vertical geophones. Line 2 was not acquired.

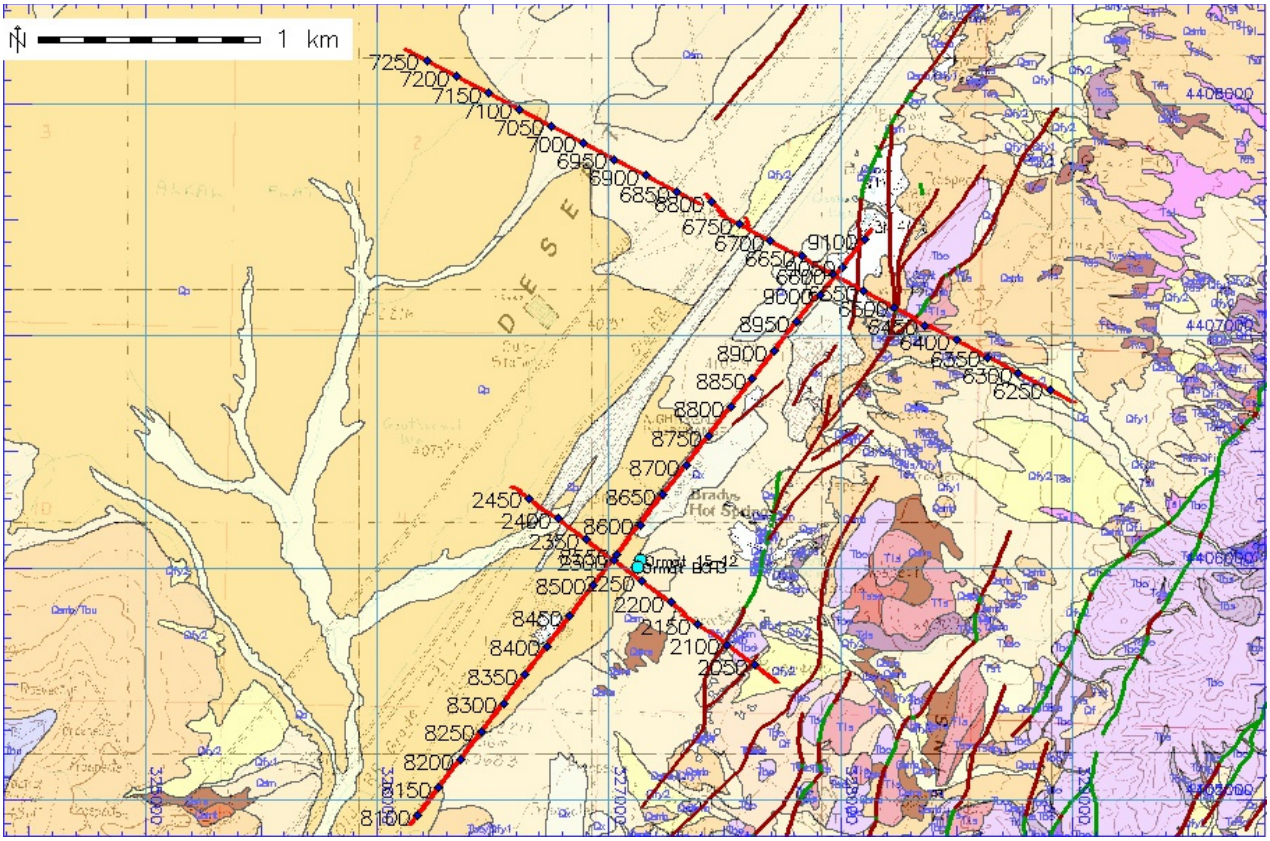

Figure 4.7: CDP location map overlain on surface geology. CDP image points are for the pre-stack time migration results. The surface geology has developed significantly since this map was produced.

Processing Choices

One of the first tasks was to decide which processing stream to carry forward to interpretation. Figure 4.8 shows a time section of the data from Line 3 after full stack. Figure 4.9 shows the same data after post stack time migration. Figure 4.10 is the data from Line 3 after pre-stack time migration. In each of these figures, Random Noise Attenuation and time varying filters have also been applied.

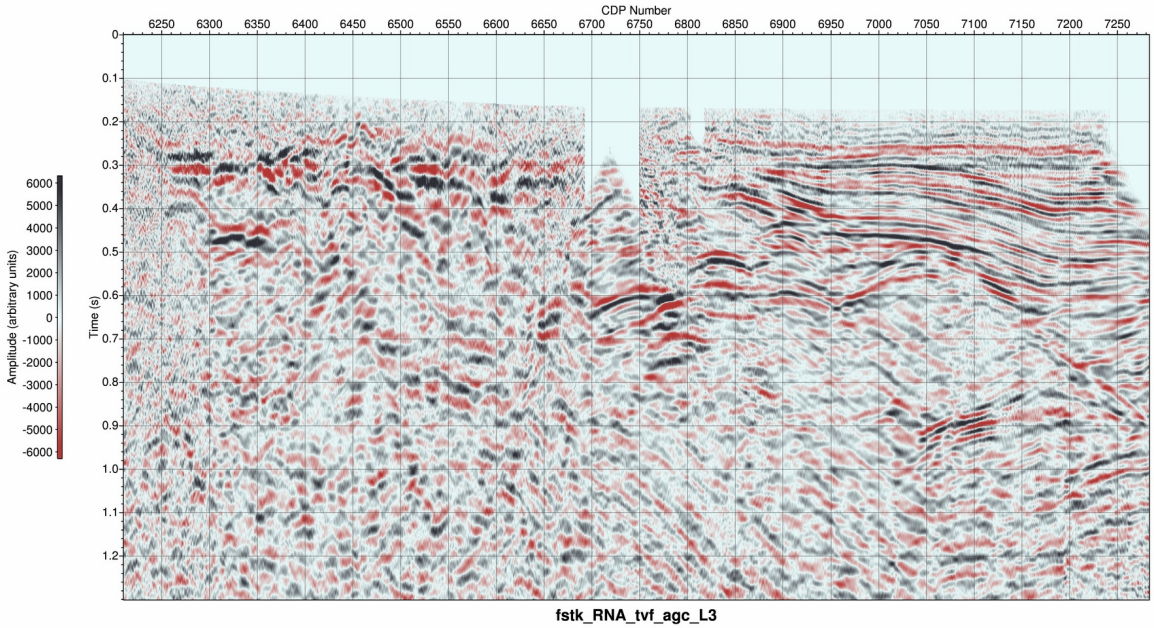

Figure 4.8: Time section of the Line 3 data after processing to full stack. The left side is to the southeast and the right to the northwest.

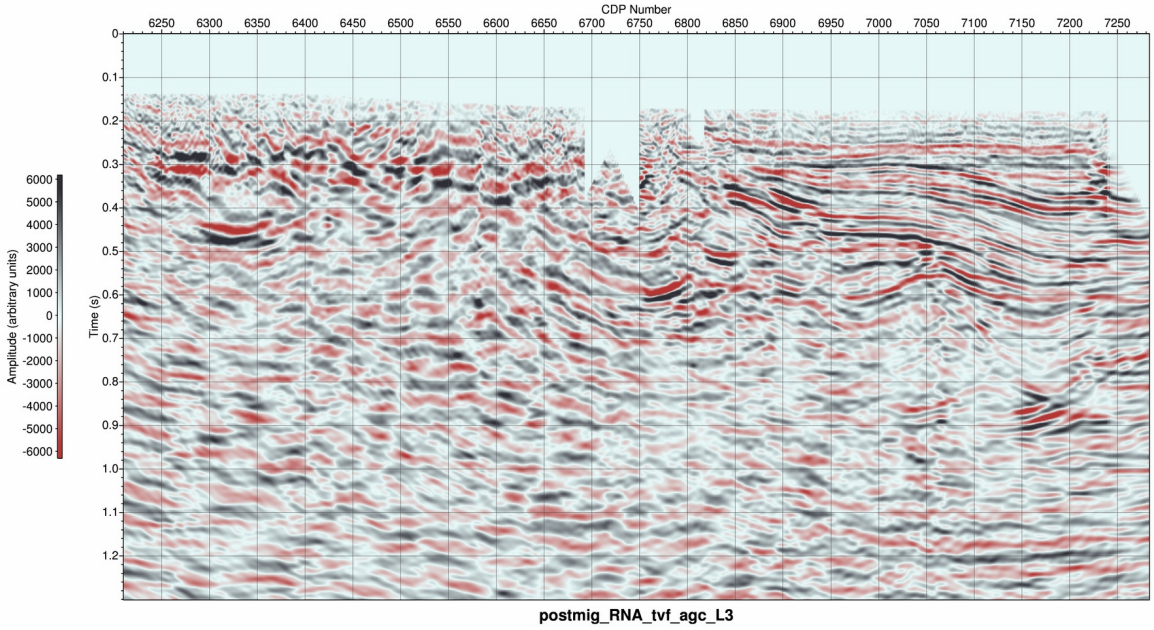

Figure 4.9: Time section of the Line 3 data after post stack time migration. The left side is to the southeast and the right to the northwest.

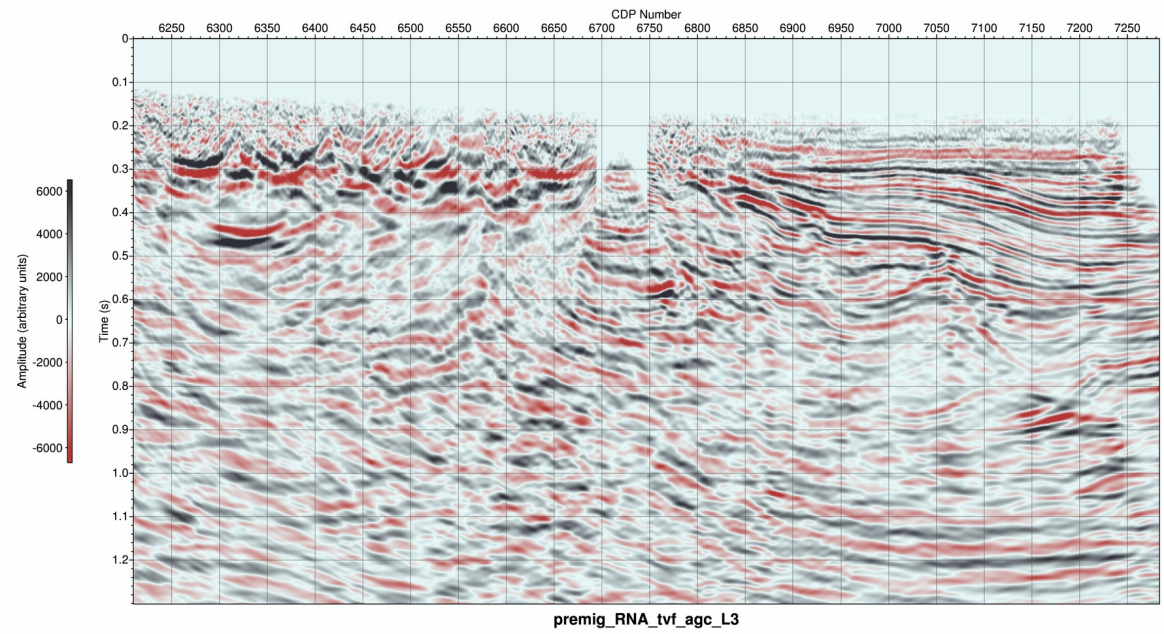

Figure 4.10: Time section of the Line 3 data after pre-stack time migration. The left side is to the southeast and the right to the northwest.

Comparison of Figures 4.8 and 4.9 show that post stack migration has collapsed a number of diffraction arcs, particularly in the vicinity of CDP 6650. A number of events have moved up dip as expected with post stack migration. Comparison of Figures 4.9 and 4.10 suggest the pre-stack migration process has been more effective at imaging deeper events. However, a number of migration arcs can be seen in the vicinity of CDP 6725 where there is a gap in the data due to Interstate 80. Which of these two results better shows the subsurface geology in this highly complex area is unknown. Since the pre-stack time migration is supposedly more robust, it was decided to go forward with the pre-stack time migration results of Figure 4.10.

Time to Depth Conversion

The next step was to convert the data from time to depth. There is almost no velocity control in the Brady's area. The only real control is from the 15-12 VSP results discussed under Task 5. Interval velocities from that VSP were factored into estimating the stacking and migration velocities in the vicinity of the 15-12 well along Line 1. Unfortunately, that VSP only extended to 600 m depth below surface. The only velocity control for deeper depths was from the normal moveout (NMO) stacking and migration velocities.

NMO velocities can be closely approximated as a root mean square (RMS) average of the interval velocities along the seismic ray path. Dix (1955) developed an algorithm for inverting interval velocities from NMO velocities. This inversion process is notoriously unstable. Very small changes in NMO velocities can lead to very large changes in interval velocity. This instability grows with increasing time or depth. In spite of this instability, NMO derived interval velocities were the only path open for performing time/depth conversions.

Stacking and migration velocities provided by the processor were inverted for interval velocities.

Those interval velocities were then interpolated laterally and used to perform a simple time to depth conversion of the pre-stack migrated data.

Figure 4.11 shows the pre-stack time migrated data from Line 3 after such a depth conversion. Figures 4.12 and 4.13 show similar plots for Line 1 and Line 4 respectively.

In Figure 4.11, Interstate 80 cuts across Line 3 between CDP's 6700 and 6750. Interstate 80 cuts across Line 1 between CDP's 2360 and 2450 in Figure 4.12. This is the cause of the “notch” in the data at those image points.

In Figures 4.11 – 4.13, the blue hack marks at the top of the data show where faults from Jim Faulds preliminary surface geology map cross the given line. The light green hack mark shows where another seismic line intersects the displayed line. The well track for the 15-12 well (the potential EGS treatment well) projected onto Line 1 and Line 4 is shown in green. The curve at the top of each plot shows the fold of stack. CDP spacing is approximately 3.048 m (10 ft), so these depth converted sections have an approximate 1:1 vertical exaggeration. Depths are referenced to a datum elevation of 1400 m above mean sea level.

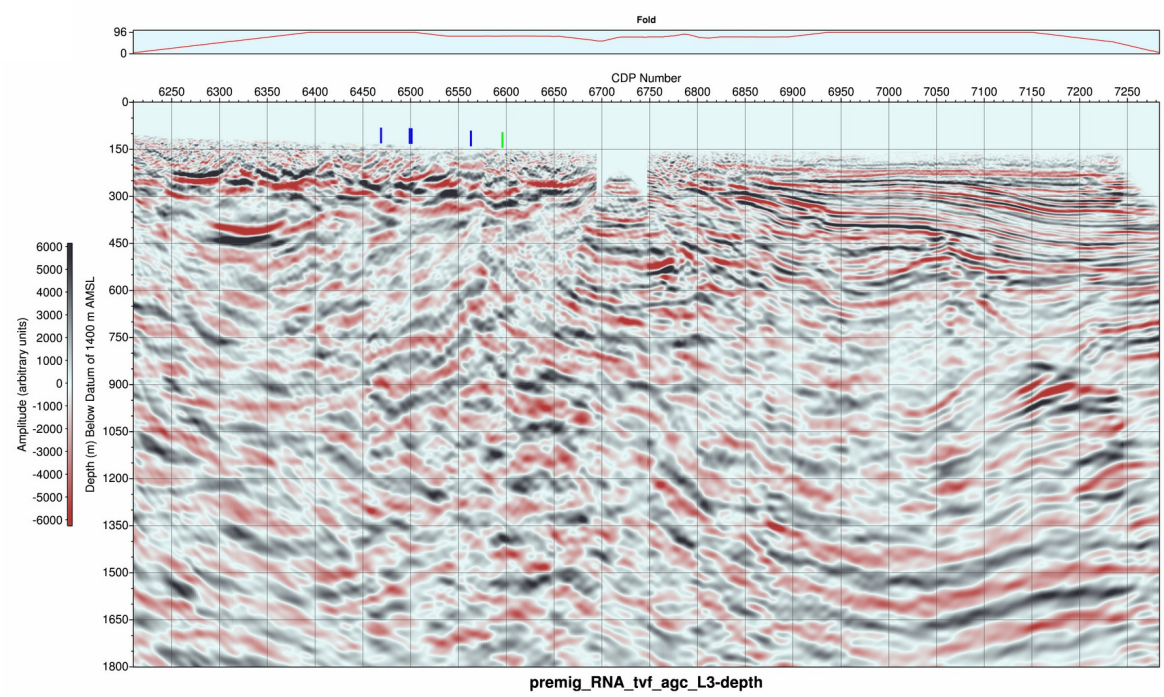

Figure 4.11: Depth converted pre-stack time migrated data from Line 3. Depths are referenced to a datum of 1400 m above mean sea level. The left side is to the southeast and the right to the northwest.

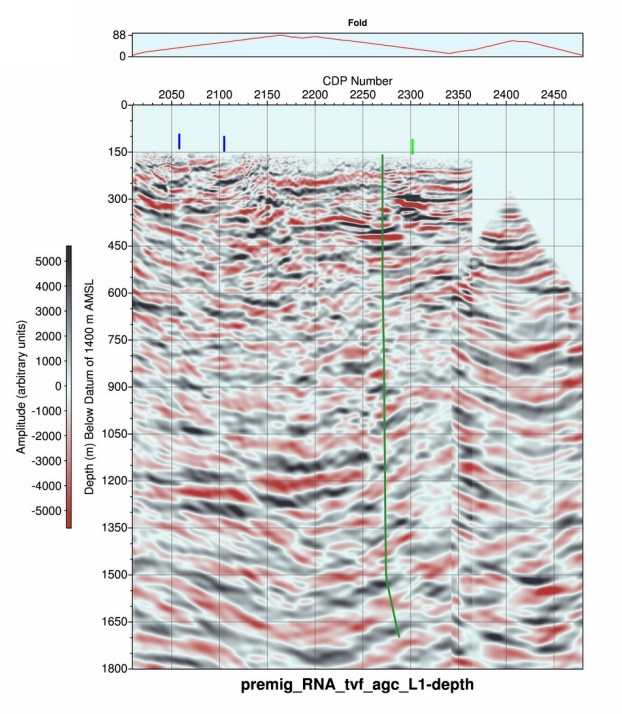

Figure 4.12: Depth converted pre-stack time migrated data from Line 1. The green line is the projected well track of the 15-12 well. The left side is to the southeast and the right to the northwest.

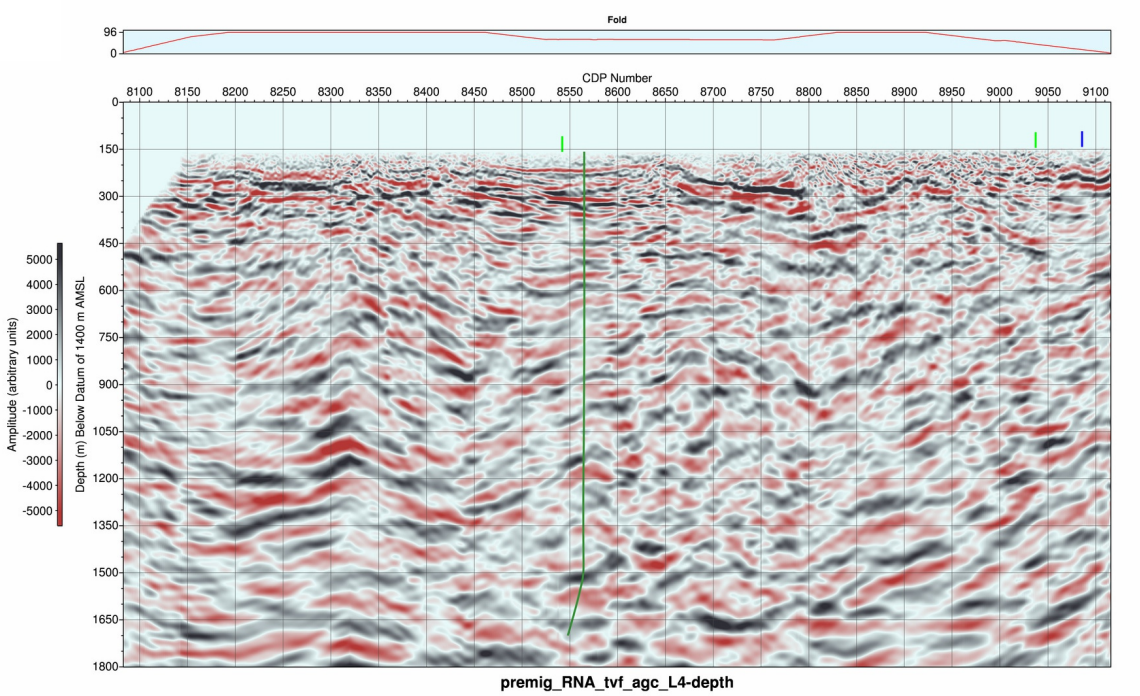

Figure 4.13: Depth converted pre-stack time migrated data from Line 4. The green line is the projected well track of the 15-12 well. The left side is to the southwest and the right to the northeast.

With the poor velocity control available, the depths shown in Figures 4.11 – 4.13 must be taken with a grain of salt. Estimates of interval velocities from stacking or migration velocities are known to be highly unstable. Slight changes in the stacking velocities could easily lead to depth changes on the order of several hundred meters at deeper depths.

Comparison with Near Offset VSP

Figure 4.14 shows a comparison between the corridor stack obtained from the 15-12 well VSP, discussed under Task 5, and the pre-stack time migrated results from Line 1. Here the corridor stack from one near offset shot point (SP – 1) is overlain on the reflection seismic at the projected location of the 15-12 well. Line 1 passes close to the 15-12 well.

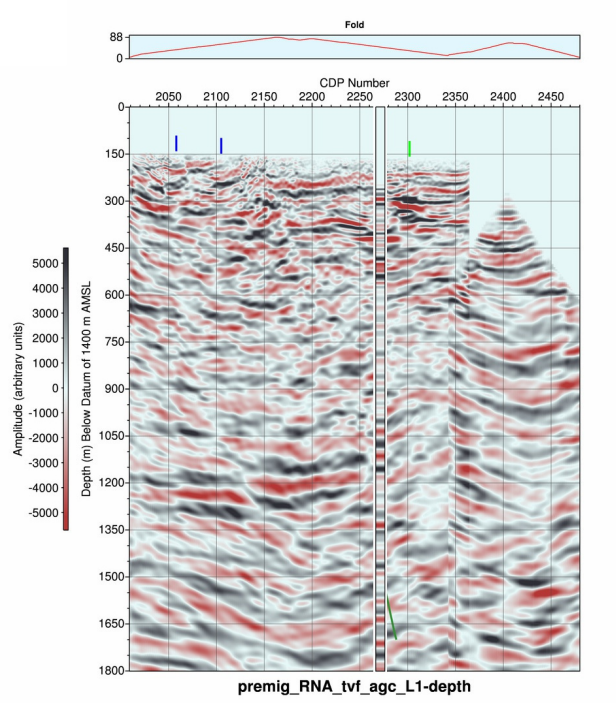

Figure 4.14: Comparison of the 15-12 VSP corridor stack from SP-1 to pre-stack time migration results for Line 1. The corridor stack is plotted at the projected location of the nearby 15-12 well. The left side is to the southeast and the right to the northwest.

The VSP corridor stack is seen to match the surface seismic in overall character. For depths greater than 600 m below surface, the only velocity control are the stacking/migration velocities. For many depths, the VSP response is seen to be higher frequency. Filtering of the corridor stack would probably show a better match at these depths. The bright reflection packages seen in the VSP at 300m, 550m, and 1050m do correspond to bright reflection packages on the surface seismic data.

Preparation for Interpretation

Figure 4.15 shows one possible interpretation of the faults and horizons based on the seismic data and

well information. Such interpretations changed as the project progressed. Geo referenced picks of the faults and horizons were later used as input for building new seismic models described in later tasks.

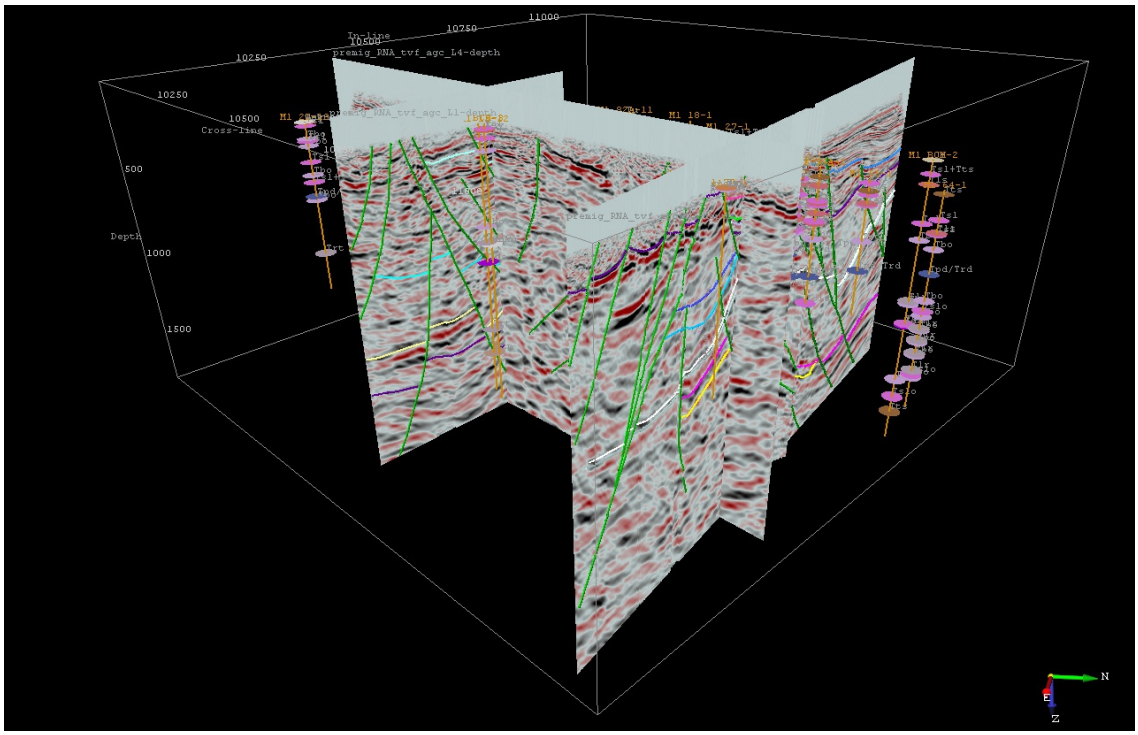

Figure 4.15: Interpretation workstation screen shot. This view looking West shows seismic data, various wells and formation tops, and possible fault and horizon interpretations.

Gravity Data

As part of their cost share contribution, Major Participant Stephen G. Muir, Consulting Geologist and Geophysicist have contributed a large gravity data set acquired over the Brady's Hot Springs area as part of Task 4. Over 800 stations were acquired. These data have been reduced to Simple Bouguer Anomaly (SBA). They were then merged and tied with SBA data from Opplinger supplied by NBMG.

Figure 4.16 shows the SBA over the Brady's Hot Springs field. The contributed gravity stations are shown as green triangles, with flag numbers labeled in black. These stations included the seismic line flag locations. Data provided by NBMG from Opplinger are shown in red. Data acquired as part of this project have most of the influence on the SBA map at this scale.

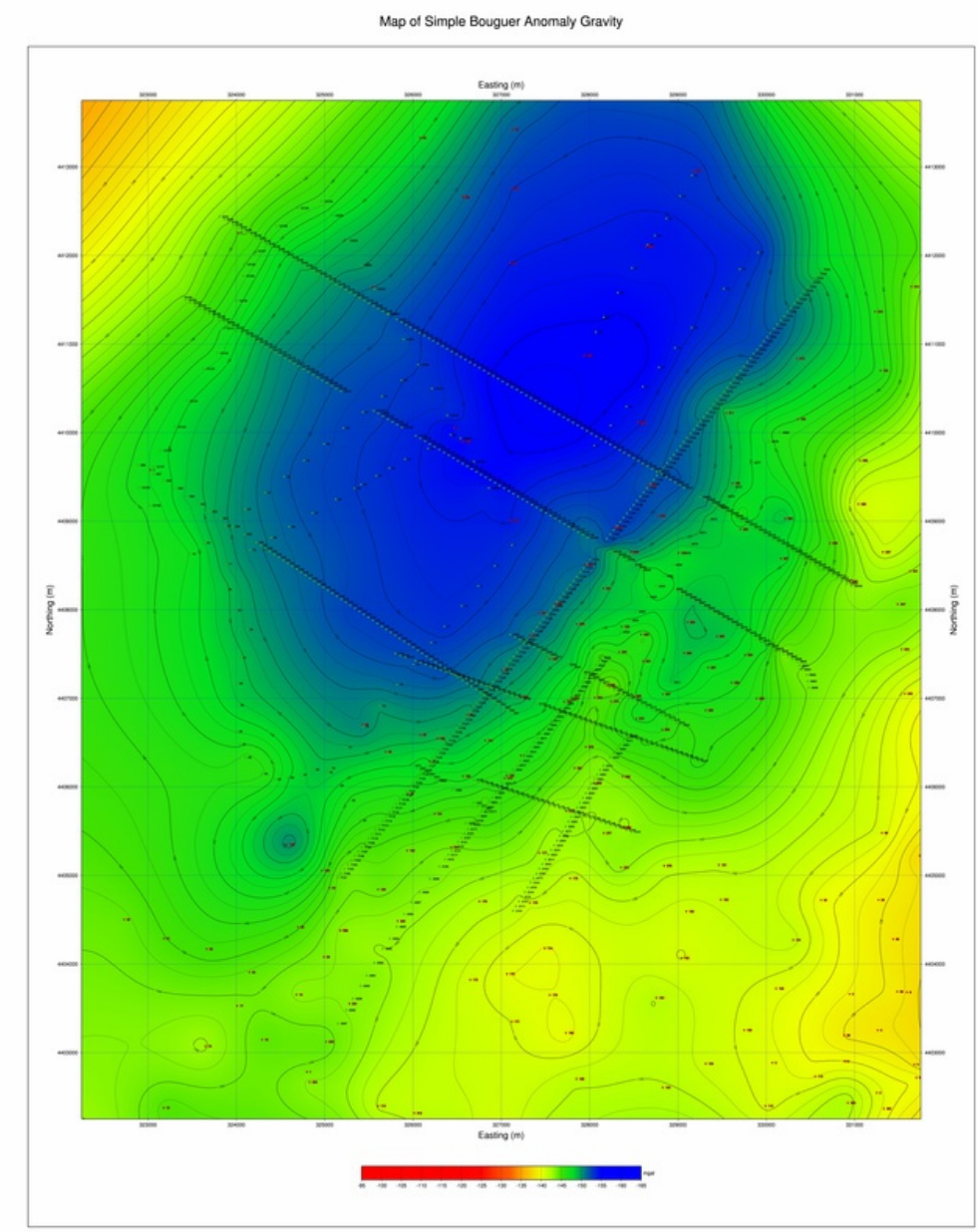

Figure 4.16: Simple Bouguer Anomaly over the study area. The contributed gravity stations are shown as green triangles, with flag numbers labeled in black. Red triangles and labels are from data provided by NBMG.

The SBA results shown in Figure 4.16 are unremarkable in that the previously known deepening of the basin to the North West remains unchanged. However, some finer details of the structure are apparent. These detailed gravity results should be useful in constraining fault block locations during the later interpretation phase of the project.

Task 5: Near Offset VSP

Proposed Objectives

The proposed objective for this task was to acquire a near offset VSP. Completion of this task will require the assistance of a Federally Funded Research and Development Center (FFRDC). This VSP will be acquired in a well made available by Ormat Technologies Inc. at the Brady's Hot Springs area. Source offset and borehole geophone depth spacings will be based on model simulations conducted in Budget Period I Task 3: Seismic Simulation and Survey Design. This task will require the use of “hot hole” VSP tools for evaluation during this acquisition. Upon successful completion of the acquisition, results will be processed, producing both compressional and shear velocity profiles for depths penetrated by the well. In addition, these data will be processed to produce a corridor stack for any reflections present in the data. VSP derived velocity parameters will then be compared to the original model parameters, and model parameters will be adjusted. In order to successfully complete this task it is anticipated that Lawrence Berkeley National Laboratory (a FFRDC) is uniquely qualified to aid Hi-Q Geophysical Inc. due to its past experience and equipment in deploying VSP tools in high temperature environments and their experience and facilities for processing and interpreting VSP data in Geothermal environments.

Accomplishments

Permitting

In view of the permitting problems encountered with the surface seismic work, permitting for this task was undertaken. ORMAT Inc. was contacted, and an approved Sundry Notice has been received from the BLM for the near offset VSP.

VSP Data Acquisition

Primary responsibility for this task was with Lawrence Berkeley National Laboratory (LBNL), a Major Participant in the project. A very beneficial change to the survey design discussed under Task 3 came about when it was learned that a modern commercial VSP acquisition system would be operating in the area of Brady's Hot Springs. LBNL contracted Apex HiPoint, a major provider of bore hole geophysical seismic data acquisition services, to acquire a near offset Vertical Seismic Profile (VSP) in the Ormat 15-12 well located in the Brady's Hot Springs KGRA. Data acquisition efforts began on September 8, 2010, and were completed on September 10, 2010.

To acquire the Near Offset VSP, a 40 level multicomponent geophone string provided by Apex HiPoint with 15 m spacing between geophone sondes was loaded into well 15-12 located in the Brady's Hot Springs KGRA. The initial plan was to reach a bottom depth of 3000' at the bottom of casing. The total vertical depth reached by the bottom sonde was 2000'. This depth was limited by higher than expected temperatures encountered in the well and the rated operating temperature of the sondes (200º F).

Data were then acquired from 4 different shot points around the well using a Pelton Vib-Pro vertical vibrator. Locations of these shot points are shown in Fig. 5.1. Three of the shot points were laid out along a line striking to the North West (normal to the Brady's Fault), with a nominal spacing of 150'. Locations of these shot points were constrained to the well pad and roads. A fourth shot point was

placed at the edge of the well pad approximately 150' to the southwest of the 15-12 well, on a line approximately orthogonal to the northwest line.

At each shot point and depth level, 4 sweeps were acquired for later stacking to reduce noise. Sweep times were 12 s, with a total record time of 15 s at a sample rate of 0.001 s. Sweep frequencies were from 8 Hz to 120 Hz, with a 0.05 s taper at the beginning of the sweep and a 0.02 s taper at the end.

The geophone array was then raised 10', and data from the 4 shot points acquired. This process was repeated 5 times, leading to a depth spacing of 10'.

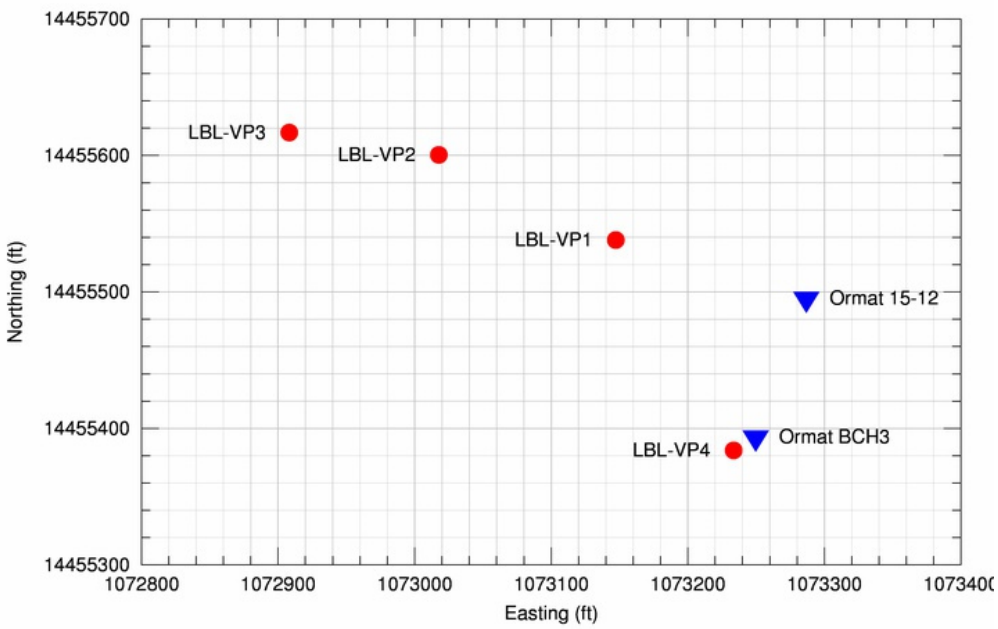

Figure 5.1: Shot Point Locations for the 15-12 Near Offset VSP

VSP data processing

Processing of these data was performed by Hi-Q Geophysical Inc. personnel. Preliminary processing consisted of: conversion of field data files from segd format to segy format; application of survey coordinates to the trace headers giving the unique geographic location of source and geophone for each trace; and editing and stacking of the multiple shots for each source/geophone location;

After preliminary processing, down going compressional wave first break events were picked from the vertical component geophones for all four shot points. Horizontal rotation analysis of the traces based on these picks was applied. Median filtering was then applied in order to isolate and separate the down going compressional waves.

Down going shear first break events were then picked from the separated in-line horizontal components from each shot point. These picked times were then used as input to a median filtering process applied to separate and isolate the down going shear events. The shear separated sections then primarily show

the reflected compressional waves on the vertical components and reflected shear waves on the horizontal components.

Arrival times of the isolated down going compressional wave first breaks were then picked and input to a process giving interval velocities based on a straight ray approximation. These interval velocity estimates were then passed on to the group processing the surface reflection data from Task 4 to provide control for their velocity analysis.

Figure 5.2 shows the traces from shot point LBL-VP4 after preliminary processing and picking P-wave first breaks. P-wave first breaks are very clear and coherent. They also appear to be fairly high frequency. A number of significant reflection events are also visible on these unprocessed data. A strong p-wave reflection is visible at approximately 2000'. A prominent reflection is seen at 1050'. Very strong mode converted shear waves are also visible on the vertical component, but they are much more apparent on the horizontal component sections.

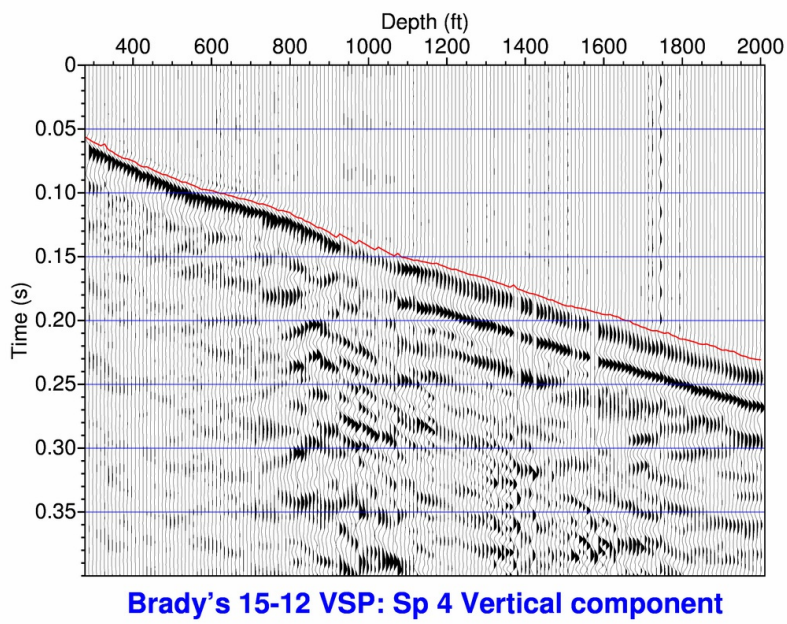

Figure 5.2: Vertical traces from shot point LBNL VP4 after editing, stacking. Displays have been trace normalized. The red line shows P-wave first break picks.

Rotation Analysis

When multicomponent VSP data are acquired, the azimuth of the horizontal geophones is fairly random. To properly analyze the events recorded on horizontal geophones, they must first be computer rotated to an orientation with one horizontal geophone aligned along the line from the source to the well (in-line), and the other aligned perpendicular to the line from the source to the well (cross-line). The usual method for determining the horizontal rotation angle needed to bring the geophones to this alignment is to look at the particle motion direction of arriving compressional waves.

The particle motion of a compressional wave is longitudinal, and is assumed to be along the ray direction. The ray direction for a direct arrival is presumably along the line from the source to the well (in-line direction). As a seismic wave moves across a multicomponent geophone, the geophone moves in response to the wave, following the particle motion of that wave. The signals recorded by each component of the 3-component geophone are the vector components of the particle motion as the wave passes. Each 3-component time sample is a vector giving the displacement of the geophone at that particular time. A plot of the particle motion of an arriving wave can be generated by plotting the endpoints of each of these vectors. Such a plot is called a hodogram. For an ideal direct compressional wave arrival, the hodogram (or particle motion) should be a line along the ray direction. In practice, there is always a certain amount of noise, and compressional arrivals are often slightly elliptical.

Figure 5.3 shows examples of such hodograms or particle motion plots from the actual 15-12 VSP. This figure shows the horizontal particle motion for the direct down going compressional wave as it passes across the multicomponent geophone clamped at a depth of 307.63' in well 15-12. The azimuth of the geophone is unknown, but it remained fixed for all three shots.

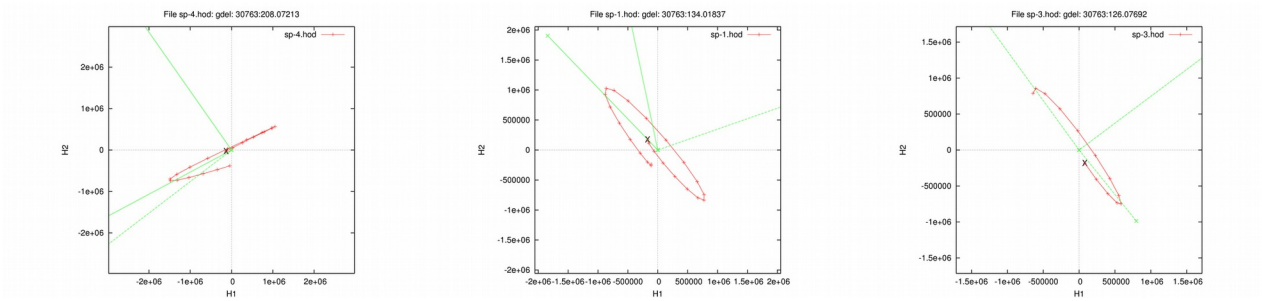

Figure 5.3: Hodograms from geophone clamped at a depth of 307.63'. On left is hodogram from SP 4, center is from SP 1, and right is from SP 3. Particle motion for SP-4 is approximately 90º to that from the other two shot points. This is consistent with the acquisition geometry.

As expected, the particle motion for all three shots is nearly linear, with some slight ellipticity. Looking at Figure 5.1, we can see that the line from source to well for SP 4 is approximately 90º from the line for the other three shot points. Accordingly, we would expect the particle motion from SP 4 to be 90º to the particle motion from the other shot points. This is the behavior shown in Figure 5.3.

While looking at the rotation angles shown by the hodograms, an anomaly was seen for traces from SP-4. For depths deeper than ~450', the hodograms from SP-4 were no longer aligned at 90º to hodograms from the other shot points. This behavior is seen in Figure 5.4 which shows the horizontal particle motion for the direct down going compressional wave as it passes across the multicomponent geophone clamped at a depth of 582.91' in well 15-12.

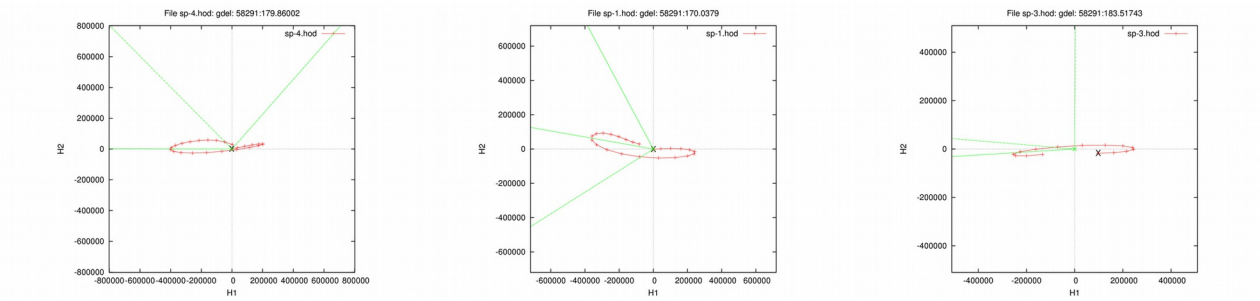

Figure 5.4: Hodograms from geophone clamped at a depth of 582.91'. On left is hodogram from SP 4, center is from SP 1, and right is from SP 3. Particle motion for SP-4 is aligned with the motion from the other two shot points. This is inconsistent with the acquisition geometry.

This behavior is not understood. It may be related to poor casing coupling with the magnetic clamps on the sondes used by the acquisition contractor. However, it does throw into question the geophone azimuths estimated from SP 4.

To estimate geophone azimuths, traces are windowed in time about the P-wave first break picks for each geophone depth. An ellipse is then fit to each of these windowed arrivals. The direction of the major axis of the ellipse is then taken to be the particle motion direction. Given this angle, the horizontal components can then be rotated on the computer to bring the geophone into the in-line / cross-line coordinate frame.

In the end, it was decided to use the geophone azimuths estimated from SP 3 to rotate all of the data from the other shot points. The only exception to this was for depths where the SP 3 data were particularly noisy. In those few cases, the azimuths estimated from SP 2 were used.

These geophone azimuths were then used to rotate all the horizontal traces into in-line and cross-line coordinates. Results after the application of these rotations are shown in Figure 5.5.

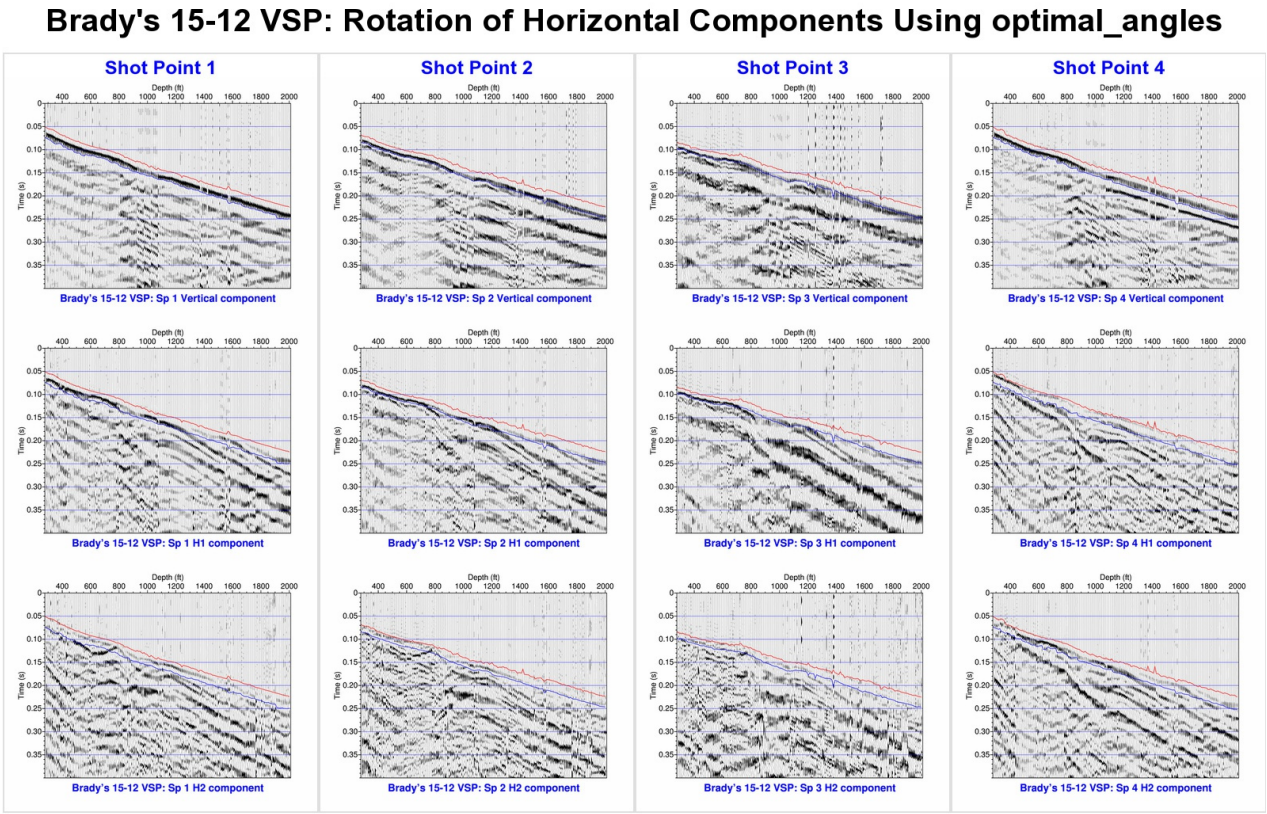

Figure 5.5: 15-12 VSP traces from all four shot points after rotation to in-line coordinate frame. Data from all four shot points were rotated using geophone azimuths primarily estimated from SP 3 data. Top row is vertical component, middle row is in-line (H1) component, and bottom row is cross-line (H2) component. The red and blue lines show the top and bottom of the particle motion analysis window respectively.

Examination of Figure 5.5 shows that horizontal rotation has been successful. Most of the down going compressional first breaks have been removed from the cross-line components (bottom row: H2 component) in the analysis window. They show up as coherent events on the in-line (middle row: H1). Vertical components are not changed by the horizontal rotations.

Median Filtering and Mode Separation

The next step in the processing of the VSP data was to subtract the down going compressional and shear arrivals. In principle, this isolates the reflected and scattered events.

Using the data shown in Figure 5.5, down going compressional wave first break events were picked from the vertical component geophones for all four shot points. Median filtering was then applied in order to isolate and separate the down going compressional waves.

Down going shear first breaks were then picked from the in-line traces after subtracting the down going compressional waves. These picked shear wave times were then used as input to a median filtering process applied to separate and isolate the reflected shear events. Since the shear events are not as clear and coherent as the compressional events, the picks are much less reliable. For this reason, a

much lighter median filter was used to separate the down-going shear events than was used for the compressional events.

Results of these two passes of median filtering are shown in Figure 5.6. Both down going compressional and shear events have been filtered.

Figure 5.6 primarily shows the reflected up-going compressional waves on the vertical components (top row), and the reflected up-going shear waves on the horizontal components (middle and bottom rows). One exception to this is the vertical component from SP 3 which s hows significant reflected shear events at the shallower depths. Additional median filtering based on picked times of shear reflections would be required to isolate the up-going compressional events on data from SP 3.

This process also brought out scattered events not moving at the apparent compressional or shear velocities. One interesting feature is the persistence of events with near horizontal moveout (slope of the events) after separating out the down going compressional and shear waves. Figure 5.7 highlights two of these events, one on data from SP 3 and the other from SP 4.

As discussed extensively under Tasks 2 and 3, such events can be generated by vertical contacts such as faults. Detailed 3D modeling will be required to qualify and interpret these events. This modeling will be undertaken as part of Task 6: Final Modeling and Acquisition Design.

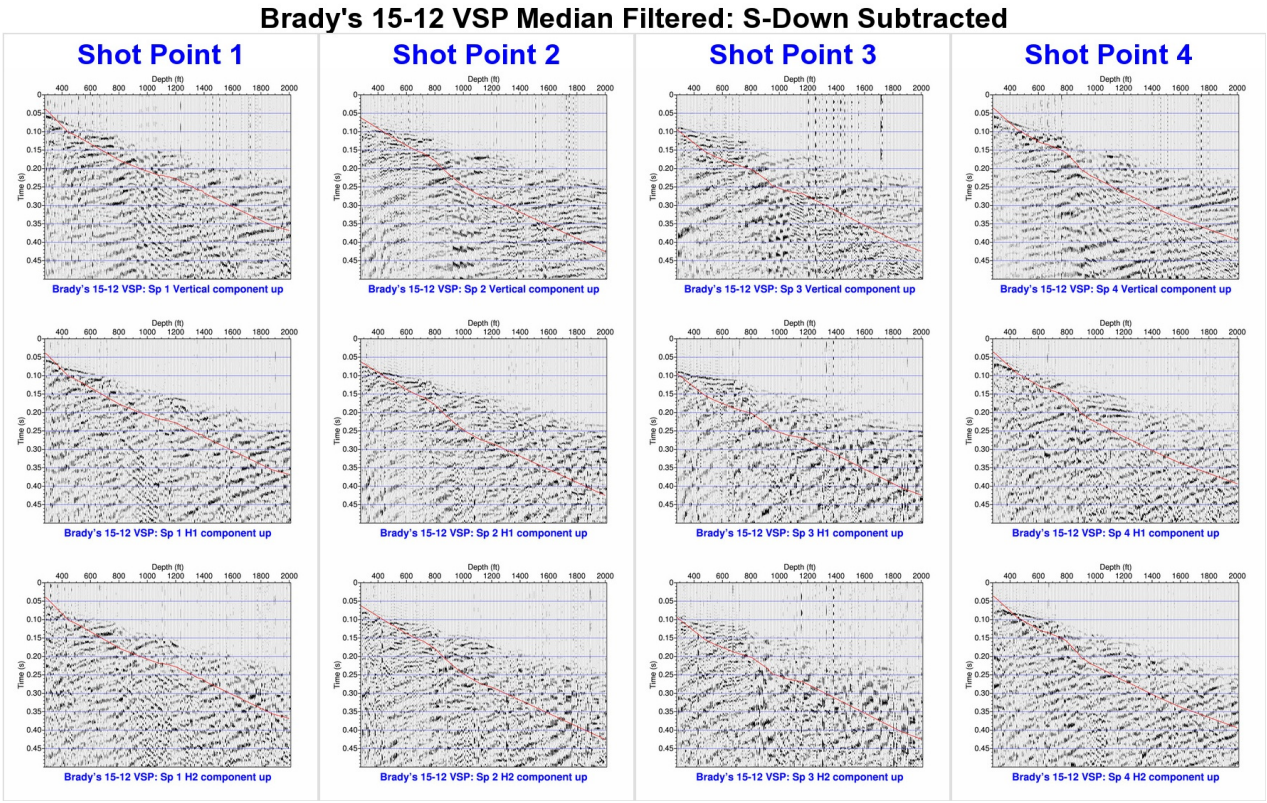

Figure 5.6: "Up" going traces after subtracting P-down and S-down median filtered traces. Reflected compressional waves are visible on the vertical component traces (top row). Reflected shear waves are on the in-line (middle row) and cross-line (bottom row) traces. Note the nearly horizontal event visible at approximately 0.2 s between depths of ~900' – 1300' on the SP 4 in-line traces (last column, middle row).

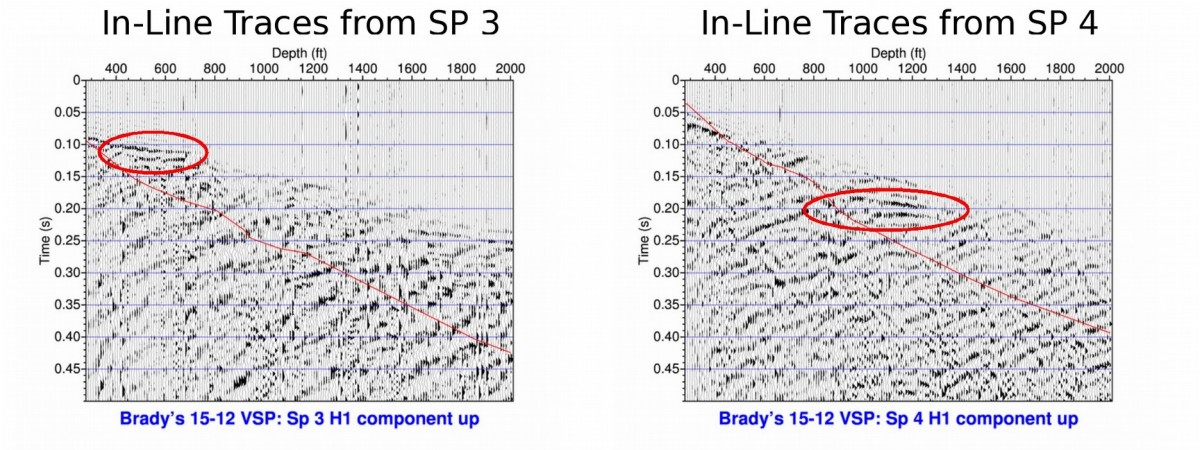

Figure 5.7: In-line traces from SP 3 (left) and SP 4 (right) after median filtering. Note the events circled in red with near horizontal moveout. Such events can be caused by fault scattering.

Corridor Stacks

To produce corridor stacks, the up-going P-data from all four shot points was flattened using a two way time correction based on down-going P-wave first break picks. Then a top and bottom mutes were applied using these same picks. For the deepest traces, no bottom mute was applied. Following this, the traces were stacked. A datum shift correcting the data to a datum of 1400 m above mean sea level (AMSL) was then applied to allow comparison to the surface reflection data.

Figure 5.8 shows the corridor stack results for all four shot points. Comparison of these results to Line 1 of the surface reflection data is shown in Figure 4.14.

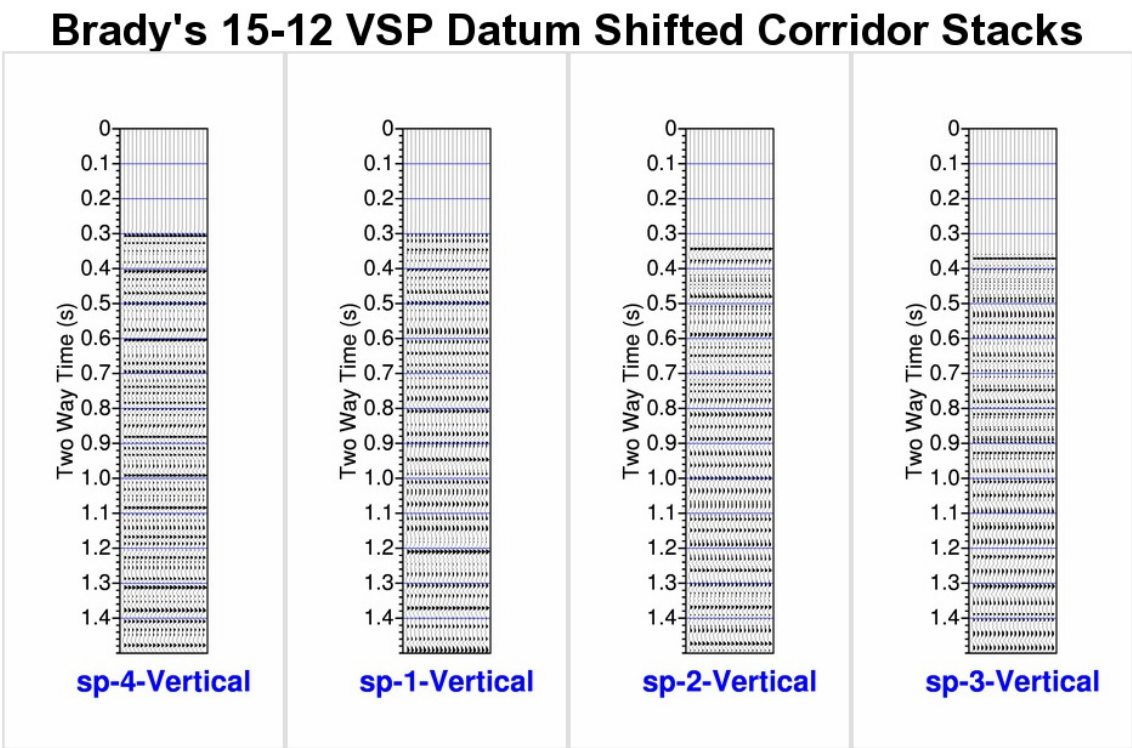

Figure 5.8: Corridor stack for all four shot points after datum correction to 1400 m AMSL.

Interval Velocities

One of the major objectives for the near offset VSP was to provide interval velocity estimates for use in processing of the surface seismic data acquired in Task 4. Compressional wave first breaks were picked for the first arrivals shown on the median filtered P-down going waveforms for each shot point. These arrival times were then used as input to a process giving interval velocity estimates for each shot point. These estimates are based on a straight ray approximation.

Figure 5.9 shows some of these interval velocity results. These are estimates derived using an interval of approximately 100'.

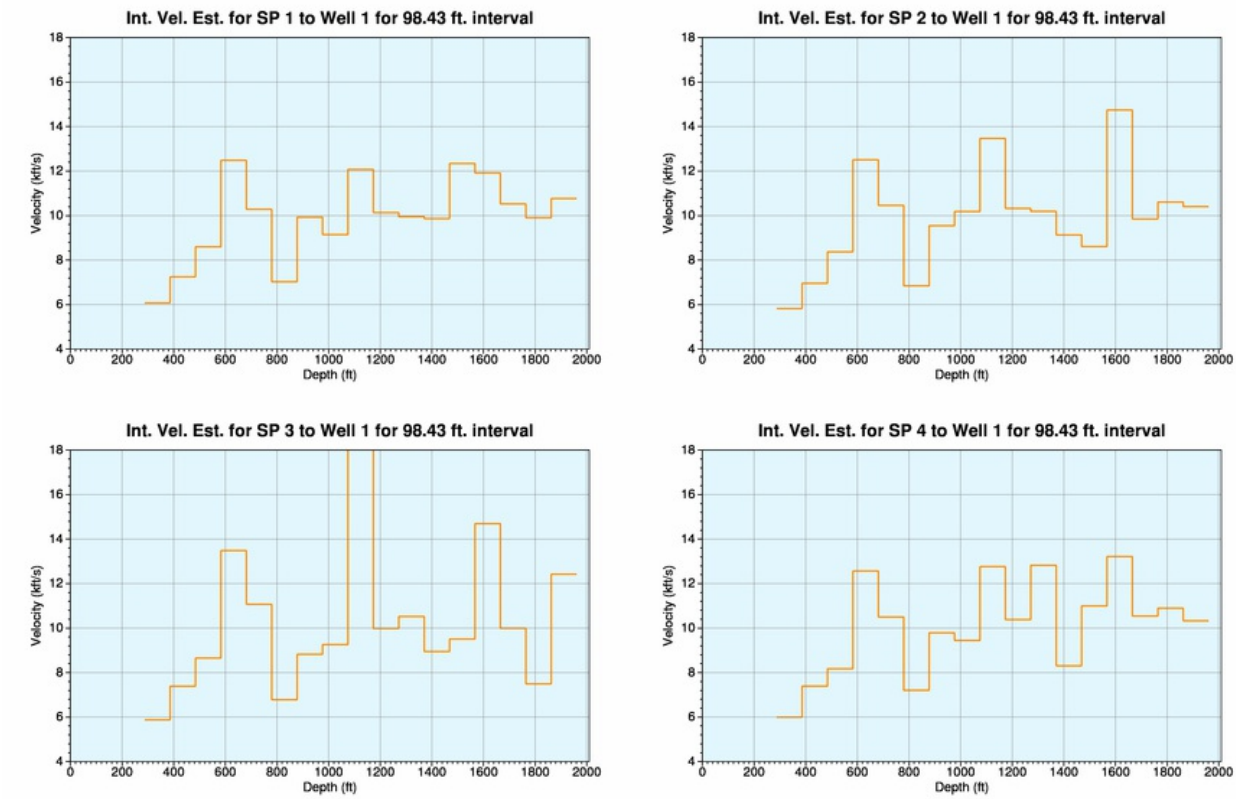

Figure 5.9: Compressional wave interval velocity estimates derived using an interval of approximately 100'.

One of the interesting features of these results is the velocity inversion occurring at a depth of approximately 800' below the top of the 15-12 well. Velocities are seen to drop from a value of approximately 13,000 f/s at a depth of 700' to 7,000 f/s at a depth of 800'. This inversion is consistent on estimates from all four shot points, and is actually visible in the raw VSP data shown in Figure 5.5. Such inversions are problematic for processing of surface reflection data.

Many of the features seen in Figure 5.9 are consistent from shot point to shot point. However, there are some interesting differences. Velocity is seen to increase with offset between shot points 1 through 3. The velocity structure shown at shot points 1 and 4 is very similar down to a depth of 1200'. Below this depth they begin to differ. These two shot points have nearly the same offset, but have almost orthogonal azimuths.

These differences may be due to limitations associated with the straight ray approximation. They may also be related to heterogeneities or anisotropy. More sophisticated modeling will be required to understand these differences.

A more sophisticated approach was to invert the picked down-going travel times from all four shot points to a 1D (layered) model using a ray bending method (Nowack, 1992). Both compressional and shear down-going first breaks were used as input to an eikonal equation inversion. Outputs of this

inversion process are 1D compressional and shear wave velocity models honoring all first break picks from the four offsets. Figure 5.10 shows the resulting interval velocity structure.

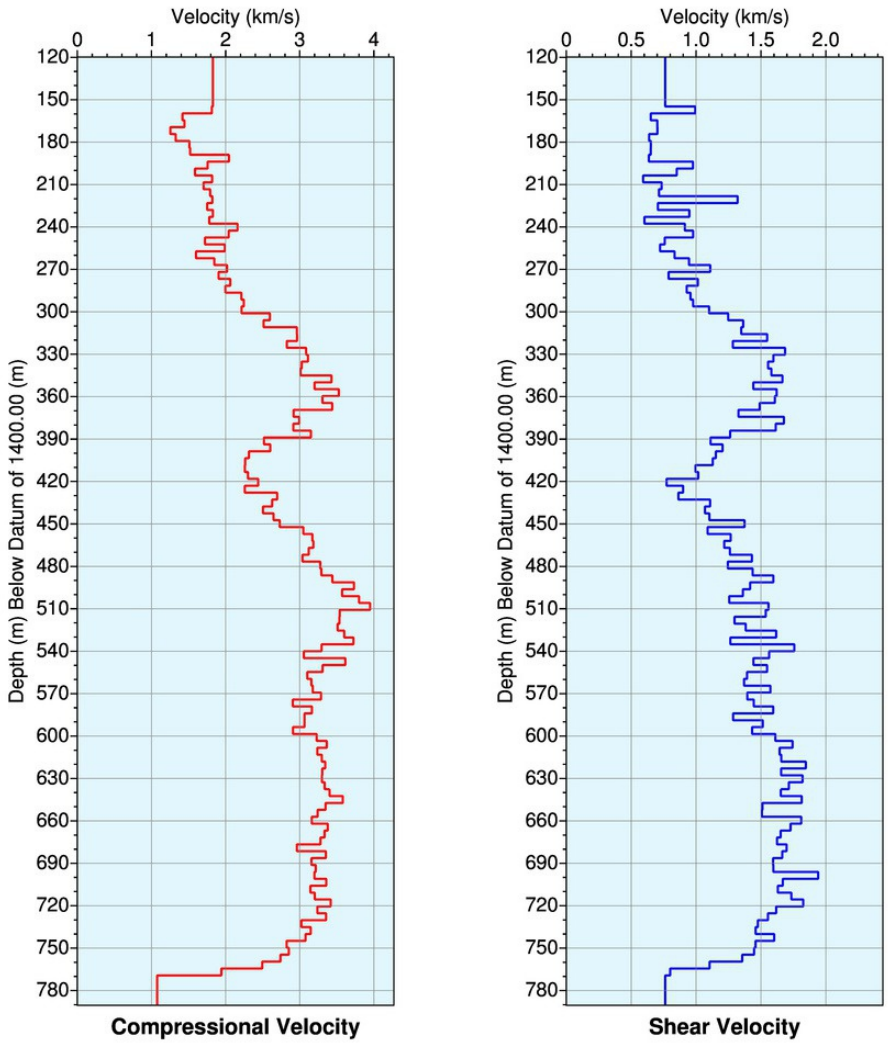

Figure 5.10: Well 15-12 VSP compressional and shear velocities inverted from down-going first break picks from all 4 shot points.

This 1D velocity model will be integrated into the 3D model to be developed as part of Task 6.

Task 6: Final Modeling and Acquisition Design

Proposed Objectives

Ongoing with tasks 4 and 5, results of the surface orientation and near offset VSP will be integrated into the existing geophysical model. Several more simulations will be performed. Based on the results of these simulations, the acquisition plan for the full areal coverage seismic acquisition will be

modified, and a final full areal coverage acquisition plan will be developed.

Accomplishments

Permitting

Due to problems and delays encountered with the permitting process during Phase II, we moved ahead with a preliminary design for Phase III data acquisition. Based on experiences gained during Task 4, this acquisition plan was extensive. It was also flexible enough to be adapted to meet the needs identified by the final modeling and data acquisition design coming out of the efforts of this task.

Figure 6.1 shows the planned layout of the Phase III acquisition program submitted for permitting. From a permitting point of view, it was an extension of the Phase II program. Several new source and receiver lines were added. New source lines are shown in green, and new receiver lines shown in red. After approval, these source and receiver locations formed the basis for developing the actual Phase III program to be implemented in the field based on processing, modeling, and interpretation results from Phase II.

This plan was submitted to the Bureau of Land Management (BLM) as an extension of the Notice of Intent (NOI) approved for Phase II. All required permits for both Task 7 and Task 8 were approved. NEPA clearance for Phase III was also received

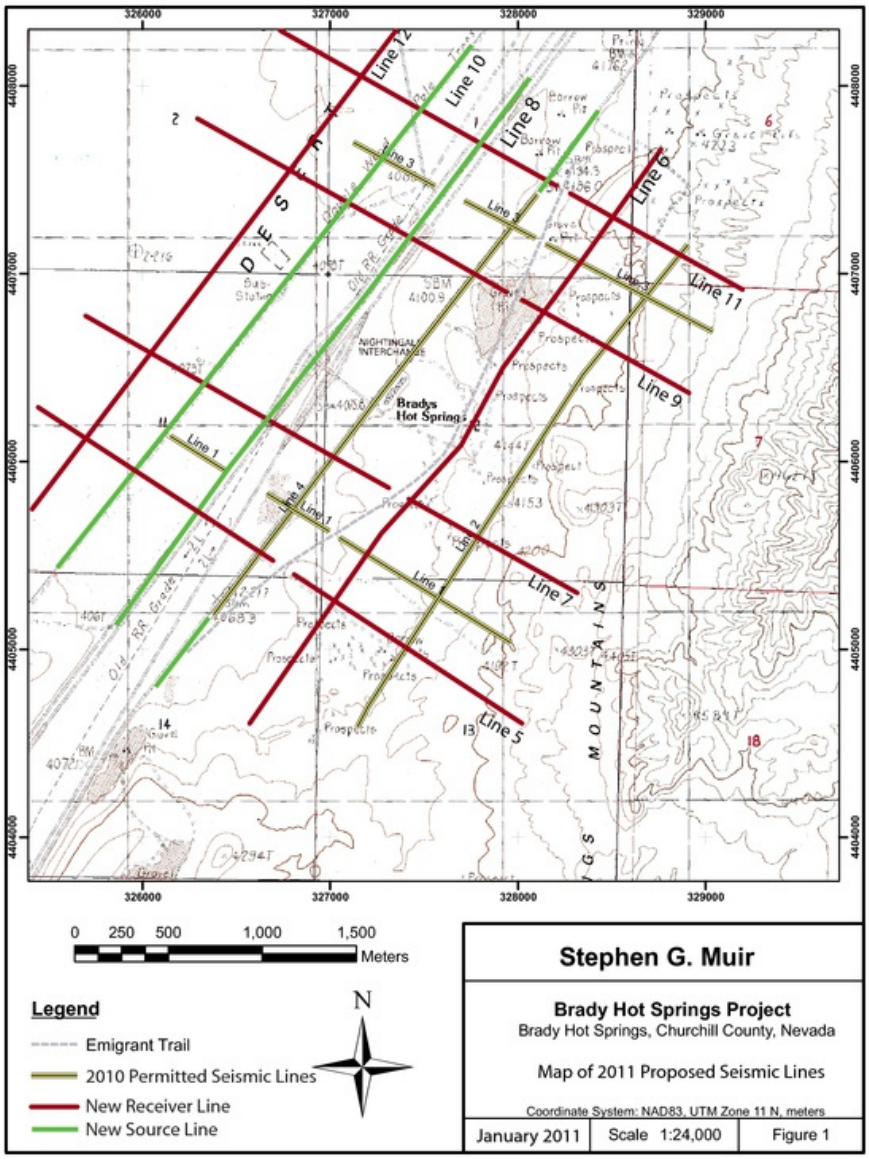

Figure 6.1: Planned layout of source and receiver lines for Phase III acquisition submitted for permitting. This acquisition plan is extensive. It is flexible enough to be adapted to meet the needs identified by the final modeling and data acquisition design coming out of the efforts of this task.

Surface Seismic Interpretation

Seismic interpretation was conducted in collaboration with Prof. James Faulds of the University of Nevada, Reno (UNR) and Nevada Bureau of Mines and Geology (NBMG). As described under Task 4, seismic prestack time migrated data from Task 4 were loaded into a seismic interpretation workstation. This provided for georeferenced picking of fault locations and seismic horizons. Faults were picked, and then adjusted after integrating Prof. Faulds' surface geological mapping results. Horizons were

then picked based on the character of reflection events between faults. Horizons were adjusted after consulting core and cuttings analysis results from several nearby wells, and comparison to the gravity results discussed previously.

Figure 6.2 shows the interpreted data from Line 1, which passes close to the 15-12 well. The final interpreted faults and horizons are shown in black. Lithological boundaries are primarily based on core and well cuttings analysis. Locations of many of these faults were known from where they cut through core in the nearby BCH-3 well and from surface mapping.

It can be seen that many of these boundaries do correspond to reflection events in the seismic data. In these cases, the reflectors were influential in determining the shape of the boundaries away from the wells, coupled with knowledge of the overall structural style in the area. One anomaly is the bright reflector just left and below center. No major changes in lithology were apparent at the location of this reflector in the well data, and it is not well understood. One shortcoming of this particular seismic line is the lack of long offsets. Long offsets are really needed to properly image such deeper reflectors. The planned acquisition for Phase III will include significantly longer offsets for this line.

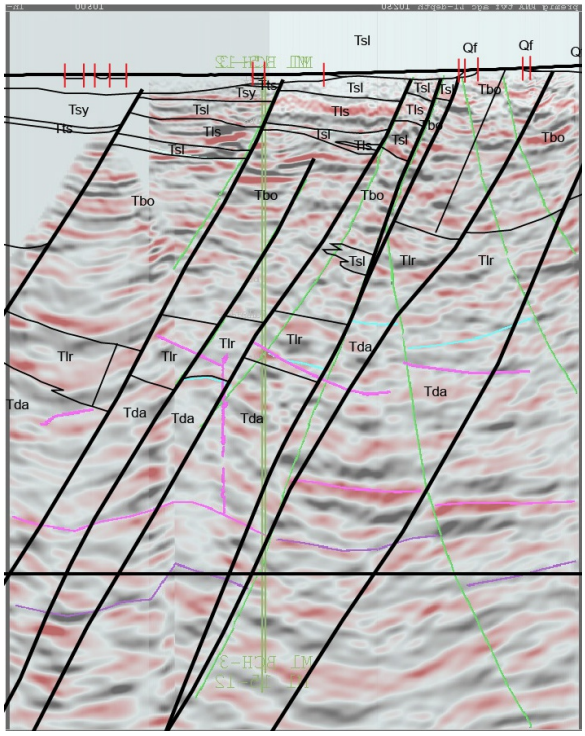

Figure 6.2: Interpretation of Line 1. This view is looking to the North East. Five of the interpreted faults which cut the 15-12 well (faint near vertical green line near center of the plot) were known from core from the nearby BCH-3 well.

Figure 6.3 shows the interpretation for Line 3. This line is a dip line passing near the most productive wells in the field. Again, lithological boundaries are primarily based on core and well cuttings analysis. As with Line 1 (Figure 6.2), many of the lithological boundaries correspond to reflection events in the seismic data. Again, a number of bright reflectors are anomalous in that they do not correspond to

lithological boundaries. A number of these reflectors show dips that are counter to what is expected based on assumptions of structural style. These reflectors are not understood. This line is significantly longer than Line 1, and included offsets in excess of 5000'.

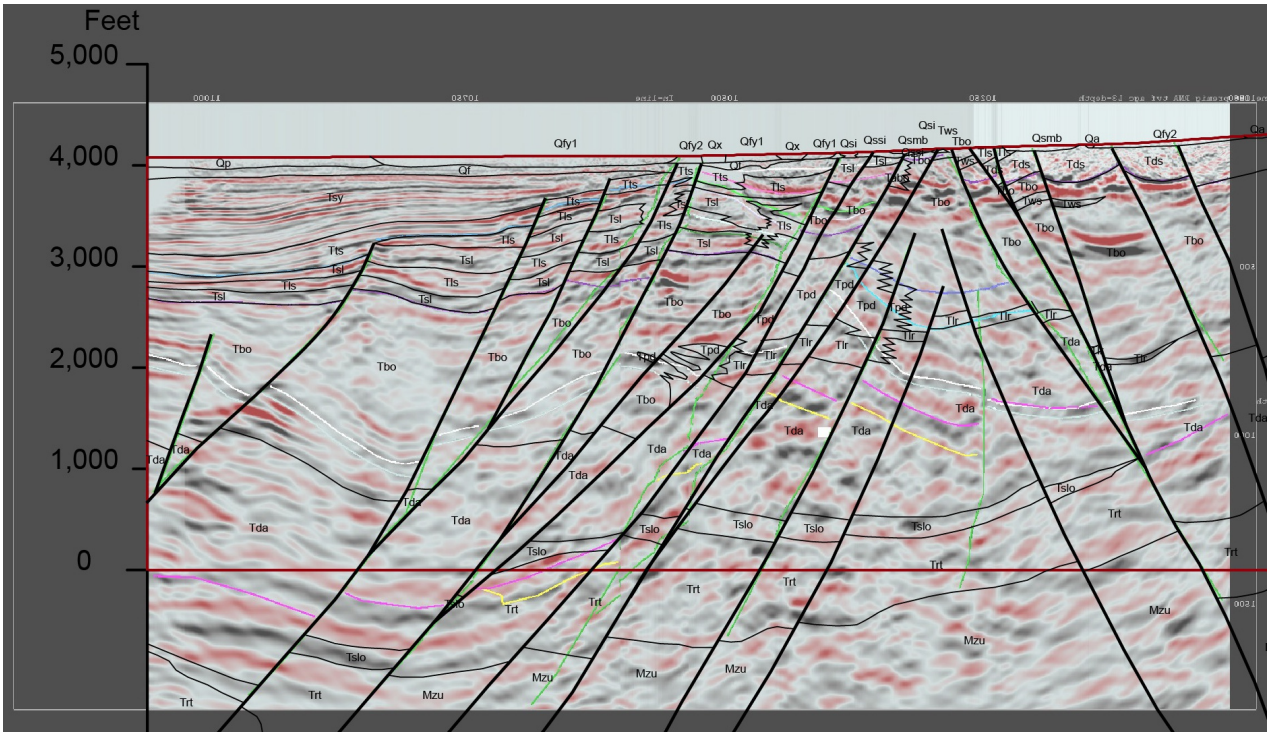

Figure 6.3: Interpretation of Line 3. This view is looking to the North East.

In conclusion, the seismic results were found to be useful in characterizing the subsurface geological interpretation over the Brady's Hot Springs field. However, a number of reflectors are anomalous. It is hoped that the increased coverage planned for Phase III will shed some light on these anomalies.

Geophysical Model Building and Seismic Simulation

In support of acquisition design and interpretation, seismic simulations were run using models of the Brady's Hot Springs KGRA. Two generations of 3D isotropic models of seismic velocities and densities were developed. The first generation of seismic models was based on simple geological models from 2009 with sub-horizontal lithological beds and a few near vertical faults. These models are discussed under Task 2. After the completion of Phase II reflection data interpretation, the second more sophisticated generation of models were formulated.

Interpretations of depth converted surface seismic reflection profiles from lines 1, 3, and 4 (discussed above) were integrated with well cuttings and core analysis, available well logs, surface mapping of faults and other geological features, and gravity data to produce a geological model. Cross sections from this geological model were then used to build a 3D isotropic geophysical model of the area around the Brady's 15-12 well. Velocities in this model were based on interval velocities inferred from processing generated stacking velocities, augmented by typical values for the given lithologies. The

VSP derived velocity estimates reported in in Task 5 were used for those units penetrated by the Near Offset VSP. Densities were also chosen from typical values. A view of one such 3D model is shown in Figure 6.4.

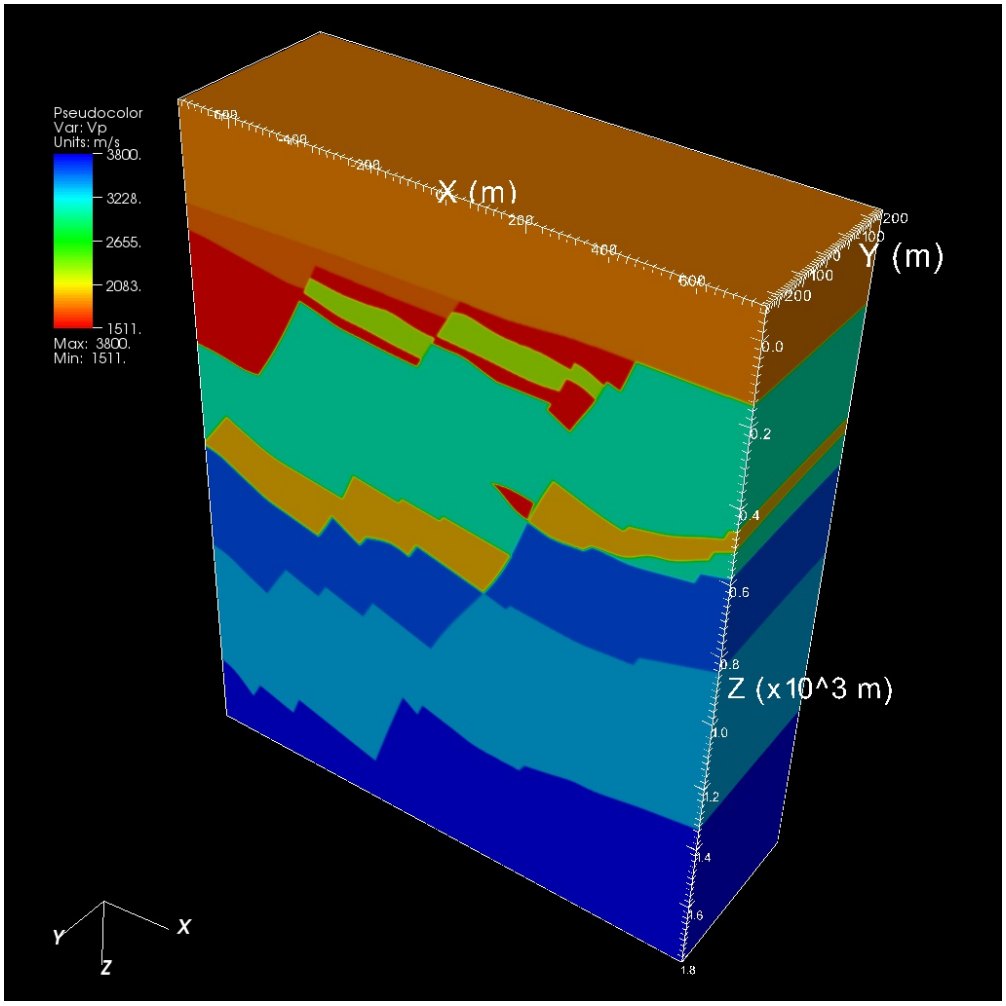

Figure 6.4: View of the 3D geophysical model from around the vicinity of the Brady's 15-12 well. Colors represent the compressional wave velocities. The horizontal location of the 15-12 well is near the center of the model.

In Figure 6.4, colors represent the compressional wave velocities. The top layer has the datum velocity used in processing the surface reflection seismic data (1830 m/s). Vertical coordinate Z=0 m is at the processing datum elevation of 1400 m above mean sea level (AMSL). The base of the first layer is at ground level. Horizontal X coordinates run from -750 m to 750 m. The Y coordinates start at -250.5 m and end at 250.5 m.

Simulations of surface reflection seismic and VSP were run. The surface location of the simulated Brady's 15-12 VSP well is near the center of the model. The surface location of the simulated well is

obscured by the datum layer in the model figure.

Simulated seismic traces were calculated using the isotropic 3D finite difference staggered grid algorithm discussed under Task 2. A grid spacing of 1.5 m and a time step of 0.0001 s were used in the simulations. The seismic wavelet was a Ricker wavelet with a peak frequency of 35 Hz. There were 1001 grid nodes in the X direction, 335 in the Y direction, and 1251 in the Z direction for the model in the figure.

A simpler variation of the model in Figure 6.4 was also constructed. This model only contained one major fault. Its purpose was to demonstrate the types of events scattered from an individual fault. In all cases, faults were simply modeled by the velocity contrast in offset beds. Features such as fault gouge and damage zones were not included as they were in the modeling of Gritto and Majer (2003).

Simplified Geophysical Model Results

Figure 6.5 shows the results of simulations over the simplified 3D model. This model only contains one fault, and has horizontal beds. Figures 6.5(A-D) show 2D XZ plane slices of vertical motion wave field snapshots at four different times, 0.30 s, 0.50 s, 0.55 s, and 0.75 s respectively. Wave field amplitudes are shown in gray scale.

The wave field snapshots are overlain on a color coded 2D slice of the compressional wave velocity grid. Model and snapshots were sliced at the source and geophone Y coordinate of -0.5 m, near the center of the 3D model. The vertical dark purple line shows the location of simulated VSP receivers, and is at the location of the Brady's 15-12 well relative to the geological model. The two magenta horizontal lines at depths of approximately 257 m and 775 m below datum bracket the depth intervals covered by the actual VSP measurements of Task 7 (not yet discussed). The yellow circle represents the simulated vertical force source location with horizontal offset of 46.5 m from the well. The cyan colored horizontal line gives the location of the simulated 2D surface reflection seismic array.

The events circled in yellow on the wave field snapshots are near surface waves trapped in the low to high to low near surface velocity layers. They move horizontally to the right across the model with time, until they reach offset beds of the near surface fault. There they begin to scatter, with scattered energy moving back in the opposite direction. Figure 6.5E shows the simulated vertical geophone surface seismic common source gather plotted with trace spacings and offsets typical of the actual field acquisition of the surface seismic data. The back scattered near surface waves are circled in yellow. They are a dominant feature of the simulated common source gather.

The wave field circled in magenta in Figure 6.5A shows the down going direct compressional wave impinging on the offset beds of the major fault in the model (vertical fault offset of approximately 250 m). The wave field circled in magenta in Figure 6.5B at time of 0.50 s shows the compressional wave scattered from this fault as it crosses the VSP array at depths of approximately 650 m to 730 m. It is just barely discernible and suffers from strong interference from down going multiples and other scattered events. Figure 6.5F shows the simulated vertical VSP traces plotted with the same depths and spacings as the actual Task 7 field data. The events circled in magenta are at the same time and depths as the magenta area circled in Figure 6.5B.

The wave field circled in green in Figure 6.5C is the direct down going shear wave as it encounters the offset beds of the fault. The area circled in green in Figure 6.5D shows the scattered wave field generated by this encounter as it crosses the VSP array. In contrast to the wave field circled in Figure

6.5B (scattered from the down-going compressional wave), this wave field is quite strong and is relatively free of interference. The event underlined in green in the simulated VSP (Figure 5.6F) is at the same time and depths as the green circled area in Figure 5.6D.

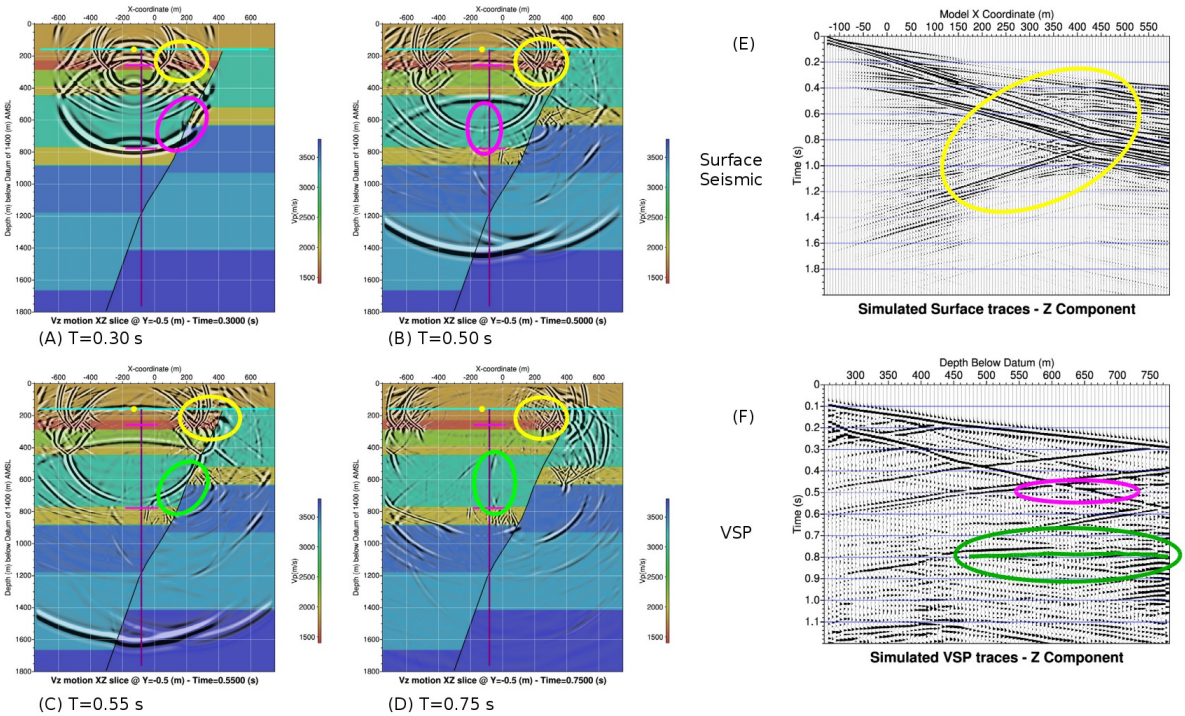

Figure 6.5: Simulation results from the simple geophysical model with one major fault and horizontal beds.

As with the modeling and simulations discussed under Task 2, the dominant affect of the faulting on the surface seismic data is to generate slow apparent velocity back scattered events coming from the near surface faulting (Figure 6.5E). Sub horizontal events in the VSP with apparent velocities higher than the compressional waves remains as one of the key signatures of fault scattered events (Figure 6.5F).

Complex Geophysical Model Results

Figure 6.6 shows similar results from the complex geophysical model of Figure 6.4. Arrival times of the various waves differ from Figure 6.5 because of the slightly different velocity structure. Again, the back scattered near surface trapped waves circled in yellow are seen to dominate the surface reflection common shot gather. The scattered wave field from the down going compressional wave is slightly less visible in Figure 6.6B. It still suffers from interference from multiples as well as the down going direct shear wave. The wave field scattered by the fault from the down going shear wave (Figure 6.6D, circled in green) is seen to be clear, though somewhat different in character from that shown in Figure 6.5D. There is also a strong corresponding event underlined in green in the simulated VSP of Figure 6.6F.

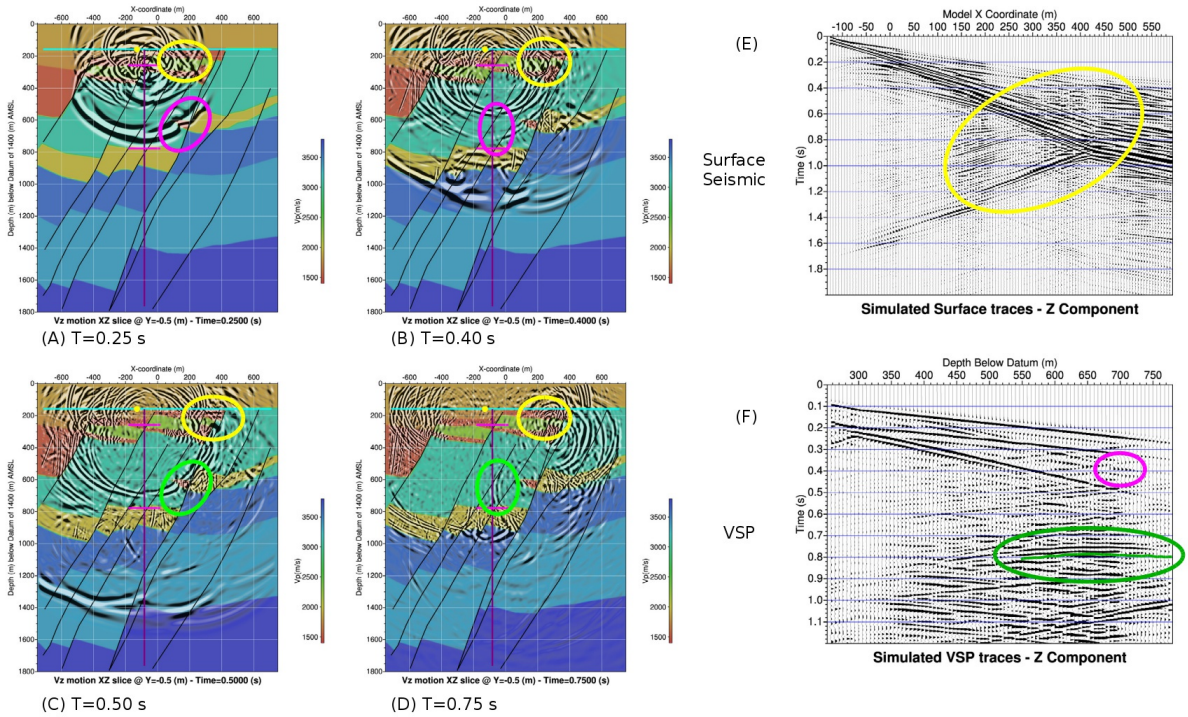

Figure 6.6: Simulation results from the complex geophysical model of Figure 6.4.

These results support the interpretation that a number of events with near horizontal moveout observed in the VSP data are reflections from faults in the vicinity of the 15-12 well. As such, the amplitude and frequency content of these events may carry information about the specific stiffness of the Brady's Fault at these depths. It has been widely suggested in the literature (e. g., Pyrak-Nolte and Morris, 2000, Zhu and Snieder, 2002) that specific stiffness can be related to fluid flow properties of fractures and faults.

Acquisition Design

Multi Offset VSP Design

The primary parameters to be determined in designing the Task 7 Multi Offset VSP are geophone spacings, record time, type of geophone string, source type, and selection of source points. One advantage is previous experience in the 15-12 well during Task 5 Near Offset VSP acquisition.

One setback in the previous VSP acquisition (Task 5) was the lack of a shear wave source. For Task 7 use of a vibrator source capable of both P and S motion without major modification in the field has been arranged.

Anomalous hodograms seen in the near offset VSP data were discussed under Task 5. The clamping mechanism for the geophone string used in Task 5 was less than ideal, and may be related to a lack of vector fidelity leading to the hodogram problem. An additional concern with that geophone string was

the relatively low temperature tolerance. For Task 7, LBNL intends to deploy a new high temperature fiber optic geophone string that they are currently developing. This new string should allow for recording at deeper depths than were reached during Task 5. It is planned to record down to the bottom of casing at 2883' below surface (see Figure 6.7). Based on results from Task 5, it is clear that a geophone spacing of 10' was advantageous. That spacing will be used again if at all possible.

As shown by the modeling above, many of the high amplitude events reflected from faulting around the 15-12 well travel through lower velocity formations. Some events may arrive later than the 2 s record time used in Task 5. For that reason, 4 s record times are planned for Task 7.

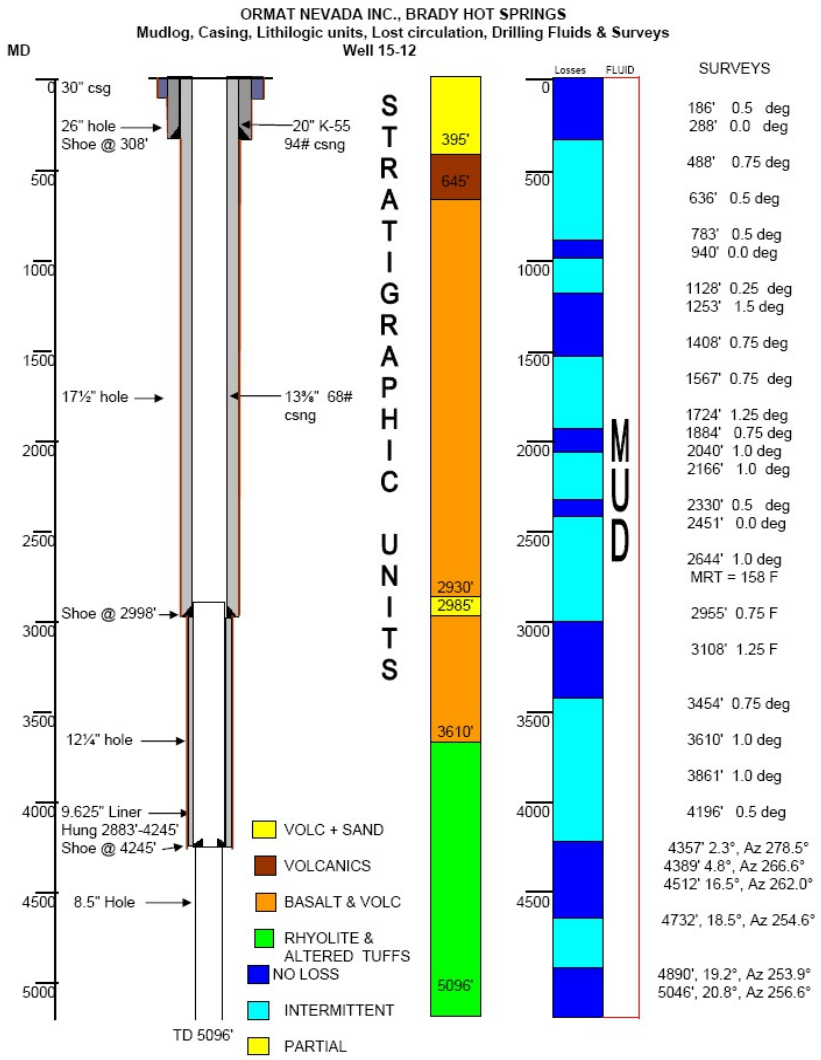

Figure 6.7: 15-12 Well completion plan. Data will be recorded from bottom of casing at 2883'.

Figure 6.8 shows the planned layout of the source points to be used in the Task 7 Multi Offset VSP. Approximately 70 shot points with offsets out to approximately 1 km are planned. This represents a significant increase in effort over the 4 shot points used in the Task 5 Near Offset VSP.

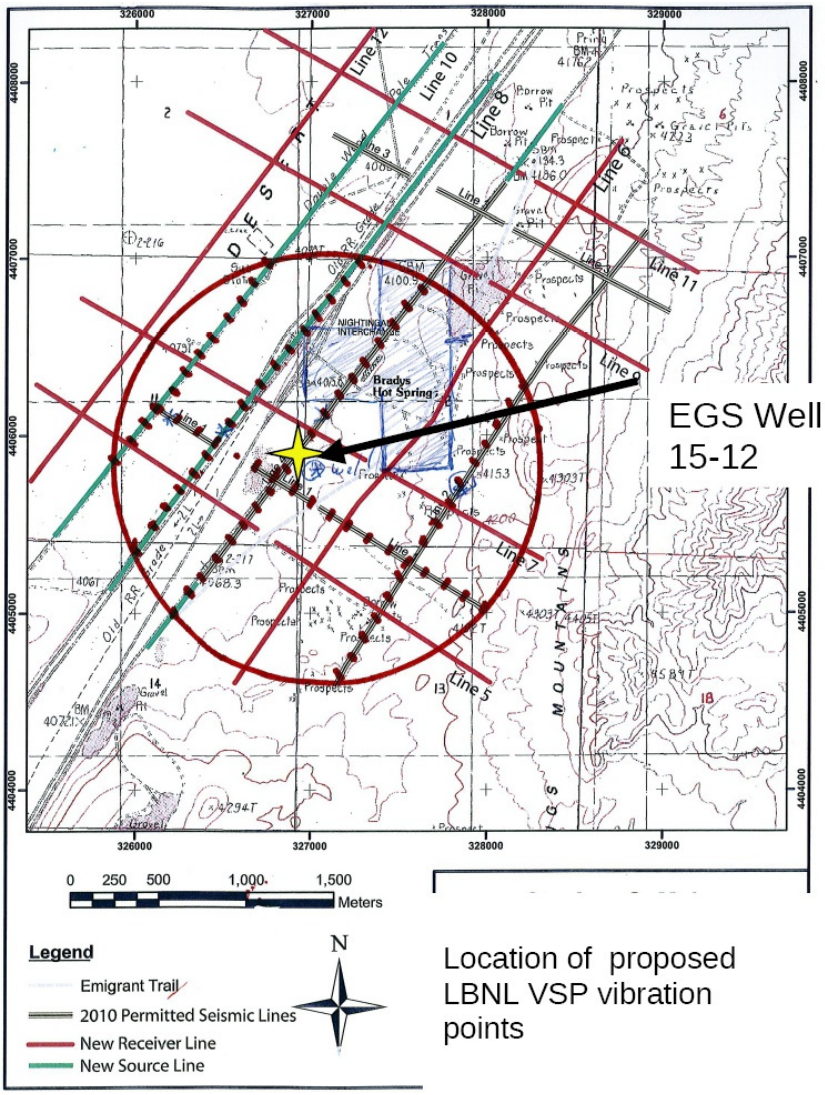

Figure 6.8: Planned Task 7 Multi Offset VSP source point locations.

High Areal Coverage Surface Seismic Design

High Areal Coverage Surface Seismic acquisition (Task 8) will greatly expand on the three seismic lines acquired under Task 4. Additional source and receiver lines have been permitted, and a series of near orthogonal swath lines are planned. Source and geophone spacings of 20' will again be used. Conventional vertical geophones will be used as receivers. Sourcing will be accomplished with a Bolt land air gun as with Task 4. Line lengths will be extended over those used in Task 4, with additional coverage North West of I-80. Only vertical geophones will be used. This is due to the disappointing results with mulitcomponent geophones in Task 4.

A recording system with up to 360 channels will be used, in contrast to the 240 channels used in Task

4. This will allow significantly farther offsets to be used than were recorded in Task 4. A total of approximately 15 line miles of data are planned. At the much finer source and geophone spacings planned, this is equivalent to nearly 75 line miles of conventional seismic data.

Figure 6.9 shows the planned layout of the seismic lines.

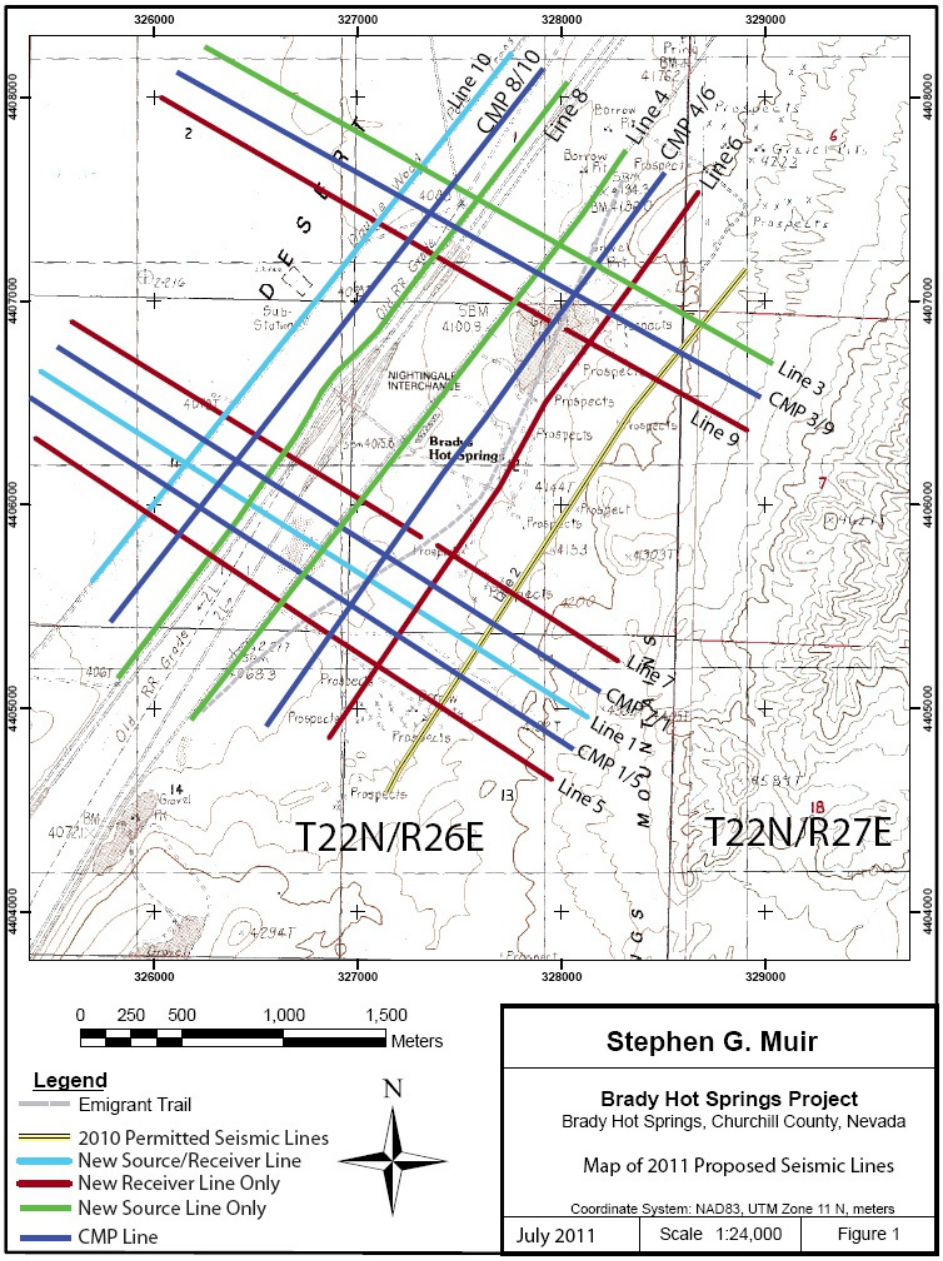

Figure 6.9: Planned layout of the standard and swath reflection seismic lines to be used in the Task 8 High Areal Coverage Seismic acquisition.

In Figure 6.9, as planned, Lines 5, 7, 8, and 9 will be acquired as swath lines. This means that, for

example for Line 5, sources will be applied along Line 1 recording to geophones along Line 5. Image point coverage will be at the midpoints between Line 1 and Line 5, and are shown as CMP Line 1/5 in Figure 6.9. Swath coverage has the advantage of not requiring extensive permitting of source lines. Archeological and cultural considerations were a limiting factor in permitting source lines. Remaining lines will be acquired as standard 2D CMP reflection lines. While 10 lines were originally envisioned, Line 2 (not labeled in Figure 6.9) was dropped from the acquisition plan due to access problems.

Line 1, which was acquired under Task 4, will be re-acquired. It will be extended significantly to the northwest.

Phase III

Task 7: Multi Offset VSP

Proposed Objectives

An extensive VSP survey will be acquired over the Brady's Hot Springs geothermal area using multiple source locations. These source locations will be selected on the basis of the Budget Period II Task 6 acquisition design plan. These data will then be processed using VSP migration imaging algorithms, giving a limited 3D image of the area around the well. These data will also be analyzed for fracture scattering events. Detected events will then be subjected to time-frequency analysis. VSP images will then be interpreted for structure. Fracture scattering events will be interpreted in the context of displacement discontinuity discrete fracture models. With their expertise in deploying VSP tools in high temperature environments, their facilities and experience with VSP migration imaging, and their deep understanding of discrete fracture models, it is anticipated that Lawrence Berkeley National Laboratory (a FFRDC) is uniquely qualified to aid Hi-Q Geophysical Inc. in these tasks.

Accomplishments

Completion of this task was delayed by several years. This led to numerous requests and approvals for no cost extensions of the project.

This task was primarily conducted by Major Participant Lawrence Berkeley National Laboratory (LBNL). One of the major reasons for delays in this task was that LBNL did not receive any of the funding for this task from DOE for several years. Under the FOA under which this project was conducted, negotiation and funding of FFRDC components of the project are the responsibility of DOE. Until that funding was received, it was difficult to proceed with this task. Funding was finally received and work on the task moved forward.

There were several other causes for these delays. LBNL was working with a company to develop a high temperature fiber optic VSP sensor string. This sensor string offered several advantages over conventional VSP strings available from industry contractors. It had a much higher temperature rating. It was extremely sensitive. It had a locking arm clamping mechanism as opposed to the magnetic clamps offered by many contractors. Unfortunately, the company developing and building this string missed many of LBNL's delivery dates. After several years of delays, the string was finally delivered to LBNL. It was used in the acquisition for Task 7.

As delivery of the high temperature fiber optic string drug on, as an alternative, Ernie Majer of LBNL

had successfully designed, planned and contracted all the necessary elements for the Task 7 Multi Offset VSP using industry contractors for the VSP string. Acquisition was scheduled to begin in early July 2013. Unfortunately, due to confusion between Ormat and DOE, acquisition was delayed at the last moment beyond dates when critical equipment was available.

Once the Multi Offset VSP data were acquired, there were additional delays with processing. Final processed results were passed on to Hi-Q Geophysical Inc. on January 8, 2016, three weeks before the end date of the project. This left very little time to integrate these results into the overall Final Interpretation (Task 9).

VSP Data Acquisition

Due to increasing costs, the planned VSP data acquisition plan shown in Figure 6.8 was revised. The revised planned layout is shown in Figure 7.1.

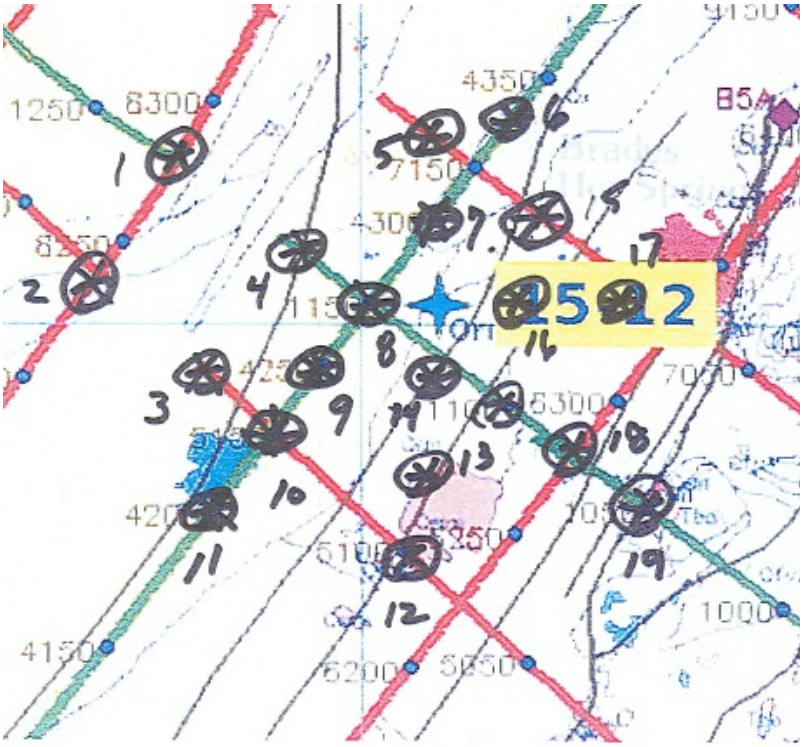

Figure 7.1: Plan view of the revised Multi Offset VSP acquisition plan. Shot points shown as circled black stars, and the VSP well (15-12) is the blue star in the middle. These are approximate points which may be shifted up to 100 feet due to permitting related biological constraints of nesting birds.

The number of source points was reduced from the originally planned 70 to 19. In addition, permitting conditions required that a biological survey be conducted to identify nesting bird locations. Source points might be shifted to honor those constraints.

Vertical seismic profile acquisition utilizes surface sources and borehole sensors. The high temperatures encountered in geothermal wells are a fundamental challenge for acquiring VSP data.

They are typically too high for conventional borehole seismic sensors. To address the high temperature issue, a novel fiber optic accelerometer array fabricated by US Sensors Inc. (USSI) was used in the Brady's 15-12 VSP. The sondes in this array were designed to have an operating temperature rating of 200º C, with sensitivity of 1 ng/bit and a frequency range of 3 – 600 Hz. They were clamping wireline deployed units each containing one vertical and two orthogonal horizontal fiber optic accelerometers. The array used in the Brady's 15-12 VSP had 36 sondes spaced at 20 ft. The array was set at three different depths, spanning intervals of 300 – 1000 ft., 1000 – 1700 ft., and 1320 – 2020 ft. relative to the top of the well. Data were acquired by first lowering the array to the shallowest depth, then the intermediate depth, and then the deepest depth. A well bore obstruction was encountered by the bottom sonde at a depth of 2050 ft., preventing acquisition from deeper depths. The well was nearly vertical (deviation less than 0.1 degree) in the depth range covered by the array.

The seismic source was a vibroseis truck, with an unusual triaxial design allowing three components of ground forcing: vertical (P); horizontal-longitudinal (SL); and horizontal-transverse (ST). The horizontal orientations were in-line (SL) and transverse (ST) to the azimuth connecting the source location and the 15-12 well. The vibroseis source used a linear sweep of 8 – 80 Hz, 12 s length with a 0.5 s taper on each end. The specified force output in the vertical mode is about 267 kN and decreases as frequency decreases below 12 Hz. In the horizontal mode, the force output only decreases with decreasing frequency below 5 Hz. The maximum force output in the horizontal mode is about 133 kN, about one-half of the maximum force output in the vertical mode. The combination of three source components and 3 sensor components is known as a 9-component VSP.

Data were acquired using a USSI recording system. Data were recorded at a sample rate of 0.25 ms, with a record length of 15 s. A total of 10 source locations (each with 3 source orientations) were occupied and 4 source sweeps were recorded at each. Source locations were limited by site access, time and funding constraints. Due to time constraints, the decision was made prior to beginning production acquisition to focus imaging to the north-west, west, and south-west of the well. Figure 7.2 shows the locations of the 10 source points occupied and the Brady's 15-12 sensor well.

Production data were recorded for eight hours on June 26, 2015 and two hours on June 27, 2015. Approximately two to three hours were needed to move the array from one depth level to the next. Including rigging up, testing, production acquisition, and rigging down, approximately six days were spent in the field from June 23 – June 28, 2015.

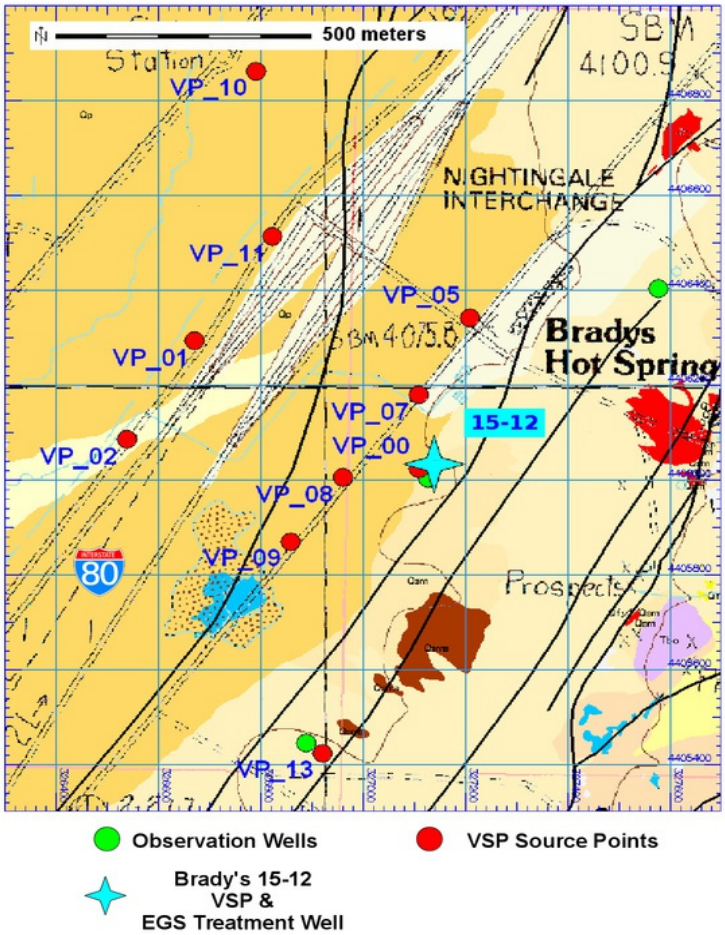

Figure 7.2: Actual VSP source point locations occupied at Brady's Hot Springs, overlain on a map of surface faults and geothermal features from (Faulds et al., 2012; unpublished data). Cultural features such as Interstate 80 cutting diagonally through the study area are also shown.

VSP Processing

The VSP data were processed by Paulsson Inc., an oil and gas industry processor. Initial data processing targeted production of a velocity model for compressional and shear waves and generation of upgoing and downgoing wave fields. The processing flow included: Geometry assignment; bandpass filtering of uncorrelated data with filter corner parameters of 3-5-90-100 Hz; vibroseis correlation with theoretical sweep; bad trace removal and polarity correction of correlated data; stacking for each source location; rotation of horizontal traces into north and east directions; polarity correction of rotated data; F-K filtering for wave field separation; calculation of velocities.

VSP Results

Figure 7.3 shows time vs. depth VSP traces acquired from the vertical vibrator at the near offset (= ~32 m) source point (VP_00 in Figure 7.2). This offset is similar to the offset of the source in the model

simulations discussed under Task 6. Figure 7.3 (A) and 7.3 (B) are the east and north oriented traces after rotation. Depths are plotted relative to datum elevation of 1400 m. Traces have been divergence corrected, and each trace has been normalized with the maximum amplitude set to one. The event highlighted in green on the vertical traces (Figure 7.3C) is at approximately the same time and depths as the event shown in green in the modeling results (Figures 6.5F and 6.6F). This event has an apparent velocity (inverse of the slope of the event) much higher than the apparent velocities of the up and down going compressional and shear waves. It is not apparent on the horizontal east or north oriented traces.

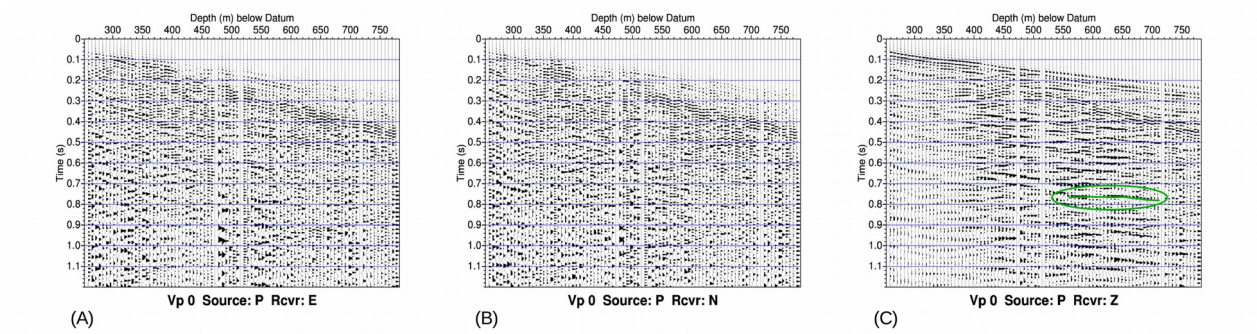

Figure 7.3: Normalized VSP traces from a vertical vibrator at the near offset source point Vp 0. (A) and (B) are the horizontal east and north oriented traces after rotation respectively. The event highlighted in green on (C) (vertical traces) is at approximately the same time and depths as the event shown in green in the modeling results.

Figure 7.4 shows similar trace equalized plots for the traces from the vertical vibrator at source point 8 (offset = ~ 181 m, VP_08 in figure 7.2). This source point is almost due west of the well. East oriented horizontal traces (Figure 7.4A) approximately correspond to the SL direction and north oriented horizontal traces (Figure 7.4B) to the ST direction.

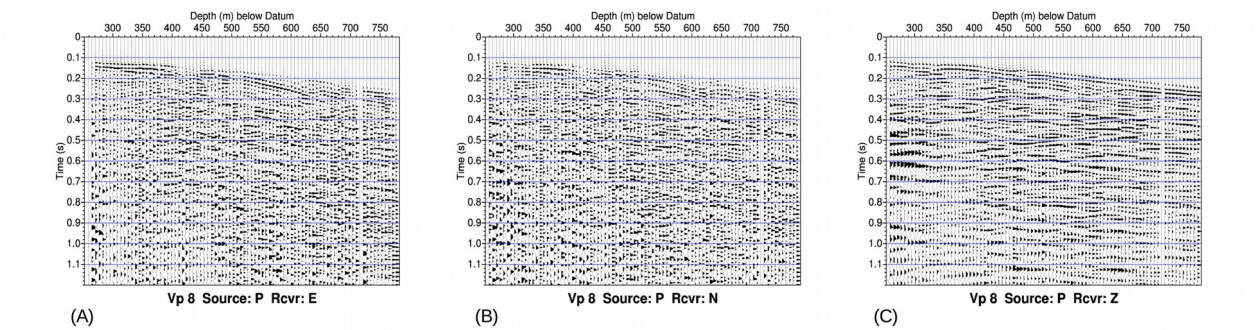

Figure 7.4: Normalized VSP traces from a vertical vibrator at source point Vp 8. (A) and (B) are the horizontal east and north oriented traces after rotation respectively. The source point is almost due west of the receiver array. (C) are vertical traces.

Figure 7.5 shows the full 9-C display of the traces from Vp 8. In this figure, relative trace amplitudes have been preserved. The top row is from the in-line (SL) source, the middle row from the cross-line

(ST) source, and the bottom row from the Vertical source (Z). The left column shows east orientated traces, the middle column north orientated traces, and the left column vertical traces. Since the source is almost due west, these first two columns correspond approximately to SL and ST traces. Depths are plotted relative to datum elevation of 1400 m.

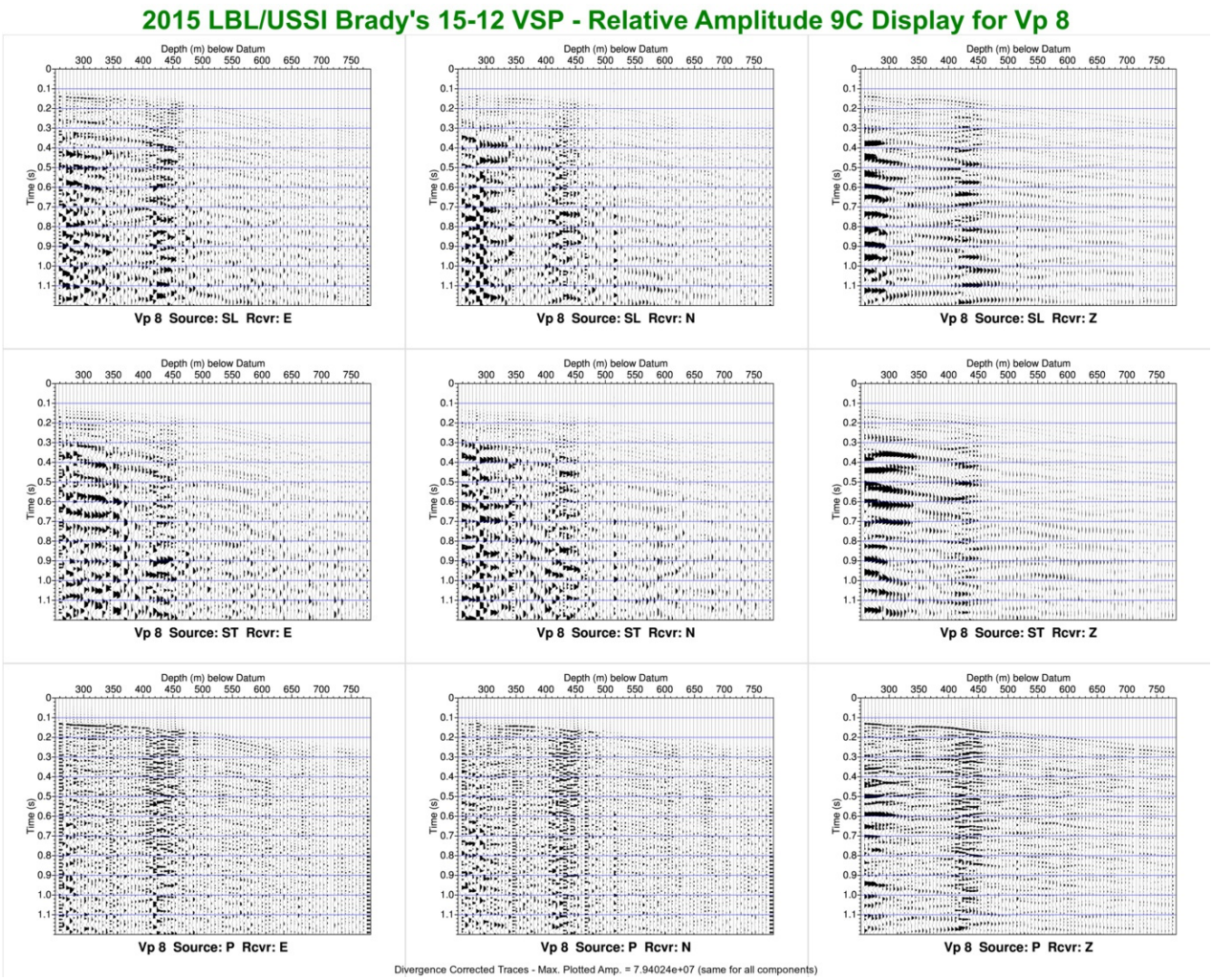

Figure 7.5: Full 9-C display of the traces from Vp 8. Relative trace amplitudes have been preserved. The top row is from the in-line (SL) source, the middle row from the cross-line (ST) source, and the bottom row from the Vertical source (Z). The left column shows east orientated traces, the middle column north orientated traces, and the left column vertical traces. Very few shear events are visible.

Very few, if any, shear wave events are visible in Figure 7.5 for depths greater than 450 m below datum. This is remarkable for the SL and ST source data in particular since these sources usually generate strong down going shear waves. This suggests that the near surface strongly attenuates shear waves in the Brady's area. By comparison, the vertical source to vertical receiver traces (bottom right corner) show strong down-going and reflected up-going compressional waves at all depths, though there is a noticeable decrease in amplitude below 450 m.

Figure 7.6 shows the full 9-C display of the traces from Vp 7. As with Figure 7.5, relative trace amplitudes have been preserved. The top row is from the in-line (SL) source, the middle row from the cross-line (ST) source, and the bottom row from the Vertical source (Z). The left column shows east orientated traces, the middle column north orientated traces, and the left column vertical traces. Figure 7.2 shows that Vp 7 is almost due north of the well. This implies that the left most column is approximately ST, and the center column SL.

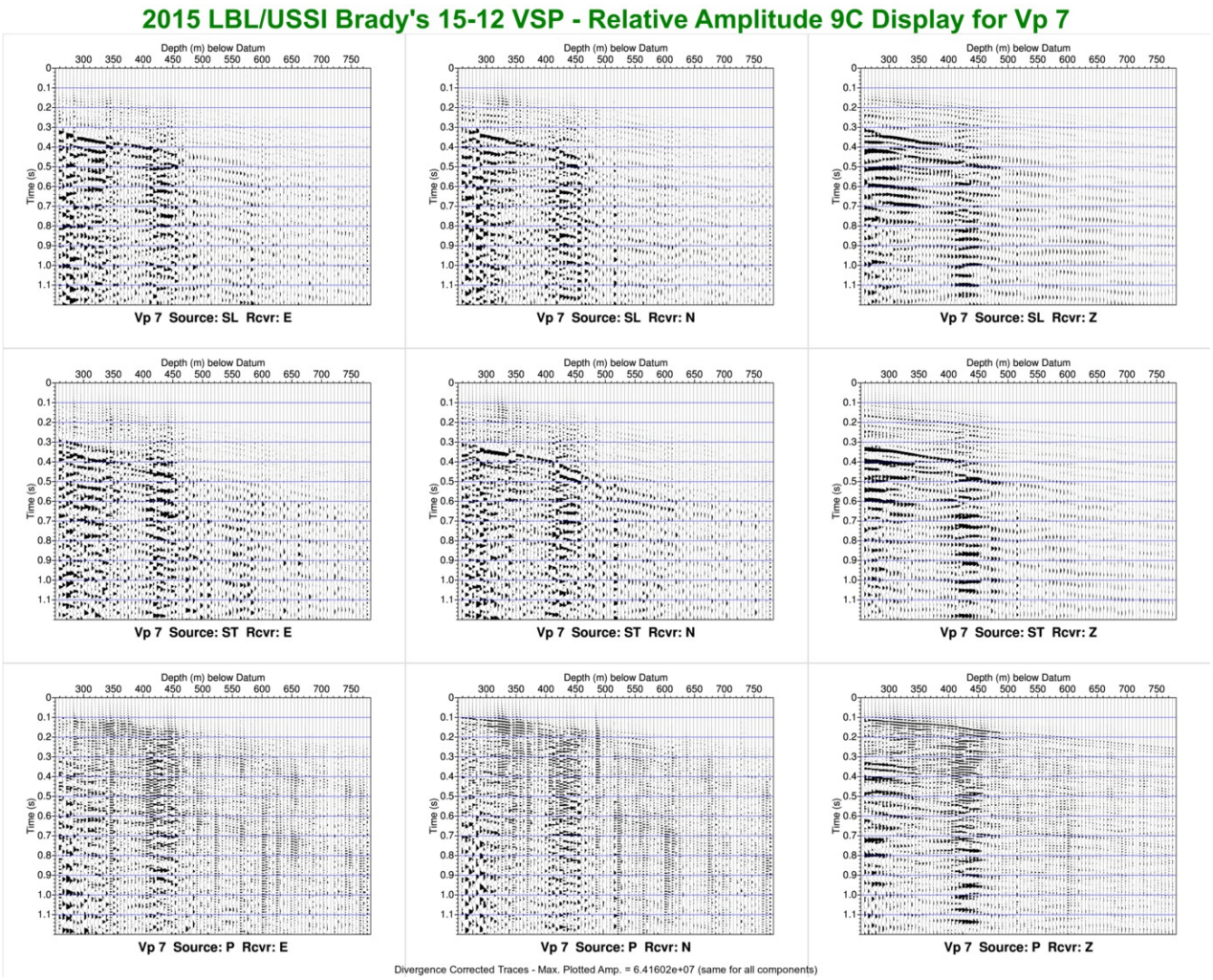

Figure 7.6: Full 9-C display of the traces from Vp 7. Relative trace amplitudes have been preserved. The top row is from the in-line (SL) source, the middle row from the cross-line (ST) source, and the bottom row from the Vertical source (Z). The left column shows east orientated traces, the middle column north orientated traces, and the left column vertical traces.

Again, there are almost no events below 450 m moving at shear velocities in these plots.

Figure 7.7 shows the compressional and shear interval velocities inverted from first break picks of the near offset VSP (Figure 7.3). The processing contractor did not provide details of how these velocities were estimated.

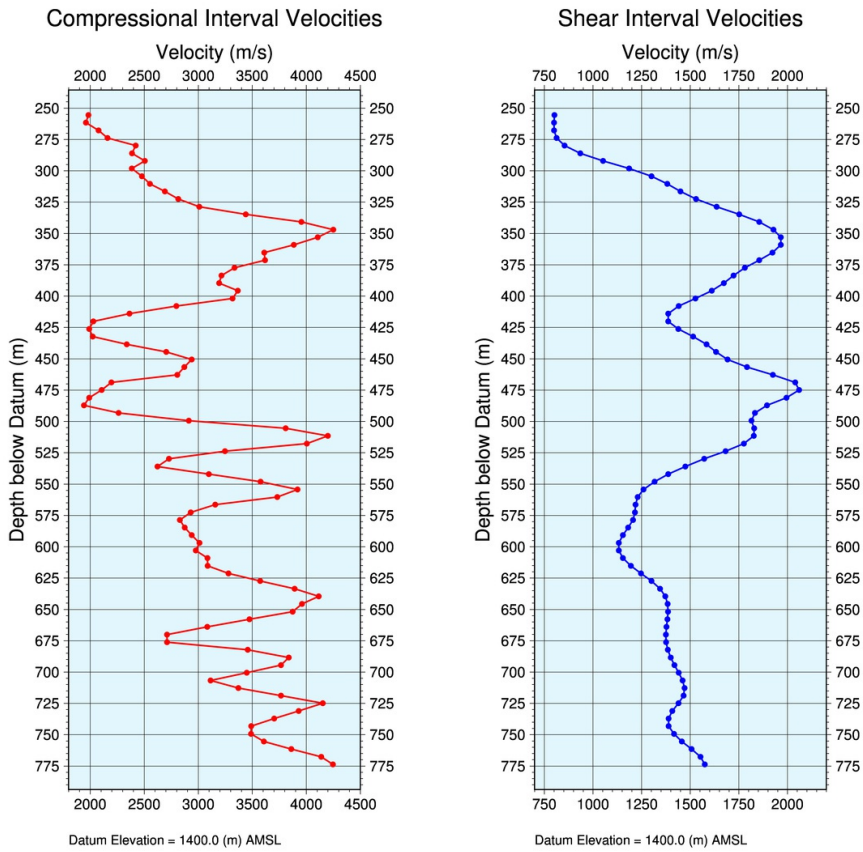

Figure 7.7: Inverted compressional and shear interval velocities from the near offset source point VSP (Figure 7.3).

The VSP data show a number of events with very high apparent-velocity (Figures 7.3 and 7.4), some at the same depths and time predicted by the modeling (Figure 7.3C). Modeling suggests that these events in the VSP data are fault scattered events. Unfortunately, many things besides fault scattering can cause such events, including interfering up and down going bed reflections. To truly qualify these events as scattering from faults or fractures processing more advanced processing would be needed. Reverse time migration such as discussed by Wang et al., (2011) would be beneficial, but the available source points may not be optimal for such imaging.

The VSP did produce important velocity information down to depths of 775 m below datum (Figure 7.7). Comparison of the arrival times of the down going compressional waves (first breaks) in Figures 7.3C, 6.5F and 6.6F shows that the velocities in the model are slightly slow. Incorporation of these new VSP interval velocity estimates would improve both the modeling and the time to depth conversion of the surface reflection data in the vicinity of the VSP well.

Task 8: High Areal Coverage Surface Seismic

Proposed Objectives

Dependent on the final acquisition plan developed in Budget Period II Task 6, 10 miles of 3 line swaths of surface multicomponent data will be acquired over the Brady's Hot Springs geothermal area. This work will be conducted by Stephen G. Muir, consulting geologist and geophysicist, utilizing in house equipment. These data will then be processed and imaged using advanced seismic migration imaging techniques, integrating available VSP results to constrain migration velocity models. Mode converted shear wave processing and imaging algorithms will also be applied. The final compressional and shear migrated images will then be interpreted.

Accomplishments

Data Acquisition

The final data acquisition plan for the High Areal Coverage Surface Seismic was discussed under Task 6. The planned layout of the surface seismic lines is shown in Figure 6.9. As planned, Lines 5, 7, 8, and 9 were to be acquired as swath lines. This means that, for example for Line 5, sources will be applied along Line 1 recording to geophones along Line 5. Image point coverage will be at the midpoints between Line 1 and Line 5, and are shown as CMP Line 1/5 in Figure 6.9. Swath coverage has the advantage of not requiring extensive permitting of source lines. Archeological and cultural considerations were a limiting factor in permitting source lines. Remaining lines will be acquired as standard 2D CMP reflection lines.

Figure 8.1 shows the actual field layout of station flags used in the acquisition of Task 8 seismic data. Surveyed seismic ground stations are overlain on the surface geology map produced by James Faulds at Nevada Bureau of Mines and Geology. Those shown in green (Lines 1, 3, and 4) were laid out during the acquisition undertaken in Task 4. Stations shown in red (Lines 5 – 10) were added for use in the seismic acquisition of Task 8.

Data acquisition, processing, and interpretation using the green stations along Lines 1, 3, and 4 have been described above under Tasks 4 and 6. Those data were integrated with newer data acquired as part of this Task during Task 9.

Data acquisition activities including surveying and seismic recording began at Brady's Hot Springs in August 2011. They were completed in December 2011.

Lines 5 through 8 were acquired as 2D swath lines. Lines 1, 9, and 10 were acquired as standard 2D CMP reflection lines. Line 9, which was originally planned as a swath line was acquired as a standard reflection line. Lines 3 and 4 were not re-acquired.

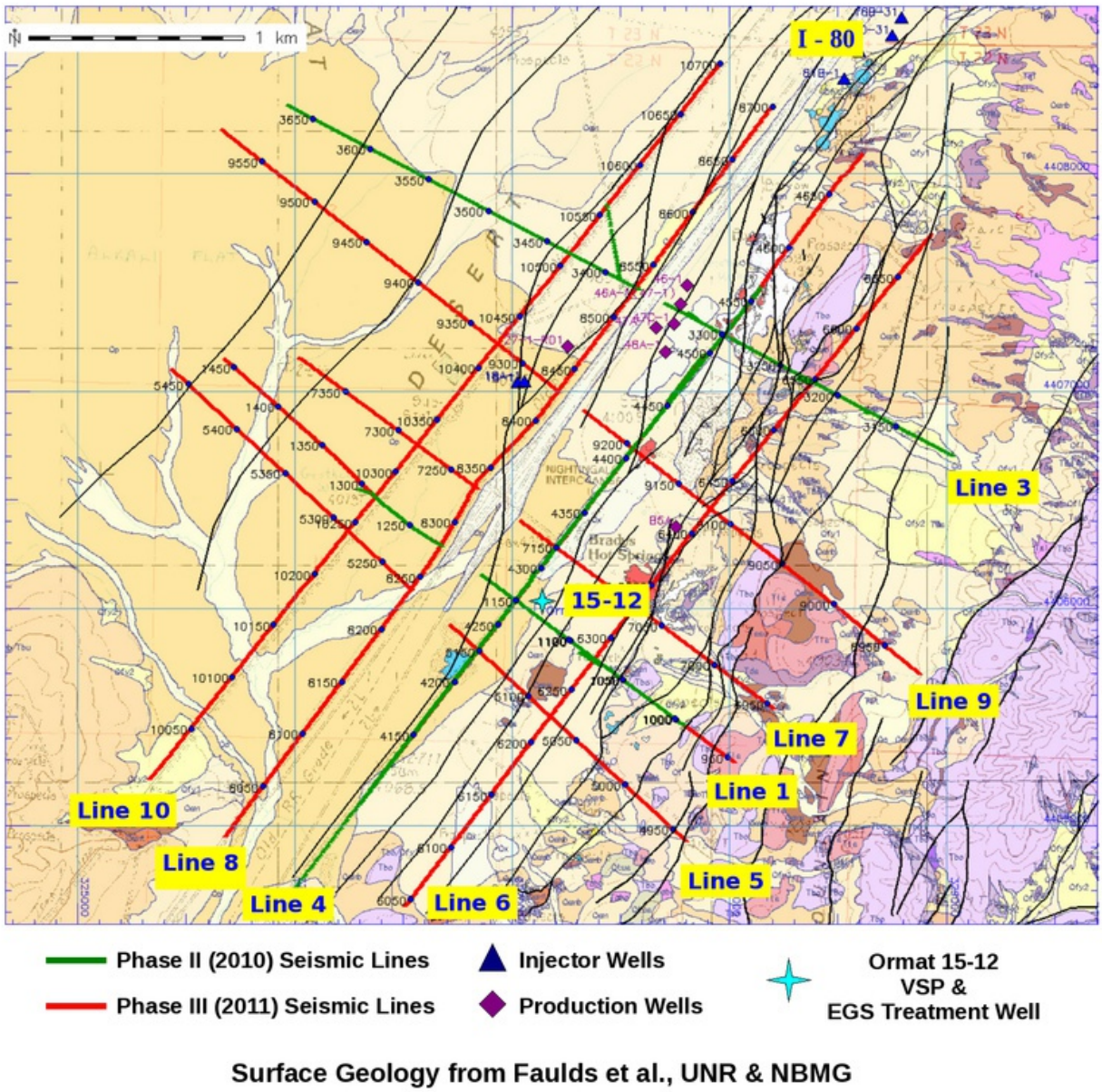

Figure 8.1: Seismic ground station location map overlain on surface geology. Ground stations used during Phase II are shown in green, while those added in Phase III are shown in red. Active production and injection wells are also shown.

For the acquisition of the surface seismic data, 240 channels were recorded in Phase I. This was increased to 324 channels in Phase II. Geophone and source spacing were nominally 20 ft. (6.1 m), though in some areas a 40 ft. (12.2 m) source spacing was used. This was due to archeological and other cultural constraints such as buildings and highways. A sample rate of 1 ms was used, and record lengths of 4 s were recorded. Sourcing was accomplished using a Bolt Land Air Gun. 8 – 12 pops of the source were stacked at each shot point.

A maximum of 648 vertical geophones were laid out as point receivers. At 20 ft. spacing, this gave approximately 4 km of line length. For conventional 2D recording, shots were recorded from the beginning of the line to the end. With a maximum of 324 live channels, the entire line could not be recorded, so a roll box was used to roll the line. Off end shooting was used, with the source at the lowest active flag of the geophones. This gave a nominal maximum offset of approximately 6400 ft. (1.95 km). Similar strategies were used for the swath lines, with the sources applied on offset lines parallel to the geophone line.. A total of approximately 1780 shot gathers were acquired during the overall Task 8 program.

Interstate 80 (I-80) posed a major problem. Aside from the noise generated by traffic, approximately 36 ground stations had to be skipped because of the interstate. In these cases, geophone lines were laid out in two patches of 324 channels each, one on the northwest side of I-80 and the other on the south-east side. Shots were then acquired from ground stations on both sides of I-80 to each patch, statically (no roll). This allowed undershooting of the section of the line skipped due to the interstate.

Acquisition began along Line 10. Line 10 is a strike line (perpendicular to geological dip) running southwest to northeast on the northwestern edge of the survey area. Figure 8.2 shows an example shot gather from Line 10. In Figure 8.2, the source is at ground station 10626 near the northeast end of the line. This is a raw shot gather with automatic gain control (AGC) applied.

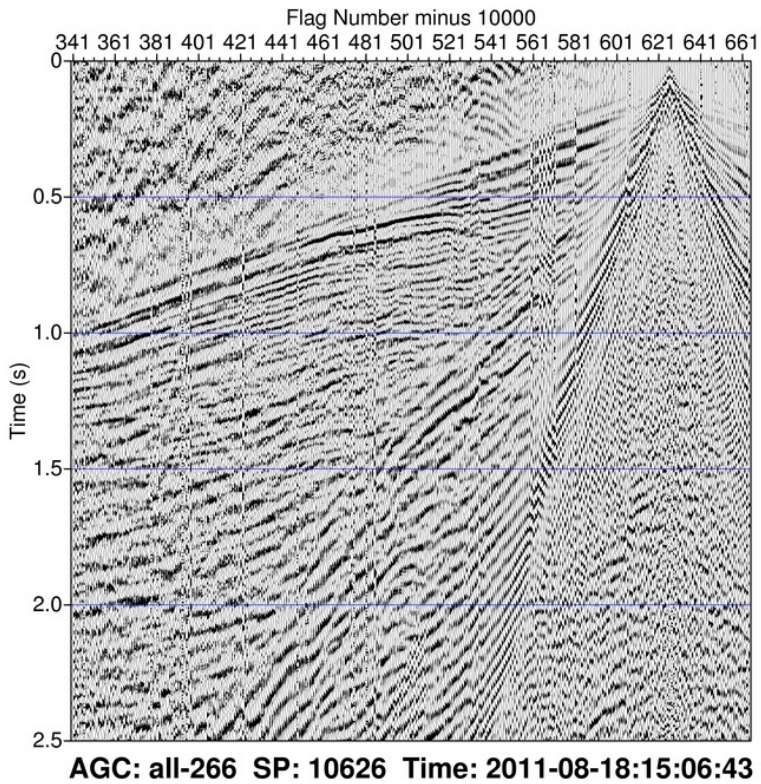

Figure 8.2: Line 10 shot gather with source located at ground station 10626. Reflections deeper than 2 s are visible out to offsets of nearly 6000'. Some reversed traces are visible (e. g. station 10581).

With receivers laid out along line 10 as described above, an offset swath line was then acquired by moving the source along Line 8. A total of 390 shot gathers were acquired, with shot locations ranging from ground stations 8102 to 8664. Figure 8.3 shows an example shot gather with the offset source location along Line 8 corresponding to that shown in Figure 8.2.

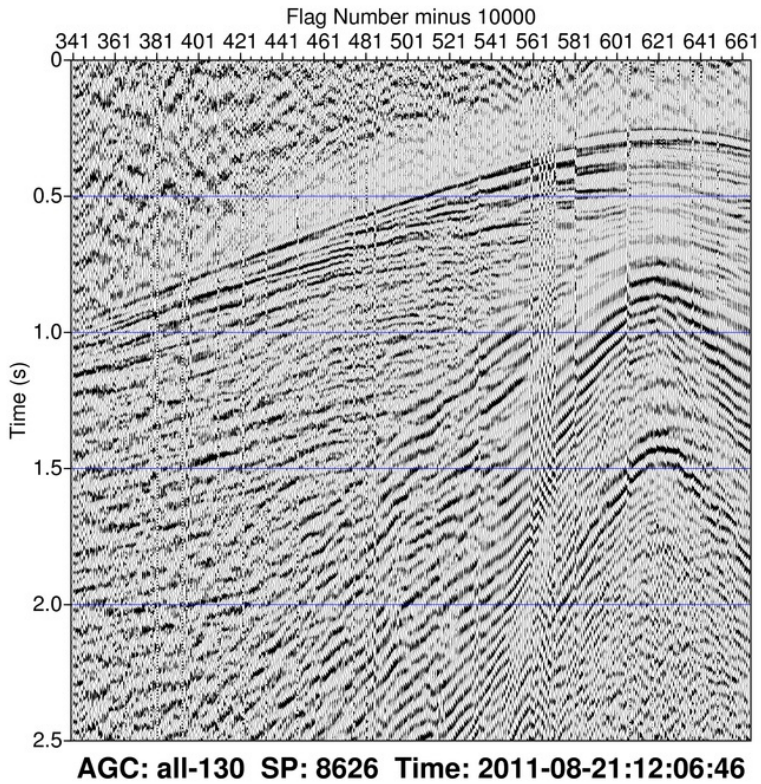

Figure 8.3: Line 8 offset source shot gather with source located at ground station 8626 and geophones located along Line 10 at same locations as in Figure 8.2.

Following acquisition along Lines 10 and 8, work moved on to Line 9. The location of this line was chosen based on the idea that it passes near some of the most productive wells in the Brady's Hot Springs Field.

Vertical geophones were again laid out as point receivers, spanning from ground station 8915 to ground station 9588. At 20' spacing, this gives approximately 4 km of line length. Ground stations between 9230 and 9265 were skipped due to Interstate 80. Because of the skips caused by the interstate, receiver lines were laid out in two patches of 324 channels each, one on the northwest side of I-80 and the other on the South East side. Shots were then acquired from ground stations on both sides of I-80 to each patch, statically (no roll). This provided undershooting of the section of the line skipped due to the interstate.

Figure 8.4 shows a shot gather from a source located along Line 9 at ground station 9268, just northwest if I-80, into the receiver patch located on the northwest side of the interstate. This source

location is on the end of the line, right next to I-80. It can be seen that these data are very clean, showing good reflection information at times deeper than 2 s. This suggests that both source and geophone coupling are good, and the structure on the North West side is fairly moderate.

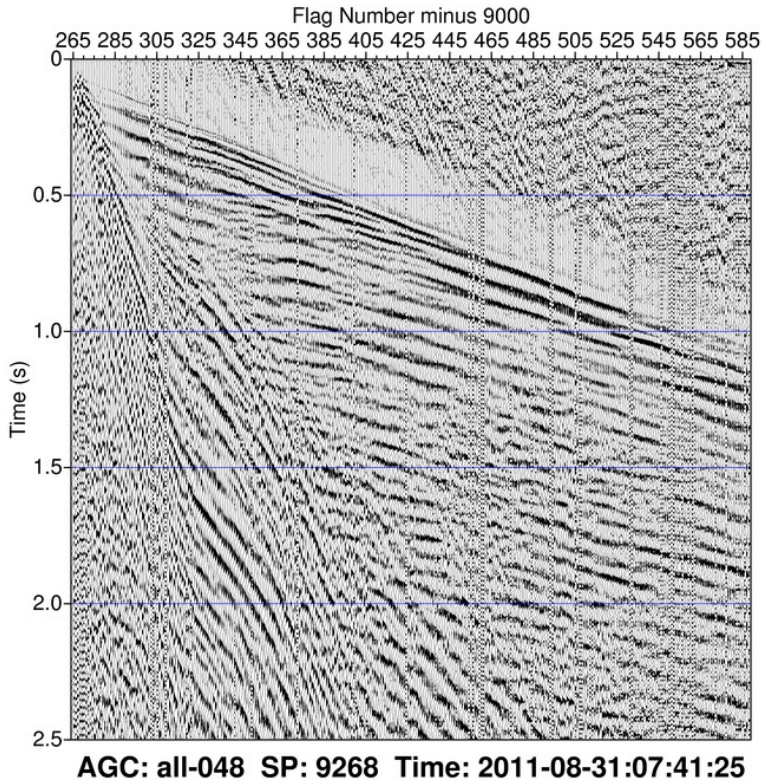

Figure 8.4: Shot gather from Line 9. Geophones for this gather are located on the northwest side of Interstate 80, with the source located on the end of the line next to the interstate at ground station 9268.

In a remarkable contrast, Figure 8.5 shows a shot gather recorded into the patch of geophones located on the southeast side of I-80, from a source located at ground station 9267. This source location, again on the northwest side of I-80, is only 20' away from the source location which generated Figure 8.4. Comparison of the two figures shows that data recorded on the southeast patch is highly corrupted compared to the northwest data of Figure 8.4.

The cause of this corruption is not understood at this time. It could be due to poor geophone coupling on the South East patch, severe structure, or both. Figure 8.1 shows a change in surface geology where Line 9 crosses I-80. It also shows a series of complex faults, particularly between ground stations 9100 and 9200.

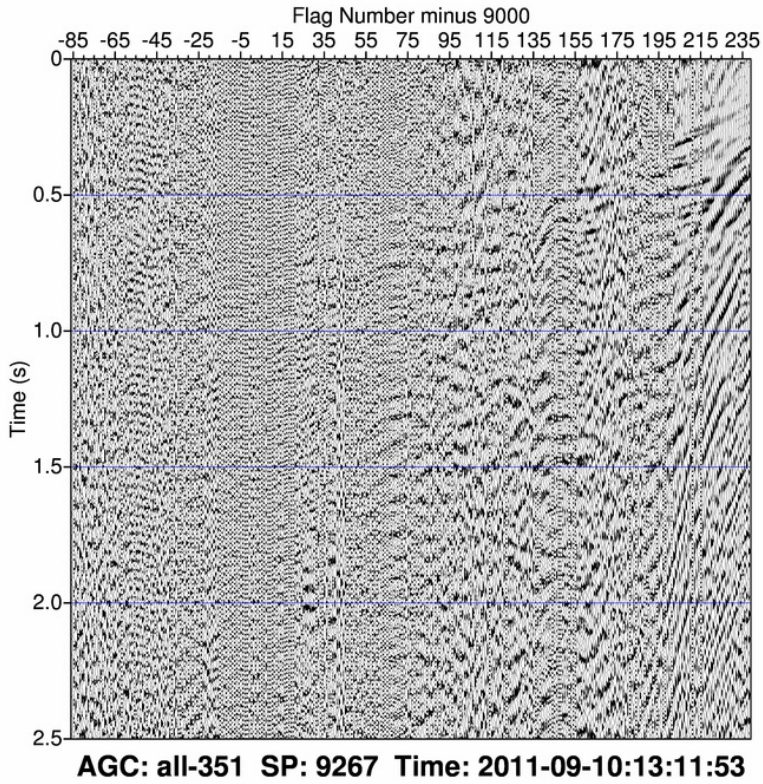

Figure 8.5: Shot gather from Line 9, with geophones for this gather located on the southeast side of Interstate 80. The source for this gather is located at ground station 9267, nearly the same position as the source for Figure 8.4. This illustrates the loss of data quality when crossing from the northwest side of I-80 to the southeast side. Figure 8.1 shows a change in surface geology and faults on crossing I-80 along Line 9

Figure 8.6 shows another shot gather recorded on the Line 9 southeast patch of geophones from a source located at ground station 9169 (also southeast of I-80). While certainly not outstanding, the data quality for this shot gather is significantly improved over that shown in Figure 8.5. This shot gather shows a very complex series of events suggesting severe faulting. This is particularly evident near ground stations 9125 and 9085. The steep dip of the events in these areas further confirms the need for fine spacings in order to avoid spatial aliasing, critical in the processing of these data.

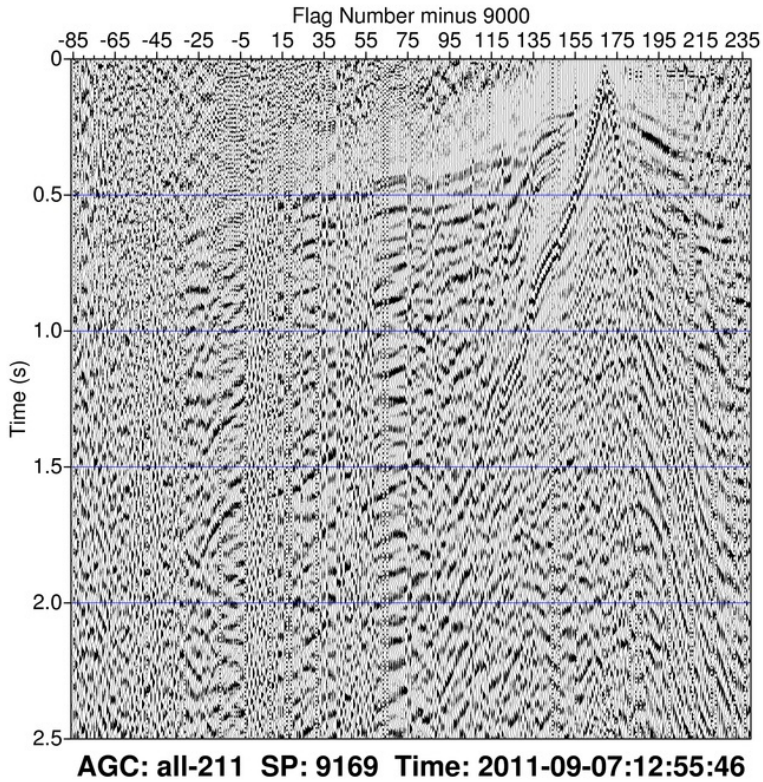

Figure 8.6: Shot gather from Line 9, with geophones for this gather again located on the southeast side of Interstate 80. This is the same geophones that produced Figure 8.5. The source for this gather is located at ground station 9169 (also southeast of I-80). Data quality are improved over that of Figure 8.5.

The next step was the acquisition of an offset source line using sources along Line 4 shooting into geophones located along Line 6. This was followed by the acquisition of a three line swath centered on Line 1. Line 1 was extended over that used in Phase II Task 4. For this part of the program, sourcing took place along Line 1 while recording geophones along Lines 1, 5, and 7. This summarizes the acquisition for Phase III Task 8.

Data Processing

Ongoing with the acquisition, seismic field data were sent to Sterling Seismic Services Ltd. for advanced processing. The individual processing the Task 8 data was the same person who processed the Task 4 data. In between the two tasks, this person changed companies from Western Geco to Sterling. Using the same processor helped maintain continuity between the processing products from Task 4 and those from Task 8.

Processed results for Lines 1, 6, 8, 9, and 10 were delivered by Sterling Seismic Services Ltd. These products included CMP stacks, post stack time migration, and pre stack time migration results. For each of these three general categories, products with various combinations of random noise attenuation

(RNA), automatic gain control (agc), and time varying filtering (tvf) were delivered.

Processed results for lines 5 and 7 (swath lines acquired with Line 1) were also delivered. These did not include pre stack time migration results.

It was initially envisioned that pre stack time migration results would be used in Task 9: Final Interpretation. Pre stack time migration operates on seismic traces sorted into common offset gathers. Reliable pre stack migration results depend on uniform and extensive coverage. These coverage requirements were met for all lines with the exception of the two swath lines 5 and 7. Due to access restrictions related to permitting, archeology, and roads (including Interstate 80), these two lines suffered severe holes in some of the common offset gathers, and were not judged suitable for pre stack migration by the processor.

It was felt that these two lines should be included in the overall final interpretation since they bracket the Brady's 15-12 well, the candidate well for future EGS treatment and VSP acquisition. For these reasons, it was decided to use the post stack time migration RNA tvf results for all lines in Task 9. This insured consistent processing for all the seismic data. Previous comparisons of the pre stack and post stack migration results have shown that there are only minor differences between the two processing results

For discussion of the processing results, we will primarily focus on the post stack time migration results with RNA, tvf, and agc processes applied. Some results with and without tvf applied will be shown. A limited number of pre stack migrations will be displayed for comparison.

Figure 8.7 shows a map of image points or Common Depth Points (CDP), also called Common Mid Points (CMP) produced by the post stack time migration processing stream. They are overlain on a preliminary surface geology map produced by James Faulds at University of Nevada, Reno (UNR), and Nevada Bureau of Mines and Geology (NBMG) (Faulds et al., 2012; unpublished data). Lines acquired during Phase II are shown in green, while those added in Phase III are shown in red. Active production, injection, and observation wells are shown. The 15-12 well, the well used for VSP acquisition and planned EGS treatment is shown as a cyan star. Cultural features such as Interstate 80 cutting diagonally through the study area are also shown.

A limited number of production, injector and observation wells are shown in Figure 8.7. All of the wells from the Brady's Hot Springs area are not shown. Data from additional wells later became available during Task 9: Final Interpretation. With the exception of 15-12, well names were left off the map in the interest of more clearly showing line locations and CDP numbers.

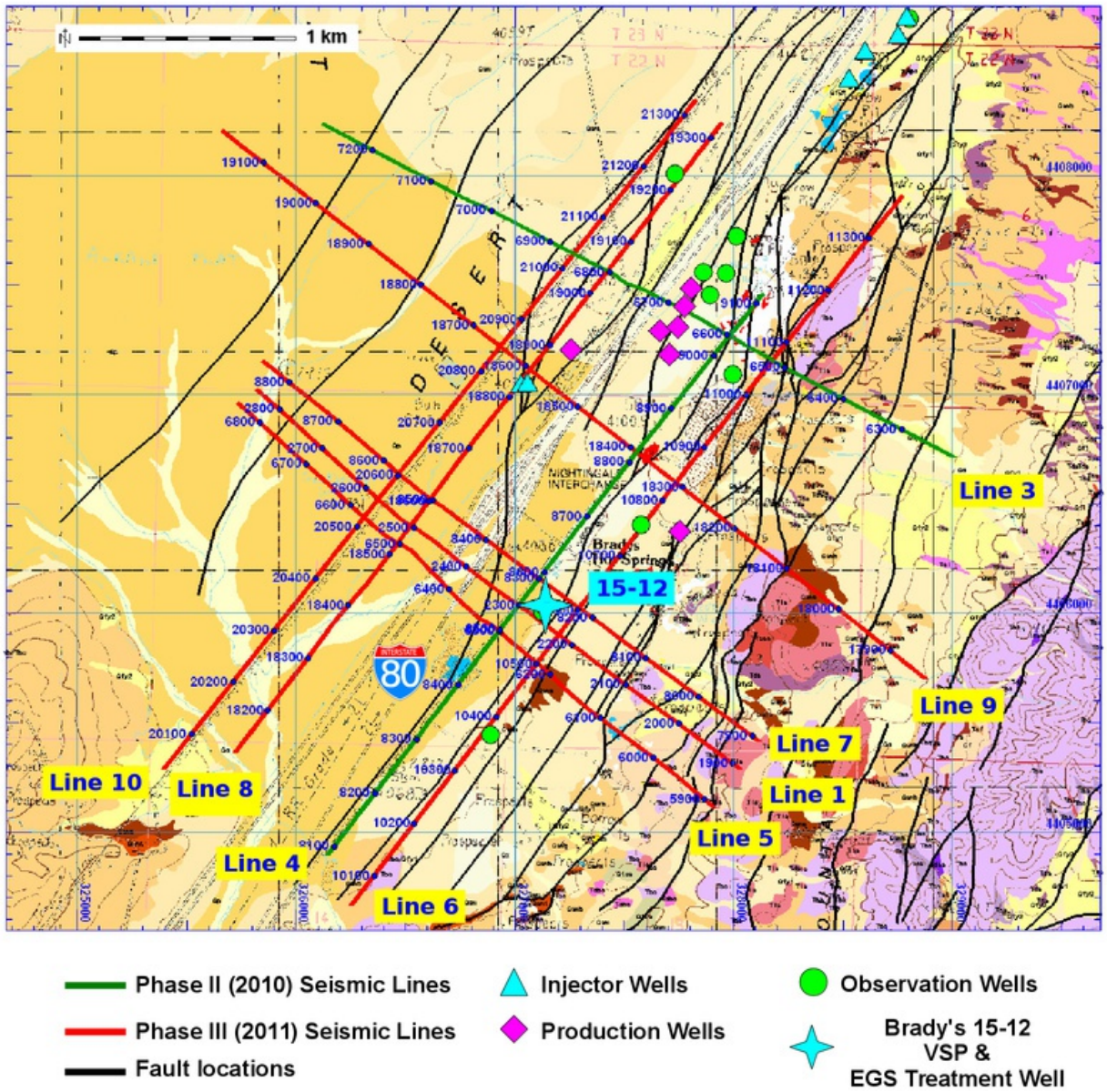

Figure 8.7: Map of image points or Common Depth Points (CDP), also called Common Mid Points (CMP) produced by the post stack time migration processing stream overlain on a preliminary surface geology map produced by James Faulds at University of Nevada, Reno, and Nevada Bureau of Mines and Geology (Faulds et al., 2012; unpublished data).

Line 9 Results

Line 9 is a dip line oriented NW-SE passing approximately ½ km SW of the main cluster of production wells at Brady's Hot Springs. It passes very close to the 18-11 injection well.

Figure 8.8 shows a time section trace plot of the post stack time migration results for Line 9 after

application of RNA, tvf, and agc. Figure 8.9 shows the same data after time to depth conversion using the stacking normal moveout (NMO) root mean squared (RMS) velocities. Converting time to depth was discussed under Task 4.

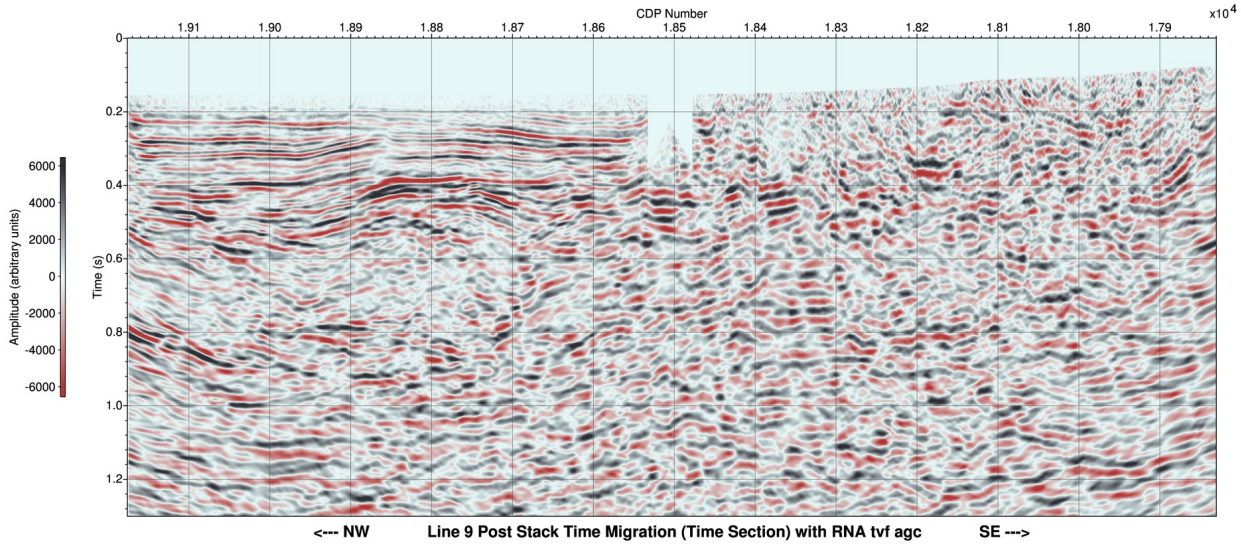

Figure 8.8: Post stack time migration time section for Line 9, with RNA, tvf, and agc applied. Surface locations corresponding to CDP numbers are shown in Figure 8.7. The left side of the plot is to the northwest, and the right side to the southeast.

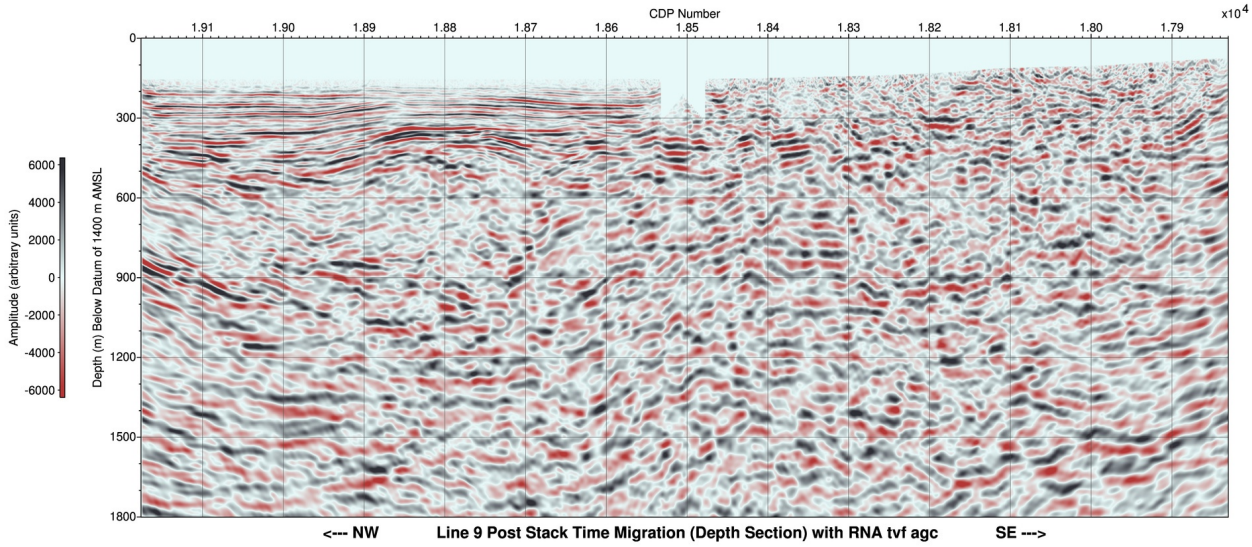

Figure 8.9: Post stack time migration depth section for Line 9 after time to depth conversion using normal moveout (NMO) stacking RMS velocities. RNA, tvf, and agc have been applied. The left side of the plot is to the northwest, and the right side to the southeast.

Figure 8.10 shows the depth converted Line 9 pre stack time migration results. A number of migration "smiles" are apparent for deeper events near the edges of the line in Figure 8.10. This is caused by missing events cut off at the ends of the line, and is related to finite aperture. Coherent reflections are visible down to the deepest depths displayed (1.8 km). The near surface "notch" in the data around CDP 18500 is caused by the need to skip shot points that would have fallen in Interstate 80.

Comparing this figure to the post stack migration (Figure 8.9) shows slight differences. Many of the same reflections can be seen. Coherency of the post stack reflections is not as high as in the pre stack migration, particularly for deeper events. Another difference is the lack of many of the migration "smiles" in the post stack migration data.

A profound change in the reflection character is seen when crossing Interstate 80. This is seen in both the pre stack and post stack time migration results. Much better data quality is apparent NW of the Interstate (left side of figures). On-lapping reflectors can be seen at depths around 300 m below datum in the vicinity of CDP 18900.

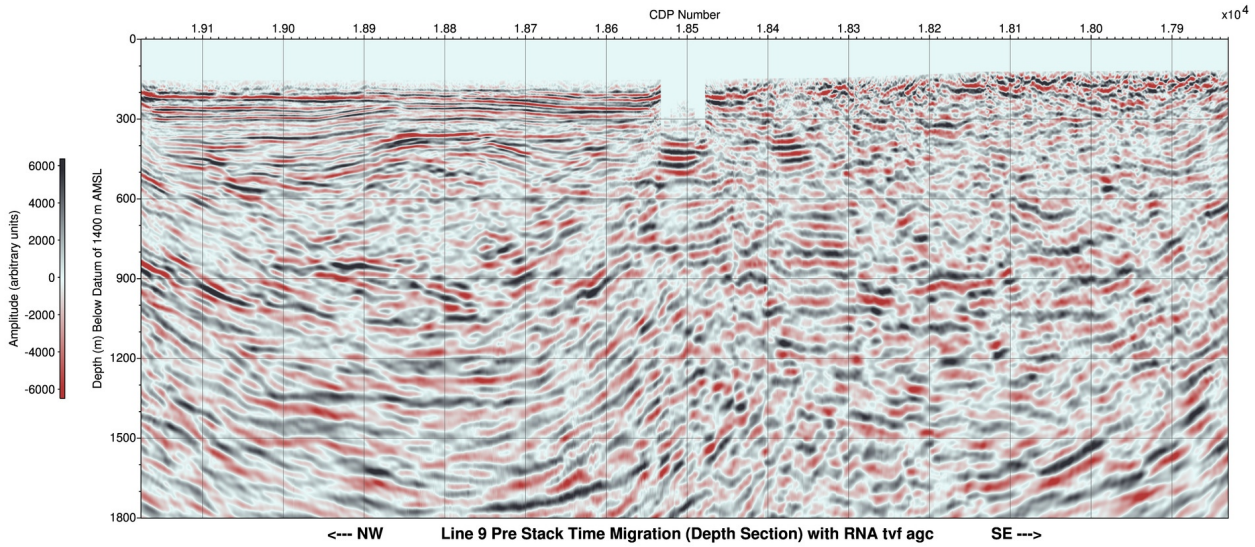

Figure 8.10: Pre stack time migration depth section for Line 9 after time to depth conversion using migration stacking RMS velocities. RNA, tvf, and agc have been applied. These results can be compared to the post stack time migration results of Figure 8.9. The left side of the plot is to the northwest, and the right side to the southeast.

Figure 8.11 shows the depth converted post stack time migration data of Figure 8.9 overlain with the interval velocities inferred from the Line 9 normal moveout (NMO) RMS velocities. Velocities are seen to follow the general structure of the reflectors. A higher velocity pull up can be seen near CDP 18600, where the line pass close to the 18-11 injector well.

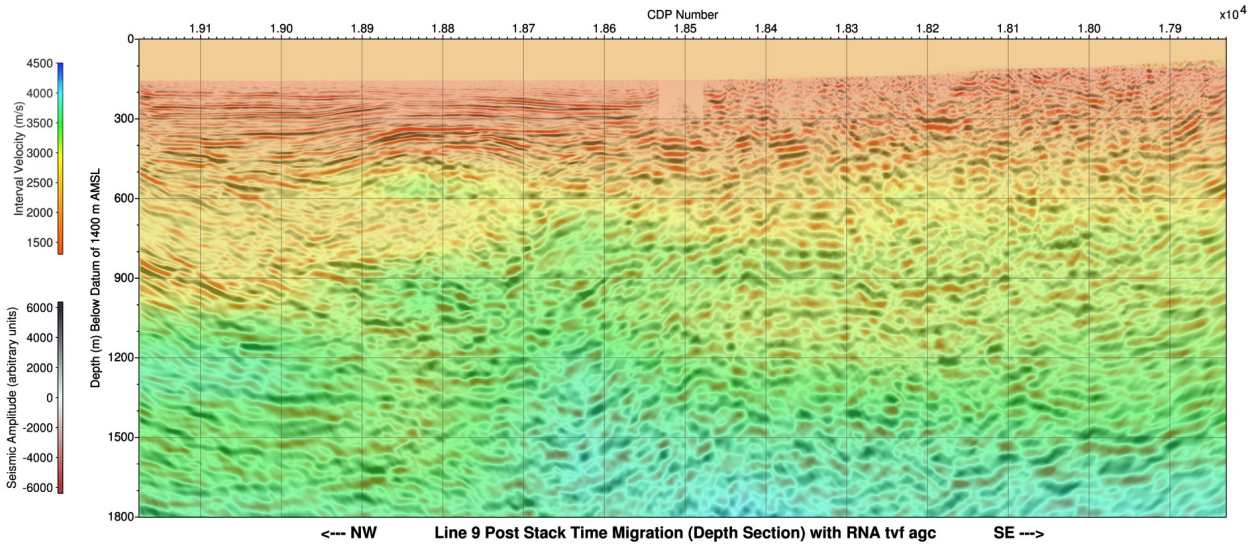

Figure 8.11: Post stack time migration depth section for Line 9 after time to depth conversion using normal moveout (NMO) RMS velocities, overlain by color coded interval velocities inferred from the NMO velocities. RNA, tvf, and agc have been applied. The left side of the plot is to the northwest, and the right side to the southeast.

Figure 8.12 shows the same data as Figure 8.9 only without the application of time varying filter (tvf). A number of events are enhanced in Figure 8.9 compared to Figure 8.12. An example is the series of reflections between CDP's 18300 and 18400 between depths of 600 m and 900 m below datum.

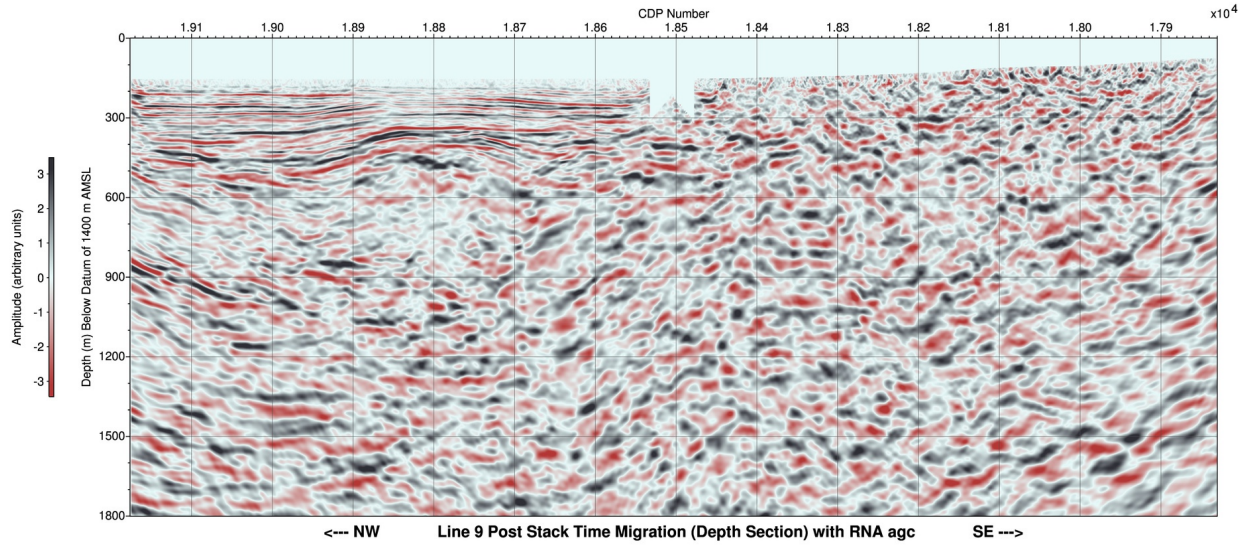

Figure 8.12: Post stack time migration depth section for Line 9 after time to depth conversion using NMO RMS velocities. In contrast to Figure 8.9, no time varying filter (tvf) has been applied.

Figure 8.13 shows the data from Figure 8.12 after spectral color time-frequency analysis (Theophanis

and Queen, 2000). Data without tvf were chosen since the tvf process can distort the frequency content in the data. The spectral color display (LRGB) is a simple way of displaying the frequency and amplitude content of large data sets. A luminance channel has been added to the RGB display described in Theophanis and Queen (2000) based on the seismic amplitude traces shown in Figure 8.12. Reds correspond to lower frequency content while blues corresponds to higher frequencies. For this and all subsequent LRGB displays, the red band extends from 7-21 Hz with a center frequency of 14 Hz, the green band extends from 12.5-37.5 Hz with a center frequency of 25 Hz, and the blue band extends from 27.5-82.5 Hz with a center frequency of 55 Hz.

A general loss of frequency with depth is visible as the spectral color grades from blue to red. A noticeable change in frequency content is also visible with position along the line. For lower CDP locations to the SE, events are much redder than those to the NW, which show a much greener response. This break in frequency content occurs near the location of Interstate 80. It appears to correlate with the loss of data quality on crossing Interstate 80 shown by Figures 8.4 and 8.5. Loss of higher frequencies also onsets near CDP 18600 where the line passes close to the 18-11 injector well.

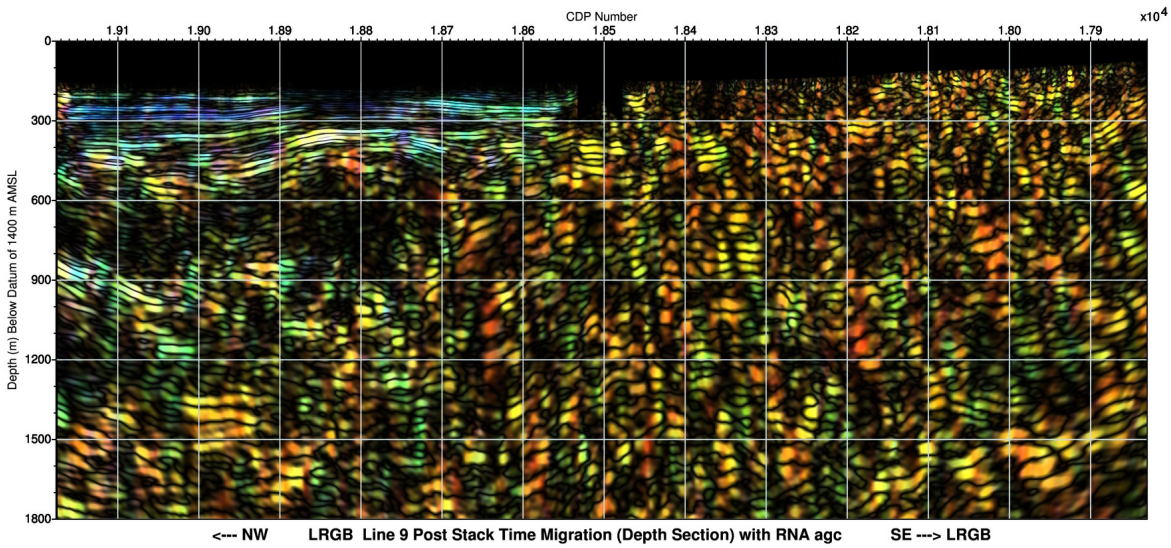

Figure 8.13: Spectral color LRGB representation of the Line 9 data from Figure 8.12 (Line 9 post stack migration data without tvf). RNA and agc data were used in the spectral color analysis.

The spectral color plots were interesting, particularly the change to higher frequencies northwest of Interstate 80. They were not, however, considered to be terribly useful in the overall interpretation. One problem is that colors and contrast of these plots change from one computer monitor to another. Printed hard copies suffer from similar effects. However, the frequency changes across the section indicated by these plots are not evident from trace displays such as shown in Figure 8.12

Line 10 Results

Line 10 is a strike line oriented SW-NE. Image points for Line 10 shown in Figure 8.7. It is the northwestern most of the strike lines. It mainly crosses an area overlain by basin fill sediments. It passes a few hundred meters northwest of the 18-11 injector well, projected onto the line near CDP

20810. Line 10 also passes northwest of the 27-1 production well. This well is slightly further offset than the 18-11 well, and projects onto Line 10 near CDP 20900.

Figure 8.14 shows a time section trace plot of the post stack time migration results for Line 10 after application of RNA, tvf, and agc. Figure 8.15 shows the same data after time to depth conversion using the stacking NMO velocities.

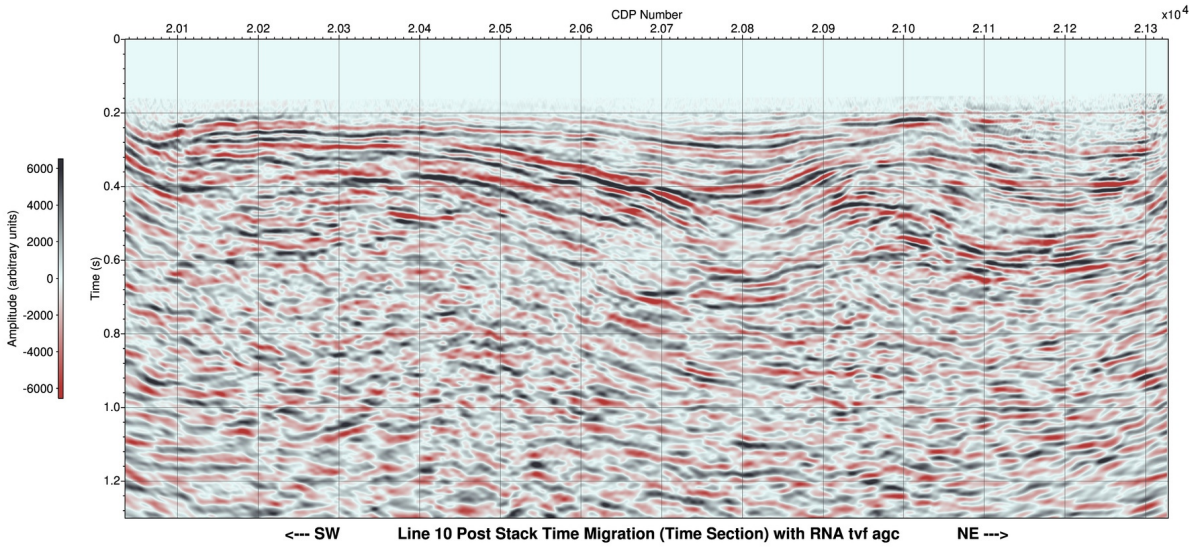

Figure 8.14: Post stack time migration time section for Line 10, with RNA, tvf, and agc applied. Surface locations corresponding to CDP numbers are shown in Figure 8.7. The left side of the plot is to the southwest, and the right side to the northeast.

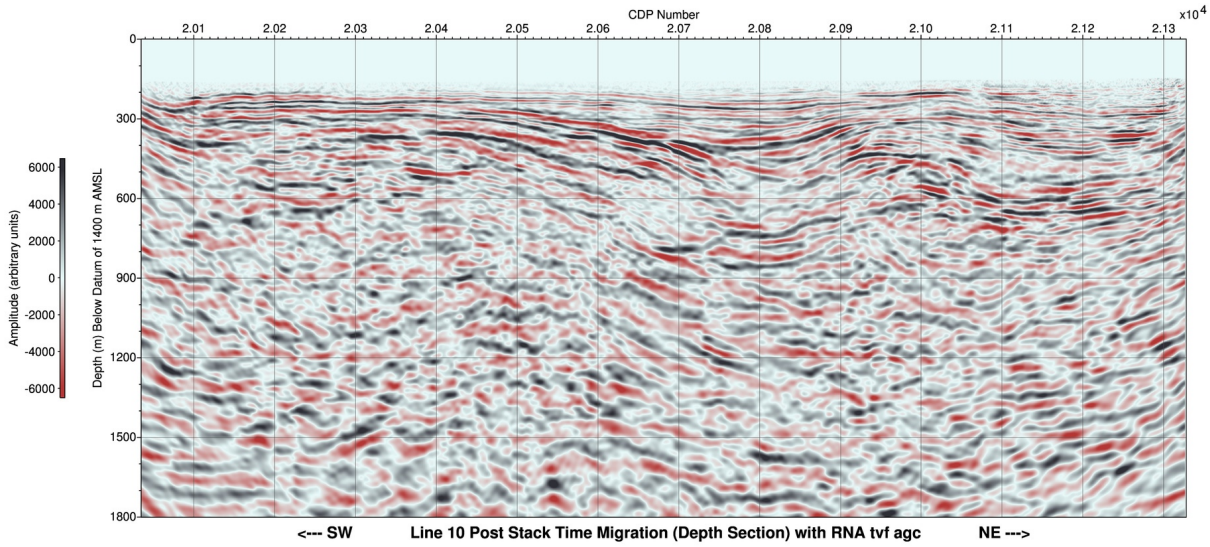

Figure 8.15: Post stack time migration depth section for Line 10 after time to depth conversion using normal moveout (NMO) stacking RMS velocities. RNA, tvf, and agc have been applied. The left side of the plot is to the southwest, and the right side to the northeast.

As is typical for seismic lines acquired over basin fill, a series of long coherent reflections are visible. This is seen even for many of the deeper reflection events.

Figure 8.16 shows the depth converted post stack time migration data of Line 10 (Figure 8.15) overlain with the interval velocities inferred from the Line 10 normal moveout (NMO) RMS velocities.

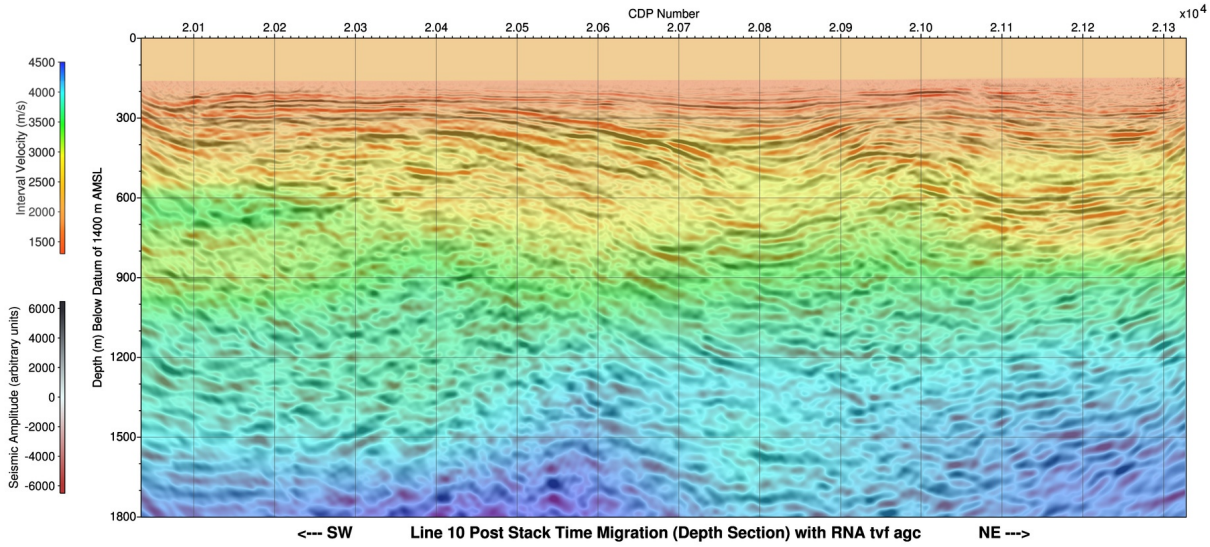

Figure 8.16: Post stack time migration depth section for Line 10 after time to depth conversion using NMO velocities, overlain by color coded interval velocities inferred from those velocities. RNA, tvf, and agc have been applied.

Figure 8.17 shows the Line 10 depth converted post stack migration data without tvf processing after spectral color time-frequency analysis. A loss of high frequencies on the southwest side of the line is indicated by the change from green to red events. This change onsets near the middle of the line near CDP 20700. This is just southwest of the projected locations of the 18-11 injector and 27-1 production wells.

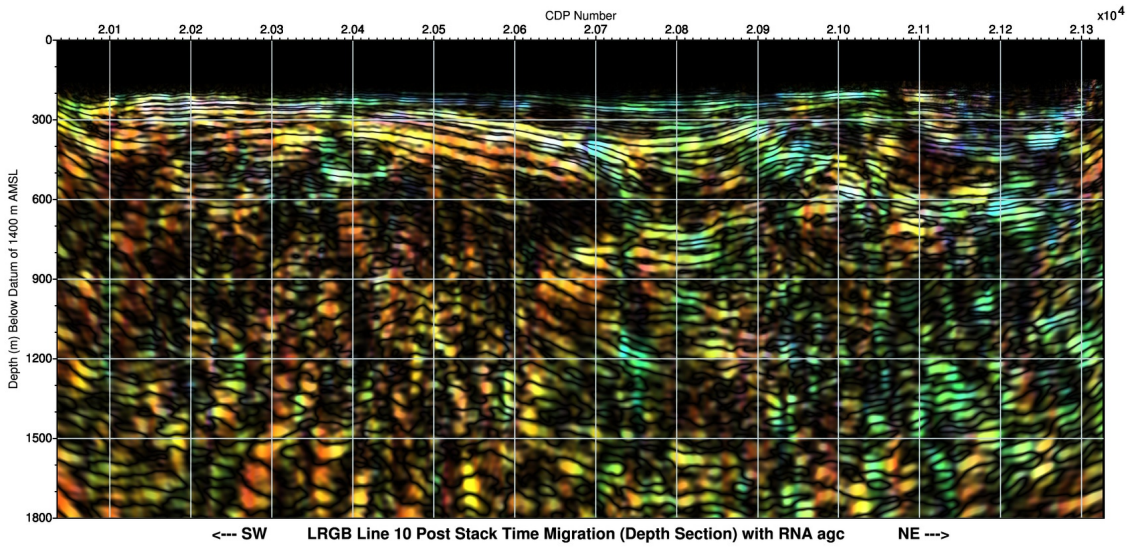

Figure 8.17: Spectral color LRGB representation of Line 10 post stack time migration data without the tvf process applied. RNA and agc data were used in the spectral color analysis.

Line 8 Results

Line 8 is a swath line recorded with geophones deployed along Line 10 acquisition stations and sources applied along Line 8 acquisition stations (Figure 8.1). The CDP image points lie approximately halfway between the two acquisition lines, and are shown in Figure 8.7. Similar to Line 10, this is a SW-NE strike line. It passes close to the 18-11 injector well near CDP 18820. Line 8 passes slightly further to the northwest of the 27-1 production well.

Figure 8.18 shows a time section trace plot of the post stack time migration results for Line 8 after application of RNA, tvf, and agc. Figure 8.19 shows the same data after time to depth conversion using the stacking NMO velocities.

The lack of seismic events for times earlier than ~0.4s on the time section (Figure 8.18) and shallower than ~300 m below datum on the depth section (Figure 8.19) is due to the swath acquisition. Because the source is offset from the geophone line, direct arrivals come in at later times. This effect can be seen in Figure 8.3, a shot gather from swath Line 8. In processing, the direct arrivals are “noise”, and must be muted off. All information from shallower reflectors is obscured by the direct arrivals, and is removed by the mute. This is one of the disadvantages of swath acquisition.

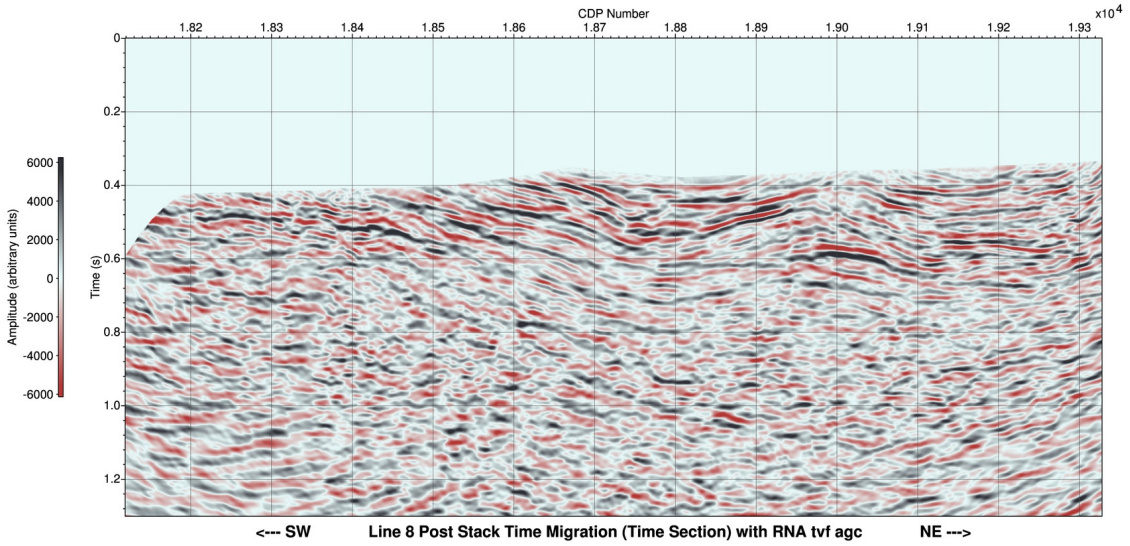

Figure 8.18: Post stack time migration time section for swath Line 8, with RNA, tvf, and agc applied. The lack of reflection events for times earlier than ~0.4 s is an artifact of the swath acquisition. The left side of the plot is to the southwest, and the right side to the northeast.

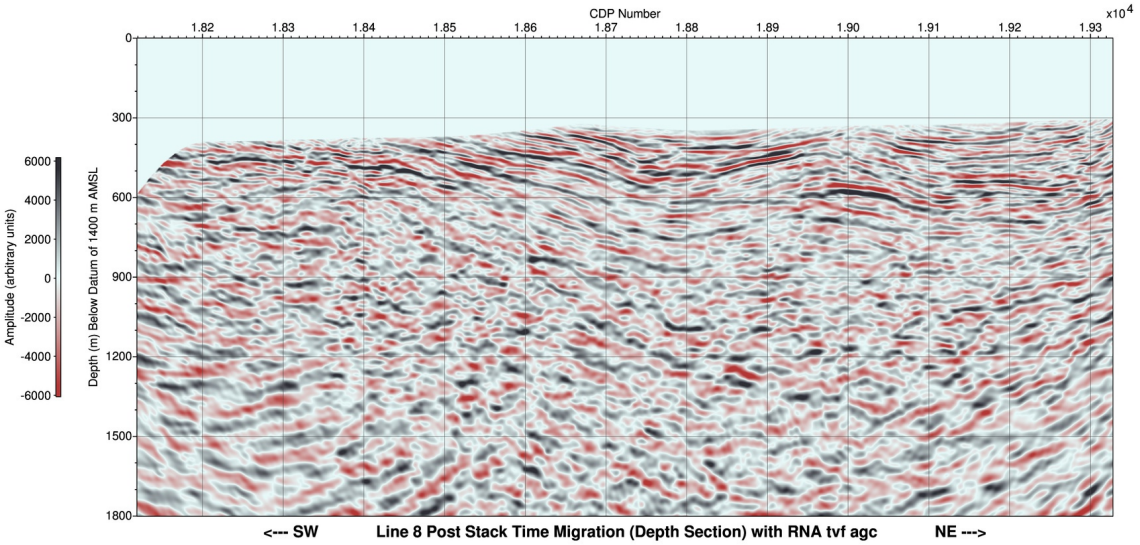

Figure 8.19: Post stack time migration depth section for swath Line 8 after time to depth conversion using NMO velocities. RNA, tvf, and agc have been applied. The lack of reflection events for depths shallower than ~300 m below datum is an artifact of the swath acquisition. The left side of the plot is to the southwest, and the right side to the northeast.

Figure 8.20 shows the depth converted post stack time migration data of Line 8 (Figure 8.19) overlain with the interval velocities inferred from the Line 8 normal moveout (NMO) RMS velocities.

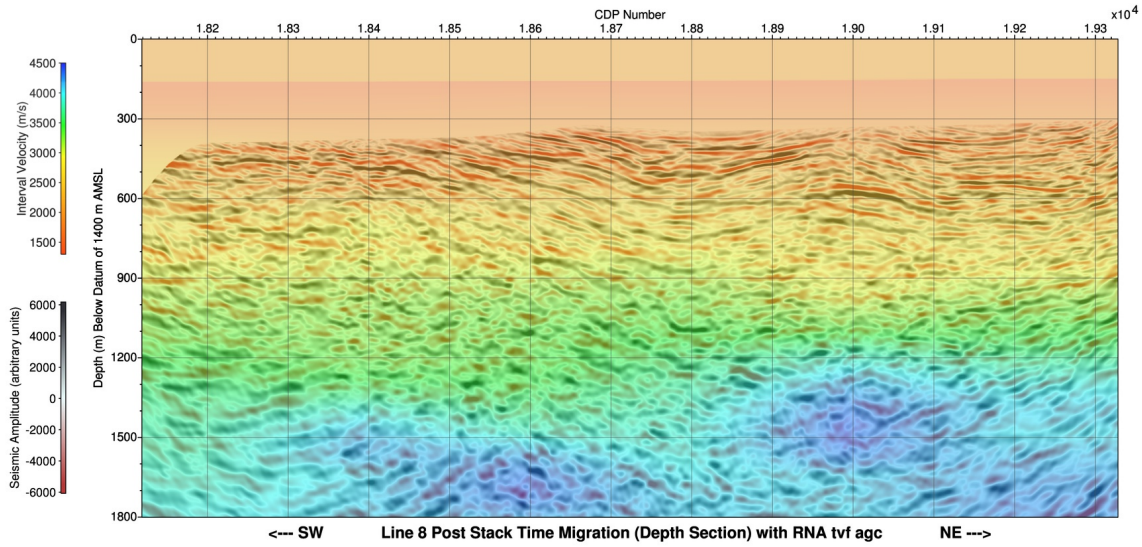

Figure 8.20: Post stack time migration depth section for Line 8 after time to depth conversion using NMO velocities, overlain by color coded interval velocities inferred from those velocities. RNA, tvf, and agc have been applied.

Line 6 Results

Line 6 is a swath line recorded with geophones deployed along Line 6 acquisition stations and sources applied along Line 4 acquisition stations (Figure 8.1). The CDP image points lie approximately halfway between the two acquisition lines, and are shown in Figure 8.7. Similar to Lines 10 and 8, this is a SW-NE strike line. It passes just southeast of the 15-12 VSP and EGS well near CDP 10590. On the northeast end, Line 6 passes several hundred meters southeast of the main producing area at Brady's.

Figure 8.21 shows a time section trace plot of the post stack time migration results for Line 6 after application of RNA, tvf, and agc. Figure 8.22 shows the same data after time to depth conversion using the stacking NMO velocities.

As with Line 8, there are no seismic events for times earlier than ~0.45s on the time section (Figure 8.21) and shallower than ~400 m below datum on the depth section (Figure 8.22). This is due to the swath acquisition.

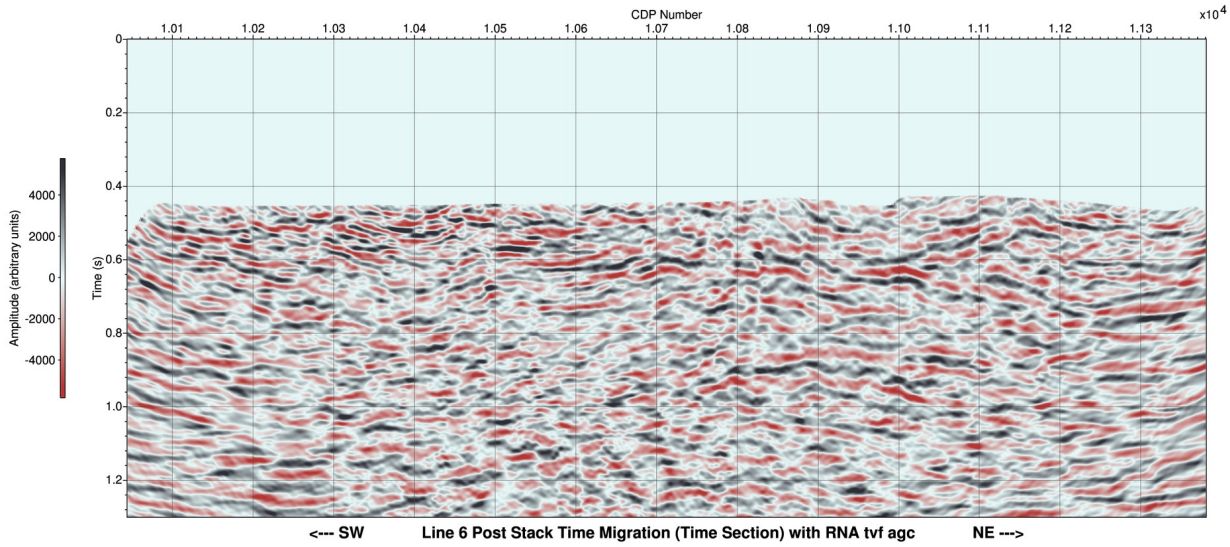

Figure 8.21: Post stack time migration time section for swath Line 6, with RNA, tvf, and agc applied. The lack of reflection events for times earlier than ~0.45 s is an artifact of the swath acquisition. The left side of the plot is to the southwest, and the right side to the northeast.

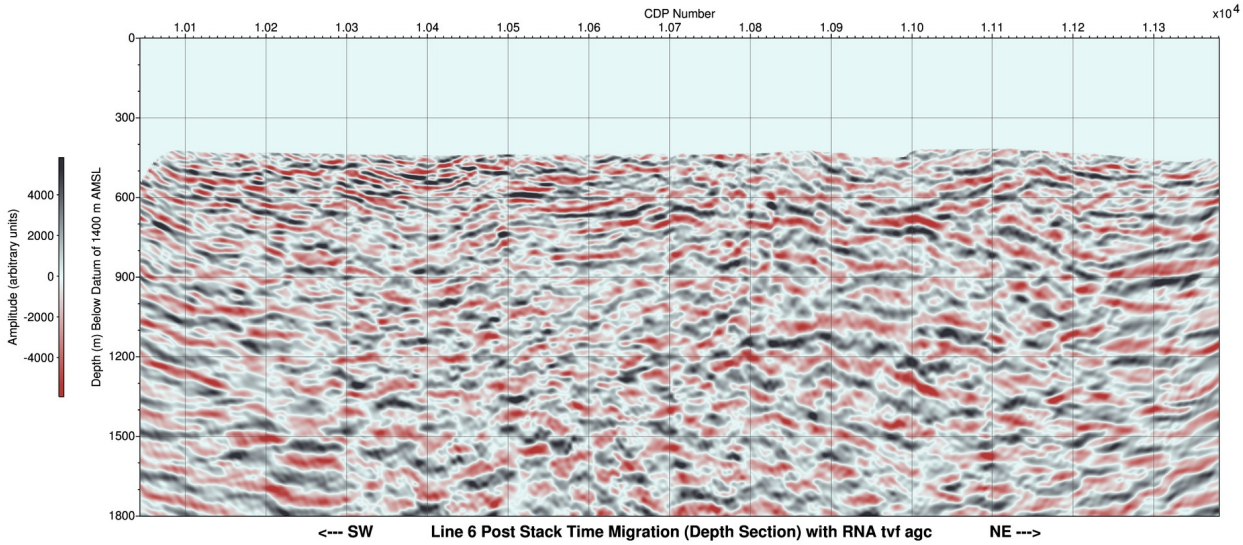

Figure 8.22: Post stack time migration depth section for swath Line 6 after time to depth conversion using NMO velocities. RNA, tvf, and agc have been applied. The lack of reflection events for depths shallower than ~400 m below datum is an artifact of the swath acquisition. The left side of the plot is to the southwest, and the right side to the northeast.

Reflection events shown in Figures 8.21 and 8.22 are much less coherent than those shown for Lines 8 and 10. Those lines primarily crossed valley fill areas with relatively little faulting.. Line 6 crosses through the highly faulted area at the foot of the Hot Springs Mountains. It also crosses areas of

igneous and metamorphic cover on the northeast end of the line. Interestingly, a number of semi coherent events are visible on the northeast part of the line. Examples are the strong series of events at depths around 1100 m below datum between CDPs 10800 and 11100.

Figure 8.23 shows the depth converted post stack time migration data of Line 6 (Figure 8.22) overlain with the interval velocities inferred from the Line 6 normal moveout (NMO) RMS velocities.

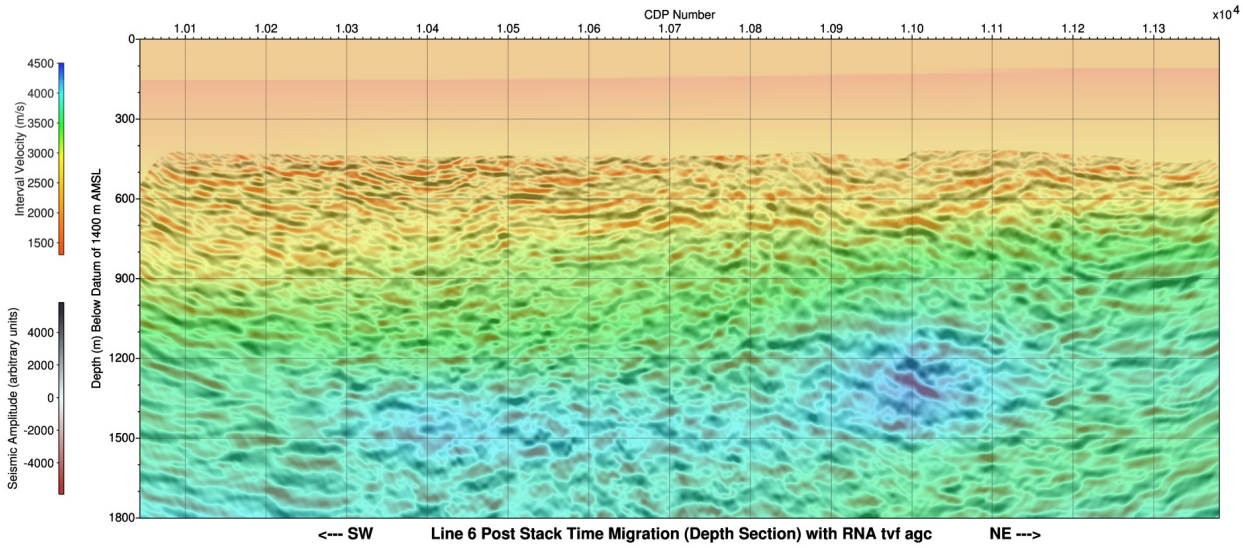

Figure 8.23: Post stack time migration depth section for Line 6 after time to depth conversion using NMO velocities, overlain by color coded interval velocities inferred from those velocities. RNA, tvf, and agc have been applied.

Line 1 Results

Line 1 was re-acquired as part of the effort under Task 8. It was significantly extended to the northwest compared to the acquisition described under Task 4. Line 1 is a dip line oriented NW-SE. It passes within approximately 50 m SW of the 15-1 well, the VSP and EGS well at Brady's. It was acquired as a standard 2D CDP line with sources and geophones along the same station locations. Image points (CDPs) lie at the midpoint between the source and geophone along the line.

Figure 8.24 shows a time section trace plot of the post stack time migration results for Line 1 after application of RNA, tvf, and agc. Figure 8.25 shows the same data after time to depth conversion using the stacking NMO velocities.

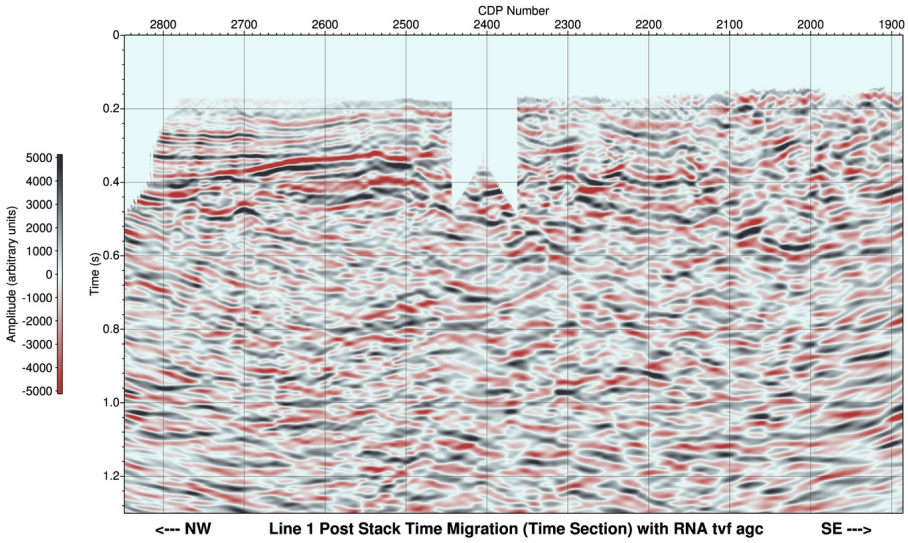

Figure 8.24: Post stack time migration time section for Line 1, with RNA, tvf, and agc applied. The left side of the plot is to the northwest, and the right side to the southeast. The notch in the data around CDP 2400 is due to Interstate 80.

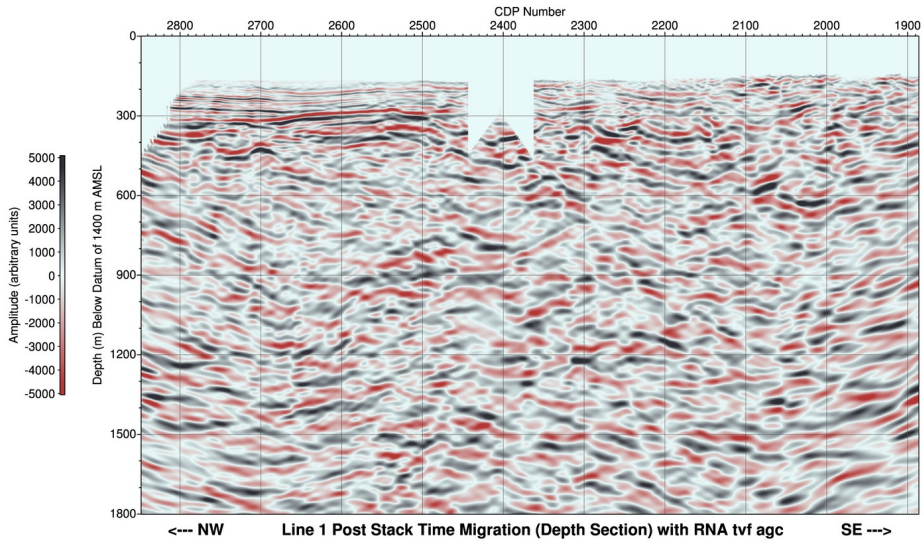

Figure 8.25: Post stack time migration depth section for Line 1 after time to depth conversion using NMO velocities. RNA, tvf, and agc have been applied. The left side of the plot is to the northwest, and the right side to the southeast.

Figure 8.26 shows the depth converted post stack time migration data of Line 1 (Figure 8.25) overlain with the interval velocities inferred from the Line 6 normal moveout (NMO) RMS velocities.

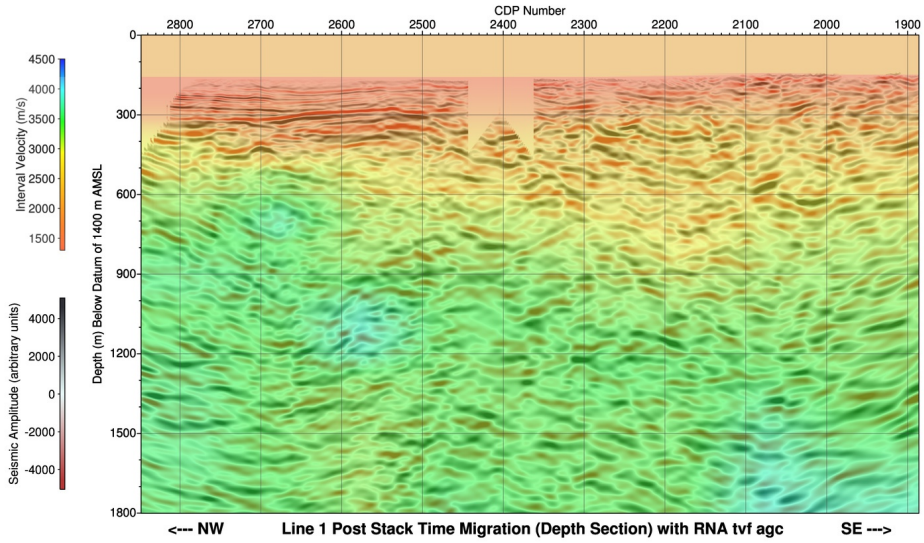

Figure 8.26: Post stack time migration depth section for Line 1 after time to depth conversion using NMO velocities, overlain by color coded interval velocities inferred from those velocities. RNA, tvf, and agc have been applied.

Figure 8.27 shows the Line 1 depth converted post stack migration data without tvf processing after spectral color time-frequency analysis.

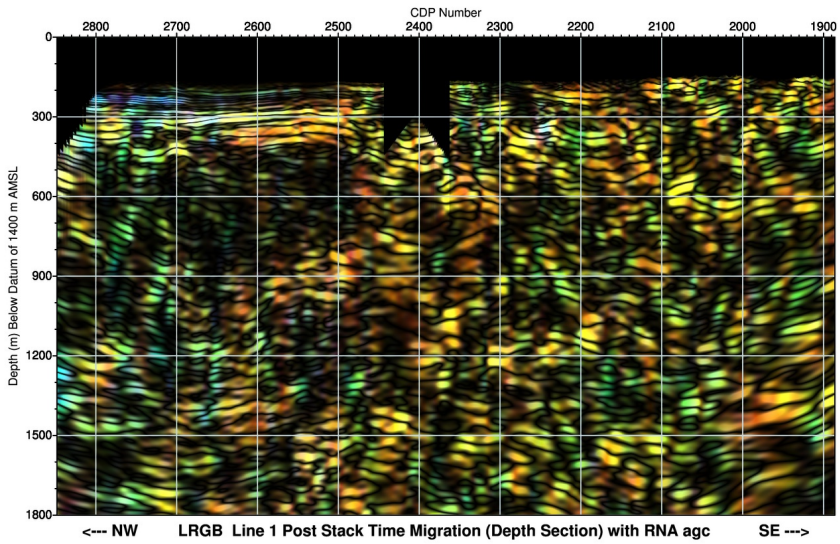

Figure 8.27: Spectral color LRGB representation of Line 1 post stack time migration data without the tvf process applied. RNA and agc data were used in the spectral color analysis.

The spectral color shows a loss of higher frequencies near the middle of the figure in the vicinity of Interstate 80. Colors are seen to be greener on the left side of the plot, changing to reds near the center, and then back to green on the right. Figure 8.7 shows that this is also in the vicinity of a major fault.

Line 1 crosses the surface mapped location of this fault near CDP 2340.

Line 5 Results

Line 5 is a swath line. It is a dip line oriented NW-SE. It parallels Line 1, and passes a few hundred meters to the southwest of Line 1. It was acquired as a swath line with sources along Line 1 station locations and geophones along Line 5 station locations (Figure 8.1). Image points (CDPs) lie approximately at the midpoint between the source and geophone lines (Figure 8.7).

Figure 8.28 shows a time section trace plot of the post stack time migration results for Line 5 after application of RNA, tvf, and agc. Figure 8.29 shows the same data after time to depth conversion using the stacking NMO velocities.

As with the other swath lines, there are no seismic events for times earlier than ~0.3s on the time section (Figure 8.28) and shallower than ~300 m below datum on the depth section (Figure 8.29). This is due to the swath acquisition.

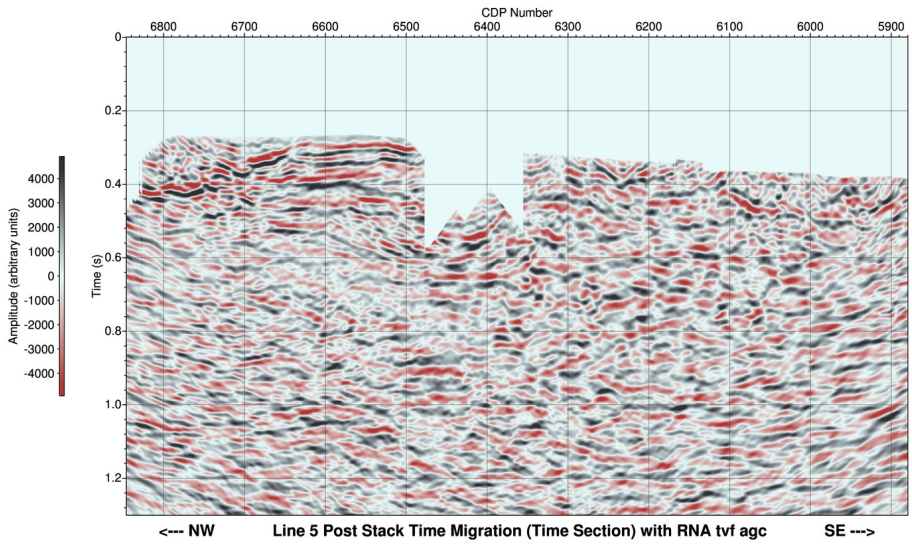

Figure 8.28: Post stack time migration time section for swath Line 5, with RNA, tvf, and agc applied. The lack of reflection events for times earlier than ~0.3 s is an artifact of the swath acquisition. The left side of the plot is to the northwest, and the right side to the southeast.

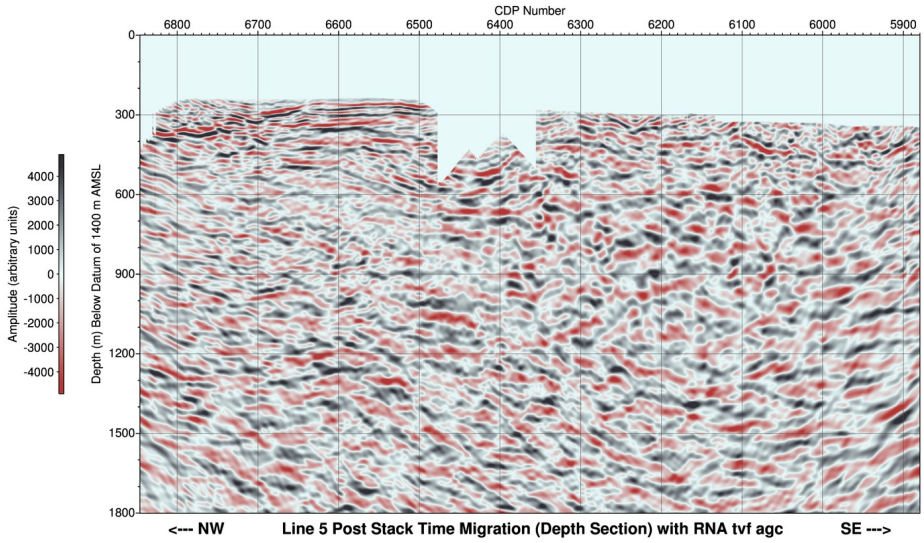

Figure 8.29: Post stack time migration depth section for swath Line 5 after time to depth conversion using NMO velocities. RNA, tvf, and agc have been applied. The lack of reflection events for depths shallower than ~300 m below datum is an artifact of the swath acquisition. The left side of the plot is to the northwest, and the right side to the southeast.

Figure 8.30 shows the depth converted post stack time migration data of Line 5 (Figure 8.29) overlain with the interval velocities inferred from the Line 6 normal moveout (NMO) RMS velocities.

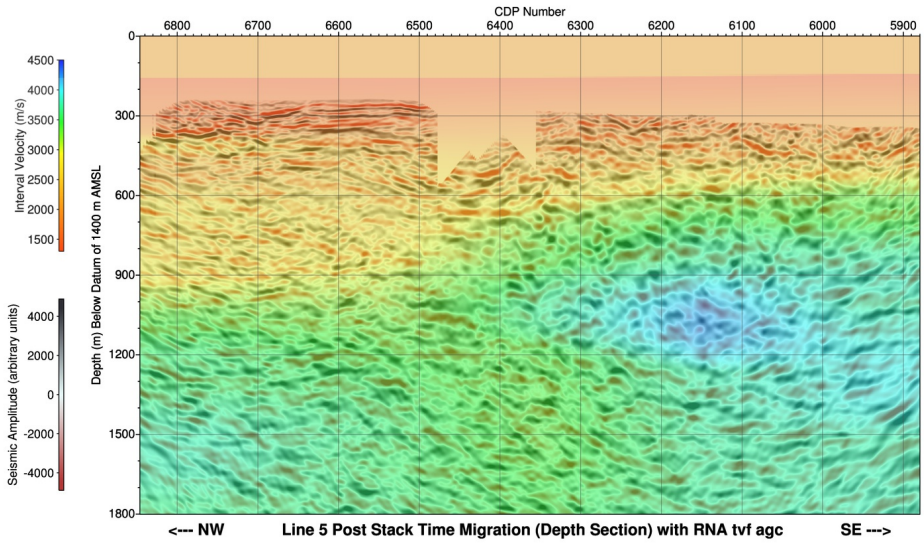

Figure 8.30: Post stack time migration depth section for swath Line 5 after time to depth conversion using NMO velocities, overlain by color coded interval velocities inferred from those velocities. RNA, tvf, and agc have been applied.

The velocity overlays shown in Figures 8.26 (Line 1) and 8.30 (Line 5) both show a number of

heterogeneous higher velocity zones indicated by the blue colors. With a CDP spacing of approximately 3 m, these features are seen to have a scale of around 500 m along the lines. These structures do not correlate well between the two lines, even though the lines are only separated by a few hundred meters. A number of possibilities may explain this. This may be an indication of the unreliability of the interval velocity estimates derived from NMO velocities. Alternatively, it may indicate a significant velocity heterogeneity in the area of the 15-12 well.

Line 7 Results

Line 7 is a swath line. It is a dip line oriented NW-SE. Similar to Line 5, it parallels Line 1, passing a few hundred meters to the northeast of Line 1. It was acquired as a swath line with sources along Line 1 station locations and geophones along Line 7 station locations (Figure 8.1). Image points (CDPs) lie approximately at the midpoint between the source and geophone lines (Figure 8.7).

Figure 8.31 shows a time section trace plot of the post stack time migration results for Line 5 after application of RNA, tvf, and agc. Figure 8.32 shows the same data after time to depth conversion using the stacking NMO velocities.

As with the other swath lines, there are no seismic events for times earlier than ~0.3s on the time section (Figure 8.31) and shallower than ~300 m below datum on the depth section (Figure 8.32). This is due to the swath acquisition.

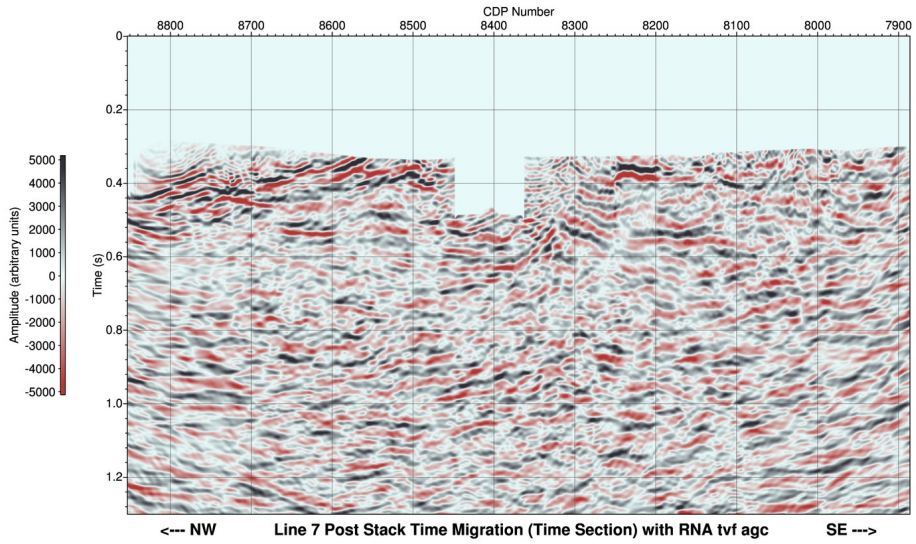

Figure 8.31: Post stack time migration time section for swath Line 7, with RNA, tvf, and agc applied. The lack of reflection events for times earlier than ~0.3 s is an artifact of the swath acquisition. The left side of the plot is to the northwest, and the right side to the southeast.

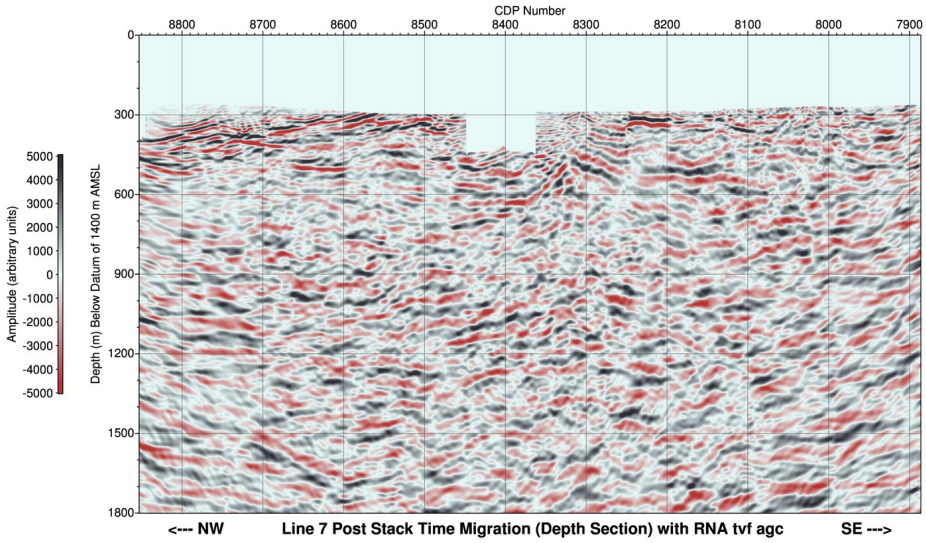

Figure 8.32: Post stack time migration depth section for swath Line 7 after time to depth conversion using NMO velocities. RNA, tvf, and agc have been applied. The lack of reflection events for depths shallower than ~300 m below datum is an artifact of the swath acquisition. The left side of the plot is to the northwest, and the right side to the southeast.

Figure 8.33 shows the depth converted post stack time migration data of Line 5 (Figure 8.32) overlain with the interval velocities inferred from the Line 6 normal moveout (NMO) RMS velocities.

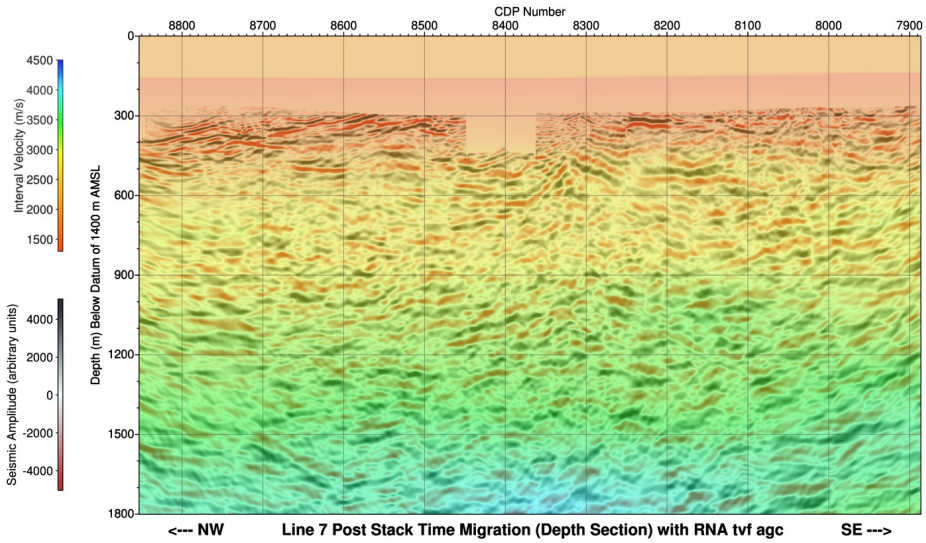

Figure 8.33: Post stack time migration depth section for swath Line 7 after time to depth conversion using NMO velocities, overlain by color coded interval velocities inferred from those velocities. RNA, tvf, and agc have been applied.

The velocity heterogeneity shown by Line 7 is much less than shown by Lines 1 and 5. Again, it is

difficult to correlate these zones between the three lines.

Task 9: Final Interpretation

Proposed Objectives

Working with John Queen of Hi-Q Geophysical Inc. and Gene Suemnicht of Ormat Technologies Inc., Stephen G. Muir, consulting geologist and geophysicist, will then produce a final interpretation of these data. Pre-existing geological data will be integrated with the VSP and surface seismic results. Any additional data acquired by Ormat Technologies Inc. during the course of the project will also be integrated into the final interpretation. Assuming 100% success in all previous tasks and phases, an interpretation of the distribution and orientation of the rock mass fractures and their relationship to lithological and structural elements in the Brady's Hot Springs geothermal area will be delivered.

Accomplishments

Shortly after the beginning of the project, Gene Suemnicht left Ormat. Peter Drakos of Ormat took over these duties. He was further supported by Ezra Zemach, Ormat leader of the Brady's EGS project.

A collaboration was also built with Prof. James Faulds and co-workers at the University of Nevada, Reno (UNR) and the Nevada Bureau of Mines and Geology (NBMG). They played a major role in the final interpretation of these data.

Due to delays with the Multi Offset VSP work, data were not delivered from Task 7 until a few weeks before the end of the project. This left very little time to integrate these results into the overall interpretation. Some results from the Task 7 VSP will be discussed below in terms of the final interpretation.

Surface Reflection Seismic

Following the acquisition of Lines 1, 3, and 4 during Phase II, James Faulds and co-workers (including Nick Hinz and Drew Siler) of UNR and NBMG formulated an updated geological interpretation of the Brady's Hot Springs KGRA. They combined geological surface mapping, analysis of well logs, core and cuttings from 21 wells, and the three seismic lines to produce a series of four geological cross sections. These cross sections were discussed under Task 6. Related surface mapping results were later published (Faulds et al., 2012).

These results, along with some results from the additional seismic lines, were then integrated into an overall digital 3D geological model of the Brady's Hot Springs KGRA. The construction of this digital geological model was described by Siler et al., (2016). Siler et al., (2016) discuss the elements of lithology and faulting in this geological model, and how, when combined with other proxies, they lead to a geothermal fluid flow favorability map for Brady's Hot Springs.

Digital cross section slices along image point locations for each of the seismic lines were extracted from the digital 3D geological model by Drew Siler of UNR. This provided digital fault and lithological boundary data for each individual seismic line at the points where a given geological feature intersected the line. These faults and lithological boundaries were then posted on plots of all 9 surface reflection seismic lines produced by the project.

Stephen G. Muir, Consulting Geologist and Geophysicist, a major participant in the project, acquired an extensive gravity survey over the Brady's Hot Springs KGRA as part of their in kind contribution to the project. This work was previously discussed under Task 4. Simple Bouguer Anomaly (SBA) results along profiles provided by them were combined with previous profiles acquired by Opplinger supplied by NBMG. These combined results were then gridded. SBA gravity profiles were then extracted from this grid along image point locations for the surface reflection seismic lines, and were posted on the seismic plots.

As discussed under Task 8, it was decided to use the post stack time migration results for all lines in Task 9: Final Interpretation. This insured consistent processing for all the seismic data. Previous comparisons of the pre stack and post stack migration results have shown that there are only minor differences between the two processing results. Time to depth converted displays were used in this final interpretation. The time to depth conversion process, as well as its limitations, were discussed under Tasks 4 and 8.

Geological strike direction at Brady's Hot Springs KGRA is approximately N30E. Most of the faulting in this area trends in this direction. Seismic Lines 1, 3, 5, 7, and 9 are seen to be dip lines, running sub-parallel to the approximate dip direction of N60W (Figure 8.7). Lines 4, 6, 8, and 10 are seen to be strike lines.

Post stack time migrated depth converted seismic plots are presented below. Seismic lines are shown with fault and horizon picks extracted from the 3D digital geological model along the image point locations.

The 3D geological model is extremely complex. Figure 9.1 (adapted from Siler et al., 2016) displays one view of this model. The model is fairly heterogeneous. Many of the lithological units do not extend uniformly across the model, and are limited in their 3D extent.

The density of faults shown in Figure 9.1 is quite high, particularly around the cluster of production wells. Mean fault spacing at Brady's Hot Springs is on the order of 250 m (Siler et al., 2016). Fault spacings as low as ~50 m are seen. Using standard seismic industry acquisition spacings for sources and geophones (~30 m), many fault blocks would be covered by only a few image traces. With fault offsets of reflectors occurring every 3 to 4 traces, the seismic images would be very incoherent. Identifying faults from such reflection images is difficult.

In order to get picks of intersections of horizons with a seismic line, each sampled depth level in the seismic line had to be treated as a near horizontal well by the geological modeling software. The software then looked for intersections of the horizon with the “well” at each depth. Occasionally, a given lithological unit is nearly horizontal and only intersects the seismic line at a few points using this approach. In extreme cases they only intersect at one point. This leads to a sparse number of points for some lithological boundaries on the seismic plots.

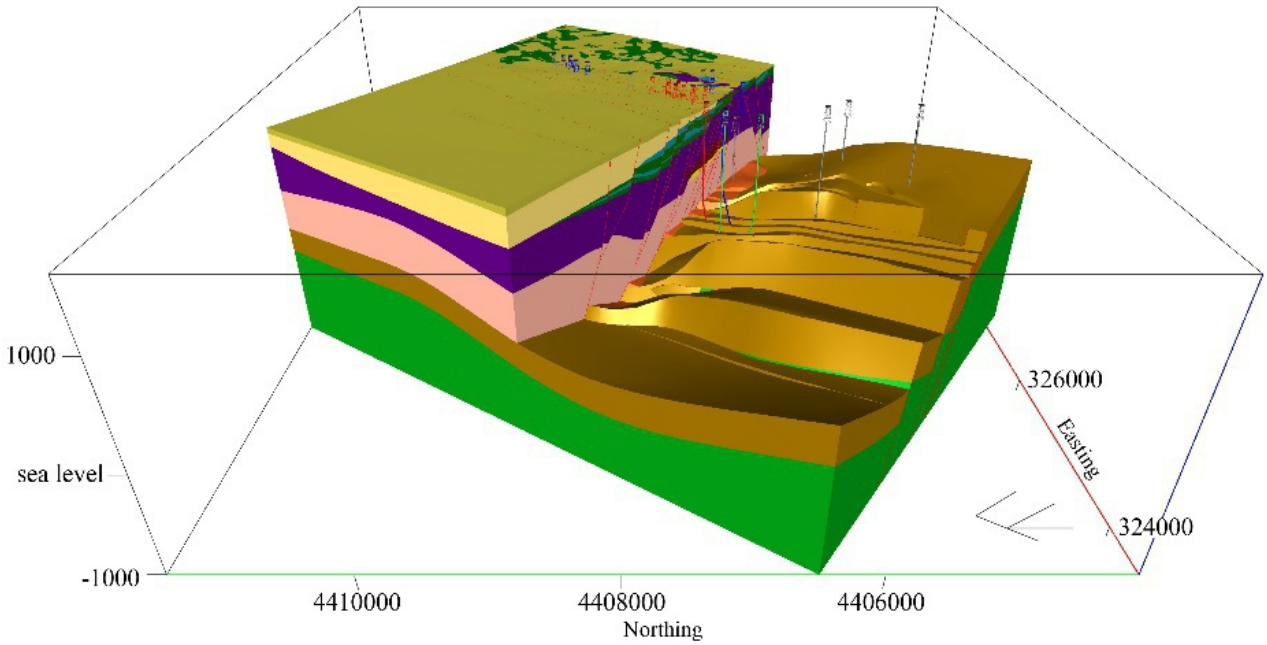

Figure 9.1: 3D geological model for Brady's geothermal system. The model is sliced vertically through the Brady's step-over revealing a high density of faults within the step-over. Red and blue wells are production and injection wells. Green wells have been used for both production and injection. Grey wells are non-productive wells. All distances in meters. Figure adapted from Siler et al., (2016).

In the plots seismic data shown below, interpreted faults are displayed as solid red lines. Picks of interpreted tops of lithological boundaries are shown as filled circles with connecting lines, with the color corresponding to the lithologies shown in Figure 9.2. Corresponding codes for each lithology (Figure 9.2) are posted just below the tops, and are shown in black.

Nick Hinz of UNR and NBMG has provided lithological interpretation data for a total of 21 wells from the Brady's Hot Springs KGRA. These interpretations are based on well logs, core, and drill cuttings. For each of the seismic sections shown below, lithological interpretation results from nearby wells are projected onto the seismic plots along the well tracks, again with color for each lithological unit shown in Figure 9.2. Actual projected well tracks are shown for those wells having orientation surveys provided by Ormat.

For dip seismic lines, wells were projected horizontally along the strike direction. For each dip line, wells were selected based on their surface offset from the line, as well as being in the same fault block crossed by the line. For strike seismic lines, wells were projected horizontally along the dip direction, and only included wells with minimal surface offset from the line.

Lithology Codes

COLOR	CODE	DESCRIPTION
	Mzm, Mzu	Mesozoic undistinguished
	Qf	Alluvial fan deposits
	Tu	Tertiary undistinguished
	Tabo	Older basaltic lavas, altered
	Tbo	Older basaltic lavas
	Tda	Andesite-dacite lavas
	Tls	Limestone
	Trt	Oligocene ash-flow tuffs
	Tlr	Rhyolite lavas and lesser tuffs
	Tsl	Lacustrine sediments
	Tslo	Older lacustrine sediments
	Tslo+Tlr	Tslo+Tlr
	Tsy	Sandstone and conglomerate
	Tts	Non-welded tuffs
	Tpd	Porphyritic Hb-Bt dacite to rhyodacite flows and domes

Figure 9.2: Color table, codes, and descriptions corresponding to lithologies used in well interpretations and lithological boundaries provided by Faulds and co-workers.

Tie points with other surface reflection seismic lines are shown as white vertical lines. The name of the intersecting line is shown in gray just to the right of the tie line at the top of the plot.

SBA gravity profiles extracted from the gridded gravity results along each line are plotted in red at the top of each seismic line plot.

Dip Lines

Dip lines will be shown first. They are oriented NW-SE. They will be shown in order going from southwestern most to northeastern most (Lines 5, 1, 7, 9, and 3).

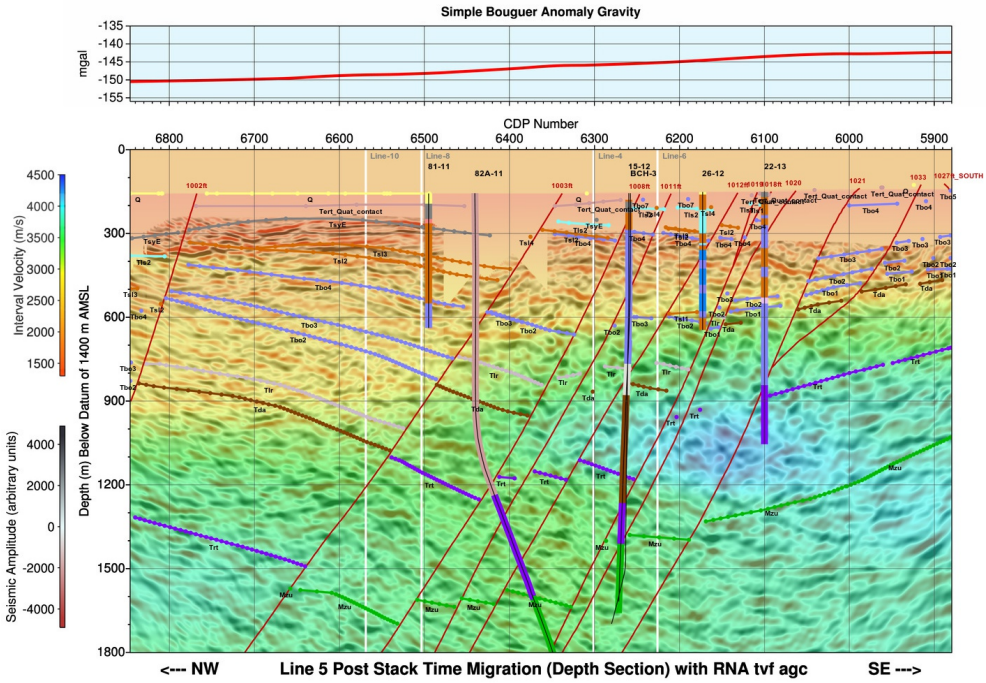

Figure 9.3: Post stack time migrated dip Line 5 after depth conversion using overlain interval velocities estimated from stacking velocities. Projected well lithologies are shown color coded following Figure 9.2. Interpreted faults from the 3D geological model are shown as red lines, and interpreted lithology picks as filled circles with connecting lines color coded following Figure 9.2.

Figure 9.3 shows interpretation results plotted on top of Line 5. Time to depth converted post stack migration results with interval velocity overlay are displayed. Line 5 is a swath line. It parallels Line 1, and passes a few hundred meters to the southwest of Line 1. It is one of 3 dip lines covering the area around the Brady's 15-12 well, the VSP and EGS well. That well projects onto the line near CDP 6260.

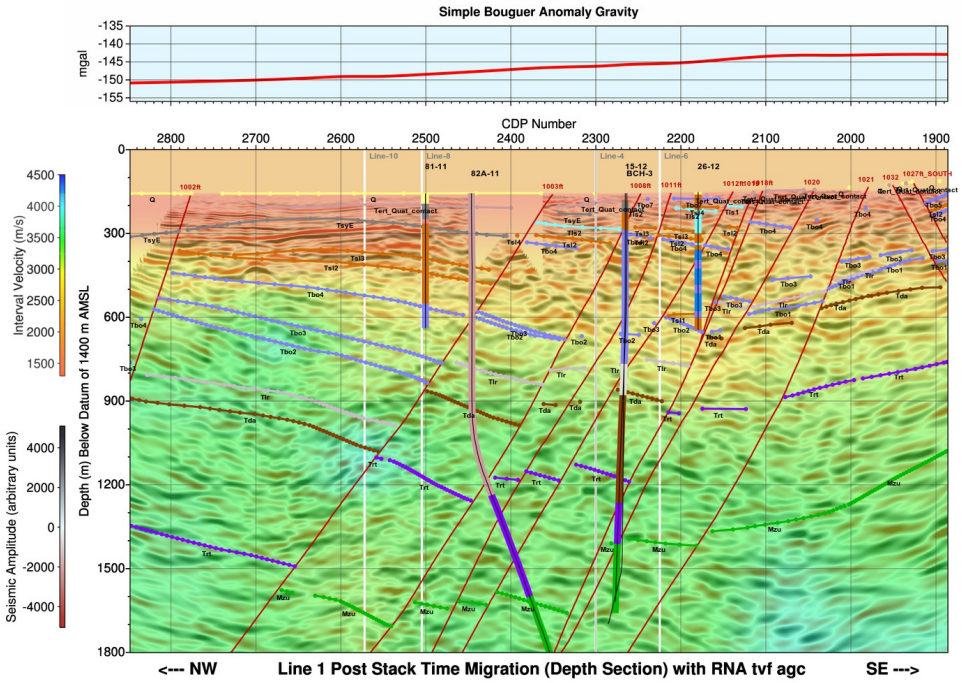

Figure 9.4: Post stack time migrated dip Line 1 after depth conversion using overlain interval velocities estimated from stacking velocities. Projected well lithologies are shown color coded following Figure 9.2. Interpreted faults from the 3D geological model are shown as red lines, and interpreted lithology picks as filled circles with connecting lines color coded following Figure 9.2.

Figure 9.4 shows Line 1 interpretation results. Line 1 was re-acquired as part of the effort under Task 8. It was significantly extended to the northwest compared to the acquisition described under Task 4. It passes within approximately 50 m SW of the 15-1 well, the VSP and EGS well at Brady's. That well projects on to the line near CDP 2260. It was acquired as a standard 2D CDP line.

A number of reflection segments shown in Figure 9.4 correspond to geological model lithological horizons. However, not all of the model horizons have associated reflection events. Similarly, there are a number of very strong coherent reflection events with not corresponding model horizon.

Tracking the Trt horizon (purple horizon on Figure 9.4) shows that only two major faults offset the beds along Line 1. The first major fault breaks the surface near CDP 2350 (fault 1003ft), It dips to the north-west and has a vertical offset of near 250 m where it crosses Line 1. The top of the second major fault along Line 1 is near CDP 2105, labeled as fault 1018ft. This fault also dips to the north-west with offset of around 250 m. It is the fault included in the simplified 3D model of Figure 6.5 and cuts through the Brady's 15-12 well. Its location is well established by its observation in core from the BCH-3 well. Surface location of BCH-3 is only offset by about 30 m from the 15-12 well.

A number of short but continuous reflections are visible along Line 1 near these faults. An example is between CDP's 2290 and 2150 at depths between ~440 m and ~520 m. This event terminates on the left against the fault labeled as 1008ft and on the right against the major 1018ft fault.. This Line 1 reflection event is also visible in the near offset Multi Offset VSP results to be discussed later. This event does not appear to correspond to any geological model horizons.

A similar event lies just below the top of the Tbo4 lithological horizon from the 3D geological model. This event is also found in the Line 5 (Figure 9.3) and Line 7 (Figure 9.5) results just below the top of Tbo4 between these same two faults. An analogous event is apparent in many places across the seismic section below the Tbo4 horizon. This apparently Tbo4 related event is seen on many of the other lines.

These terminations were considered useful (though not definitive) when combined with other geological data in constraining the subsurface locations of faults. A significant number of reflections with sudden offsets or terminations are visible in Figure 9.4. Many of these have no interpreted model faults associated with them. Reflector terminations and offsets can only be qualified as fault related when integrated with other geological and geophysical information.

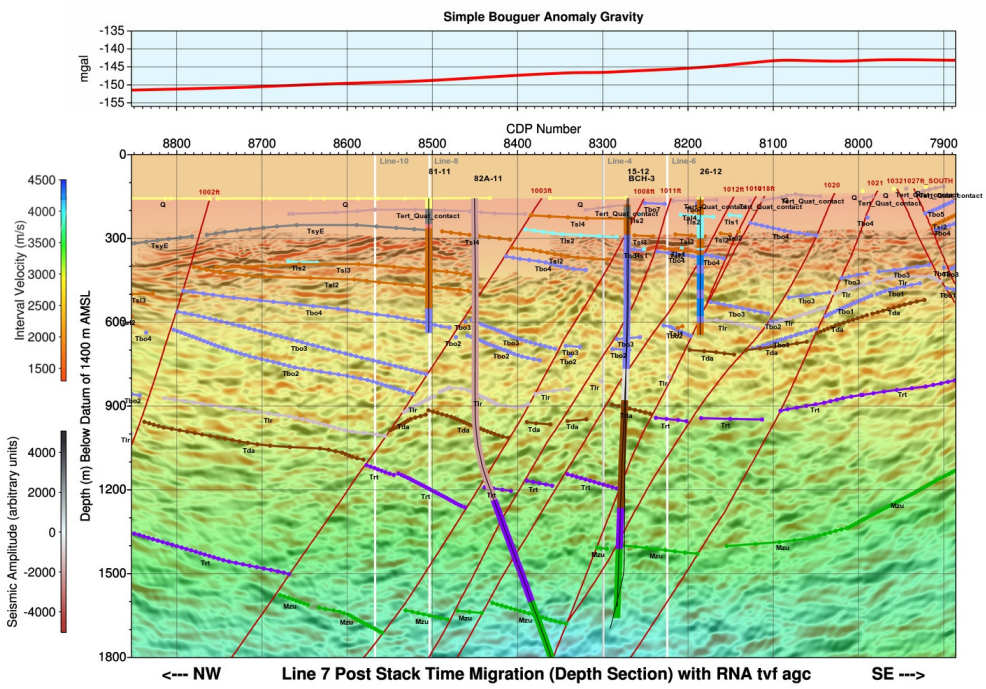

Figure 9.5: Post stack time migrated dip Line 7 after depth conversion using overlain interval velocities estimated from stacking velocities. Projected well lithologies are shown color coded following Figure 9.2. Interpreted faults from the 3D geological model are shown as red lines, and interpreted lithology picks as filled circles with connecting lines color coded following Figure 9.2.

Figure 9.5 shows interpretation results plotted on top of Line 7. Time to depth converted post stack migration results with interval velocity overlay are displayed. Line 7 is a swath line. It parallels Line 1, and passes a few hundred meters to the northeast of Line 1. It is one of 3 dip lines covering the area around the Brady's 15-12 well, the VSP and EGS well. That well projects onto the line near CDP 8270.

As with Line 1, a number of reflection segments are seen to correspond to geological model horizons. A number of reflection segments are seen to terminate near or against model faults. Also similar to the Line 1 interpretation, a number of these segments do not correlate with model horizons or faults.

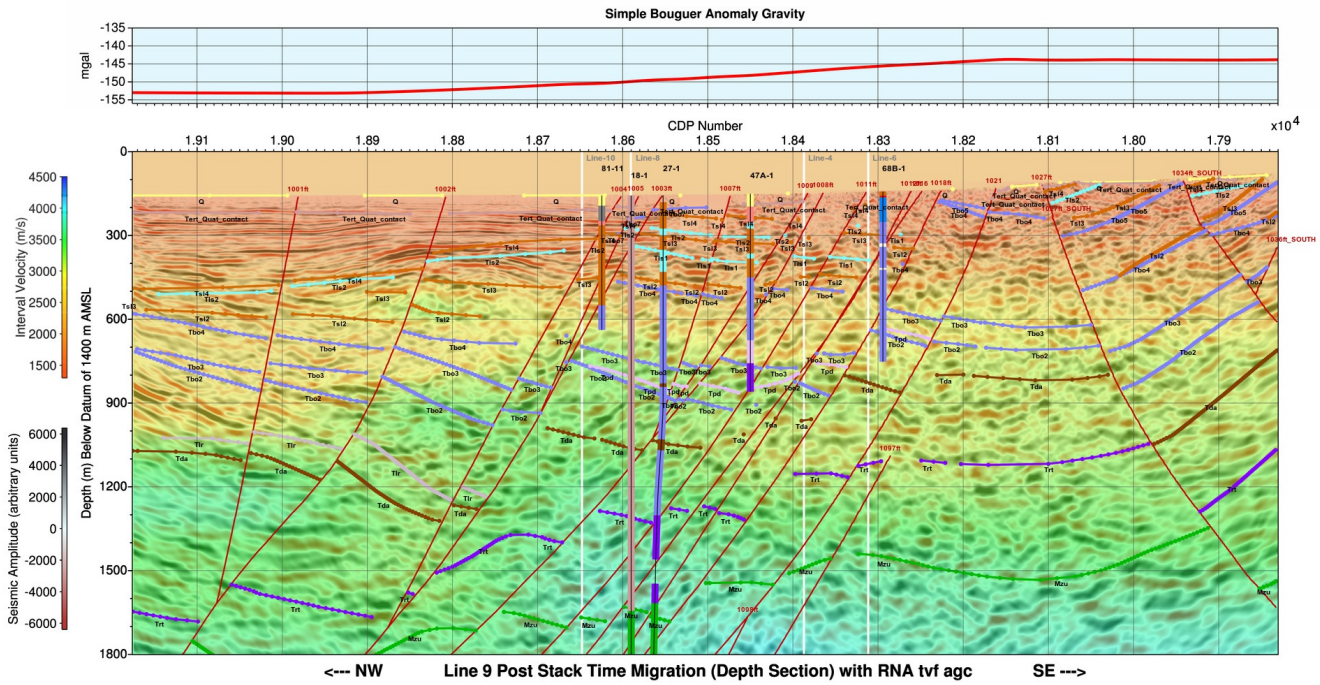

Figure 9.6: Post stack time migrated dip Line 9 after depth conversion using overlain interval velocities estimated from stacking velocities. Projected well lithologies are shown color coded following Figure 9.2. Interpreted faults from the 3D geological model are shown as red lines, and interpreted lithology picks as filled circles with connecting lines color coded following Figure 9.2.

Line 9 was acquired as a standard 2D CDP line. It lies between the area of the 15-12 VSP and EGS well to the southwest and the main producing area to the northeast. It passes a few hundred meters southwest of the surface location of the highly deviated 27-1 production well. The bottom hole location of the 27-1 well is several hundred meters to the northeast of Line 9 (into the plane of the figure) near Line 3.

Events on this line show perhaps the weakest correspondence with geological model faults and horizons of all the lines. This line was the last delivered by the processor, and did not have a major influence on the final reconciliation of the 3D geological model.

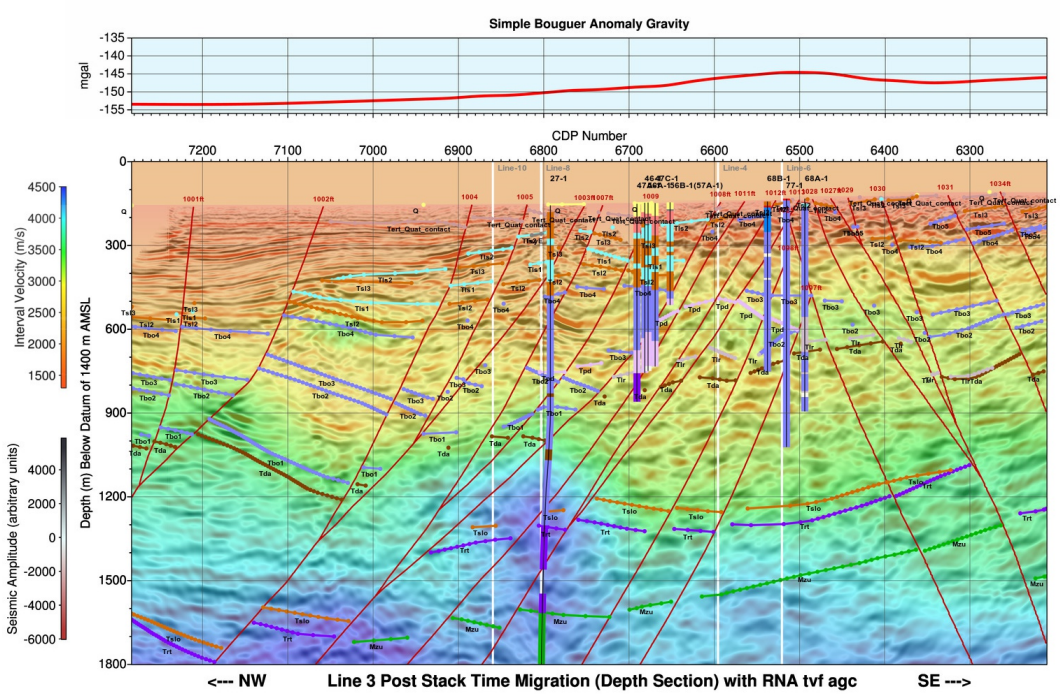

Figure 9.7: Post stack time migrated dip Line 3 after depth conversion using overlain interval velocities estimated from stacking velocities. Projected well lithologies are shown color coded following Figure 9.2. Interpreted faults from the 3D geological model are shown as red lines, and interpreted lithology picks as filled circles with connecting lines color coded following Figure 9.2.

Line 3 was acquired as a standard 2D CDP line as part of Phase II Task 4. It passes through the main producing area of the Brady's hot springs KGRA. It also passes over the bottom hole location of the highly deviated 27-1 production well. This well deviates to the northeast from its surface location into the plane of the figure.

Figure 9.7 shows a very complex structure for the Brady's Hot Springs KGRA. Similar to the Line 1 results (Figure 9.4), tracking the Trt horizon (purple horizon on Figure 9.7) shows that, in spite of this complexity, only two major faults offset the beds along Line 3.

The first major fault (from the left) intersects the surface near CDP 6590. It is labeled as fault 1003ft in the figure. It is the same major fault which intersects Line 1. This fault dips to the northwest and has a vertical offset of approximately 300 m. The second major fault along Line 3 cuts the surface near CDP 6405 (fault 1030) and dips to the southeast with approximately 200 m of vertical offset.

As was the case with Line 1, a number of short but continuous reflections are seen to terminate near these faults. A significant number of reflections with sudden offsets or terminations are visible in Figure 9.7. While several of these are seen to terminate against model faults, many have no interpreted model faults associated with them. Again, reflector terminations and offsets can only be qualified as fault related when integrated with other geological and geophysical information.

Figure 9.7 shows a relatively high velocity zone around the bottom hole location of the 27-1 production well. This is indicated by the darker blue feature near the bottom center of the figure. Similar features

are seen in several of the seismic lines. There origin is not well understood.

Jones et al., (1980) investigated the effects of temperature on seismic velocities in geothermal reservoirs. They found that the temperature dependence of seismic velocities depend on, among other things, fluid thermal properties and thermal fracturing at elevated temperatures. Based on laboratory measurements on Berea sandstone, they found that initially, velocities increase rapidly with increasing temperature due to drying. Near 160º C, thermal fracturing became dominant. This lead to a rapid decrease in velocities with increasing temperature above 160º C. After cooling the sample, they found that velocities were lower than their initial low temperature values.

Jaya et al., (2010) reported on the temperature dependence of seismic velocities on two geothermal core samples from Iceland. Each of these cores was from a different geothermal field. They were of different rock type (Basalt and Hyaloclastite). Both were from alteration zones. Using very low salinity water as a saturating fluid, they measured the compressional velocity as a function of temperature on these two different cores. For each core, they first raised and then lowered the temperature, repeating this through several cycles. They observed a decreasing trend of compressional velocity with increasing temperature for each cycle. Based on Gassmann equation modeling, they concluded that the decrease in velocity with temperature was related to fluid characteristics.

One possible cause for the high velocity zone near the bottom hole location of the 27-1 production well is lower temperature caused by the production process. It was beyond the scope of this project to investigate possible correlations between the seismic interval velocities along each line and the temperature profiles of nearby wells.

As similarly discussed under Task 8, the velocity overlays shown in Figures 9.3 (Line 5) and 9.4 (Line 1) also show a number of heterogeneous higher velocity zones indicated by the blue colors. The velocity contrast of these high velocity zones is smaller than the one along Line 3. With a CDP spacing of approximately 3 m, these features are seen to have a scale of around 500 m along the lines. These structures do not correlate well between the two lines, even though the lines are only separated by a few hundred meters. A number of possibilities may explain this. This may be an indication of the unreliability of the interval velocity estimates derived from NMO velocities. Alternatively, it may indicate a significant velocity heterogeneity in the area of the 15-12 well related to variations of rock type, alteration, fluid content, fracturing, and temperature.

Strike Lines

Strike lines will now be shown. They are oriented SW-NE. They will be shown in order going from northwestern most to southeastern most (Lines 10, 8, 4, and 6). Lines are plotted looking to the NW.

Strike lines are generally more difficult to interpret. Faults can intersect obliquely and at very low angles. They may have repeated section related to offset of lithologies by faults. For the 2D lines acquired in this project, they are also more prone to out of plane reflections and migration errors related to out of plane dip.

Figure 9.8 – 9.11 show interpretation results for lines 10, 8, 4, and 6 respectively. Time to depth converted post stack migration results with interval velocity overlay are displayed. Lines 10 and 4 were acquired as standard 2D CDP lines. Lines 8 and 6 were swath lines.

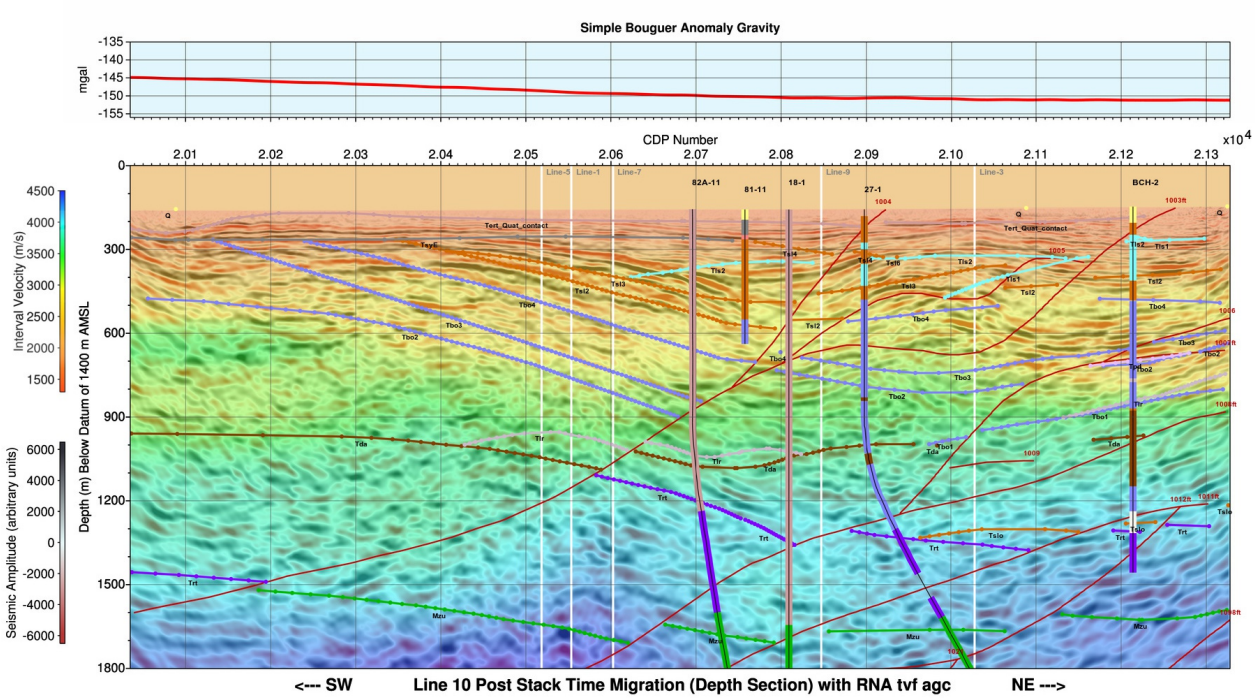

Figure 9.8: Post stack time migrated strike Line 10 after depth conversion using overlain interval velocities estimated from stacking velocities. Projected well lithologies are shown color coded following Figure 9.2. Interpreted faults from the 3D geological model are shown as red lines, and interpreted lithology picks as filled circles with connecting lines color coded following Figure 9.2.

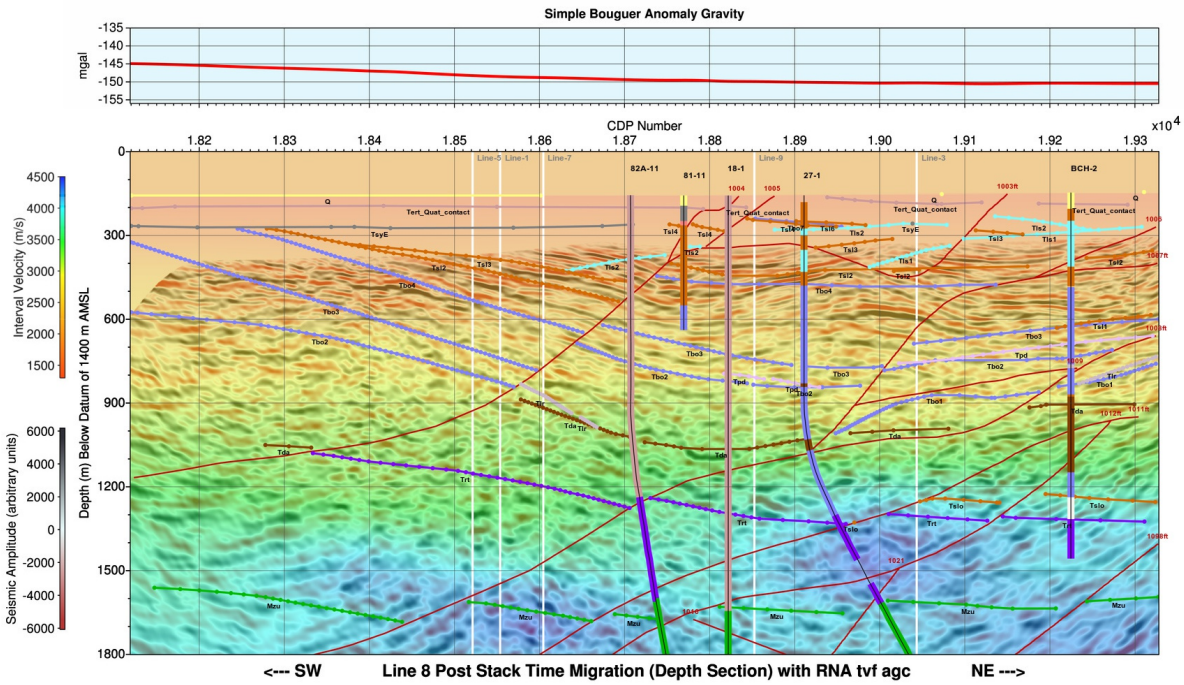

Figure 9.9: Post stack time migrated strike Line 8 after depth conversion using overlain interval velocities estimated from stacking velocities. Projected well lithologies are shown color coded following Figure 9.2. Interpreted faults from the 3D geological model are shown as red lines, and interpreted lithology picks as filled circles with connecting lines color coded following Figure 9.2.

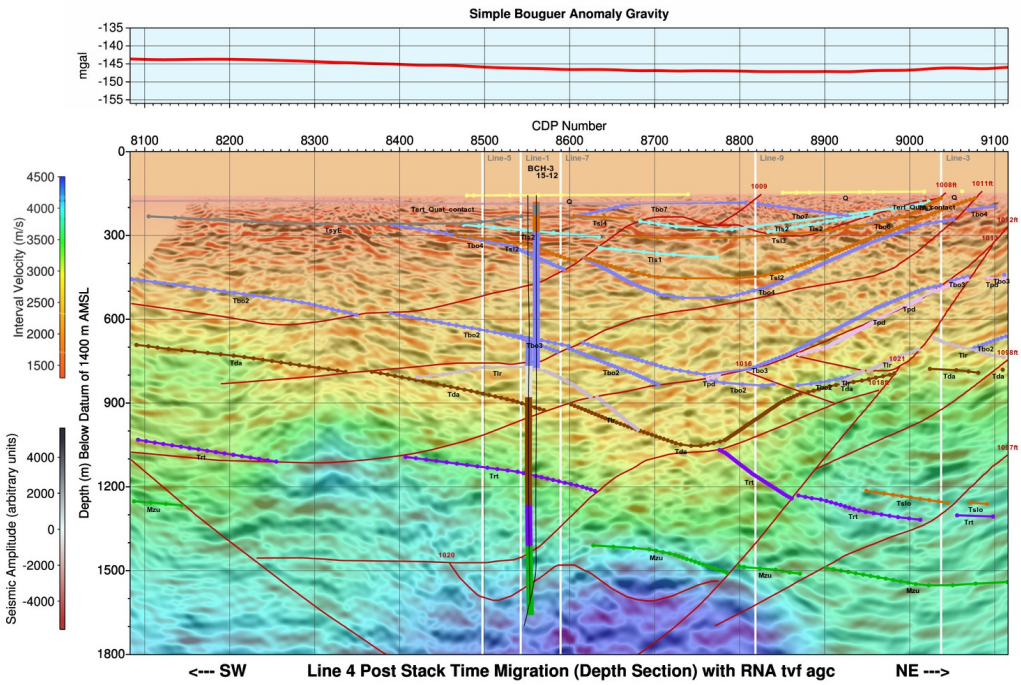

Figure 9.10: Post stack time migrated strike Line 4 after depth conversion using overlain interval velocities estimated from stacking velocities. Projected well lithologies are shown color coded following Figure 9.2. Interpreted faults from the 3D geological model are shown as red lines, and interpreted lithology picks as filled circles with connecting lines color coded following Figure 9.2.

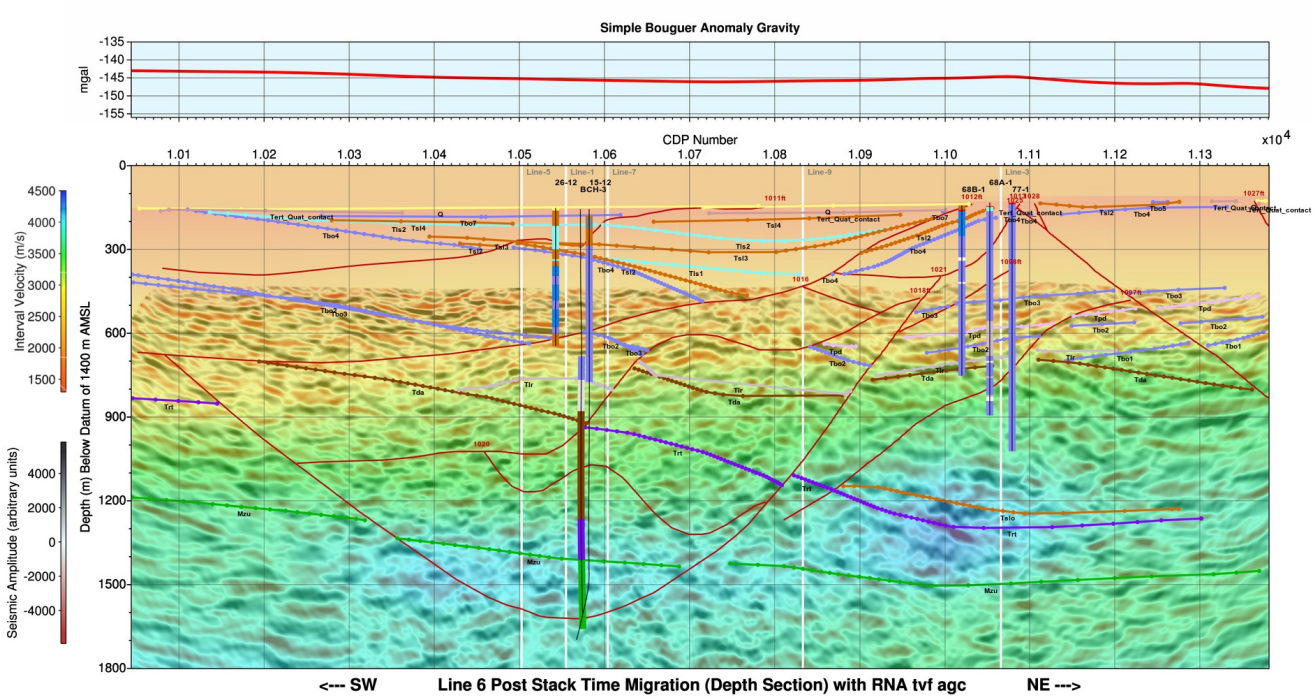

Figure 9.11: Post stack time migrated strike Line 6 after depth conversion using overlain interval velocities estimated from stacking velocities. Projected well lithologies are shown color coded following Figure 9.2. Interpreted faults from the 3D geological model are shown as red lines, and interpreted lithology picks as filled circles with connecting lines color coded following Figure 9.2.

Lines 10 and 8 were acquired over valley fill regions of the Brady's area. Lines 4 and 6 were acquired over areas dominated by igneous and metamorphic rocks. The data quality of the valley fill lines is noticeably better.

As with the dip lines, a number of heterogeneous velocity zones are apparent on the strike lines. Lines 8 (Figure 9.9) and 3 (Figure 9.7) intersect near the bottom hole location of production well 27-1. The intersection point is near CDP 6800 on Line 3 and CDP 19040 on Line 8. The lateral deviation of the 27-1 well to the northeast is evident on Line 8.

The higher velocity zone visible on the Line 3 results near the bottom hole location of production well 27-1 was discussed earlier. It is also manifested on the Line 8 results. Comparing this feature on the two lines, some discrepancies can be seen. The depth of the zone is different on the two lines. The values of the interval velocities also differ along the tie line.

These kinds of velocity discrepancies can be seen on several other lines where they intersect. There are a number of possible causes for these discrepancies.

The line orientations between the strike and dip lines differ by nearly 90º. If extensive orientated fractures are present, they should lead to an azimuthal anisotropy (Hudson 1980, 1981). Velocities in one propagation direction should be different from those in another. This should lead to a difference in interval velocities estimated from NMO velocities for nearly orthogonal lines.

Another, and perhaps more likely cause of these discrepancies, is that the interval velocity estimates

from NMO velocities is unstable. It is not clear if these interval velocities can be relied upon to tell anything about the geology.

Comparison of reflection events between strike and dip lines shows a number of reflections which tie at the intersections. Others do not. Some of those are only slightly shifted in depth. This effect seems to increase with depth. This may be related to the use of NMO derived interval velocities in time to depth conversion.

Shot Gathers

The modeling discussed under Task 6 suggests that locations where faults are present in the near surface will generate major effects in surface reflection shot gathers (Figures 6.5E and 6.6E). Such faults should generate back scattered surface waves which cut across shot gather trace displays. Near surface guided waves trapped between high and low velocity contrasts propagate horizontally in the near surface. When they reach a near surface fault, they scatter in the reverse direction.

Figure 9.12 shows a comparison between: (A) an actual field data shot gather from Line 1; and (B) the simulated shot gather from the complex 3D model.

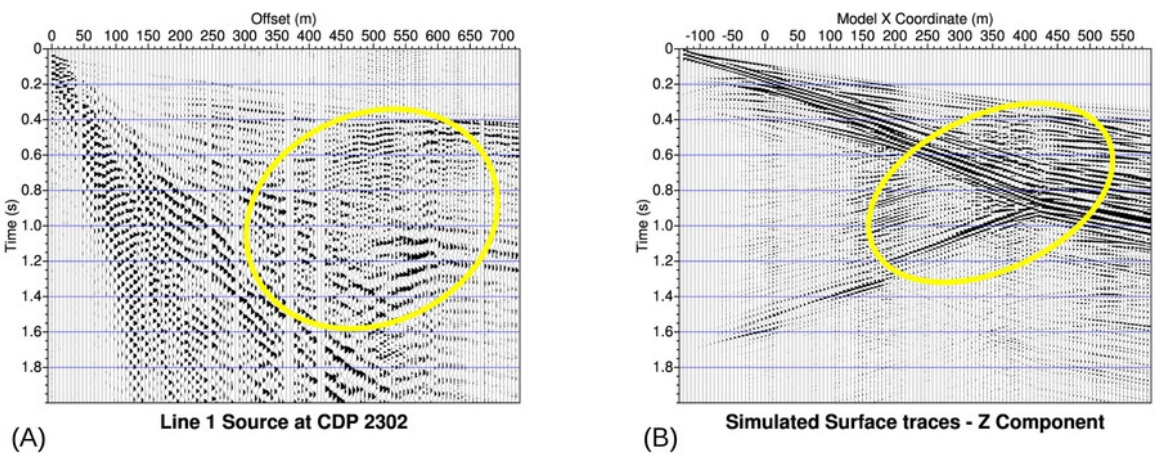

Figure 9.12: (A) Common source gather from Line 1. Source is at CDP 2302. Trace at offset 601 m is at CDP 2104; (B) Surface seismic shot gather results from simulations over the complex 3D model shown in Figure 6.6.

Figure 9.12A shows a common shot gather from Line 1. The source is located at CDP 2302. The apparent back scattered energy circled in yellow originates near offset 600 m, which corresponds to CDP 2104. This is the CDP location where a major fault is seen to break the surface in Figure 8.07. This is also the CDP where the major fault 1018ft breaks the surface in Figure 9.4, the interpreted Line 1 results. Figure 6.6E is reproduced in Figure 9.12B. It shows the complex 3D model shot gather. The back scattered energy circled in yellow originates at the location of the major fault in the geophysical model corresponding to fault 1018ft from the geological model. These back scattered events carry no information about the structure of the deeper fault.

These events would be aliased at normal seismic spacing. The events from 0 to ~150 m offset in Figure 9.12A are spatially aliased even at the fine spacing used in the acquisition. Fortunately, these events could be muted without losing much of the deeper reflection information.

Multi Offset VSP

As discussed under Task 7, delivery of the Multi Offset VSP data was delayed. By the time the data were delivered, only 3 weeks were left before the project end data. This left very little time to integrated VSP results into the final interpretation.

Despite this limitation, a few observations can be made regarding the Multi Offset VSP data. Figure 9.13 shows a comparison of the near offset processed VSP data from source point Vp 0 with the simulated traces from the complex model. Figure 9.13A reproduces Figure 7.3C and Figure 9.13B reproduces Figure 6.6F.

The offset of the source in Figure 9.13A is ~32 m. This offset is similar to the offset of the source in the model simulations (Figure 9.13B).

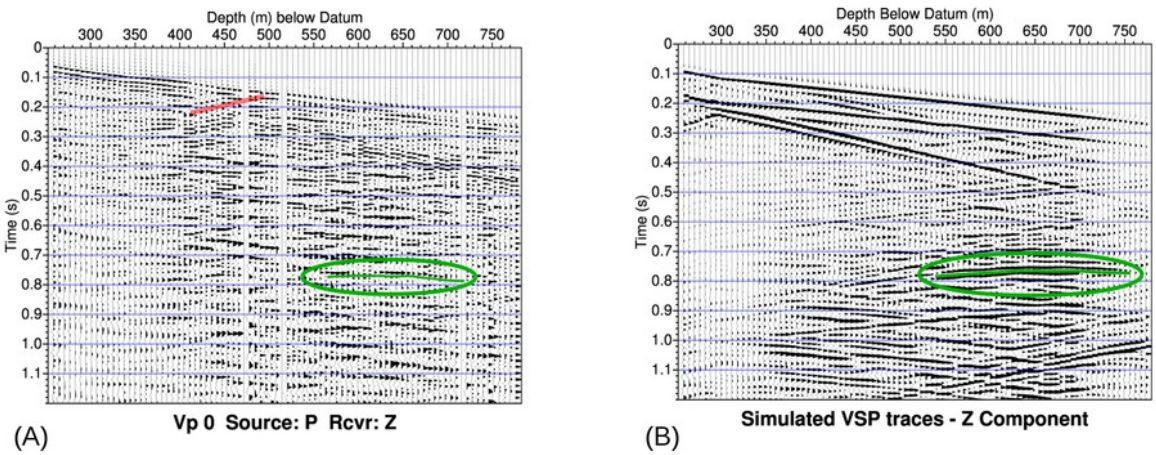

Figure 9.13: (A) Multi Offset VSP data traces from a vertical vibrator at the near offset source point Vp 0; (B) Near offset VSP results from simulations over the complex 3D model shown in Figure 6.6.

The event highlighted in green on the Multi Offset VSP traces (Figure 9.13A) is at approximately the same time and depths as the event shown in green in the modeling results (Figures 9.13B). This event has an apparent velocity (inverse of the slope of the event) much higher than the apparent velocities of the up and down going compressional and shear waves.

As discussed under the seismic modeling in Task 6, the event highlighted in green in Figure 9.13B is a scattered shear wave coming off the 1018ft fault. It is possible that the green highlighted event in Figure 9.13A is a fault scattered event. To truly qualify these events as scattering from faults or fractures more advanced processing would be needed. If it is truly a fault scattered event, the amplitude, arrival time, and depths at which this event occurs should vary systematically as the source is moved away from the well. Reverse time migration such as discussed by Wang et al., (2011) would

formalize this process. Unfortunately, the available source points are not sufficient for such imaging.

The event highlighted in red on Figure 9.13A is a compressional wave reflection. It originates at a depth of approximately 480 m below datum in the well. This same event was seen in the vicinity of the 15-12 well in the Line 1 reflection seismic data (Figure 9.4). This event does not correspond to any of the lithological horizons in the 3D geological model. It was never incorporated into the geophysical model. As a consequence, it does not appear in the synthetic VSP traces.

Task 10: Technology Transfer

Proposed Objectives

At the end of the project, the Principal Investigator and Major Participants will submit results of the work at regional and international professional society meetings, and travel to those meetings to present results. Results will also be submitted to a major professional journal for publication.

Accomplishments

An abstract was submitted and accepted for presentation of results of this project at the internationally recognized 41st Workshop on Geothermal Reservoir Engineering, held at Stanford University, Stanford, California, February 22-24, 2016. A presentation was prepared and presented at this workshop. A formal paper describing the results was also written. This paper was uploaded to the Stanford Workshop on Geothermal Reservoir Engineering web site where it is freely available for download (Queen et al., 2016).

A companion paper (Siler et al., 2016) describing the development of the geological model and its application to geothermal favorability mapping at Brady's Hot Springs was submitted to this same workshop. This paper was accepted for presentation and a presentation was made by the lead author, Drew Siler, now at Lawrence Berkeley Laboratory. A formal paper was written and uploaded to the Stanford Workshop on Geothermal Reservoir Engineering web site.

Informal presentations of results to date were made at Ormat internal meetings. This included meetings of the Brady's EGS team on April 6, 2010, and August 31, 2011.

Presentations and documents were presented at two Geothermal Technologies Program Peer Reviews. The first was presented on May 19 2010 in Crystal City, Arlington, VA.. The second was presented on May 9, 2012 in Westminster, CO.

Task 11: Project Management and Reporting

Accomplishments

With the exception of delays related to Task 7 described above, all tasks were completed on time. Several no cost extensions were requested and approved. The project was completed by the final end date of January 31, 2016. Quarterly and annual financial and technical reports were completed in a timely fashion. No budget adjustments were requested, and the project came in on budget.

Products Developed Under The Award

Publications

Publications have been discussed under Task 10: Technology Transfer above. They are listed in the References section.

The two relevant publications discussed under Task 10 can be accessed using these [download] links.

Queen et al., 2016: [download]

Siler et al., 2016: [download]

Web Sites

No web sites were created as products for this project.

Collaborations

As discussed above under Task 9, a collaboration was built with Prof. James Faulds and co-workers at the University of Nevada, Reno (UNR) and the Nevada Bureau of Mines and Geology (NBMG).

Technologies/Techniques

No technologies or techniques were developed as products for this project. The ideas of using fine source/geophone spacing and VSP were widely and independently adopted for use in geothermal areas by many others during the course of this project.

Inventions

No inventions were produced as part of this project.

Other Products

No other products were produced as part of this project.

Computer Modeling

No computer modeling software was developed as part of this project.

While geological and geophysical modeling played a key role in this project, all software involved either existed in house prior to the beginning of the project, or was publicly available.

A great deal of open software was used for the construction, execution, and display of models, as well as the preparation of data displays. Many of these are listed below with links to internet sites where software and manuals can be downloaded.

SW3D

http://sw3d.mff.cuni.cz/

From the web site: "SW3D focuses primarily on the fundamental issues of high-frequency seismic wave propagation in complex 3-D isotropic and anisotropic structures." Modules from this package were used in the construction and visualization of seismic models.

Seismic Un*x

http://www.cwp.mines.edu/cwpcodes/

Seismic Unix is a comprehensive seismic processing, display, and modeling package. It includes ray trace, finite difference, and Kirchhoff modeling programs among others. It was used widely throughout the project.

SEISMIC_CPML

https://geodynamics.org/cig/software/seismic_cpml/

From the web site: "SEISMIC_CPML is a set of eleven open-source Fortran90 programs to solve the two-dimensional or three-dimensional isotropic or anisotropic elastic, viscoelastic or poroelastic wave equation using a finite-difference method with Convolutional or Auxiliary Perfectly Matched Layer (C-PML or ADE-PML) conditions, developed by Dimitri Komatitsch and Roland Martin from CNRS, France. Contributions by other authors have recently been added."

OpendTect

http://opendtect.org/

OpendTect is an extensive open source seismic interpretation platform. It was used widely in the interpretation tasks of the project. We thank dGB Earth Sciences for providing the open source OpendTect software.

GRASS GIS

https://grass.osgeo.org/

From the web site: "GRASS GIS, commonly referred to as GRASS (Geographic Resources Analysis Support System), is a free and open source Geographic Information System (GIS) software suite used for geospatial data management and analysis, image processing, graphics and maps production, spatial modeling, and visualization." It was used in the production of many of the map displays.

GMT

http://gmt.soest.hawaii.edu/

From the web site: "GMT is an open source collection of about 80 command-line tools for manipulating geographic and Cartesian data sets (including filtering, trend fitting, gridding, projecting, etc.) and producing PostScript illustrations ranging from simple x–y plots via contour maps to artificially illuminated surfaces and 3D perspective views." It was used in gridding data as well as producing a wide range of displays.

VisIt

https://wci.llnl.gov/simulation/computer-codes/visit/

From the web site: "VisIt is an Open Source, interactive, scalable, visualization, animation and analysis

tool." It was widely used in the project to produce 3D visualizations of geophysical models.

ImageMagick®

http://www.imagemagick.org/

From the web site: "ImageMagick® is a software suite to create, edit, compose, or convert bitmap images." It was used throughout the project to convert image formats, and produce overlays.

References

Alford, R. M., 1986, Shear data in the presence of azimuthal anisotropy: Dilley, Texas, *SEG Technical Program Expanded Abstracts 1986*, 476-479, doi: 10.1190/1.1893036.

Benoit, Walter R., Hiner, John E., and Forest, Robert T., 1982, Discovery and geology of the Desert Peak geothermal field: a case history, Nevada Bureau of Mines and Geology, Bulletin 97, 82p.

Bleistein, N., 1986, TWO-AND-ONE-HALF DIMENSIONAL IN-PLANE WAVE PROPAGATION, *Geophysical Prospecting*, **34**, 686-703, doi 10.1111/j.1365-2478.1986.tb00488.x.

Cohen, J. K. and Stockwell, Jr. J. W., 2008, CWP/SU: Seismic Un*x Release No. 41: an open source software package for seismic research and processing, Center for Wave Phenomena, Colorado School of Mines.

Courant, R., Friedrichs, K., and Lewy, H., (1967), On the Partial Difference Equations of Mathematical Physics, *IBM Journal of Research and Development*, **11** no. 2, 215-234.

Dix, C. H., 1955, Seismic velocities from surface measurements, *Geophysics*, **20**, 68–86, doi: 10.1190/1.1438126.

Faulds, J.E., and Garside, L.J., 2003, Preliminary geologic map of the Desert Peak – Brady geothermal fields, Churchill County, Nevada: Nevada Bureau of Mines and Geology Open-File Report 03-27.

Faulds, J.E., Coolbaugh, M.F., Vice, G.S., and Edwards, M.L., 2006, Characterizing Structural Controls of Geothermal Fields in the Northwestern Great Basin: A Progress Report: *Geothermal Resources Council Transactions*, **30**, p. 69-76.

Faulds, J.E., Ramelli, A.R., Garside, L.J., Coolbaugh, M.F., and Green, H.L., 2012, Preliminary geologic map of the Desert Peak Quadrangle, Churchill County, Nevada, *Nevada Bureau of Mines and Geology Open-File Report* **12-5**, scale 1:24,000:.

Gritto, R., and Majer, E.L., 2003, Seismic Methods for Resource Exploration in Enhanced Geothermal Systems, *Geothermal Resources Council Transactions*, **27**, 223–226.

Hanssen, P., Ziolkowski, A. and Li, X.-Y., 2003, A quantitative study on the use of converted waves for sub-basalt imaging, *Geophysical Prospecting*, **51,** 183–193, doi: 10.1046/j.1365-2478.2003.00367.x.

Hudson, J. A., 1980, Overall properties of a cracked solid, *Mathematical Proceedings of the Cambridge Philosophical Society*, **88**, 371-384, doi:10.1017/S0305004100057674.

Hudson, J. A., 1981, Wave speeds and attenuation of elastic waves in material containing cracks, *Geophysical Journal of the Royal Astronomical Society*, **64,** 133–150, doi: 10.1111/j.1365-246X.1981.tb02662.x.

Jaya, M. S., Shapiro, S., Kristindóttir, L., Bruhn, D., Milsch, H. and Spangenberg, E, Temperature-Dependent Seismic Properties of Geothermal Core Samples at In-Situ Reservoir Conditions, *Proceedings*, World Geothermal Congress 2010, Bali, Indonesia, 25-29 April, 2010.

Jones, T., Murphy, W., and Nur, A., 1980, Effects of Temperature and Saturation on the Velocity and Attenuation of Seismic Waves in Rocks: Applications to Geothermal Reservoir Evaluation, *Proceedings*, 6th Workshop on Geothermal Reservoir Engineering, Stanford University, Stanford, CA.

Juhlin, C., 1995, Finite-difference elastic wave propagation in 2D heterogeneous transversely isotropic media, *Geophysical Prospecting*, **43**, no. 6, 833-858, doi: 10.1111/j.1365-2478.1995.tb00284.x.

Levander, A.R., 1998, Fourth-order finite-difference P-SV seismograms, *Geophysics*, **53**, no. 11, 1425-1436, doi: 10.1190/1.1442422.

Nowack, R. L., 1992, Wavefronts and solutions of the eikonal equation, *Geophysical Journal International*, **110**: 55–62, doi: 10.1111/j.1365-246X.1992.tb00712.x.

Pyrak-Nolte, L. J., and J. P. Morris, 2000, Single fractures under normal stress: The relation between fracture specific stiffness and fluid flow, *Int J Rock Mech & Min Sci*, **37**, 245-262, doi: 10.1016/S1365-1609(99)00104-5.

Queen, John H. and Rizer, William D., 1990, An integrated study of seismic anisotropy and the natural fracture system at the Conoco Borehole Test Facility, Kay County, Oklahoma, Journal of Geophysical Research: Solid Earth, 95,no. B7, 11255–11273, doi: 10.1029/JB095iB07p11255.

Queen, John H., Daley, Thomas M., Majer, Ernest L., Niehi, Kurt T., Siler, Drew L., and Faulds, James E., Surface Reflection Seismic and Vertical Seismic Profile at Brady's Hot Springs, NV, USA, *Proceedings*, 41st Workshop on Geothermal Reservoir Engineering, Stanford University, Stanford, CA.

Siler, D.L., Faulds, J.E., Hinz, N.H., and Queen, J.H., 2016, 3D analysis of geothermal fluid flow favorability; Brady's, Nevada, USA, *Proceedings*, 41st Workshop on Geothermal Reservoir Engineering, Stanford University, Stanford, CA.

Theophanis, S. and Queen, J., 2000, Color display of the localized spectrum, **Geophysics**, 65, no. 4, 1330 – 1340, doi: 10.1190/1.1444825.

Wang, Y., Huang, L., and Zhang, Z., 2011, Reverse-time Migration of Time-lapse Walkaway VSP Data For Monitoring CO2 Injection At the SACROC EOR Field, *SEG Technical Program Expanded Abstracts 2011*, 4304-4308, doi: 10.1190/1.3628107.

Zhu, Yaping, and Roel Snieder, 2002, Reflected and transmitted waves from fault zones, *SEG Expanded Abstracts*,2002 2273-2276, doi: 10.1190/1.1817166.